2004 SUMMER RESEARCH PROGRAM FOR HIGH SCHOOL JUNIORS

AT THE

UNIVERSITY OF ROCHESTER'S

LABORATORY FOR LASER ENERGETICS

STUDENT RESEARCH REPORTS

PROGRAM COORDINATOR

Dr. R. Stephen Craxton

March 2005   Laboratory Report 337

2004 SUMMER RESEARCH PROGRAM FOR HIGH SCHOOL JUNIORS

AT THE

UNIVERSITY OF ROCHESTER'S

LABORATORY FOR LASER ENERGETICS

STUDENT RESEARCH REPORTS

PROGRAM COORDINATOR

Dr. R. Stephen Craxton

LABORATORY FOR LASER ENERGETICS
University of Rochester
250 East River Road
Rochester, NY 14623-1299

During the summer of 2004, 16 students from Rochester-area high schools participated in the Laboratory for Laser Energetics' Summer High School Research Program. The goal of this program is to excite a group of high school students about careers in the areas of science and technology by exposing them to research in a state-of-the-art environment. Too often, students are exposed to "research" only through classroom laboratories, which have prescribed procedures and predictable results. In LLE's summer program, the students experience many of the trials, tribulations, and

rewards of scientific research. By participating in research in a real environment, the students often become more excited about careers in science and technology. In addition, LLE gains from the contributions of the many highly talented students who are attracted to the program.

The students spent most of their time working on their individual research projects with members of LLE's scientific staff. The projects were related to current research activities at LLE and covered a broad range of areas of interest including laser optics modeling, analysis of OMEGA implosion experiments, hydrodynamics modeling, cryogenic target characterization, liquid crystal physics and chemistry, materials science, the development and control of laser fusion diagnostics, and OMEGA EP laser system design and engineering. The students, their high schools, their LLE supervisors, and their project titles are listed in the table. Their written reports are collected in this volume.

The students attended weekly seminars on technical topics associated with LLE's research. Topics this year included laser physics, fusion, holographic optics, fiber optics, femtosecond lasers and their applications, computer-controlled optics manufacturing, and global warming. The students also received safety training, learned how to give scientific presentations, and were introduced to LLE's resources, especially the computational facilities.

The program culminated on 25 August with the "High School Student Summer Research Symposium," at which the students presented the results of their research to an audience including parents, teachers, and LLE staff. Each student spoke for approximately ten minutes and answered questions. At the symposium the William D. Ryan Inspirational Teacher award was presented to Mr. Claude Meyers, a former physics

teacher at Greece Arcadia High School. This annual award honors a teacher, nominated by alumni of the LLE program, who has inspired outstanding students in the areas of science, mathematics, and technology. Mr. Meyers was nominated by David Bowen, a participant in the 2001 Summer Program.

A total of 176 high school students have participated in the program since it began in 1989. The students this year were selected from approximately 50 applicants. Each applicant submitted an essay describing their interests in science and technology, a copy of their transcript, and a letter of recommendation from a science or math teacher.

In the past, several participants of this program have gone on to become semifinalists and finalists in the prestigious, nationwide Intel Science Talent Search. This tradition of success continued this year with the selection of two students (Bruce Brewington and Jeremy Chang) as among the 300 semifinalists nationwide in this competition. Brewington was selected as a finalist in the Talent Search—an honor bestowed upon only 40 of the nearly 1600 participating students.

LLE plans to continue this program in future years. The program is strictly for students from Rochester-area high schools who have just completed their junior year. Applications are generally mailed out in early February with an application deadline near the end of March. Applications can also be obtained from the LLE website. For more information about the program, please contact Dr. R. Stephen Craxton at LLE.

High School Students and Projects (Summer 2004)			
Name	**High School**	**Supervisor**	**Project Title**
Daniel Balonek	Byron-Bergen HS	D. Jacobs-Perkins	An Optical Measurement System for Characterizing Cryogenic Fusion Targets
Gregory Balonek	Byron-Bergen HS	S. Craxton	How Good is the Bright Ring Characterization for Uniformity of Deuterium Ice Layers within Cryogenic Nuclear Fusion Targets?
Robert Balonek	Byron-Bergen HS	D. Lonobile	Design and Fabrication of a Handheld Optically Coupled Water Flow Calibrator
Bruce Brewington	Fairport HS	S. Craxton	3-D Characterization of Deuterium Ice-Layer Imperfections in Cryogenic Inertial Confinement Fusion Targets
Daniel Butler	Brighton HS	R. Boni	Automated Focusing of the ROSS Streak Tube Electron Optics
Jeremy Chang	Penfield HS	M. Guardalben	Grated Compressor Modeling
Joseph Dudek	Honeoye Falls-Lima HS	C. Stoeckl	Hexapod Motion Through Remote Computer Activation
Laurie Graham	Bloomfield HS	S. Regan	Experimental Investigation of Far Fields on OMEGA
Jivan Kurinec	Rush-Henrietta HS	M. Bonino/ D. Harding	Mechanical Properties of Spider Silk at Cryogenic Temperatures
Jonathan Kyle	Gates-Chili HS	J. DePatie	Operational Specifications for the Two-State Motor Controller
Ted Lambropoulos	Pittsford-Mendon HS	J. Marozas	Optimal Pinhole Loading via Beam Apodization
Yekaterina Merkulova	Penfield HS	J. Delettrez	Spatial Distribution of the Reflected Laser Light at the Experimental Chamber Wall
Arun Thakar	Pittsford-Mendon HS	R. Epstein	Numerically Calculated Spherical Rayleigh–Taylor Growth Rates
Glen Wagner	Fairport HS	T. Kosc/ K. Marshall	Computer Modeling of Polymer Cholesteric Liquid Crystal Flake Reorientation
Tina Wang	Webster-Schroeder HS	V. Smalyuk	Modeling of X-Ray Emission in Spherical Implosions on OMEGA
Ariel White	East Irondequoit-Eastridge	K. Marshall	Photopatterning of Liquid Crystal Alignment Cells

An Optical Measurement System for Characterizing Cryogenic Fusion Targets

Daniel Balonek

An Optical Measurement System for Characterizing Cryogenic Fusion Targets

Daniel J. Balonek

Advisor: Dr. Douglas Jacobs-Perkins

Laboratory for Laser Energetics
University of Rochester
250 East River Road
Rochester, NY 14625-1299

Summer High School Research Program
2004

Abstract:

The Laboratory for Laser Energetics (LLE) houses the OMEGA 60-beam, 30kJ laser capable of generating shaped optical pulses that are used for high-energy physics and inertial confinement fusion (ICF) research. OMEGA is seeded by an optical pulse that is repeatedly amplified and split to produce 60 individual ultraviolet beams (UV wavelength 352 nm).

LLE has developed extensive facilities and expertise for fielding cryogenic deuterium-filled targets. During a cryogenic implosion experiment, all 60 beams are focused onto a 1mm diameter plastic shell filled with a cryogenic (~18K) layer of deuterium ice. This target is heated and compressed by the lasers to initiate fusion. Some cryogenic targets do not achieve their expected performance due to vibrations that cause the target to be decentered relative to the laser beam foci. The causes of vibration are complex. However, they can be exacerbated by inconsistent target fabrication.

This report presents a new quality control instrument that has been built to ensure proper target construction. The instrument consists of an electrodynamic shaker (EDS) and a calibrated optical measurement system (OMS). As the EDS excites the target with known input, the OMS is used to measure the target's response. The EDS/OMS also can be used to test new target designs as well as new imaging equipment before implementation on OMEGA.

Introduction:

Fusion is a virtually inexhaustible energy source that holds great potential in replacing other means of power production. Fusion has almost no environmental impact in comparison to coal and oil, which produce large amounts of carbon dioxide. Fusion is a very safe alternative for power production because it produces no harmful emissions and can be safely contained without the possibility of a "meltdown".[1] Fusion has been very difficult to harness as an energy source because it needs very high pressures and temperatures to cause hydrogen atoms to fuse and produce helium and energy.

The Laboratory for Laser Energetics was established in 1970 as a center for the investigation of the interaction of intense radiation with matter, and has the five-fold mission: [2]

- Conduct implosion experiments and basic physics experiments in support of the National Inertial Confinement Fusion (ICF) program;

- Develop new laser materials and technologies;

- Provide graduate and undergraduate education in electro-optics, high-power lasers, high-energy-density physics, plasma physics, and nuclear fusion technology;

- Operate the National Laser User's Facility; and

- Conduct research and development in advanced technology related to high-energy-density phenomena.
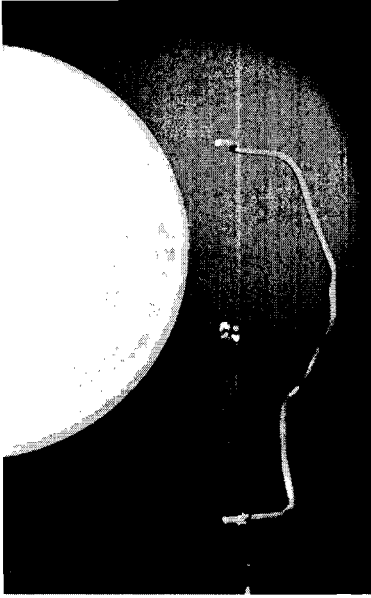
Figure 1. Target compared to a penny

Many experiments conducted at LLE use cryogenic fusion targets. These targets are comprised of a spherical plastic shell typically 3um thick and 860um in diameter (1 um = 0.001mm). These targets are suspended in a C-mount frame (similar to a staple) by four spider silk threads (fig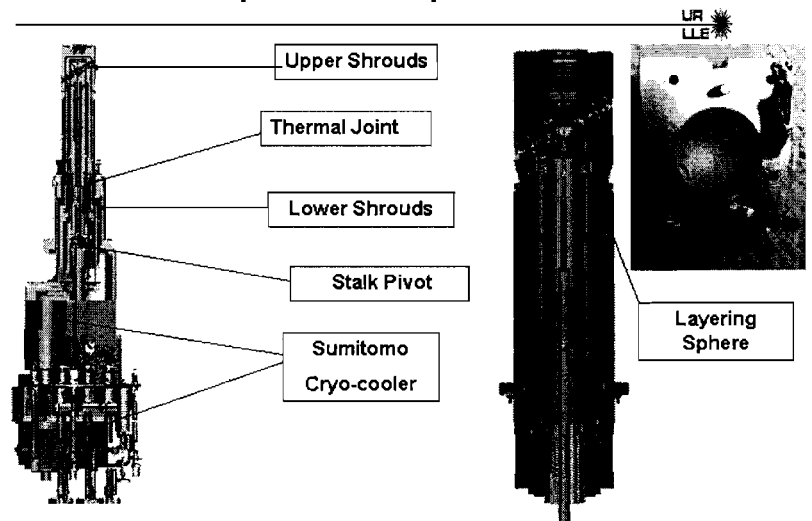ure 1). These targets are pressurized with deuterium and tritium gas, and then cooled to a temperature of 18K to form an ice layer on the inside of the target.

These targets are then placed into the OMEGA target chamber and irradiated by the OMEGA laser. Cryogenic targets require a very complex apparatus (moving cryostat (MC)) (Figure 2) to position the target at the convergence of the beam foci (=target chamber center= TCC). This apparatus also must maintain a precisely controlled thermal environment around the target prior to an experiment.

Description of the Spherical MC

Figure 2. Pieces of a Moving Cryostat

Many improvements have been made to increase the stability of the MC but target construction has remained relatively unchanged. The stability of

targets varies because each individual target is different. In order to obtain optimal performance (as measured by neutron yield or another measure of fusion efficiency), the target must be centered within +10um of the beam foci. Both static and dynamic (e.g. vibration) position errors contribute to the total error budget. Sources that cause target vibration include vacuum pumps that are attached to the target chamber and refrigeration equipment in the moving cryostat transfer cart. A target's position in the chamber is measured using images from two cameras. These images are analyzed to determine the exact center of the target. Static position errors can result from viewing the target through windows in the MC shrouds.

The EDS/OMS will be used as a quality control device to ensure good target manufacturing by testing the stability of the target (by measuring its resonant frequencies) before use in the OMEGA system. The EDS/OMS will incorporate interchangeable parts so that new target structures and mounting interfaces can be evaluated. The EDS/OMS will be able to evaluate new high-speed video cameras as well as new target detection systems.

This report concentrates on the development and calibration of the OMS. Integration of the OMS with the EDS was completed later than anticipated due to delays in procuring the EDS. Photographs were taken after the integration was completed.

Overview:

A commercially available EDS unit [3] capable of exciting frequencies from DC to 4500 Hz is integrated with an Optical Measuring System (Figure 3). The Optical Measuring System is mounted onto the EDS. The OMS is constructed with two achromat doublets with 50mm and 20mm focal lengths[4]. Figure 3 shows the system layout.
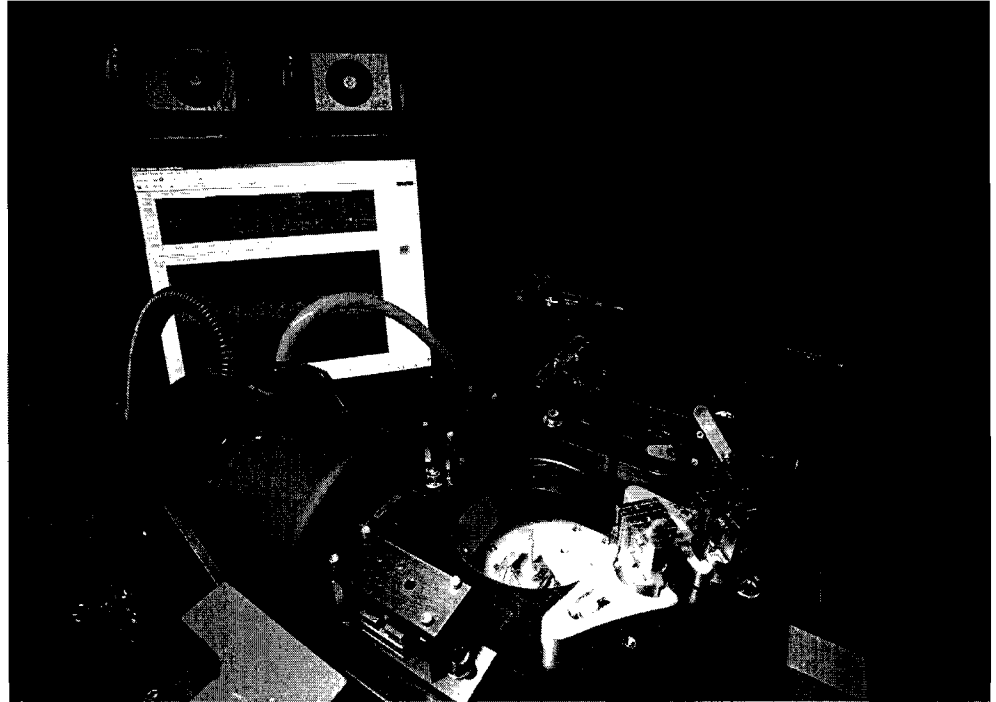

Figure 3. Completed EDS and OMS with target in place and histogram displayed on computer monitor

The optical modeling software Oslo™ [5] is used to optimize the position of the lenses inside the optical tubes of the OMS for a given working distance and magnification. The target is backlit with a red diode laser beam. The illuminated target image is focused simultaneously onto a charge-coupled device (CCD) camera and a four-quadrant photodiode (quad cell, Figure 4) [6] via a beam splitter cube, so that the camera and detector "see" the same image plane. The CCD is used to ensure that the target is aligned onto the center of the OMS viewing axis.

The quad cell contains four photodiodes in a 2x2 array; each produces a voltage (or current) proportional to the amount of light that strikes it. Since the target casts a "shadow" on the quad cell, the voltage is also proportional to target displacement.

Figure 4. Mounted Quad Cell (upper right corner)

As the target image is projected onto the center of the quad cell it produces voltages on all four quadrants, which are sent to the signal conditioner. The signal conditioner amplifies the quad cell voltages. The voltage sum from the right column is subtracted from the sum from the left column to produce a signal proportional to the horizontal target displacement. Voltage signals from the top and bottom rows are combined in a similar manner to produce a signal proportional to the vertical displacement. These signals are then feed into a spectrum analyzer that constructs a histogram of signal strength vs. frequency of excitation.

The spectrum analyzer [7] is a four-channel measurement system and a signal generator. It provides the EDS with the excitation signal source and measures the output voltages from the signal conditioner. The measured data can be analyzed and displayed in several formats including a time-history or frequency spectrum. The frequency spectrum is a mathematical representation of the data broken into discrete frequencies, with each frequency having different amplitudes, like a histogram. Spectra are computed in real time, making analysis very efficient.

Calibration of the Optical Measuring System:

The OMS needs to be aligned and calibrated in order to obtain accurate data. Proper magnification, working distance, and image quality are all important. The gain of each amplifier in the signal conditioner is adjusted to match the sensitivity of the individual quad cells. After adjustment of the amplifier gain, the quad cell is installed and optically aligned with a knife-edge fixture. The spectrum analyzer then sends the information received from the electronic signal conditioners to the computer for analysis.

The first step in calibrating the optical measuring system is to align the optics. The optical system is comprised of one, two, and three-inch optical tubes, and various accessories which can be screwed together. The optical layout is determined by using the OSLO program. The optics are secured in the optical tubes with lens rings. To check the placement of the optics, a caliper is used to measure the depth of the optics in relation to the individual tubes. After the optics are placed in the tubes the system is placed together on prefabricated boards.

After the system is assembled it is necessary to determine the magnification of the optical system (to ensure that all the optics are in the right locations). This is done by placing a target with a known diameter (d) in the view of the optical system and measuring the diameter of the target as it appears on the screen (s), the screen height (h), and the height of the CCD (c). Noting that the magnification from the CCD detector to the display screen is h/c, the magnification of the optical system is $(s/d)(c/h)$. If this magnification is correct it is

then necessary to determine if the working distance is correct for both of the optical axes. To find the focal distance of the two axes it is necessary to measure the distance from the front element of the optical system to the center of the target that is placed in the view of optical system. The working distance of the primary axis should be 4" and that of the secondary axis should be 4.5". Correct focus is determined when the contrast and definition are greatest between the backlight and the target edge. If the focal distance is not correct it is necessary to move the front optic forwards and backwards until correct focus is obtained at the specified focal distance.

After the correct magnification and focal distances are achieved it is necessary to align the optical system and laser backlight source for even illumination of the target. To make sure the alignment is correct it is necessary to remove the quad cell and replace it with a circular, semi-translucent piece of glass with a calibrated center mark on it. The laser alignment is adjusted until the laser beam center coincides with the calibrated center mark.

Finally, it is necessary to determine the rotational alignment of the quad cells themselves. This is achieved by using a
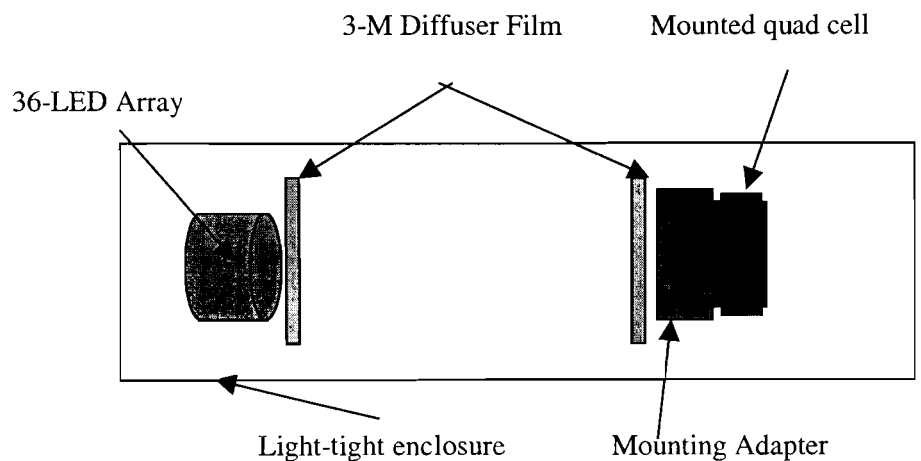

Figure 5. Illumination Source used for calibrating the quad cell

knife-edge fixture (see Figure 7 below).

Calibration of the Electronics:

The electrical signal conditioning circuit consists of four operational amplifiers that amplify the signals from each of the four quadrants of the detector. The optical sensitivity of each quadrant differs slightly, so detectors are uniquely matched to a signal conditioning circuit before any calibration is preformed. Electrical gain is adjusted with identical illumination on all four quadrants. This is

Figure 6. LED illuminator with a diffuser and quad cell attached

achieved using a flat field calibration fixture that consists of a light source, and optical diffuser film[8] between the source and detectors (figure 5) to achieve a diffuse even light source on the detectors. In this case, the illuminator is an array[9] of 36 green LEDs driven with a square wave at approximately 1 kHz (figure 6). A light–tight shroud with a

Figure 7. Knife-Edge Alignment Fixture

black, diffuse scattering interior surface surrounds the source and detector, to ensure that no outside light will interfere with the sensor. A 4-channel oscilloscope is triggered by the pulsed light source, and the square-wave output
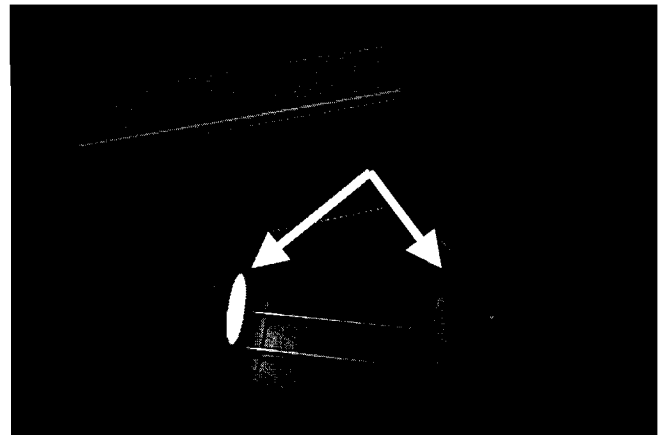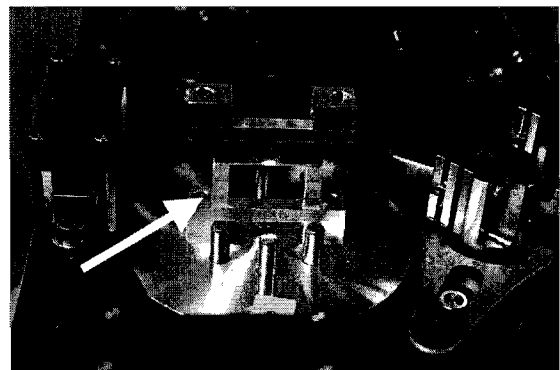
voltages from each quadrant are simultaneously adjusted until the peak-to-peak voltage from each quadrant is equal.

A knife-edge alignment fixture (Figure 7) was designed to serve as an alignment tool and consistent focal reference for each measurement axis. The fixture is used to calibrate one axis of the optical system at a time. When it is installed and the system is fully aligned, the edge of a razor blade is at the center of the optical system, half of the detector is shadowed, and half is illuminated. Calibration marks on the fixture can be viewed on each video display, allowing magnification to be determined.

The fixture is installed so that the knife-edge is vertical, and the quad cell is replaced by a diffuser film that serves as a screen on which the image is projected. This film is mounted on an SM1[10] focus ring that has a centerline reference mark that can be rotated vertically or horizontally. Starting with lenses in the positions determined by the optical model, the knife-edge calibration marks are imaged and displayed on the video monitor. The imaging system is moved longitudinally and the focus ring is adjusted until the desired magnification and focus are achieved. An iris on the input lens is closed down, and the shadow of the knife-edge is aligned with the vertical center of the iris. With the lens-end of the imager bolted in place to avoid changing the longitudinal position of the imager, the detector-end of the imager is rotated until the knife-edge image is aligned with the vertical centerline reference on the diffuser. The process is iteratively repeated until the knife-edge image is centered on both the entrance iris and the diffuser. Once completed, the side cover is removed from the

mounting cube, and the beam splitter cube is rotated until the knife-edge is centered on the video display.

In order to accurately resolve target motion, each detector must be rotated until the horizontal axis of the detector coincides with the horizontal direction of shaker motion. This is done by installing the alignment fixture so that the knife-edge is horizontal (bottom or top quadrants are shadowed). The detector is installed and rotated until the signal voltage from the exposed quadrants is equal, after which the detector is clamped in place. With the fixture in any other orientation, the voltage from a different pair of quadrants will be near zero, and another pair will be maximized. The entire calibration and alignment procedure is performed on both axes.

The final step is to measure the output voltage generated when the target is moved by a known displacement. The alignment fixture is removed, and a stalk-mounted target is installed on the EDS. With the shaker power off, the shaker position is adjusted until the target is centered on both video displays. The target diameter displayed on the video screen is measured. The EDS is set up to generate a low frequency output (e.g. 9-13 Hz), and the drive amplitude is adjusted until the target image is blurred to approximately 120% of its original size. The video image is re-measured, and the "Transverse" signal output voltage is measured (in the time-domain) using either an oscilloscope or the spectrometer. Knowing the static diameter (D_s), the blurred diameter (D_b), and the output voltage (V_o), the sensitivity is calculated as ($V_o / D_b - D_s$). This

calibration constant is entered into the RT-Pro software[11], and is used by the software when plotting measurement data.

Summary:

A new inspection instrument has been described that will be used to fully characterize the mechanical stability of targets used for cryogenic ICF research. The instrument consists of an Electrodynamic Shaker (EDS) and Optical Measurement system (OMS) that are used to stimulate a target and measure its response. The EDS and OMS have been fully integrated, and the system is now being used to characterize production targets. Initial plans are to acquire data on many targets prior to conducting implosion experiments. This data will be correlated with the target's stability during an implosion experiment to establish acceptance and rejection criteria.

[1] http://www.cartage.org.lb/en/themes/Sciences/Chemistry/NuclearChemistry/NuclearReactions/NuclearFusion/NuclearFusion.htm 3/6/05

[2] http://www.lle.rochester.edu/02_visitors/02_aboutlle.html.

[3] Labworks Inc. DuoBase-140 (DB-140). http://labworks-inc.com/products/accessories/db_140.htm. 11/13/2004

[4] Thorlabs Inc. AC254-050-A1, AC080-020-A1 http://www.thorlabs.com/NewGroupPage2.cfm?Guide=45&Category_ID=142&ObjectGroup_ID=120. 11/13/2004

[5] Sinclair Optics. Oslo Optical Design Software. www.sinopt.com. 11/13/2004

[6] UDT Sensors Inc. SPOT-9DMI. http://www.udt.com/Datasheets/Products/SPOTSeries.pdf. 11/13/2004

[7] Dactron Inc. Photon Portable Dynamic Signal Analyzer. www.dactron.com 11/13/2004

[8] 3M diffuser film 3635-70 Light Management film http://multimedia.mmm.com/mws/mediawebserver.dyn?NNNNNNwuFZaNgqON9qONNNOvXyIQQWcI-

[9] Advanced Illumination SL1236 http://www.advancedillumination.com/category/SLimages/pdfs/SL1236.pdf

[10] Thor Labs http://www.thorlabs.com/NewGroupPage4.cfm?Guide=4&Category_ID=25&ObjectGroup_ID=55

[11] RT-Pro software is a product of LDS-Dactron, Inc.

How Good is the Bright Ring Characterization for Uniformity of Deuterium Ice Layers within Cryogenic Nuclear Fusion Targets?

Gregory Balonek

How Good is the Bright Ring Characterization for Uniformity of Deuterium Ice Layers within Cryogenic Nuclear Fusion Targets?

Gregory Balonek

Byron-Bergen High School
Bergen, NY

Advisor: Dr. R.S. Craxton
Senior Scientist

Laboratory for Laser Energetics
University of Rochester
Rochester, NY

Abstract:

Cryogenic targets, thin plastic shells surrounding thick cryogenic deuterium layers, are used to achieve nuclear fusion. These targets are irradiated by lasers causing the targets to implode and create fusion reactions by forcing the deuterium inside to fuse together. The cryogenic targets are pressurized with deuterium gas, and then the targets are chilled to about 20K to freeze an ice layer on the inside of the target. The ice layer needs to be as uniform as possible for the targets to implode correctly and thus create a successful fusion reaction.

Cryogenic targets have suffered from nonuniform deuterium ice coating. This nonuniformity causes irregular implosions and is the source of nuclear fusion reaction failure. The uniformity of the ice layer is measured by using the technique of shadowgraphy. A shadowgraphic target image exhibits a characteristic bright ring when viewed with a CCD camera. This bright ring can be used to estimate the ice thickness in the cryogenic targets. This method is based on the assumption that the bright ring radius uniquely determines the ice layer radius in the target. A computer program has been developed to test the shadowgraphic technique. The result is that the bright ring does not uniquely define the inner ice surface. When the experimental ring radius is compared with the radius predicted by the current model, significant inconsistencies (up to 1 micron) are observed. However, if two opposite views of the bright ring are averaged, then the inner ice layer can be measured to an accuracy of less than 0.2 microns. This is a five-fold increase in the accuracy of measuring the uniformity of the deuterium ice layer within a nuclear fusion target.

Introduction

The goal of the Laboratory for Laser Energetics (LLE) is to create fusion

reactions and to make fusion a safe and viable source of

energy. To achieve fusion the LLE has an array of 60

beams (called the OMEGA Laser System) that focus onto

the target. The cryogenic targets are filled with

pressurized deuterium gas and frozen to about 20K (see

figure 1). The cryogenic targets need to have a consistent

deuterium ice layer to produce high amounts of energy

from fusion reactions. The cryogenic targets that the LLE

uses consist of an outer shell, an inner layer of ice, and a

Cryogenic Target
Cross Section View

Plastic Shell ⌐

Figure 1. Target
Cross-section
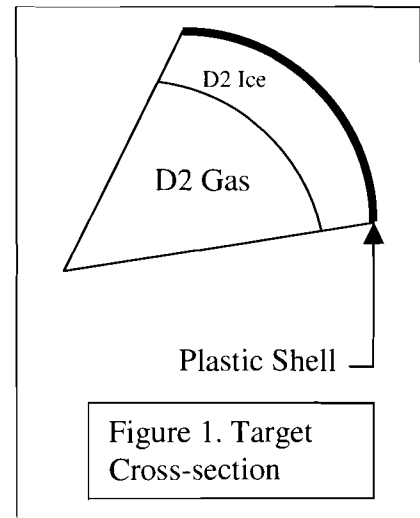
gaseous center. The outer shell of the target is fabricated from hydrocarbon plastic

(CH) that is approximately 3 microns thick. The inner ice layer consists of frozen

deuterium (D2) gas (sometimes deuterium tritium (DT)), that is approximately 100

microns thick, cooled to about 20K. The ice layer must be uniform for a successful

fusion reaction.

The OMEGA laser system focuses all of its 60 beams onto this small target and

creates uniform pressure around the outside of the target. When the target implodes it

generates massive amounts of heat and this heat is necessary to start a fusion reaction.

Thus, you need uniform laser irradiation and a uniform thickness of the target. If part of

the shell or ice is too thin, that part of the target will implode too fast and cause a

nonuniform implosion, which will not create enough heat for a fusion reaction. Also for

3

uniform irradiation, the target must be suspended. Spider silk is used to suspend the

target and can be seen on Figure. 3.

Shadowgraphy is a technique used to look at the inner ice surface of a target.

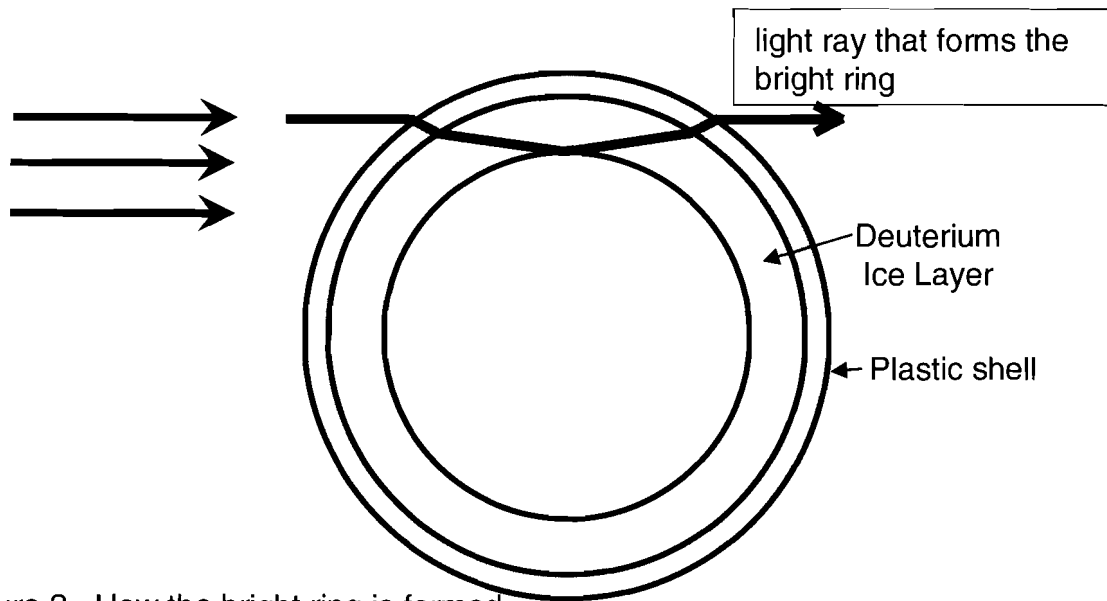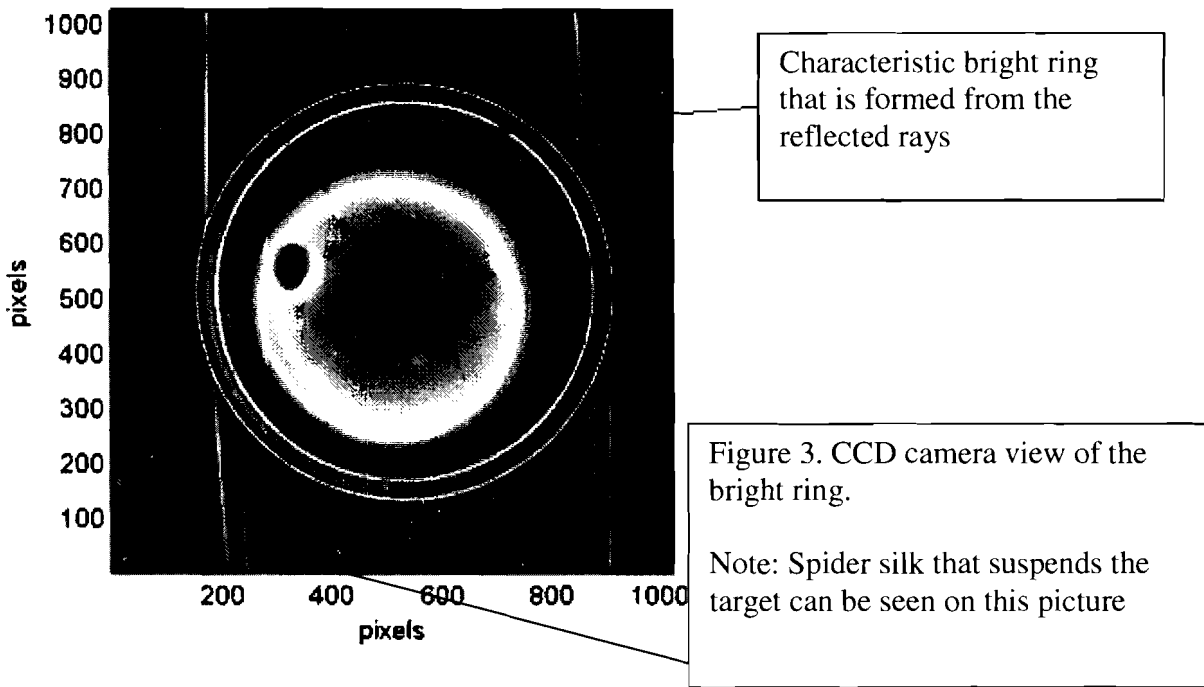This technique requires that you backlight the target with a collimated light source.

light ray that forms the bright ring

Deuterium Ice Layer

← Plastic shell

Figure 2. How the bright ring is formed

Characteristic bright ring that is formed from the reflected rays

Figure 3. CCD camera view of the bright ring.

Note: Spider silk that suspends the target can be seen on this picture

4

Some of the rays of light from the source will reflect off the inner ice surface (figure. 2) and will form a bright ring on an opposing CCD camera (figure 3.). Since these rays reflect off the inner ice surface you can use them to measure the inner ice surface. A simple theory valid for spherical surfaces has been used to calculate the relationship between the inner ice layer radius and the bright ring radius. Thus, by measuring the nonuniformities in the radius of the bright ring it should be possible to measure the nonunformities of the inner ice radius as well. Looking at many different views (two cameras, 25 each) of the target a 3-D model can be created using spherical harmonics. The radius R is given as a function of direction (theta, phi) as

$$R(\Theta,\Phi)= \sum_{L=0}^{Lmax} \sum_{M=0}^{L} [Ac(l,m)Clm(\Theta,\Phi)+As(l,m)Slm(\Theta,\Phi)]$$

Equation. 1

where Clm's and Slm's are standard spherical harmonic functions, Ac's and As's are coefficients predetermined for this particular model [1], and Lmax is typically 11.

A computer program has been developed to trace rays though a target with such a reconstructed ice layer that can calculate the actual bright ring radius that the target will produce. The recreated bright ring can be compared with the experimental ring radius and the radius predicted by the simple model. While all three radii generally agree quite closely, significant inconsistencies (up to 1 micron) are observed. This indicates that there are limitations to the accuracy with which the 3-D ice thickness can be reconstructed and that the bright ring radius does not uniquely define the inner ice

radius. This problem has been solved by tracing rays from a directly opposite view creating another bright ring. By averaging these two views together the inner ice radius can be determined to an accuracy of less than 0.2 microns.

Ray Tracing Program

The research project involved creating a computer code to calculate the bright ring radius as a function of angle based upon the spherical harmonic representation (Equation 1) of the thickness of the plastic shell and the inner ice layer of the target. This representation was obtained on the basis of many different views of the target [1]. The program started by using some existing programs that traced rays through a target. Pieces of the code *Pegasus* written by Sharon Jin [2] were used. *Pegasus* traces light rays through an ideal target and provides information on the position and intensity of the expected bright ring. Other subroutines were also used that had been written by Dr. Craxton. These included a routine to find the exact intersection of a ray with the interface between two layers (such as the plastic and the ice).

First the computer program starts out by setting up a cube in three-dimensional space with grids on each side so that, if given a line passing through the origin with a given direction (in the form phi and theta), you can find the intersection point of that line with one of the six grids. Given any formula such as Equation 1 that expresses the radius of a surface in terms of phi and theta it is possible to set the radius at each point on each grid. This also allows for this program to be used to trace rays through any other type of perturbed surface as long as the radius can be expressed in terms of phi and theta.

6

Once the grids are set up, the program uses the spherical harmonic formula for each point on the six grids and stores three quantities: R1 for the plastic radius, R2 for the plastic-ice interface, and R3 for the ice-gas interface. Once these quantities are stored they can be recalled at any time when the program needs it. This is done to avoid computing Equation 1 many times and thus saving time.

A small iterative procedure was written to find the side on which the ray hit and exactly where it hit on the grids. This is done by taking the unit vector of the ray and breaking it up into x, y, and z components. Once this is done the sign and value of the largest component will determine what side the ray intersects. For example, if the vector is proportional to (1,y, z) where y and z are smaller in magnitude than 1, it is on the first side of the cube, if it's proportional to (-1,y, z) it is on the second side, if it's proportional to (x, 1,z) where x and z are smaller in magnitude than 1, it is on the third face, and so on. When the side the ray intersects is found, simple two-dimensional interpolation can be used to find the radius where it hit.

Tracing Rays

A program was put together to find the true paths of the rays. Many factors had to be taken into account since the tilts of the surfaces caused the rays to be deflected out of the plane in which they would otherwise have propagated. The simple ray tracing methods used in Reference 2 could not be used, so a ray tracing step program was created.

The program starts by launching rays from the plane on the left of figure 4 towards the reconstructed target. The first ray is launched from a predetermined radius

7

that is below the starting radius of the bright ring rays and emerges with a positive angle to the vertical (the dashed ray). Successive rays are launched higher with the goal of finding the "bright ring ray" (see figure 2) that emerges parallel to the incoming ray (i.e. horizontal). Once a ray is launched, the program makes the ray travel a certain distance, usually less than the distance to the next interface. As the program continues to "step" the ray this distance is allowed to increase until the new point is the other side of the next interface determined by interpolation from the grids. Once this occurs, the program uses an iterative algorithm, reducing the space step size by a carefully chosen factor to find the exact point where the ray crosses the new interface. The point at which the ray intersects the new interface is calculated to an accuracy of 1×10^{-5} micron (smaller than an atom).

The program also deciphers which rays will actually make up the bright ring. These rays must follow the path through five interfaces: air-plastic, plastic-ice, reflect off inner ice surface, ice-plastic, and plastic-air. The modified program *Pegasus,* is used to sift through the rays to find only those that met the determined path.

Once a good ray is found it is tagged and stored. The first such ray has a positive angle to the vertical when leaving the target. As the new rays are launched successively higher, their angle leaving the target becomes smaller and then becomes negative (see the solid black ray in figure 4).
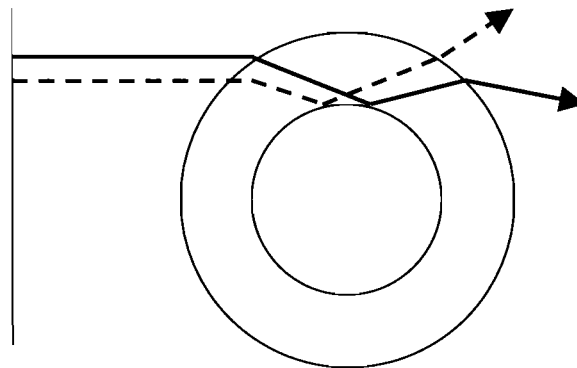
Figure 4. First rays launched (Dashed) have positive angle and further rays have negative angles (solid black).

8

Once a ray is found to have a negative angle the program stops tracing rays. It

interpolates to find the parallel ray exiting the target based upon the final ray and the ray

before it. This parallel ray gives the radius of the bright ring at that point. This is done

360 times, as the rays are moved 360 degrees around the target, one degree at a time.

This is all repeated 50 times for the 50 different views. A typical graph giving the bright

ring radius as a function of angle for one of the views is shown in figure 5 as the Dashed

Curve #3 ("Actual Bright Ring").

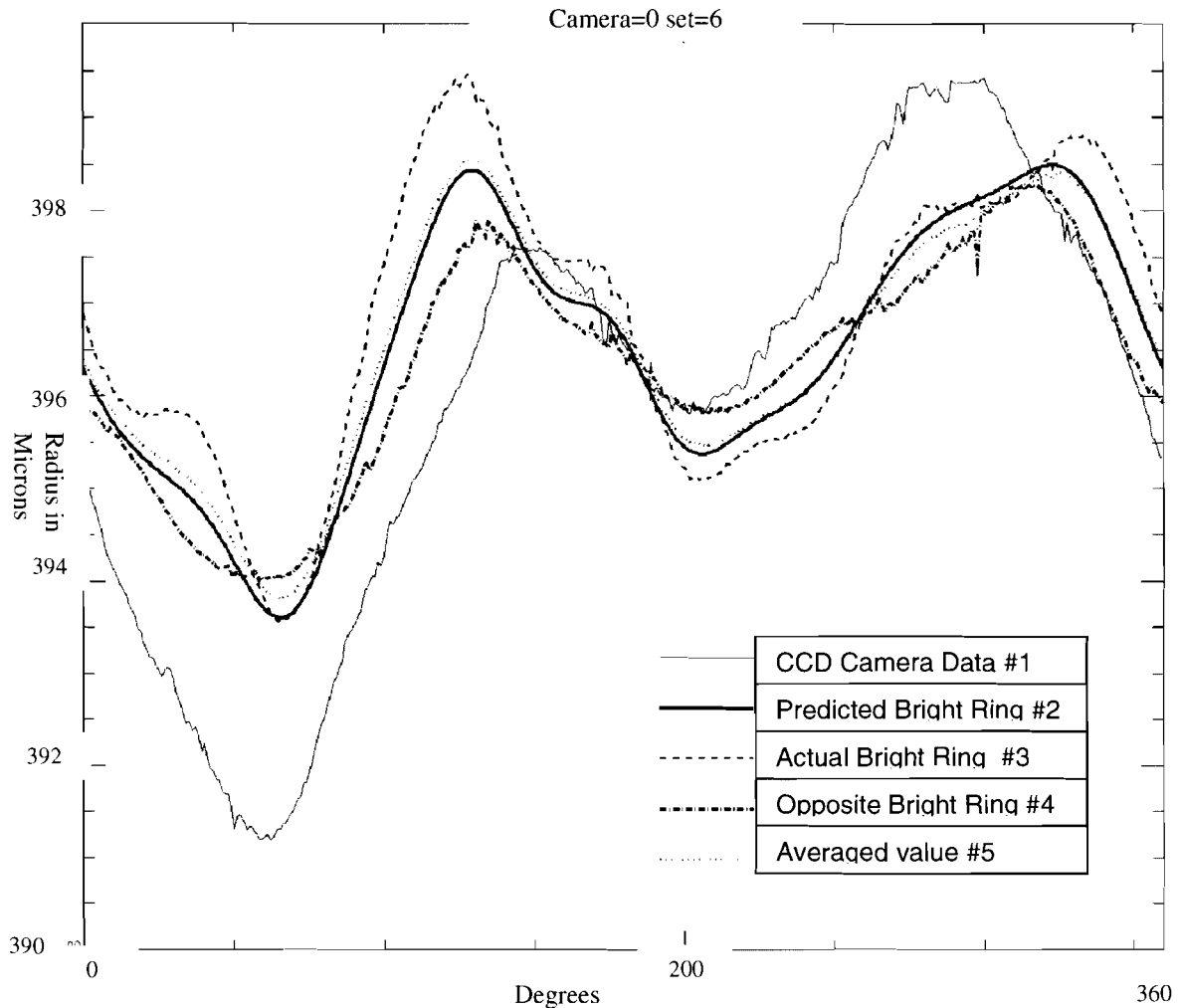|	
———	CCD Camera Data #1
———	Predicted Bright Ring #2
- - - - - -	Actual Bright Ring #3
▪—▪—▪—▪	Opposite Bright Ring #4
· · · · · · ·	Averaged value #5
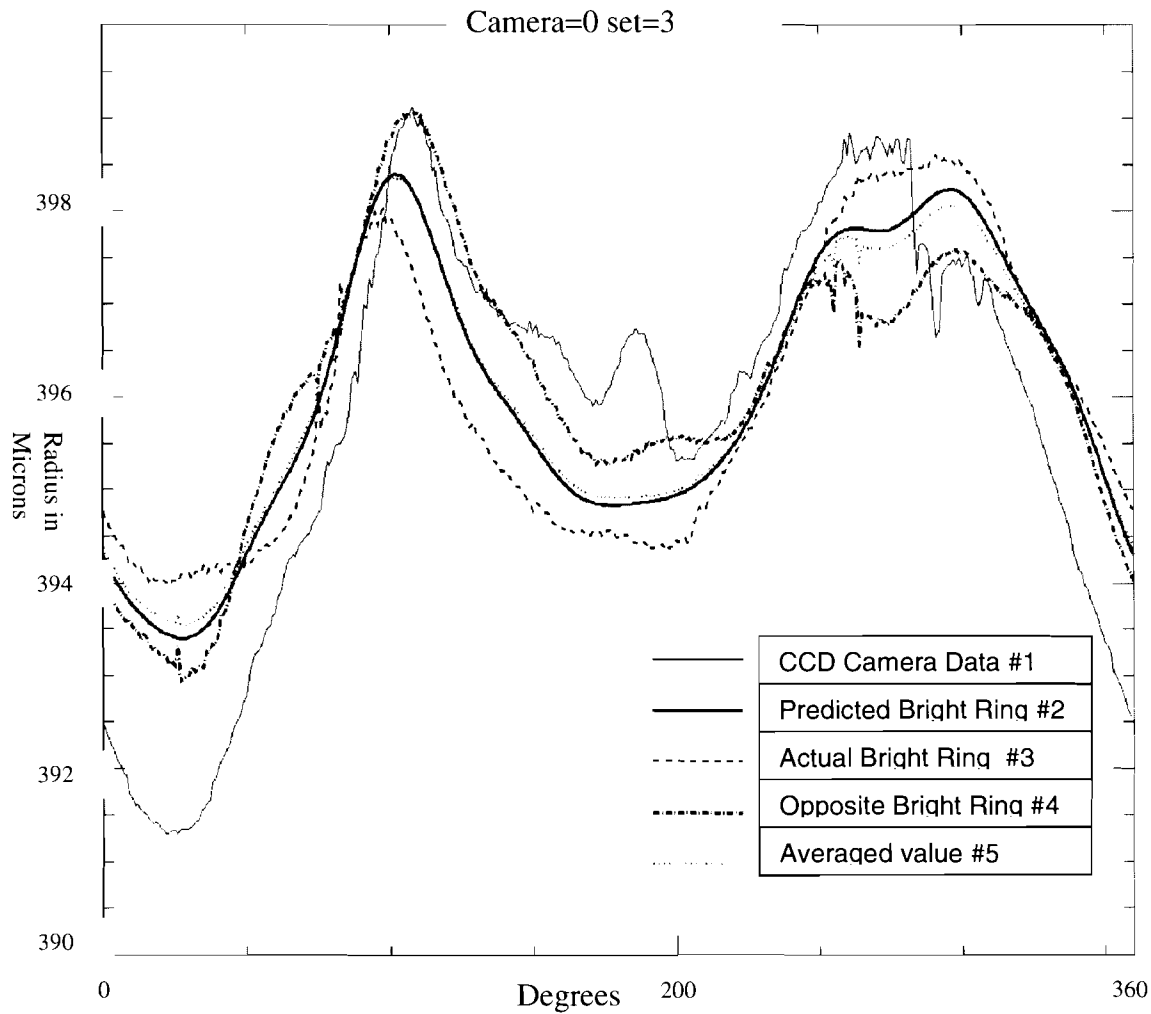
Figure 5: Radius vs. Degrees

Figure 6: Radius vs. Degrees for a different view

Results

Figure 5 also shows several other curves. Curve #1 gives the original

experimental data for this target (obtained from the CCD camera). Curve #2 ("Predicted

Bright Ring") is derived from the spherical harmonic model (based on the CCD data

from all 50 different views) under the simple assumption that the ice thickness and

bright ring radius are under a direct relationship. The first two curves do not match

10

exactly because the model was made from a best-fit interpolation from the 50 images.

The third curve, the bright ring produced by the exact ray-tracing calculation based on

the spherical harmonic model, doesn't correlate very well with the second curve. It

typically has an error of plus or minus 0.75 microns. A possible explanation for this

error lies in the ice layer itself. The ice layer is assumed to be spherical in nature in the

simple interpretation that the bright ring radius uniquely gives the ice thickness.

However, if the ice layer is tipped in a certain direction it can affect the position of the

bright ring even though the ice thickness is unchanged (Figure 7). This tipped ice layer

can explain the difference between curves two and three.

To correct this problem of the ice layer being tipped, it is proposed that two opposite views should be used. This was tested by tracing rays in both directions. The opposite view is graphed as curve four.
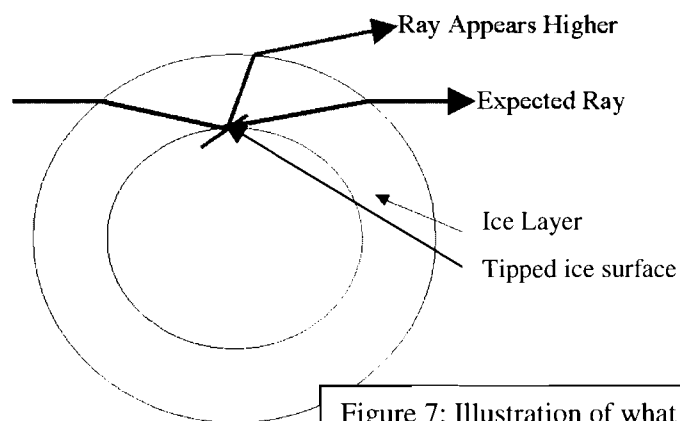

Figure 7: Illustration of what a tipped surface will do to the expected bright ring ray.

This curve is also different from curve three. Thus, if the simple relationship between the

bright ring and ice thickness were true, the thickness would depend on which way the

target is viewed. However, when the actual bright ring curve (number three) is averaged

together with the opposite-traced bright ring curve (number four), the resulting curve

(number five) matches quite closely with the predicted bright ring (number two) with

11

deviations from that curve less than 0.2 microns. This holds up for all of the views of the target (see figure 6 for another example). The main result is that if the average of two opposite views is taken, an accurate reproduction of the ice layer is possible.

Conclusion

A ray-tracing program has been developed to calculate the bright ring for a cryogenic target with non-spherical surfaces. This program allows for exact ray tracing through the target and can trace rays through a variety of perturbed surfaces as long as their radii are expressed as functions of phi and theta. It has been found that, from a single view of the target, the shadowgraphic technique is limited because the expected ring position and the actual ring position do not correlate exactly; i.e., the bright ring does not uniquely define the ice thickness. This is believed to be due to ice surface tipping. However, by finding the averaged value of two opposite views, it can be seen that the predicted bright ring and the averaged value only differ by about 0.2 microns. Using this method it is possible to accurately measure the ice thickness.

Acknowledgements

I would like to especially thank Dr. Craxton for allowing me to work at such a wonderful place and giving me the opportunity to participate in the High School Summer Research program. I would also like to thank him for spending countless hours helping me understand the difficult concepts involved for this project. I would also like to recognize everyone in the lab for being so helpful when I needed it.

<u>References</u>

[1] Edgell, Dana, private communication (2004).

[2] Jin, Sharon. "A Ray-Tracing Model for Cryogenic Target Uniformity Characterization," 2002 Summer High School Research Program at the University of Rochester's Laboratory for Laser Energetics.

Design and Fabrication of a Handheld Optically Coupled Water Flow Calibrator

Robert Balonek

Design and Fabrication of a Handheld Optically Coupled Water Flow Calibrator

Robert M. Balonek

Byron-Bergen High School
Bergen NY

Advisor: David Lonobile
Mgr., Controls Eng.

Laboratory for Laser Energetics
University of Rochester
250 East River Road
Rochester, NY 14625-1299

Abstract:

Hundreds of fiber optic coupled flow detectors are planned for use on the OMEGA EP laser system [1] to measure the flow of coolant water through the laser amplifier flashlamps. A handheld device capable of sending precise optical frequencies was created, which will allow the flow detectors to be tested and calibrated to within +/- 1 gallon per hour. The handheld device, known as the Flow Detector Calibrator (FDC), can measure the voltage output of the flow detector to an accuracy of +/-1%, and can determine if a flow detector is transmitting its optical 10 kHz stimulus frequency. The FDC will be utilized as a test fixture initially for incoming inspection of production quantities of Omega EP flow detectors and subsequently will support in debugging and maintenance operations within the laser bay.

Introduction

The Laboratory for Laser Energetics in Rochester, NY is home to the Omega laser, the world's largest laser (Fig 1, Ref. 2). Omega has sixty individual 12-inch diameter beams that each deliver 500 joules of 351 nanometer ultraviolet laser energy. The combined

Omega Laser
Figure 1.

30 kilojoules of laser energy is focused onto a single fuel target. The resulting extreme pressure and temperature creates a momentary fusion reaction. The
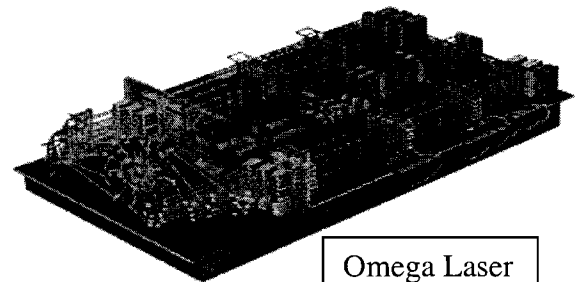
Omega laser system enables scientists to study fusion as a potentially clean

renewable source of future energy. Construction of a new laser system Omega

EP (Extended Performance) is currently underway that will complement the

research capabilities of the laboratory.

Figure 2. OMEGA disk amplifier with flash lamps at the bottom

Background:

In order to get the maximum

possible energy on target it is necessary to

amplify the laser beam. Each of the 60

beams is comprised of a sequence of laser

amplification stages with increasing beam

diameter. Each amplifier stage contains a

neodymium center that is the active laser element that the beam propagates

through (see Fig. 2). The neodymium core is stimulated by xenon flashlamps that

convert stored electrical energy into photons. These are similar in function to a

Amplifier's Flash Lamps

camera flash but thousands of times more powerful. Prior to the laser event the

flashlamps discharge 14,000 volt capacitor banks. The resulting 10,000 ampere

current pulse "pumps" the neodymium core with intense white light. Subsequently

the laser propagates through the neodymium core and is amplified by the energy

it extracts. The process of electron energy conversion to photon energy creates

intense thermal heat inside the flashlamp due to the large amounts of infrared

light that is emitted. The excess thermal energy has to be removed so that the

flash lamps do not overheat, fatigue, and crack. If the flash lamps crack during
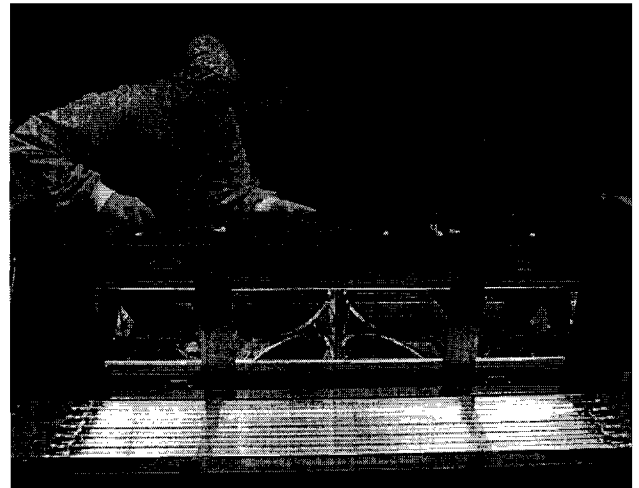
discharge of the 10000 ampere current pulse, they will explode and damage the delicate interior of the amplifier.
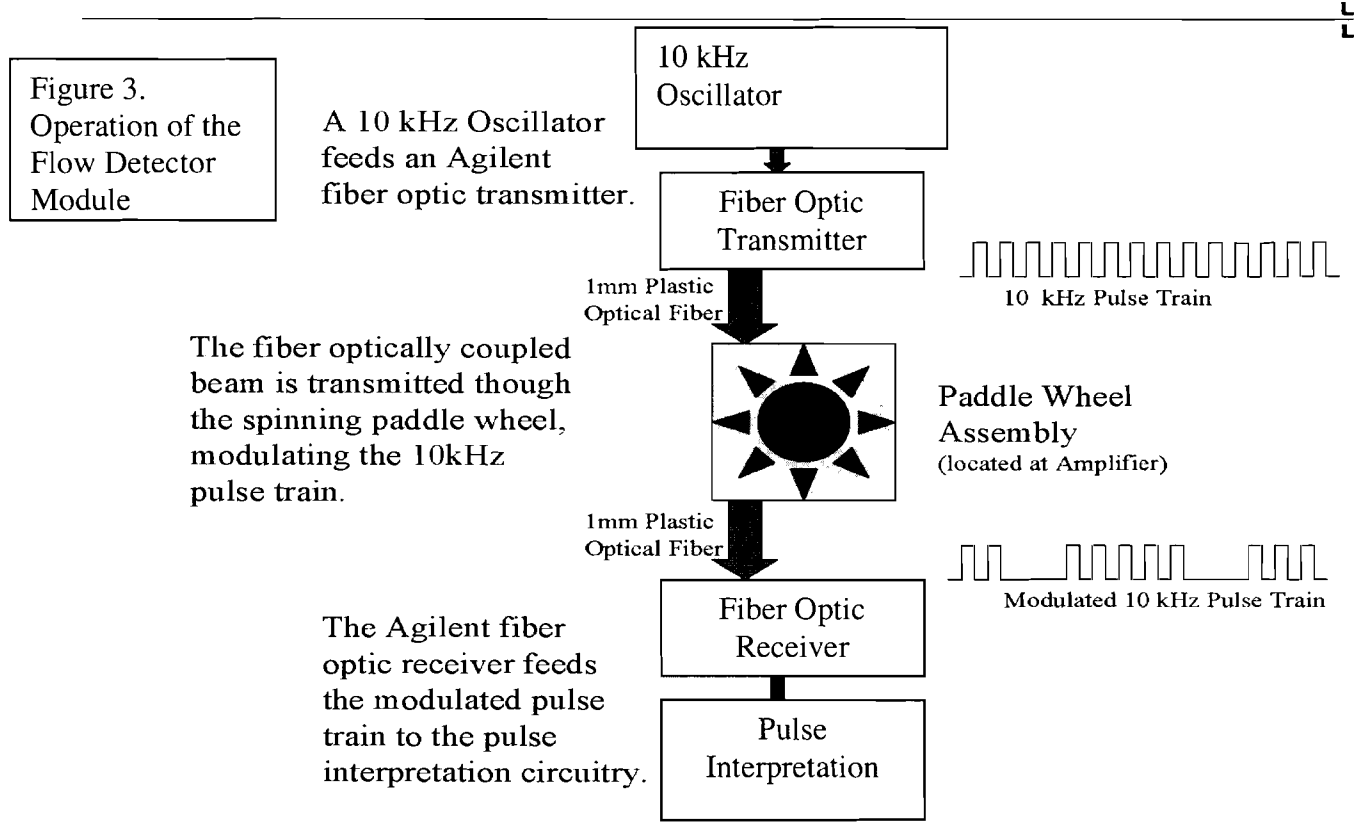
To cool the flashlamps each tube is encased in a fused silica sheath. Through the sheath de-ionized water is pumped at a constant flow rate. Pumping water over the flash lamps allows the heat to be transported away from the tubes. Cooler flash lamps last longer, and will have less of a chance for catastrophic failure. Regulating the water flow results in maintaining the flashlamps at a preferred operating temperature regime.

Flow detector theory of operation

De-ionized water is set to flow through the flashlamps at a rate between 4-60 gallons per hour (GPH). The flow rate is monitored by the Flow Detector Module (FDM) that then sends a signal to the Amplifier Facilities Controller (AFC) [3]. The AFC will then alert the control room if too much flow is detected or too little flow is detected. The FDM is constantly monitoring flow in the amplifiers through optical fibers. Optical fibers are required to isolate the flow monitoring instrumentation from proximity to the potentially hazardous high voltage present in the flashlamps. The optical fibers enable the flow detection system to be completely isolated electrically from the flash lamps.

In operation the FDM sends a 10kHz optical pulse train through a source fiber to a remote paddle wheel. Water flowing through the paddle wheel causes it to spin at a rate proportional to the flow. As the paddle wheel spins it physically

4

"chops" or cuts the 10kHz frequency source (refer to Fig 3). The chopped frequency is then sent back to the FDM over a signal fiber where it is analyzed by a frequency to voltage converter circuit and transmitted to the AFC as gallons per hour information.

Figure 3.
Operation of the
Flow Detector
Module

A 10 kHz Oscillator
feeds an Agilent
fiber optic transmitter.

10 kHz Oscillator

Fiber Optic Transmitter

1mm Plastic
Optical Fiber

10 kHz Pulse Train

The fiber optically coupled
beam is transmitted though
the spinning paddle wheel,
modulating the 10kHz
pulse train.

Paddle Wheel Assembly
(located at Amplifier)

1mm Plastic
Optical Fiber

Modulated 10 kHz Pulse Train

The Agilent fiber
optic receiver feeds
the modulated pulse
train to the pulse
interpretation circuitry.

Fiber Optic Receiver

Pulse Interpretation

Flow Detector Calibrator

In operation each FDM employs circuits that must be setup properly to
achieve accurate measurements. Prior to installation, circuitry must be adjusted
to correct for unit-to-unit component tolerance differences. In this manner FDM's
are matched to a calibration standard that insures interchangeability of modules
and consistent characterization of water flow conditions in the laser amplifiers.

Figure 4.
Hand-Held
portable
FDC

A unit has been built that can
accurately calibrate EP's Flow Detector
Modules. This unit is a hand-held portable
calibrator (Fig. 4). It can optically calibrate
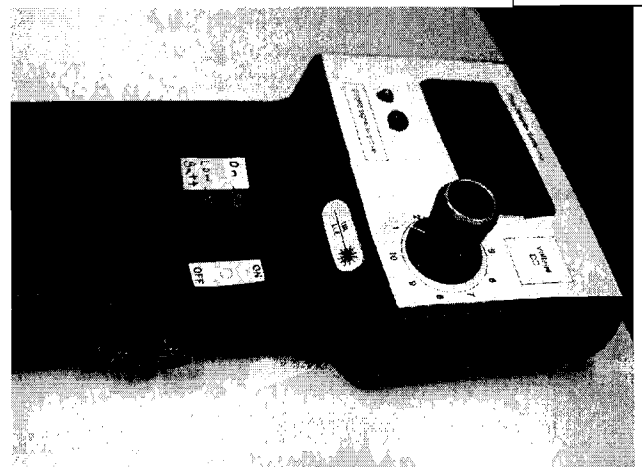
the Flow Detector Modules by sending precise optical signals. It can send ten different signals to the FDM, each signal representing a different gallon per hour reading. The FDC can represent flow from 4-60 GPH. This unit incorporates an on-board voltmeter that can measure the voltage that comes from the FDM so that calibration can take place in both the lab environment and bench top inspection. The voltage is displayed using a LCD monitor to +/- 1% accuracy. The unit incorporates a low battery indicator, using a single comparator circuit, which will alert the user to a low battery situation so that calibration accuracy will not be lost. The FDC also incorporates a feature to insure the FDM is operating properly. The FDC has two LED's that will light up indicating that the FDM is sending a 10kHz isolating signal. This will help diagnose if the systems problem resides in the optical fibers or paddle wheel assembly.

Break Down of the FDC

The FDC will become a valuable asset in the Omega Laser system in many ways. The main goal of this unit is to qualify incoming units. When Flow Detector Modules are built they need to be calibrated. The FDC will allow all new incoming units to be calibrated to a standardized set point. With all new units calibrated to the same standard, the Laboratory can be assured that all units are operating properly. The portability of this unit allows easy real-time inspections of the laser system without large complicated equipment. Its portability will allow technicians to quickly find and localize any problems that could be coming from the FDM's.

Troubleshooting Capabilities

The FDC has a simulation feature to allow the diagnosis of troublesome FDM's. The FDC has the ability to send out ten different frequencies. Each frequency has a correlating GPH reading (Table 1).

Position	GPH	Frequency Hz
1	< 8	4
2	8	30
3	16	50
4	19	60
5	26	80
6	29	90
7	47	150
8	56	180
9	60	195
10	> 60	202

Table 1. Flow rates and corresponding frequencies used by the flow detector calibrator.

The frequency output on the FDC is selected using a ten-position rotary switch. When coupled with the paddle wheel input and output optical fibers the FDC simulates water flow to the FDM. With the capability to simulate water flow, the FDM's can be calibrated before and after installation without having to have water flowing in the system. A graph of water flow vs. frequency was plotted. The frequency and GPH readings were found to have almost a linear relationship. The FDC samples ten points on this line. With ten spaced out samples on this

line an accurate calibration of the FDM is ensured. To further the calibration accuracy, the frequency output from the FDC is stable to +/- 2 Hz. The addition of an on-board voltmeter accurate to +/- 1% allows the operator to sample the voltage output pins on the FDM. This further increased the useful range of the FDC since not only can it simulate water flow but it can also accurately measure voltage readings from the FDM's without the further complications of additional equipment.

Internal Operation of the FDC

Many possibilities for different components and configurations were investigated for optimal performance of the FDC. Many options were considered for the oscillating circuit. One option was a quartz crystal that would oscillate and be controlled using voltage. The instability of voltage control led to the next choice. The inverter IC chip 74hc14 is the best choice for this circuit. It has a stability rating based on external components. The ability to control oscillations externally is why the 74HC14 inverter IC was chosen for the FDC.

An internal rechargeable battery was considered during development. Based on tests and experiments a separate charging station was ruled out due to cumbersomeness and lack of rack space in operating environments. With an external charging station ruled out internal charging was then investigated. Two options exist for an internal charging station: a charging process controlled by a IC or constant charge via a walwart transformer. The IC controlled charging would provide stability and safety to charging of the internal battery. It is a good

choice for a unit that is going to be constantly used. Due to the nature of the FDC as a calibrator and troubleshooter, the FDC may only be used on a month to month basis. Without constant use the IC would terminate charging on a full battery and not start charging until either being disconnected from the battery or a flip of a reset switch. Without the ability to charge constantly the IC was discarded for it could not keep the FDC ready for use at a moment's notice. The walwart transformer provides a constant current to the battery keeping it at a top charge indefinitely. The trade off in this situation is the long recharge time of at least 8 hours. This was considered acceptable for the ability to keep the FDC on the ready at a moment's notice for long periods of time. A Nickel Metal Hydride battery was chosen as the best choice, with its ability to take a top charge indefinitely and up to 1,000 total charges.

With a rechargeable system in place, a choice had to be made between 1.5, 3 and 5 volt logic. Initial tests proved that 1.5 volt logic was too low to provide sufficient power to the screen. Three volt logic was a optimal choice due to low current draw but made oscillations vary as much as 5%. Five volt logic was chosen because it was able to keep oscillations within a 2% variation. To keep the oscillations stable a higher current draw was considered acceptable.

With a voltage chosen for operation of the circuit, a way of qualifying that voltage was necessary. An internal low battery indicator was devised. This comparator circuit continually verifies the voltage of the circuit. When the voltage falls below a certain threshold (where oscillations fall out of the accepted +/- 2 Hz range) an orange indicator light alerts the operator to this problem. The low

battery indicator insures that the FDC is working within an acceptable voltage range.

Each component in the FDC has been carefully chosen for current draw, stability and performance characteristics. With each part chosen for a specific task, the FDC is optimized internally for peak performance.

Calibrating the Calibrator

Since the FDC plays a fundamental role in calibrating instruments at the Laboratory for Laser Energetics, each FDC must be hand tested before leaving assembly. I found that a burn-in of three days allows the assembler to accurately determine if the oscillations are stable. Each resistor and capacitor must also be hand chosen due to tolerances on each. Due to lack of time I was not able to test the long-term stability of the FDC. I recommend checking the FDC every six months to ensure optimal performance of the internal circuitry.

Conclusion:

A calibration unit has been built that will accurately calibrate Flow Detector modules. With a calibration standard that can be put into practice, accurate water flow can be determined. A constant volumetric water flow through the system that can now be accurately measured will increase the life of the flash lamps. Increasing the life of the flash lamps will save the amplifiers from undue stress caused by opening and closing the doors. This will decrease downtime, and increase the number of productive shots on the new Extended Performance laser.

References:

1. http://omegaep.lle.rochester.edu/110_overview/

2. http://www.lle.rochester.edu/05_omega/05_omega.html

3. David Lonobile; *Amplifier Facilities Controller Requirements Definition*

   A-AK-R-001 Revision B, 2004

3-D Characterization of Deuterium Ice-Layer Imperfections in Cryogenic Inertial Confinement Fusion Targets

Bruce Brewington

3-D Characterization of Deuterium Ice-Layer Imperfections in

Cryogenic Inertial Confinement Fusion Targets

Bruce Brewington

Fairport High School
Fairport, NY

Advisor: Dr. R. S. Craxton
Senior Scientist

Laboratory for Laser Energetics
University of Rochester
Rochester, NY

Bruce Brewington

3-D Characterization of Deuterium Ice-Layer Imperfections in Cryogenic Inertial Confinement Fusion Targets

Abstract

Inertial confinement fusion (ICF) is a technique that is being pursued as an option for generating power in the future. Cryogenic targets are important to ICF because they hold the fuel that undergoes fusion reactions. In order for a cryogenic target to undergo ICF, it is important for the target to compress uniformly in all directions. A computer program has been written to characterize defects in these targets. Various imperfections can show up in the ice layer, such as cracks and bubbles, which prevent the target from compressing uniformly. Characterizing imperfections leads to improvements in techniques for producing the targets. The program analyzes a large number of shadowgraphic images, typically 50, viewed from different directions. To locate the imperfections, the program traces light rays from their position in the image back through the target. By combining this information from each of the 50 images, the program creates a 3-D model that shows the locations, sizes and shapes of the imperfections. Conventional tomographic techniques can not be used in this case because the light rays do not travel straight through the target due to refraction.

1. Introduction

Plastic Shell (3 μm)

D_2 ice (80 μm)

D_2 gas

~900 μm

Fig. 1: Slice through a cryogenic target showing its contents.

One of the most promising techniques for achieving fusion for generating power is Inertial Confinement Fusion (ICF). Using this technique, a powerful laser system irradiates a small target.[1-3] A target is a pellet that contains the deuterium fuel for the fusion reaction. A typical cryogenic target is a sphere with a thin plastic outer layer (3 μm), a thick deuterium ice layer (80 μm) and a deuterium gas center (see Fig. 1).[3] These measurements can vary since different sized targets are produced.

To form the ice layer, the target is first cooled to approximately 18° K, which is just below the triple point of D_2.[3] This does not create a uniform ice layer because gravity pulls the deuterium to the bottom when it is in a liquid state. Bubbles may also form while the deuterium is in a liquid state. When the liquid deuterium freezes, cracks may form in the ice. The target undergoes this process inside a layering sphere.[4] This is a sphere with a hole to insert the target and viewing windows. A low-power IR laser beam is injected into the layering sphere through a small optical fiber and bounces off the walls of the layering sphere. The target is uniformly irradiated from these diffuse reflections, and is constantly losing heat to the cold, surrounding gas. The heating from the IR laser beams causes vaporization to occur on the inner-ice layer. The thicker portions of the ice layer experience more vaporization because they absorb more heat. The deuterium is

3

constantly vaporizing and condensing back on the inner-ice layer. This process continues for about 24 hours and approaches an equilibrium state where the ice layer is uniform.

The high-power laser system delivers energy to the target through many laser beams positioned evenly around the target. The massive amount of energy these lasers deliver causes the outer plastic layer of the target to enter a plasma state and expand outward rapidly. In accordance with Newton's Third Law, an equal but opposite force compresses the deuterium fuel in the target to about 2-3% of its original radius. This creates the high temperature and pressure necessary to make the fusion reactions start. The deuterium ions fuse with each other to form a mixture of helium-3 and tritium ions. These fusion reactions produce energy in the form of high velocity neutrons and protons. Current experiments use just deuterium, but in the future researchers plan to use a mixture of deuterium and tritium because their reaction produces more energy. Deuterium and tritium ions combine to form a helium nucleus (alpha particle) with 3.6 MeV of energy and a neutron with 14 MeV of energy.[2] Pure deuterium targets are currently used in ICF labs because they are easier to work with than tritium due to tritium's radioactivity.

It is important for the target to undergo a uniform spherical compression to maximize its compression. An imperfection in the target could prevent it from compressing uniformly, ending the fusion reactions prematurely.[3] This project involved locating and characterizing major defects such as cracks and bubbles in the ice layer of the target to improve manufacturing techniques.

2. Shadowgraphy
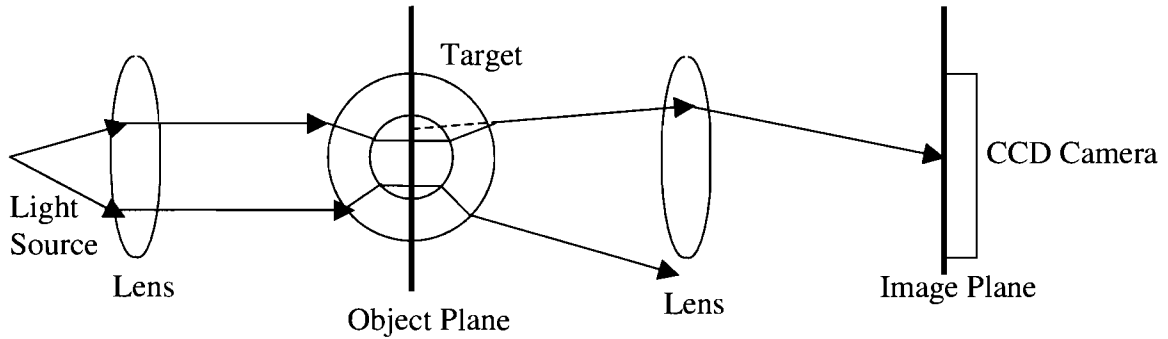
Fig. 2: Schematic of the experimental shadowgraphic imaging system. The dotted line shows where the light ray appears to be coming from. Rays incident too far from the center refract too much to be collected by the lens.

Shadowgraphy is the characterization technique currently used in most ICF labs.[3,5-9] First, a single collimated light source illuminates a target (see Fig. 2). The light travels through the target and is focused by a lens onto a CCD camera. The lens does not
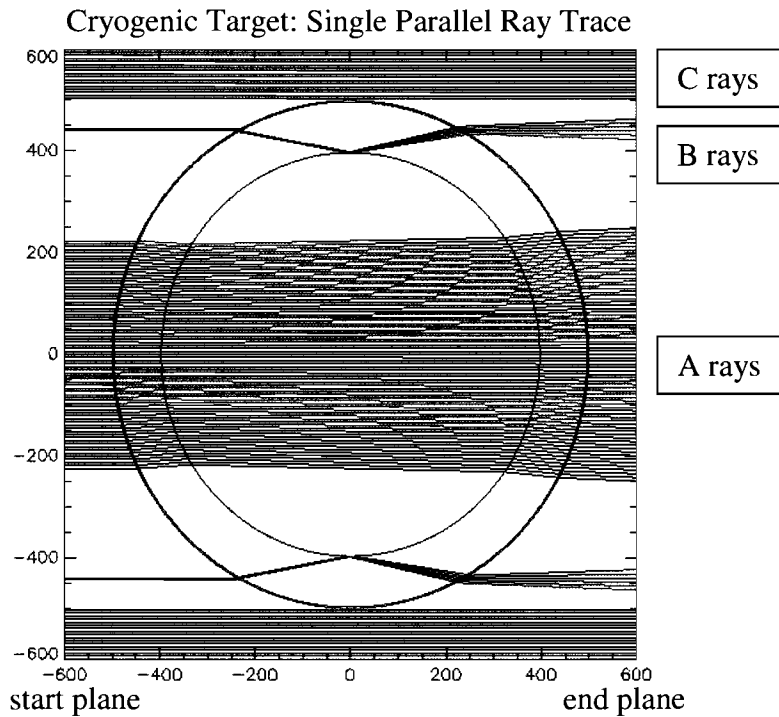

Fig 3: A ray trace demonstrating how shadowgraphy works. Light rays travel from left to right. Only rays collected by the lens are shown. All distances are in microns.

collect all of the light because some rays diverge too far for the lens to be collected.

Rays are labeled based on their path through the target (see Figure 3). The rays

Object Plane   Lens   CCD

Shell   Ice   Gas
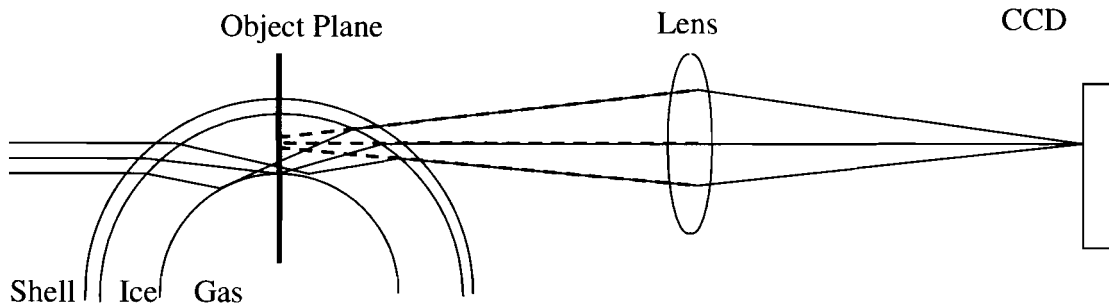
Fig. 4: Diagram showing how the B rays undergo total internal reflection at the ice-gas interface and create the bright ring. From the image on the CCD the B rays appear to come from a tiny spot in the object plane.

that refract through the plastic, ice and gas and are collected by the lens are called A rays.[8] Some rays refract when they reach the plastic shell and when they reach the ice layer but reflect when they reach the ice-gas interface, and are called B rays (see Figure 4). [8] When these rays are projected back to the object plane, they appear to come from a very thin ring called the bright ring (see Figure 4). A typical experimental shadowgraphic image containing a bright ring is shown in Figure 5. Computer programs have been written to determine the ice thickness from the bright ring position.[4] Other programs have been written that trace rays through a target with a non-uniform ice layer and predict what the position of the bright ring should be.[5,7,9] However, no programs have been reported that analyze defects.

The sample shadowgraphic image in Figure 5 provides a significant amount of information about the target. The colors indicate the intensity of light on the CCD camera with red being bright and blue being dark. The red background is made up of the light rays that did not hit the target. The vertical yellow lines are the spider-silk used to hold
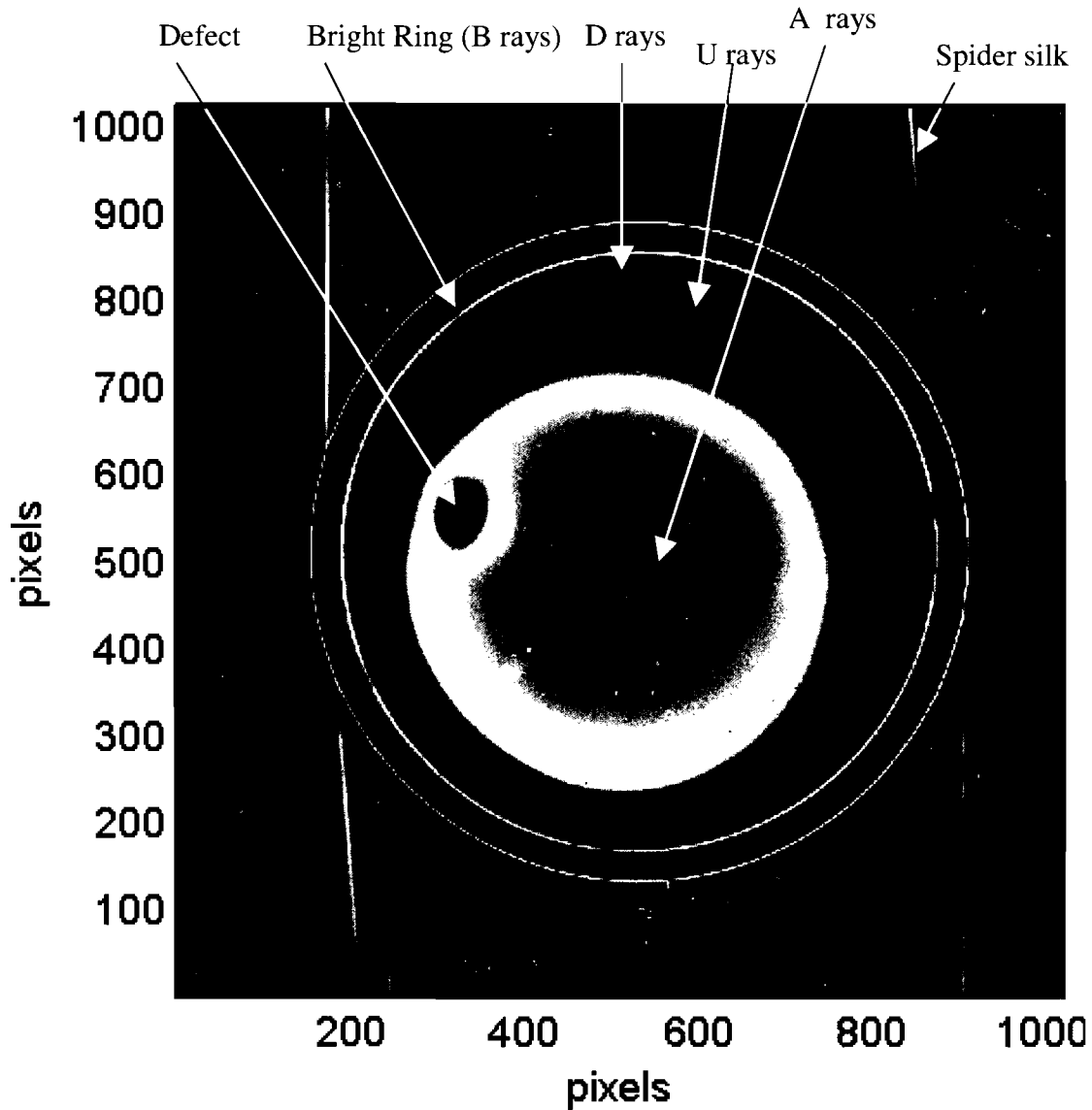
Fig. 5: A sample shadowgraphic image. The colors represent the intensity of the light with red being the most intense and blue being the least.

the target. The large yellow circle and the red area inside it consist of all the A rays. Its size is limited by the size of the lens that collects the light that went through the target. It is off center due to imperfections in the optics that take these pictures, not due to imperfections in the target. The main defect in the image is the large red oval. The brightest of the three rings is the bright ring created by the B rays.

Defects can be seen on shadowgraphic images because the light refracts through

them differently than through the area around them. Sets of 25 shadowgraphic images are taken from each of two cameras located at 12° and 27° above the equator. Each camera takes 25 pictures as the target completes a full rotation about its vertical axis. In each shadowgraphic image the defect is located to the left or to the right of its position in the previous image because the target rotated. When the defect is located near the edge on either the left or the right, the bright ring and the two fainter rings can become broken.

Reconstruction of a 3-D model capable of locating defects from these 2-D images has never been done before. Tomographic techniques can not be used to solve this problem because refraction prevents light from traveling straight through the target. The new program presented here allows the size, shape and location of defects to be estimated accurately.

2. The Program

This project involved developing a program that produces a 3-D model of the target showing the location and approximate size of the imperfections. The 3-D model is based on information from 50 shadowgraphic images taken from different angles. Each shadowgraphic image is displayed on the screen, one at a time. The user flags the areas that have defects on each picture. Based on what the user flags, the program uses an algorithm to find a large number of points that are not part of the defect. The paths of these points are traced back through the target and recorded in a 3-D array representing the target. Combining this information from each of the fifty views creates a 3-D model. This model is viewed in horizontal slices, which can be used to measure the size, shape and location of the defect.
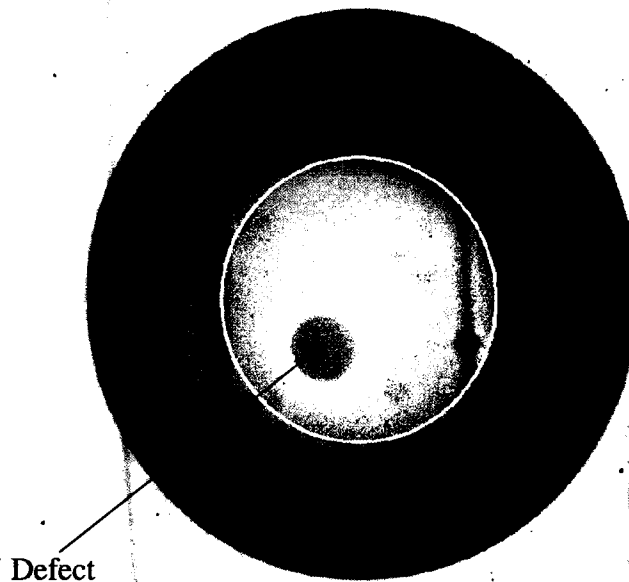
2.1 Input

Defect

Fig. 6: Screen shot showing how a polygon is drawn around the defect.

The program utilizes data from 50 shadowgraphic images taken from different angles to form the model. Image information including the camera angle, the center of the target in the image and the conversion from pixels to microns is read in from several files. The program reads in and displays the shadowgraphic images from a file. Once the picture is displayed, the user has the option of flagging defects in the paths of the A rays. The user selects the defect on each picture by drawing a polygon around it (see Figure 6). The user's clicks define the vertices of the polygon. There is a feature that allows the user to adjust the positions of the vertices. The default setting disables the adjustment feature to make the interface simpler. The user can draw any number of polygons.

9

Next, the user has the option of flagging defects shown in the bright ring. These are selected by clicking the beginning and end of the defect on the ring (see Figure 7). The program flags all the points along the ring between these two points. The user is also able to mark any number of defects in the bright ring.

The last piece of information the user supplies is a point from the A rays which does not show a defect. Based on this point, the program uses a recursive function to find a large number of points in the area bounded by the polygons
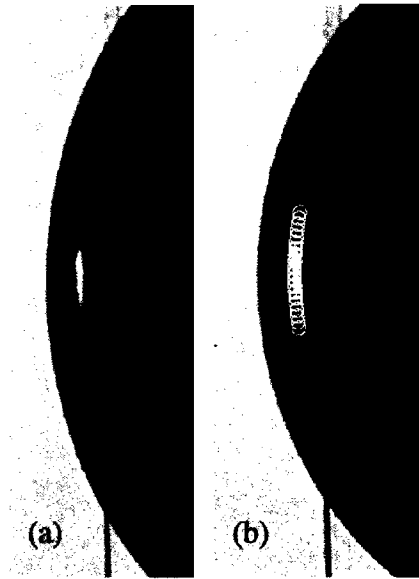
Fig. 7: (a) shows a defect in the bright ring. (b) shows that the area has been flagged.
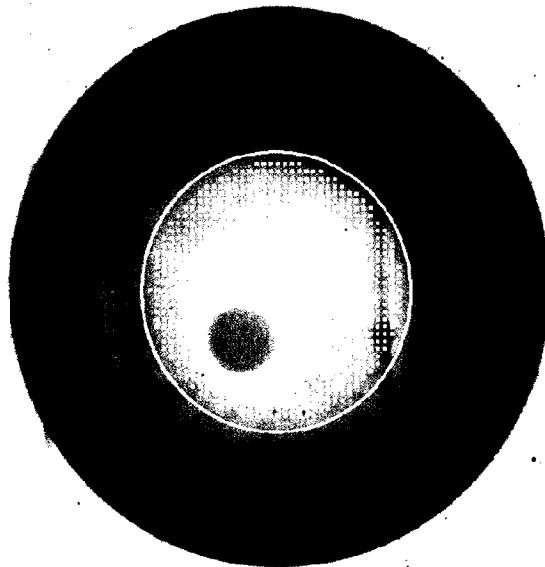
Fig. 8: Screen shot showing a dot at each point that will be traced back.

drawn earlier. This function acts like a fill function. These are the points for which paths

will be traced back later (see Figure 8). If there are multiple areas of good points that are

not connected to each other, the user can use the fill function multiple times to include all

the good points.

2.2 Tracing Rays Back

Another program traces a set of rays with different starting radii forward through

the target[8] and outputs results to a file. A table of each ray's initial radius (R_0 in Figure

9) and its radius in the object plane (R_7 in Figure 9) is created. The ray's radius is the

450

Radius
(μm)   0

R_0 R_1 R_2 R_7 R_6 R_3 R_4 R_5

Z`

-450   0   450
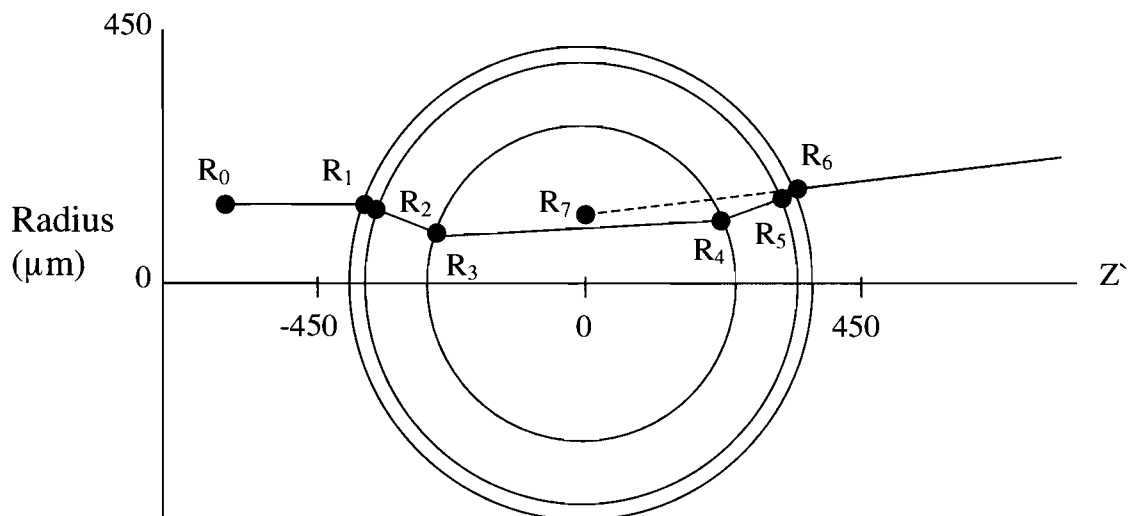
Fig. 9: Diagram showing the path of one ray through the target. R_7 is the radius when the ray is projected back to the object plane (z`=0). The center line represents a ray that passed straight through the center of the target.

distance from a ray that was initially parallel to it and that traveled straight through the

center of the target. Additional tables are created which store the complete path (R_0-R_6)

of each ray based on its initial radius (R_0). Using these tables, the program is able to

11

analyze the path of any ray. For each point being traced back, the program calculates its radius in the object plane (R_7 in Figure 9) from the image. This is calculated by finding the distance in the image from the center line of the target to the point. Then the program interpolates the initial radius (R_0 in Figure 9) from the first table. From that information, the program can interpolate the path through the target from the second table (all other R's in Figure 9). Initially, these searches were performed using a linear search. This was later replaced with a binary search to improve the speed.

Using the tables, the ray's path is obtained in the camera frame. The camera frame is a frame of reference where the camera views the target along the z` axis of Figure 9. The problem with this frame of reference is that it is different for each image since the camera moves from picture to picture. To combine the information from the different images, a reference frame is used that is constant for all the images. The ray's path can be converted from the camera frame to the reference frame based on the camera position (refer to Appendix A for a more detailed explanation).

To record the path of each ray the three-dimensional volume containing the target is divided into a 205x205x205 matrix. Three of these matrices are created to keep track of different information. Each cell of the matrix represents a cube with sides of about 6 microns and keeps track of the number of rays passing through it. The program takes small steps along each ray's
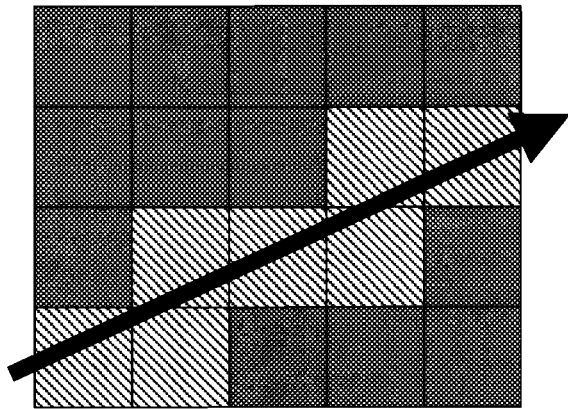

Fig. 10: A two dimensional representation of the way the program tracks the path of each ray. The counter of the red cells will be incremented to show that this ray went through them.

path and at each point it checks whether the ray has moved to a new cell. Whenever the ray moves to a new cell, it increments that cell's counter (see Figure 10).

The first matrix records the paths of the A rays that did not pass through any defects. The second matrix keeps track of the paths of the B rays that did not pass through a defect. The third matrix records the paths of the B rays that did pass through a defect. Each of these matrices is written to a file so that the results are saved. These three pieces of information can be combined to view the data in different ways.

3. Results

The program displays the data from the three matrices through horizontal slices, like a CAT scan. In Figure 11 (a) and (c) the program only displayed the A rays that did not pass through any defects. The dark areas in (a) and (c) indicate that rays were blocked by a defect. This analysis is useful for determining the approximate location of the defect, but it gives no indication of how deep in the ice layer the defect is located. This ambiguity is caused by the fact that a single A ray goes through the target almost head on. This causes it to go through the entire depth of the ice layer. Therefore, if that ray goes through a defect, it is impossible to determine at what depth that defect is located. The B rays, on the other hand, travel through the ice layer obliquely (see Figure 3), giving a strong indication of the depth of a defect. Frames (b) and (d) in Figure 11 show that the defect is on the inner ice surface. Combining the A and B rays that did not pass through a defect provides an estimate of the defect's depth. Although it is difficult to see, there are some lines missing in the B rays in the same area where the dark spot in the A rays occurs. The pattern formed by the B rays has many dark spots in it where no rays passed due to the limited number of camera positions. Each of the lines in (b) and (d)

corresponds to one of the camera views.

A more accurate picture can be found by using the A rays that did not intersect a defect and the B rays that <u>did</u> <u>intersect</u> a defect (see Figure 12). Using this method, the program draws the A rays that do not intersect a defect. Then it draws bright lines where
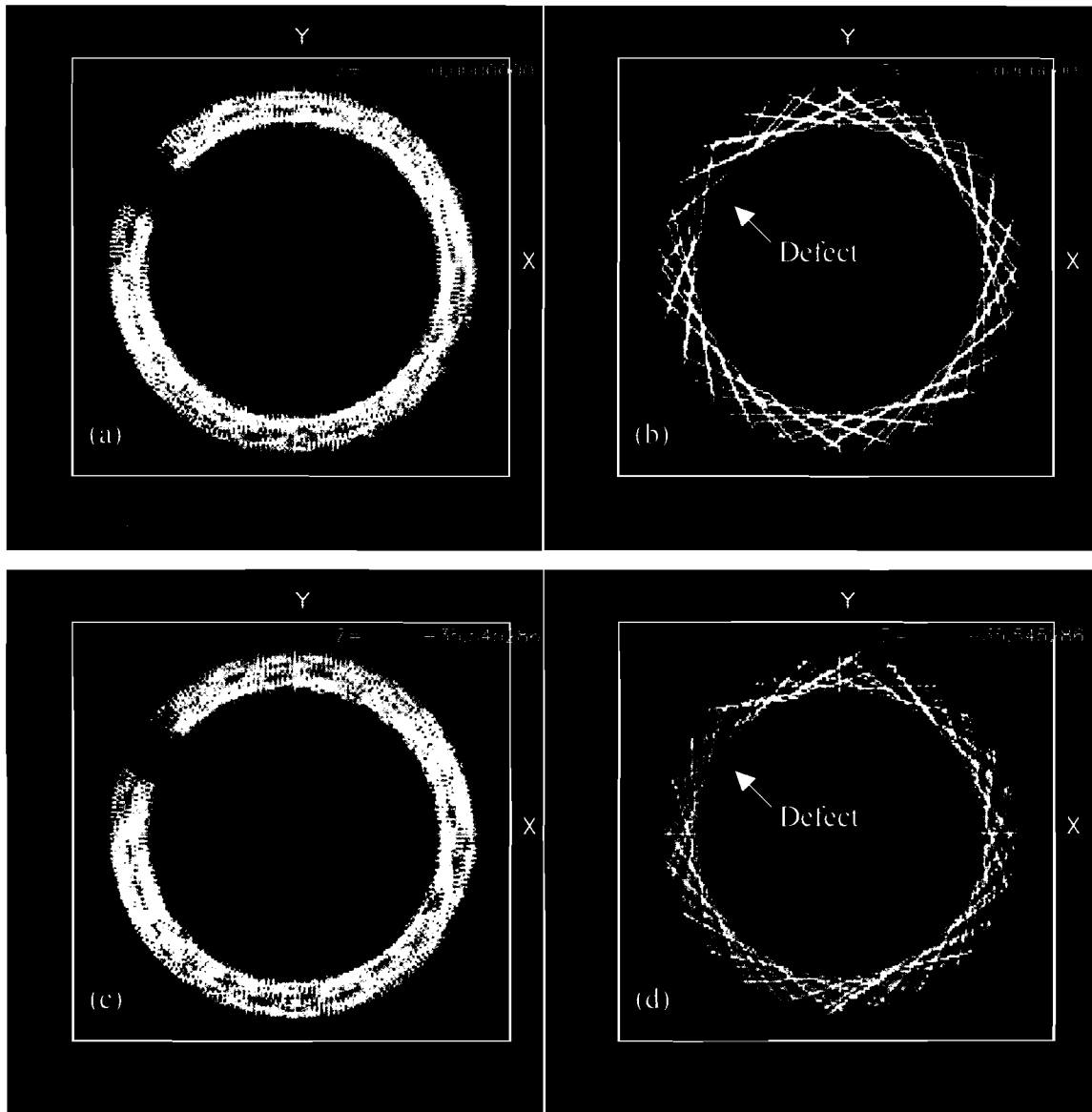

Fig. 11: (a) and (c) show slices through the matrix that recorded the paths of the A rays that didn't go through a defect. (b) and (d) show slices through the matrix that recorded the paths of the B rays that didn't go through a defect. (a) and (b) are horizontal slices at Z= 0. (c) and (d) are horizontal slices at Z=-35.5 μm. Each large white square has sides of 1024 μm.

there are no A rays that did not intersect a defect and there are B rays that intersect a
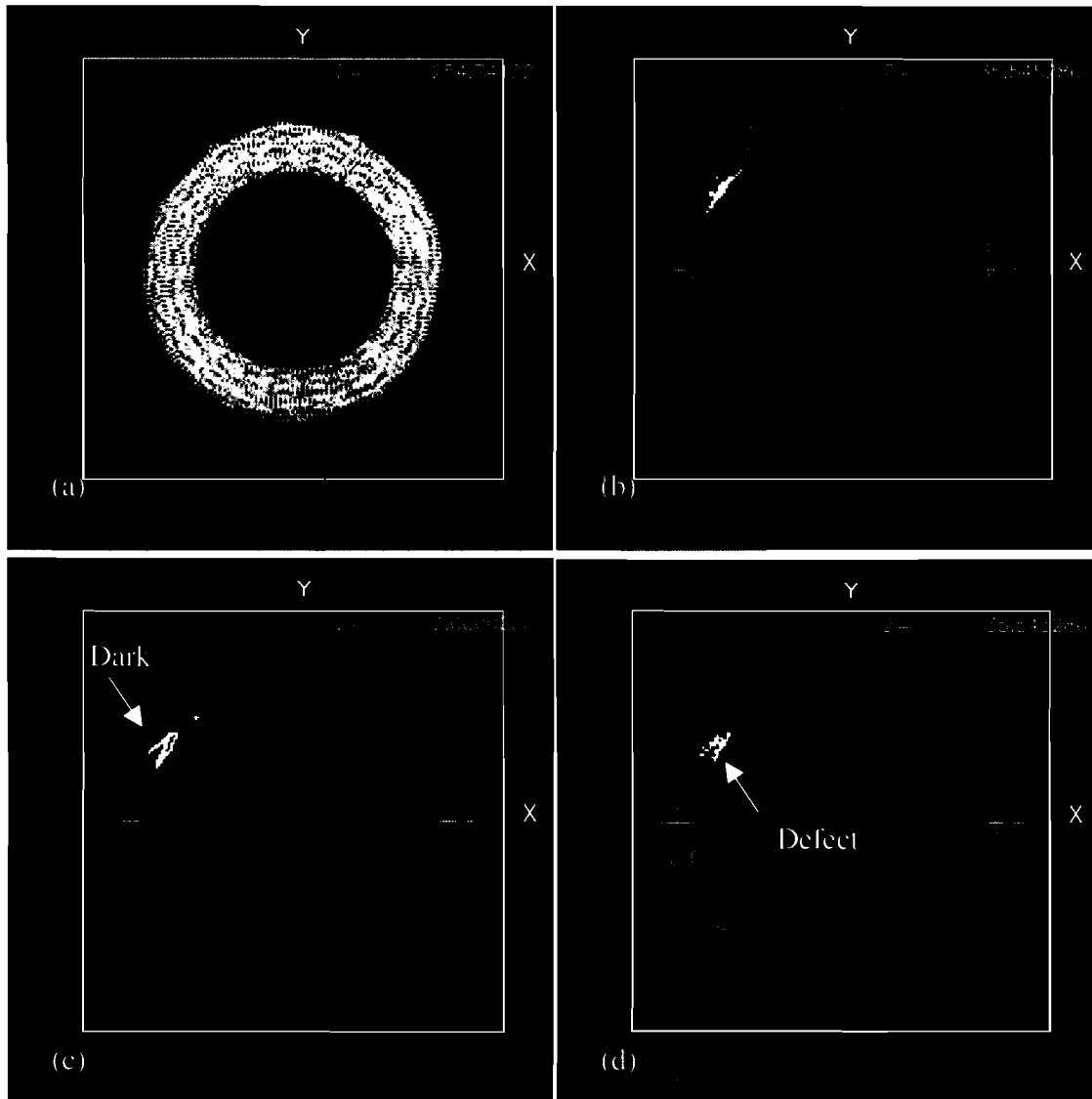
Fig. 12: Four horizontal slices through the 3-D model at Z values of 254.7, 35.5, 0.0 and –35.5 μm. (b), (c) and (d) have highlighted areas where there is a defect. There are no defects in (a). The white squares have sides of 1024 μm.

defect. This technique is much more accurate and easier to read. This method allows the

location and size to be calculated from the scale. The resolution of the output is limited

by the cell size of the 3-D matrix which is approximately 6 microns at the moment, which

is much smaller than the defect. This is enough resolution to estimate the defect's shape.

From the slices through the target shown in Figure 12, it is clear that the defect is on the inner surface of the ice layer. The defect's center is at approximately (-320, 180, 0) μm. It measures about 30 μm into the ice layer, about 70 μm in the Z direction and about 60 μm parallel to the surface of the ice. Defects of this nature have never been characterized in the past.

4. Future Work

In the future, the program will be extended to take into account the fainter rings labeled U and D in Figure 5. Since they take different paths through the target than the B rays, they would improve accuracy in identifying the depth in the ice at which the defect is located as well as the shape of the defect.

Another possible addition would be to increase the resolution of the 3-D model. The resolution could be increased throughout the entire volume or just in the regions where there is a defect. Focusing in on the defect would conserve computer memory. This would provide increased accuracy in the important areas.

The program could also be expanded to trace rays through the defect to compare the intensity perturbations with those seen on the shadowgraphic images. This would give the program the capability to determine whether the defect is a bubble or a dip or some other sort of anomaly. A program exists that determines what perturbations would occur in the bright ring radius because of bumps and dips in the inner-ice surface.[9] However, nothing has been published that is capable of modeling intensity plots like Figure 5.

5. Conclusion

The program developed in this work is the first program capable of creating a 3-D model of a cryogenic ICF target showing defects in the ice layer. The program was shown to be effective by analyzing a particular target. In this target, the program determined that the defect was on the inner ice surface and was located on the equator. Its dimensions were estimated to be approximately 30 μm deep into the ice layer, 70 μm in the Z direction and 60 μm parallel to the surface of the ice. Imperfections in the ice layer of cryogenic targets are a problem because they cause the target to compress unevenly, which decreases the target performance. Characterizing imperfections in targets will lead to improvements in manufacturing techniques and target quality.

6. Acknowledgements

7. References

[1] J. Nuckolls, et al., *Laser Compression of Matter to Super-High Densities: Thermonuclear (CTR) Applications*, **Nature** Vol. 239, pg. 139 (1972).

[2] R. S. Craxton, R. L. McCrory and J. M. Soures, *Progress in Laser Fusion,* **Scientific American** Vol. 225, pg. 68 (1986).

[3] C. Stoeckl, et al., *First Results from Cryogenic Target Implosions on OMEGA,* **Physics of Plasmas** Vol. 9, pg. 2195 (2002).

[4] D. N. Bittner, et al., *Forming Uniform HD Layers in Shells Using Infrared Radiation,* **Fusion Technology** Vol. 35, pg. 244 (1999).

[5] J. A. Koch, et al., *Quantitative Analysis of Backlit Shadowgraphy as a Diagnostic of Hydrogen Ice Surface Quality in Ice Capsules,* **Fusion Technology** Vol. 38, pg. 123 (2000).

[6] J. K. Hoffer, et al., *Surface Roughness Measurements of Beta-Layered Solid Deuterium-Tritium in Toroidal Geometries,* **Fusion Technology** Vol. 30, pg. 529 (1996).

[7] J. A. Koch, et al., *Numerical Raytrace Verification of Optical Diagnostics of Ice Surface Roughness for Inertial Confinement Fusion Experiments,* **Fusion Science and Technology** Vol. 43, pg. 55 (2003).

[8] S. Jin, *A Ray-Tracing Model for Cryogenic Target Uniformity Characterization,* **2002 Summer High School Research Program for High School Juniors,** Laboratory for Laser Energetics Report 329 (2003).

[9] J. Sater and D. Bittner, *Shadowgraphy and Spherical Capsules,* **General Atomics Report GA-A23240** pg. 5-5 (1999).

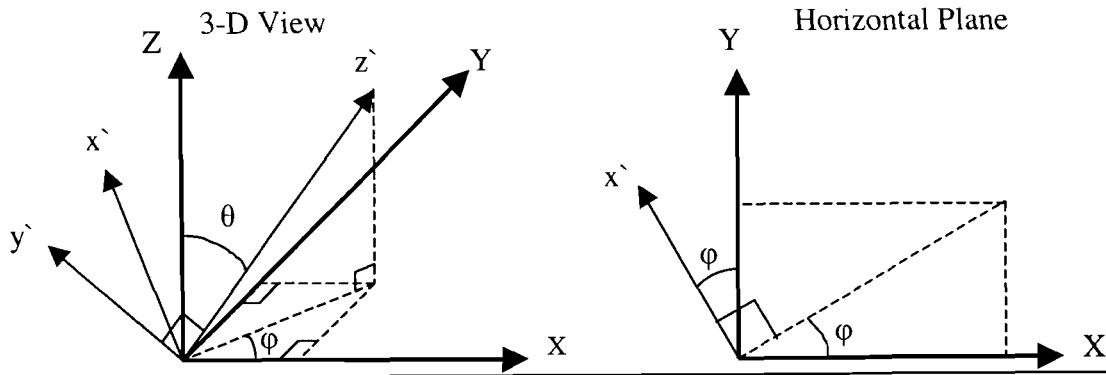# Appendix A- Obtaining the Ray Path in the Reference Frame

Fig. 13: Diagram relating the reference frame and the camera frame. XYZ is the reference frame and x`y`z` is the camera frame for an image viewed along z` defined by (θ, φ).

The purpose of this appendix is to obtain the path of a ray in the camera frame (x`y`z` in Figure 13) and to convert that path to the reference frame (xyz in Figure 13). Unit vectors $\hat{x}$, $\hat{y}$, and $\hat{z}$ correspond to x`, y`, and z` are defined as follows with respect to the reference frame:

$$\hat{z} = (\sin \theta \cos \varphi, \sin \theta \sin \varphi, \cos \theta) \qquad \hat{x} = (-\sin \varphi, \cos \varphi, 0)$$

$$\hat{y} = \underline{z}` \times \underline{x}` = (-\cos \theta \cos \varphi, -\cos \theta \sin \varphi, \sin \theta).$$

Using these conversions, coordinates in x`, y` and z` can be converted to XYZ coordinates. θ and φ define the camera location and are read in from an input file.

The coordinates in x`, y` and z` can be determined using the following method. First, the ray's position on the shadowgraphic image is calculated in terms of R_7 and ψ (see Figure 14). Then the ray's entire path (R_0-R_6 in Figure 9) is interpolated from the table described in Section 2.2 using the method described earlier. These tables provide the z` coordinate as well as the radius at each point along the ray's path. X` and y` can be calculated from this information using the following conversions:
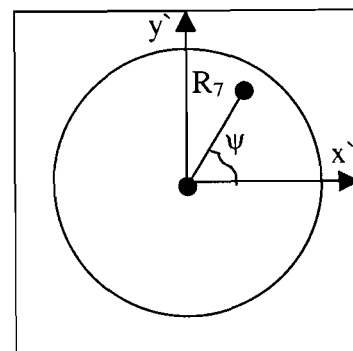

Fig. 14: Diagram showing how R_7 and ψ are obtained from a shadowgraphic image.

$$x` = R \cos \psi \qquad y` = R \sin \psi.$$

This provides sufficient information to convert to the reference frame.

Automated Focusing of the ROSS Streak Tube Electron Optics

Daniel Butler

Automated Focusing of the ROSS Streak Tube Electron Optics

Dan Butler
Advisors: R. Boni, P. Jaanimagi

Summer High School Academic Research Program, July-August 2004
University of Rochester
Laboratory for Laser Energetics (LLE)

I. Background

Many systems, including LLE's OMEGA, require fine temporal resolution of nanosecond-timescale events such as laser pulses and neutron bursts. In inertial confinement fusion (ICF), the time-varying intensity (shape) of the laser pulse that is directed at the target greatly affects the gain of the resulting fusion reaction[1]; because the ultimate goal of ICF is to increase gain and thereby produce net energy, the diagnosis of pulse shape is vital to the success of the program.

The function of measuring the pulse shape is performed by a streak camera, a device that can record intensity events from multiple channels at a temporal resolution of several picoseconds. This resolution cannot be achieved by purely optical means due to the difficulties of angularly deflecting an optical beam on such a short timescale. Instead, the streak camera uses a photocathode to convert the optical beam to an electron beam via the photoelectric effect; the electron beam is focused by electrostatic lenses (charged plates) and then swept across a phosphor screen by reversing the polarity of two deflection plates. As the electron beam sweeps across the screen, the temporal profile of the pulse is mapped onto the spatial axis in the direction of the sweep. The phosphor screen glows for several seconds, long enough for the image to be captured by a CCD

array and read into a computer. In the final image, the pulse shape appears in the x-direction (the temporal direction), and the different channels appear in the y-direction (the spatial direction).

Streak cameras have been in use for several decades, and many of the individual devices still in use are that old. The Rochester Optical Streak System (ROSS) is an implementation of the basic streak camera architecture with the incorporation of modern electronic controls. The objective of this project was to create a computer program capable of autonomously focusing the ROSS's electrostatic lenses, thus allowing optimization of cameras that are operating in remote locations.

II. Methods

Two programs for automatic focusing were written: one for the P510 ROSS (with one electrostatic lens) and another for the P820 ROSS (with three electrostatic lenses). For each, the task of focusing was divided into two separate problems: evaluating images for focus quality, and adjusting lens voltages to optimize focus quality. A controlled light source illuminated the photocathode with a control pattern in order to make image evaluation easier and more consistent.

IIa. Experimental Setup

The control pattern, a vertical slit similar in appearance to a dashed line (with 5 lp/mm), was imaged onto the photocathode with an Offner triplet. In this setup, the light source was constant instead of pulsed, and the sweep plates were not used. The Offner triplet assembly was attached to the input of the streak camera. A ROSS optical module is currently being developed that would serve the same function as the experimental setup: providing a control signal to the camera for the purposes of focusing and calibration.

IIb. Image Evaluation

In the case of the P510 tube, image evaluation was relatively simple because the radially symmetric lens focused the electron beam equally in both the temporal and spatial directions. Therefore, the working assumption was that if the image was optimally focused in one direction, it was very close to optimally focused in the other direction. The image evaluation routine used the line-spread function (LSF) in the temporal direction as the measure for overall focus quality. Full width at half maximum (FWHM) was used to

3

quantify focus quality, with a lesser FWHM indicating better focus. To determine

FWHM, the evaluation routine found the maximum intensity of the line spread, stored all

pixels with intensity greater than 25% of the maximum in a data set, and found the

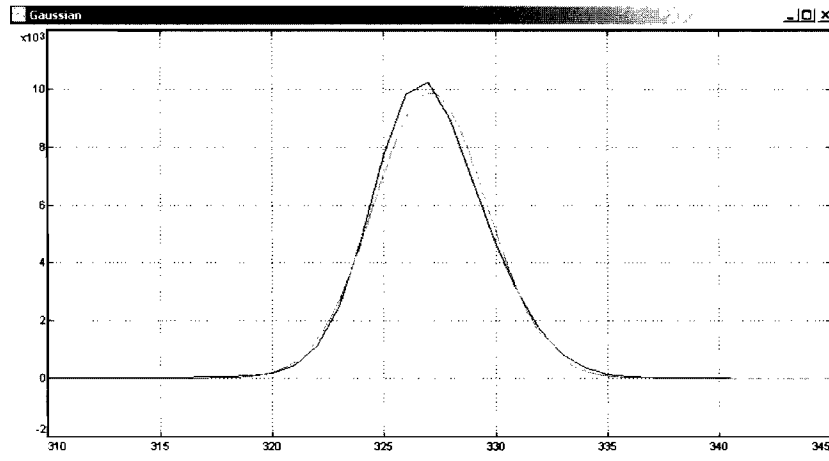coefficients of a Gaussian fit to the data (Fig. 1). These coefficients yielded the FWHM.

Fig. 1 The black (heavier) line is the LSF (image averaged over the spatial direction); the red (lighter) line is a Gaussian fit. The FWHM of the Gaussian was the measure of temporal focus quality.

In the case of the P820 tube, the image evaluation routine had to analyze temporal

and spatial focus quality separately because each direction was focused by its own lens.

The temporal focus quality, which is controlled by a cylindrical lens known as FB2, is

measured in the same way as the P510: the program finds the FWHM of the line spread

function. The spatial focus quality, which is controlled by a quadrupole lens, is quantified

in terms of contrast: the program must compare the maxima and minima of the spatial
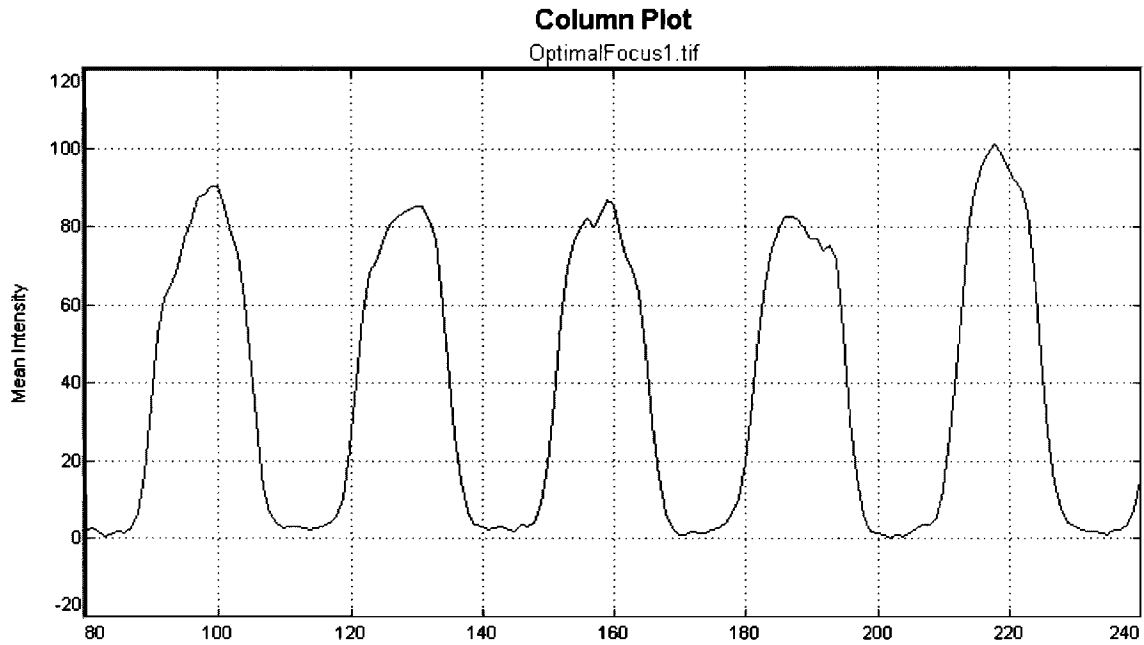
profile (Fig. 2).

4

Column Plot

OptimalFocus1.tif

Fig. 2 The spatial profile of captured image. The x-scale is measured in pixels.

Contrast (**C**), a number between 0 and 1 that indicates the difference between maxima and minima, was computed for each peak and valley pair (Eq. 1).

Eq. 1 $C = (Max - Min) / (Max + Min)$

Then to reduce the effect of noise, all values of **C** that were greater than one standard deviation away from the mean were removed from the data set and the mean was recalculated. This final mean contrast (C_f) was used as the measure of spatial focus quality; a contrast of 1.00 would indicate minima of zero intensity, while a contrast of 0.00 would indicate minima equal to maxima (no modulation).

IIc. Lens Voltage Optimization

In the case of the P510, the task of lens voltage optimization was, again, relatively simple: there was one input (a single lens voltage), one output (an LSF), and one goal

5

(minimize FWHM). Essentially, optimization consisted of capturing images at different lens voltages, applying the evaluation routine to each to find the FWHM, and selecting the voltage that yielded the smallest FWHM. The solution space was likely to be a simple parabola, and experimentation showed this to be true.

In the case of the P820, the task of lens voltage optimization was considerably more complex: there were two inputs (both the FB2 and quadrupole voltages), two outputs (both FWHM and contrast), and two goals (to minimize FWHM and to maximize contrast). Because each image capture took about 10 s, testing all of the possible combinations of lens voltages would have taken too long (there is also a prospect of future streak tubes having even more lens voltages). In addition, the quadrupole is not completely independent of temporal focus; rather, FB2 and the quadrupole both affect the temporal focus. With only two lenses, the quadrupole could be optimized for spatial focus first, and FB2 could be optimized for temporal focus second. However, this would not necessarily yield the best temporal focus possible, and the problem would be exacerbated in future tubes with more than one quadrupole lens. Therefore, a previously untested approach was taken: the use of a genetic algorithm (GA) to evolve the best-focus solution. Given a problem in which the solutions can be rated in terms of their "fitness," a number that indicates how successful they are, GAs utilize the biological evolutionary principles of genetic variation, natural selection, and inheritance to produce solutions that approach the maximum fitness with each successive generation.

III. Results

As expected, the solution space for the P510 turned out to be a parabola. To minimize the FWHM, the program captured several sample images (Fig. 3), found FWHM values via the image evaluation routine, plotted FWHM values versus lens voltages, calculated the parabolic fit, and selected the lens voltage at the minimum of the parabola (Fig. 4). Repeated testing showed that the program was indeed capable of consistently finding the lens voltage that minimized the FWHM.
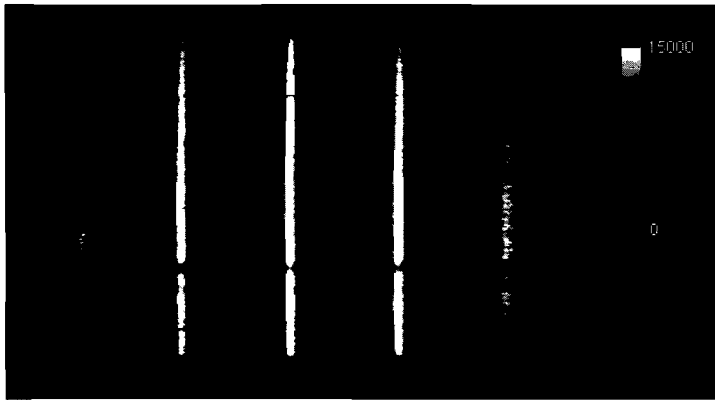

Fig. 3 Five images taken with the P510, with lens voltages ranging from −14300V to −14480V. The color scale on the right is in arbitrary units of intensity. The center image has the least FWHM, at about 6 pixels.
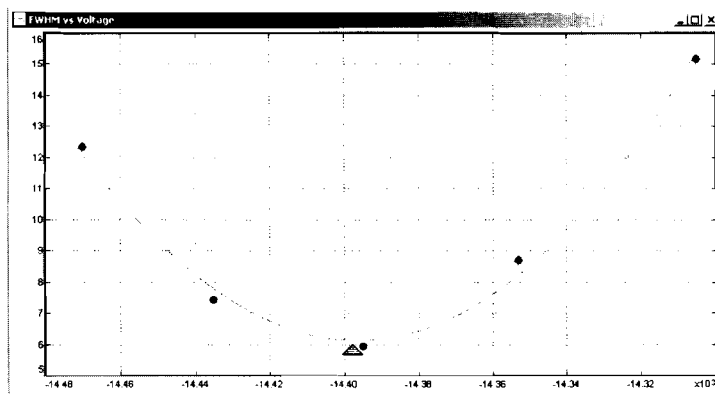
Fig. 4 FWHM (pixels) versus lens voltage (kV). This plots data from the images in Fig. 3. The green arrow indicates the predicted optimal voltage.

7

The solution space for the P820 was not as well-defined as the P510's parabola. Because the P820 had two input voltage (quadrupole and FB2), plotting its solution space required three dimensions. The total weighted fitness F_w (which measures overall quality of focus) was calculated using Eq. 2.

Eq. 2 $F_w = 0.2*C_f + -4*\ln(0.5)*FWHM^{-2}$

The second term of Eq. 2 is -1 times the x^2-coefficient of the LSF's best fit parabola (as **FWHM** increases, this term decreases and thereby lowers total fitness). The coefficient of the first term was selected so that the typical variation of both terms is approximately equal. This ensures that the contrast and line width of each image contribute about equally to that image's weighted fitness.

Fig. 5 shows the two input voltages mapped onto the two spatial directions and the weighted fitness mapped onto a color scale.
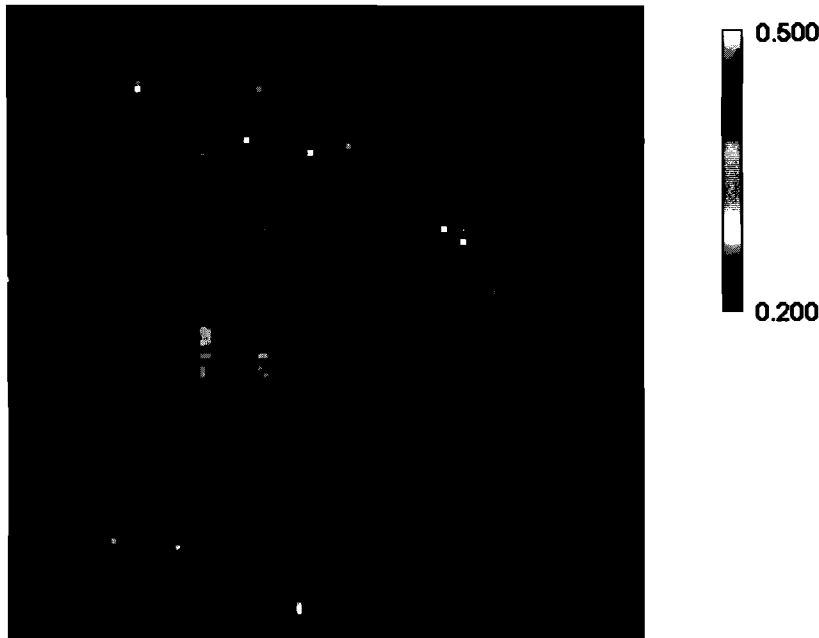

0.500

0.200

Fig. 5 A plot of the P820's solution space. The x-axis maps quadrupole voltage, and the y-axis maps FB2 voltage. The color of each point represents the weighted sum of the filtered contrast C_f and the squared inverse of **FWHM**, in arbitrary units.

Repeated trials suggested that focus quality is indeed dependent on the

interactions of all lens voltages, as opposed to being influenced by each lens

independently. This conclusion was reached because of the diagonal slant of the

contours' major axes (Fig. 6); if the lenses had affected focus quality independently, the

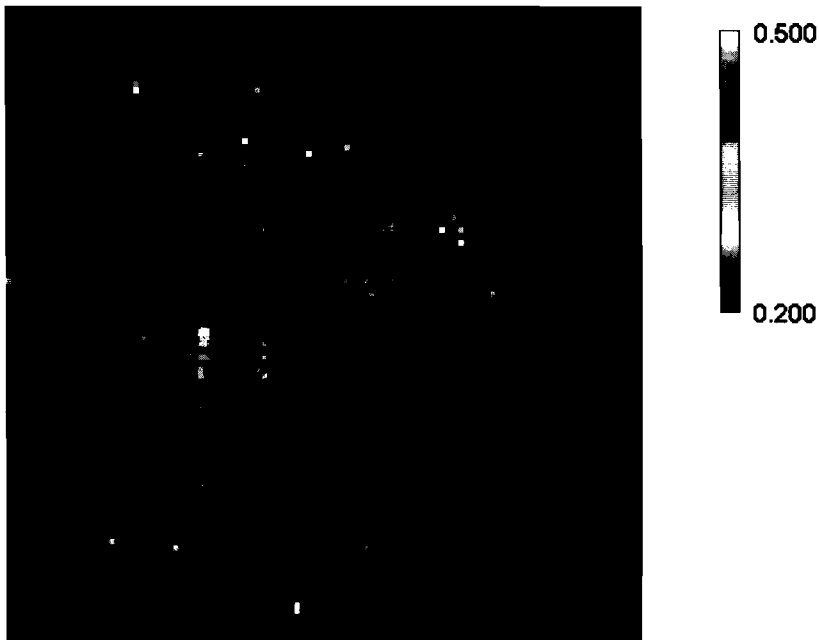contours' major axes would have been orthogonal to the x- and y-axes of the graph.

Fig. 6 Replica of Fig. 5, with contours of approximately equal fitness drawn for clarity.

IV. Conclusions

The programs written for this project should be further characterized for repeatability and effectiveness. There is a tradeoff between the speed of a focusing algorithm and its ability to find the true optimum; the programs written may not be achieving the most desirable balance between these two possibilities. Further analysis of the programs' performance could yield significant improvements. The GA developed for the focusing of the P820 should be tested against a non-GA. When applied to a streak tube like the P820, which has 2-3 lens voltages to adjust, a non-GA may prove faster and more effective; when applied to a streak tube like the PJX, which has multiple quadrupoles and many more lens voltages to adjust, the GA may prove superior than the non-GA. The reason the GA may perform better when used on a more complex system is that the GA adjusts all voltages simultaneously and is capable of searching the solution space for unforeseen interactions between lenses. The result could be faster search time and smaller FWHM.

This project was limited by time constraints, but it achieved the goal of creating a program for autonomous remote focusing of the ROSS. The project also demonstrated that a genetic algorithm is capable of reaching the optimal focus of an electron-optical system.

V. Acknowledgments

I would like to thank Bob Boni, Dr. Paul Jaanimagi, and Matt Millecchia for the large portion of time they spent helping me on my project this summer. I know the skills, techniques, and concepts that they taught me will be invaluable in whatever scientific field I eventually choose. I would also like to thank Dr. Steve Craxton for giving me the opportunity to participate in this program; I have learned a lot about what it would mean to be a professional research scientist.

VI. References

1. McCrory, R.L., *et al.*, *Nuclear Fusion* **41**:1413 (2001).

2. Lerche, R.A., McDonald, J.W., Jaanimagi, P.A., Boni, R., *et al.*, "Preliminary Performance Measurements for Streak Camera with Large-Format Direct-Coupled CCD Readout", *15th Topical Conference on High-Temperature Plasma Diagnostics* (San Diego, CA, April 19-22, 2004).

3. Obitko, Marek. "Introduction to Genetic Algorithms." <http://cs.felk.cvut.cz/~xobitko/ga/>

Grated Compressor Modeling

Jeremy Chang

Grating Compressor Modeling

Jeremy Chang
Penfield High School
Advisor: Mark Guardalben

University of Rochester
Laboratory for Laser Energetics
Summer High School Research Program

Abstract

In order to avoid laser-induced damage to optical components during

amplification of a short laser pulse, the pulse often is first stretched in time to reduce its

peak power, amplified, and then recompressed. High peak irradiance is attained when the

laser beam is subsequently focused onto a laser fusion target. In a laser system, currently

under construction, large diffraction gratings will be used in a precise alignment in order

to provide pulse compression. Misalignment of the diffraction gratings that comprise the

grating compressor can lead to less than optimal pulse compression and reduced ability to

focus the beam owing to residual angular dispersion of the pulse spectrum. A computer

program was used to model the grating compressor system. The effects of grating

alignment errors on the compressed pulse and focused beam were found. A pulse can be

broadened from the transform limit of 606 fs to the tolerance limit of 1 ps, by errors in

the alignment of diffraction gratings of 75 μrad of tilt, 250 μrad of tip, 450 μrad of

rotation, and 6 mm of distance mismatch. The requirement of 80% encircled energy in an

area of radius 10 μm is met for all errors corresponding to the 1 ps tolerance limit.

I. Introduction

1.1 Grating Compressors

Since amplification of a short laser pulse can prove to be difficult and damaging to subsequent optics, a short laser pulse must be stretched in time before it is amplified and then recompressed. This process is known as Chirped Pulse Amplification (CPA)[1]. A stretched pulse will not damage optics, because the energy is spread out over time, which means it has a low intensity. Amplification of the pulse increases the amount of energy,
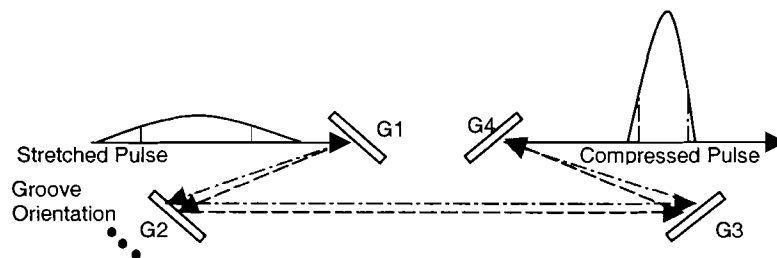

Figure 1.1 A Four-Grating Compressor System – A stretched laser pulse is propagated through a system of four diffraction gratings. Each frequency, shown here as the dotted line and dashed line, is diffracted at a different angle. This disparity in the angle of diffraction causes a path-length difference from one frequency to the next, which in turn creates a shift in time of some of the frequencies.

but does not raise the intensity over a level that would damage an optic. After amplification has been completed the laser pulse is passed through a system of four gratings, known as a grating compressor, in order to compress the pulse. This compression increases the intensity of the pulse by compressing it in time in order to heat the fusion target.

A grating compressor has the ability to shift the frequencies that compose a laser pulse in time causing a shift in time [2]. This shift is caused by the path-length difference from one frequency to the next. Since the frequencies towards the beginning of the pulse travel a longer distance, the pulse is compressed. Such compression allows a pulse to have a high intensity allowing the fusion target to heat up in a very short period of time.

2

A misalignment in the diffraction gratings, however, can cause the pulse to broaden from the transform limit, which is the compressed pulse for a perfect grating alignment.

Some misalignments cause angular dispersion in the laser beam. A number of definitions for angular dispersion are used. It can be described as either the angle between the orientation of the frequencies or the angle between the phase fronts of the frequencies [3]. Although these definitions may seem similar, they account for different phenomena in pulse and are therefore distinctly different. Angular dispersion between the phase fronts causes a wave front tilt, which causes temporal broadening of a spatially integrated temporal pulse. Angular dispersion in the orientation of the frequencies similarly accounts for a smearing in the far field of a beam.

1.2 Modeling

The grating compressor was modeled, in order to find the margin of error that will be acceptable in the alignment of the diffraction gratings. An input beam of diameter 42 cm was used in the modeling in order to collect the data. The transform limit of 606 fs was the point of comparison from which the errors of each grating was found. The same input beam, composed of 451 rays was used throughout the experiment, and only the distance between gratings and orientation of gratings were changed. Several grating misalignments were run in order to derive a relationship between broadening and grating error. The tolerance limit was then found after extrapolating a line of best fit, and the result was then tested.

II. Methodology

2.1 MANTARAY

In order to understand the effects of misalignment errors in the diffraction gratings on the pulse shape, a computer program MANTARAY was developed. Mantaray is a ray trace program. Each ray is diffracted through a component method and propagated through the grating compressor and then undergoes a Fourier Transform. This FFT allows the beam to be converted into a far field where spatial smearing can be seen. This yields information about the beam after compression both spatially and temporally.

The program is run from a configuration file, which has twelve lines. Line 3 calls a grating input file that is in the .mro file format. Within this file the optics are defined. A typical diffraction grating would be defined as: a diffraction-grating, x-y-z position, x-y-z orientation, rho/pi rotation, size, groove spacing, and back-behavior. The optics, which is used to find the far field, is also defined in the .mro file, and given a position, orientation, and grating size. Rays that fail to propagate through the system are written to a .txt file. After a run is completed another .txt file is created which stores information concerning the rays final position, time, orientation, and accumulated phase.

The running of the central ray preceded all runs. This allowed the orientation of the central ray to be found, and the optic to be set anti-parallel to the central beam. The user is prompted for the number of angles to be used in creating the encircled energy diagram. A run of the full beam then followed giving a plot of the temporal, logarithmic spatial (centered and uncentered), spatial, and encircled energy diagram. Along with this

4

numeric data concerning the temporal and spatial full width half max (FWHM) and

percent of total energy encircled are given. A number of .txt files containing data are

created, including information for the spatial, temporal, and encircled energy plots.

III. Data Collection

Data was collected for errors of rotation around the vertical axis (TILT), rotation

about the horizontal axis (TIP), rotation about the surface normal (IN-PLANE

ROTATION), and grating distance mismatch using the program mantaray.

3.1 TILT

A rotation about the vertical axis will

introduce a grating alignment error that will affect

the pulse shape. Figure 3.1.1 shows grating tilt.

A relationship between the amount of tilt

and temporal broadening of the pulse can be

observed when the Full Width at Half Max is

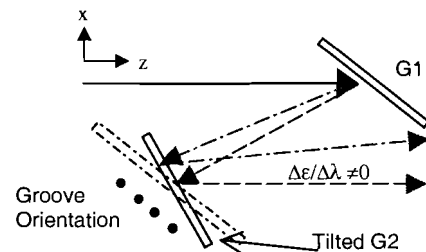plotted against the amount of error introduced to

Figure 3.1.1 Tilt of the Second Grating- A rotation about the y-axis (groove orientation) causes an angular dispersion ($\Delta\epsilon/\Delta\lambda$) in the x-z plane.
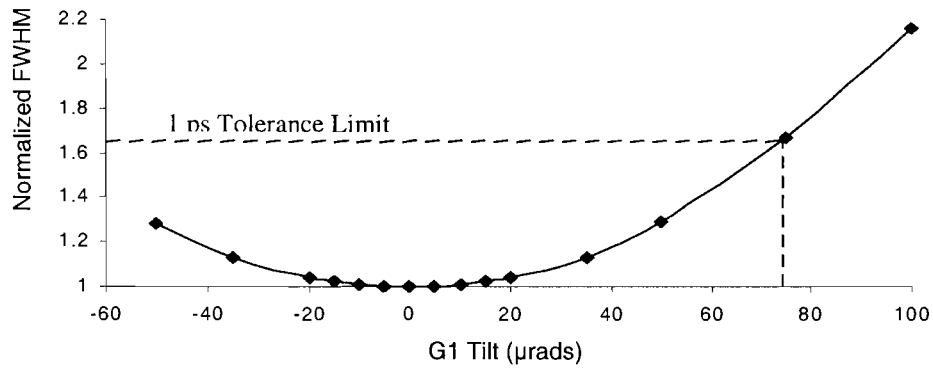
the system. The tolerance limit, of 1 ps, is met at a tilt of 75 μrad. The effect of tilt errors

is independent of the grating that is misaligned, in that the effect of tilting the first grating

50 μrad will be the same as tilting the second, third, or fourth. The results are shown in

Figure 3.1.2.

5

Figure 3.1.2 Temporal FWHM Normalized to Transform-Limited FWHM for Grating Tilt-
Increasing the μrad of tilt, causes a broadening of the FWHM of the temporal pulse. A full width half max of 606 ps corresponds to a normalized FWHM of 1. The tolerance limit, of 1 ps, is met at a rotation of 75 μrad.
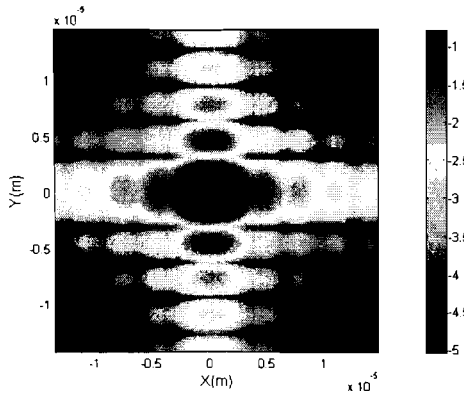

Figure 3.1.3 Smearing in the X Direction Due to Grating Tilt- The direction of angular dispersion for the far field of a grating tilt is orthogonal to the groove direction. Smearing in the x-direction is apparent in the far field of a 50 μrad tilt of the first grating. The grooves run in the y-direction.

In the far field a similar effect is seen. The focused beam for a tilt of the second grating will show smearing in the x-direction, which is the direction of residual angular dispersion. Once again, as the amount of tilt is increased, the smearing of the far field increases. An example of the smearing caused by grating tilt is shown in Figure 3.1.3.
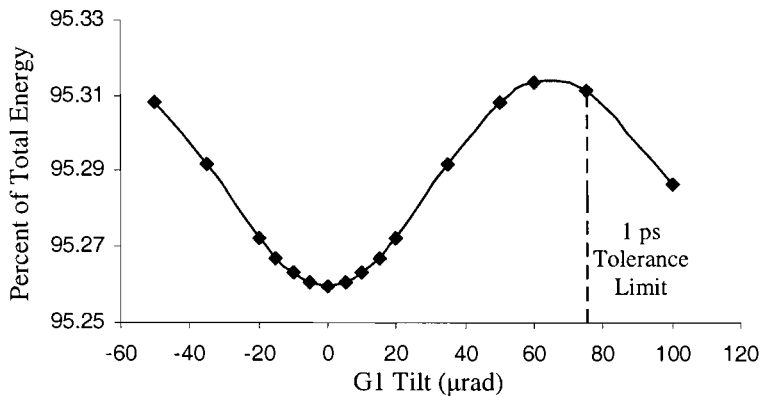

Figure 3.1.5 Encircled Energy for a radius of 10 μm for Grating Tilt- The 80% encircled energy requirement for the laser system is met for all errors below the 1ps Tolerance Limit for Grating Tilt.

The amount of smearing that is in the far field can be found quantitatively using a measurement of the pulse width at the full width at half max. This spatial FWHM displays a relationship similar to that of the temporal FWHM.

6

A parabolic relationship between the amount of tilt introduced to the system and the spatial FWHM becomes readily apparent. This plot is shown in Figure 3.1.4. The
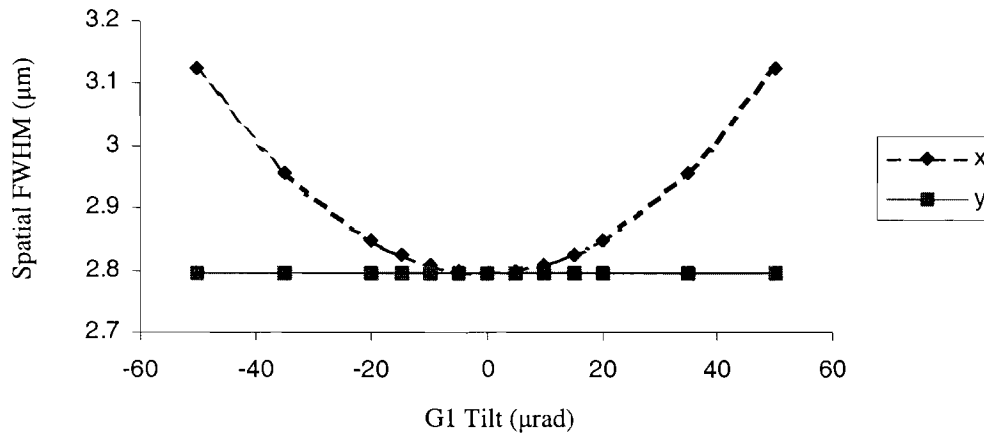

Figure 3.1.4 Spatial FWHM Increases in the X-Direction- The broadening of the spatial FWHM in the x –direction corresponds to the smearing seen in the far field of the beam. The relationship of spatial FWHM to error is similar to that of the temporal pulse.

laser system specifies that a circle of radius 10 μm must encircle 80% of the total energy that the beam contains. When the percent of total energy is plotted against the total amount of tilt error introduced to the system, it can be seen that the amount of energy for tilt errors less than the tolerance limit, provides more than 95% of the total energy meeting the standards set for the laser system. Figure 3.1.5 shows encircled energy for a circle of 1μm for varying grating tilts

3.2 TIP

A rotation about the horizontal axis will introduce an angular dispersion in the y-z plane. Grating tip will also cause broadening of the pulse temporally and spatially. An example of Grating Tip is shown in Figure 3.2.1.

7

A grating tip will introduce temporal broadening as the amount of tip is increased. A plot of the temporal Full Width at Half Max vs. grating tip shows how a pulse can be broadened as the amount of error increases. For a broadening of 1 ps, which corresponds to the tolerance limit, the grating would need
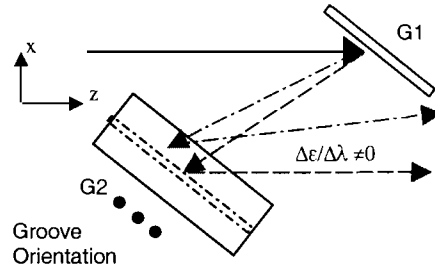

Figure 3.2.1 Tip of the Second Grating- A rotation about the x-axis of the grating, (orthogonal to the groove orientation) causes an angular dispersion ($\Delta \varepsilon / \Delta \lambda$) in the y-z plane.

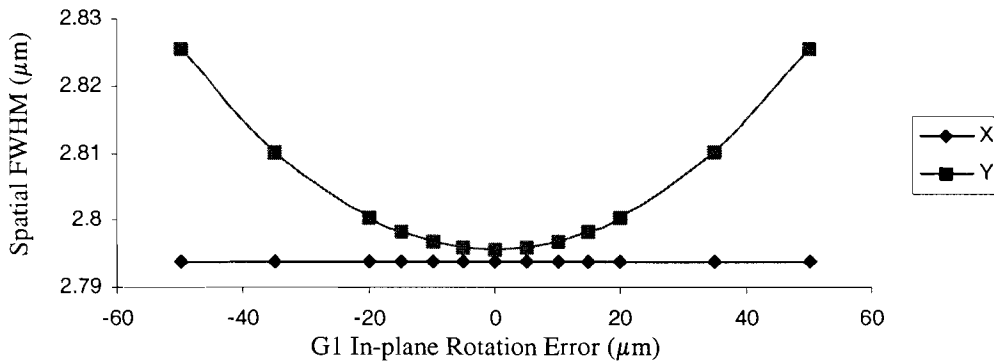to be tipped 250 μrad. The relationship between the temporal FWHM and grating tip is

Figure 3.2.4 Spatial FWHM Increases in the Y-Direction- The broadening of the spatial FWHM in the y –direction corresponds to the smearing seen in the far field of the beam. The relationship of spatial FWHM to error is similar to that of the temporal pulse.
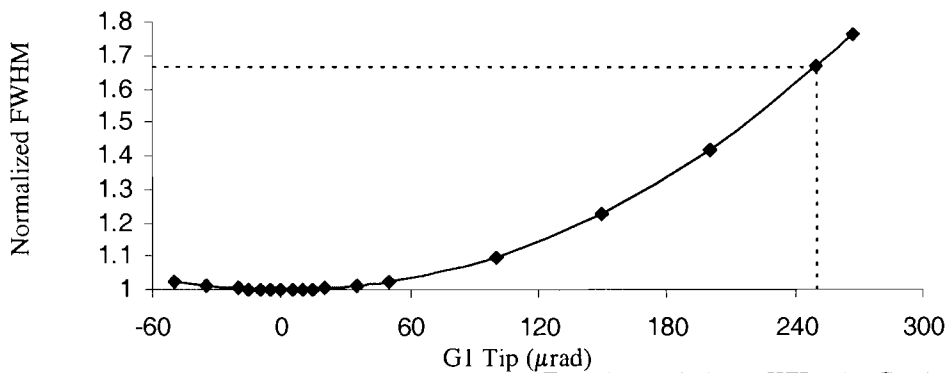

Figure 3.2.2 Temporal FWHM Normalized to Transform-Limited FWHM for Grating Tip- Increasing the μrad of tip, causes a broadening of the FWHM of the temporal pulse. The tolerance limit, of 1 ps, is met at a tip of 250 μrad.

shown in figure 3.2.2.

Spatially the far field shows smearing in

the y-direction, which is the direction of the

residual angular dispersion. This angular

dispersion is along the groove orientation, and

orthogonal to the smearing that is apparent from a

grating tilt misalignment. Figure 3.2.3 shows an

angular dispersion of the far field for a grating tip

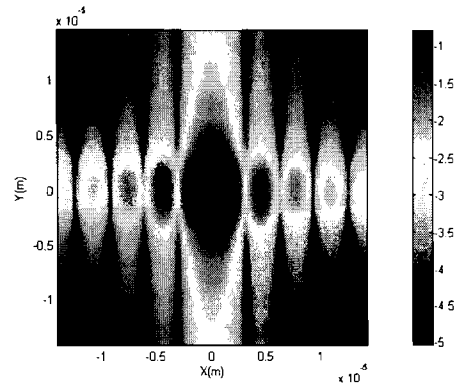of 250 μrad, which corresponds to the 1 ps

Figure 3.2.3 Smearing in the Y Direction Due to Grating Tip- The direction of angular dispersion for the far field of a grating tip is along the groove direction. Smearing in the y-direction is apparent in the far field of a 267 μrad tip of the first grating.

tolerance limit that is required by the laser system.

The required 80% of encircled energy is

met for all tip errors that fall below the 1 ps tolerance limit. Figure 3.2.4 shows the
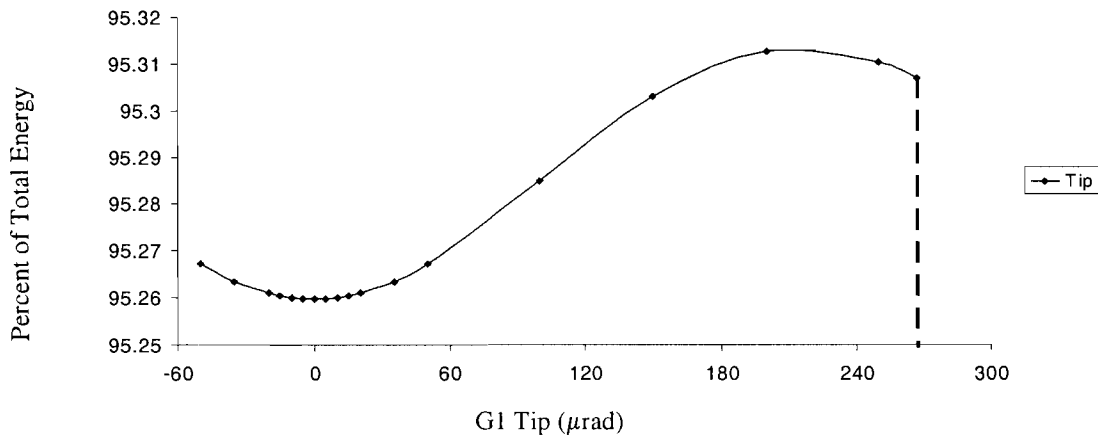
encircled energy for different amounts of tip error.

Figure 3.2.5 Encircled Energy for a radius of 10 μm- The 80% encircled energy requirement for the laser system is met for all errors below the 1ps Tolerance Limit.

3.3 IN-PLANE ROTATION

A rotation about the axis normal to the grating face will cause smearing in the y-z plane much like a grating tip. Figure 3.3.1 shows a grating rotation.
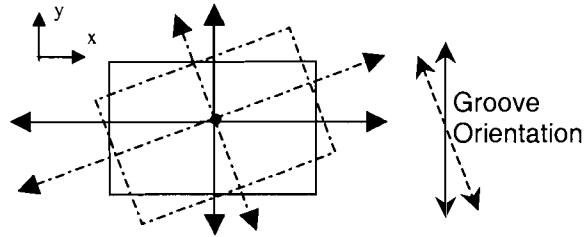

Figure 3.3.1 In-plane rotation of the Second Grating- A rotation about the z-axis of the grating, causes an angular dispersion ($\Delta\varepsilon/\Delta\lambda$) in the y-z plane, and alters groove orientation.

Temporal broadening will increase as the amount of rotation increases. A plot of the FWHM of a pulse for varying in-plane rotation errors shows this correlation (Figure 3.3.2). A broadening of 65%, which corresponds to the 1 ps tolerance limit, is met at an in-plane rotation of 450 μrad.
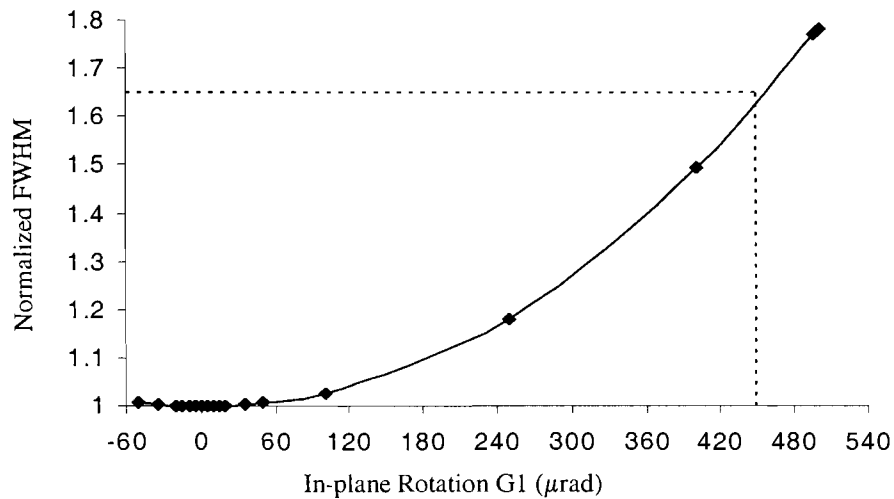

Figure 3.3.2 Temporal FWHM Normalized to Transform-Limited FWHM for Grating In-plane Rotation- Increasing the μrad of in-plane rotation, causes a broadening of the FWHM of the temporal pulse. The tolerance limit, of 1 ps, is met at a rotation of 450 μrad.

10

Spatial broadening exhibits similar behavior to grating tip. Angular dispersion in the y-z plane causes smearing the y-direction. This smearing is visible in the far field of the beam. Figure 3.3.3 shows a far field for a 450 μrad rotation. Numerically the spatial FWHM shows broadening the y-direction, similar to the effect seen in a grating tip. The 80% total energy requirement is met for all rotations that are less than the tolerance limit of 250 μrad.
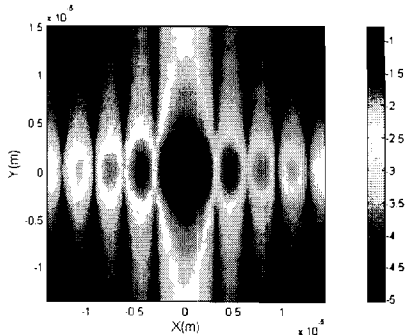

Figure 3.3.3 Smearing in the Y Direction Due to Grating In-plane Rotation- The direction of angular dispersion for the far field of a grating in-plane rotation is along the groove direction. Smearing in the y-direction is apparent in the far field of a 450 μrad rotation of the first grating, which corresponds to the 1 ps tolerance limit.
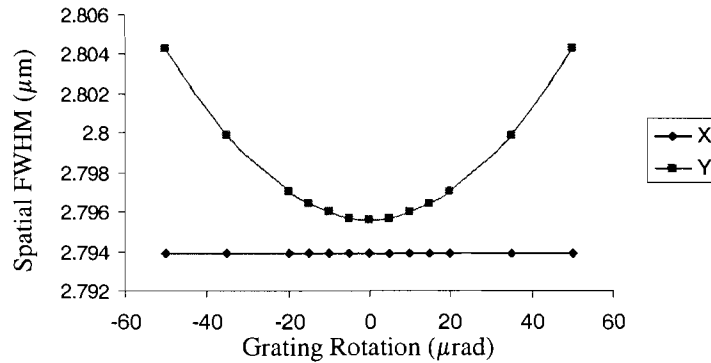
Figure 3.3.4 Spatial FWHM Increases in the Y-Direction- The broadening of the spatial FWHM in the y –direction corresponds to the smearing seen in the far field of the beam. The relationship of spatial FWHM to error is similar to that of the temporal pulse.
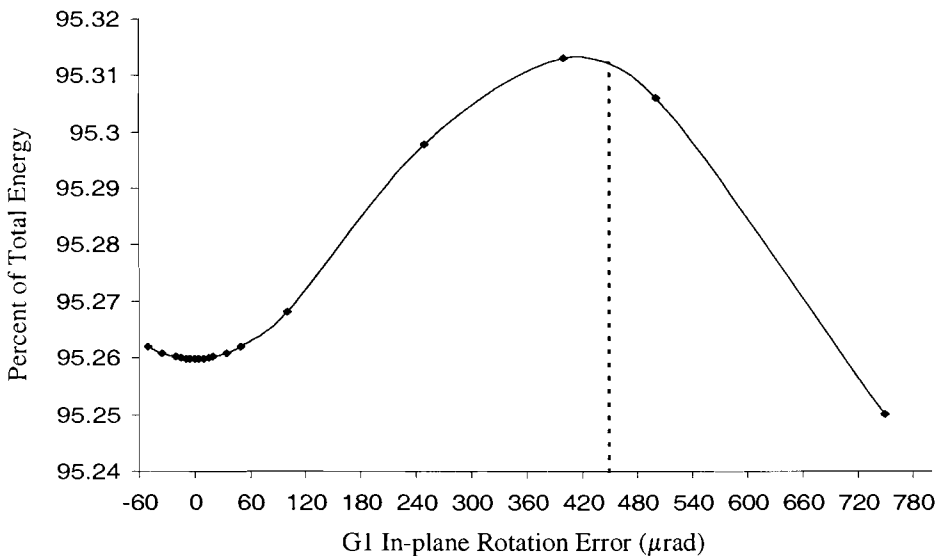

Figure 3.3.5 Encircled Energy for a radius of 10 μm- The 80% encircled energy requirement for the laser system is met for all errors below the 1ps Tolerance Limit.

11

3.4 Grating Distance Mismatch

Changing the distance between gratings without changing orientation will cause a broadening of the temporal pulse. No angular dispersion is induced, however. Figure 3.4.1 shows Grating Distance Mismatch.
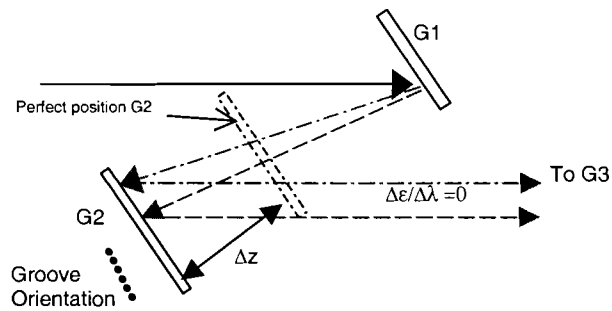
Figure 3.4.1 Grating Distance Mismatch of the Second Grating- Shifting the grating straight back causing a temporal broadening. Angular dispersion ($\Delta\varepsilon/\Delta\lambda$) is not induced and therefore equals zero .
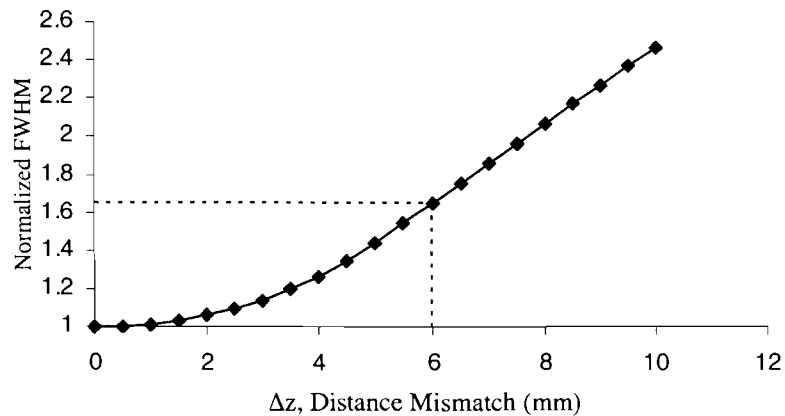
Figure 3.4.2 Temporal FWHM Normalized to Transform-Limited FWHM for Grating Distance Mismatch- Increasing the distance between gratings causes a temporal broadening. The tolerance limit of 1 ps is met at a grating distance mismatch of 6mm.

Temporally the relationship between the FWHM and the amount of distance mismatch appears to start out as a hyperbolic curve and eventually reach a linear relationship. Figure 3.4.2 shows the relationship between grating distance mismatch and pulse width.

12

Since there is no residual angular dispersion, the far fields of grating distance

mismatches show no smearing. A comparison of the far field for a perfect compressor

alignment and a compressor with a second grating displaced 9 mm shows no difference.
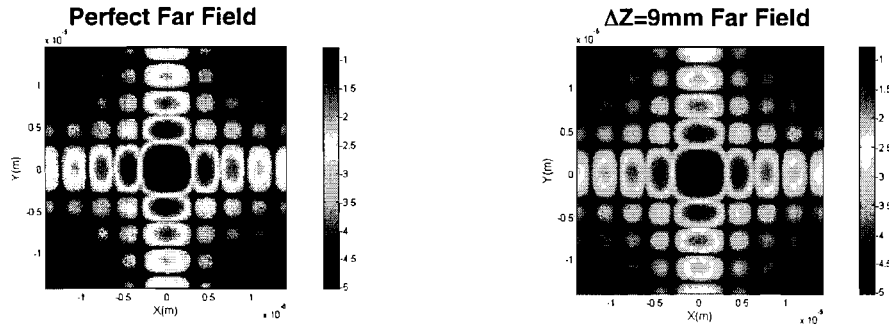
Figure 3.4.3 Far Field of Grating Distance Mismatch- Since there is not residual angular dispersion, the far field of a grating distance mismatch shows no smearing. The far field on the right shows no smearing for a grating distance mismatch of 9 mm.

IV. Discussion

4.1 Angular Error Comparison

Figure 4.1.1 Comparison of Angular Errors Temporal Effects- A comparison of the broadening caused by angular errors shows that a tilt error has the greatest effect on pulse width.
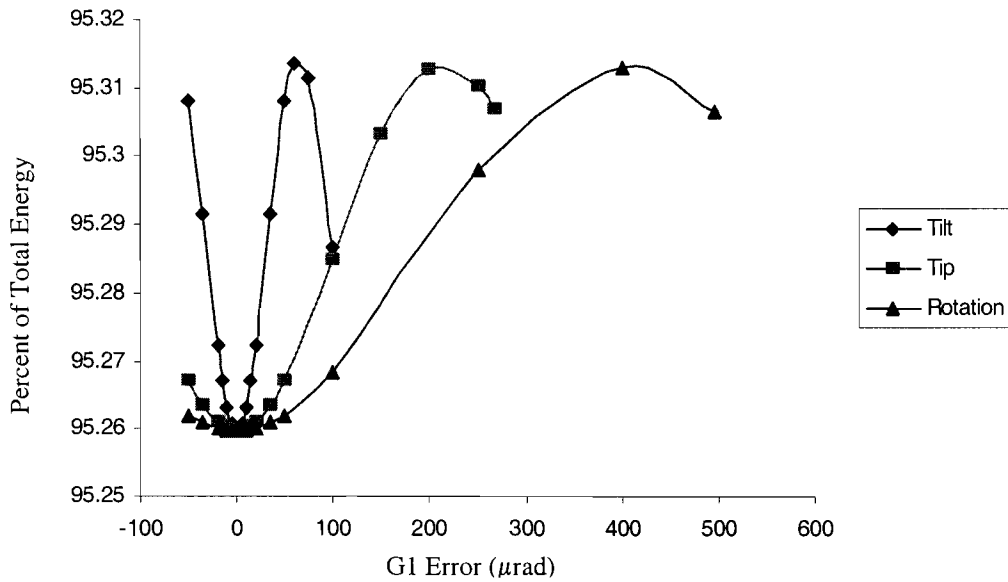
Figure 4.1.2 Comparison of Angular Errors Encircled Energy- A comparison of the encircled energy plots, shows that spatially tilt errors have the greatest effect, since the change in energy is more rapid. Percent energy is encircled in a circle of radius 20 μm

A comparison of angular errors shows that tilt errors have the greatest effect temporally and spatially, and then tip error, and finally in-plane rotation. This fits with the temporal tolerance limits of tilt, tip, and in-plane rotation, which are 75 μrad, 250μrad, and 450 μrad respectively.

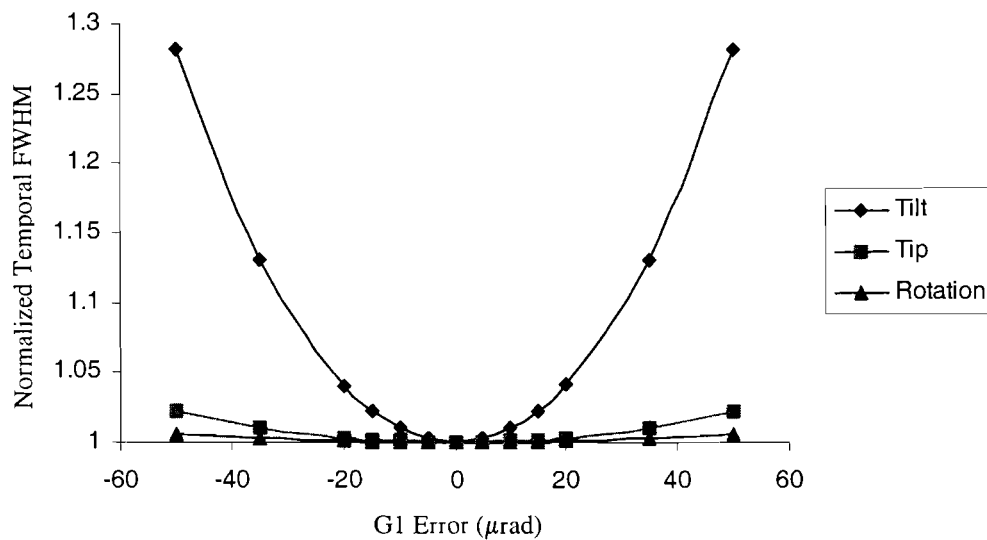A comparison of the angular errors encircled energy plots shows that spatially the effect caused by tilt is the greatest. For all angular errors, however, the 80% encircled energy requirement is met. Figure 4.1.1 shows the comparison of angular errors temporal pulse width and Figure 4.1.2 shows the comparison of angular errors encircled energy.

4.2 Temporal Broadening

Broadening of the temporal pulse is caused by a pulse front tilt introduced to the beam by the grating alignment error. This pulse front tilt can be calculated using the equation

$$\tan \gamma = \omega \frac{\delta\theta}{\delta\omega}$$

where γ is the angle of pulse front tilt and $\delta\theta/\delta\omega$ corresponds to the angular dispersion [3]. This pulse front tilt causes a shift in time of each spatial location in the beam. When these separate pulses are added together, the spatially integrated temporal pulse shows a broadening.
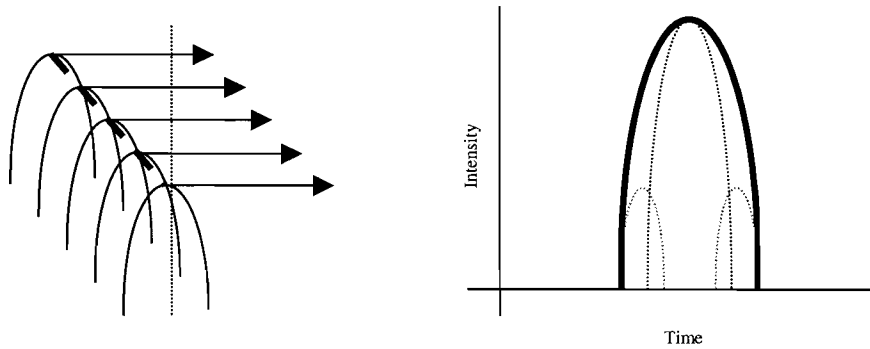
Figure 4.2.1 Temporally Integrated Pulse- When a pulse front tilt (shown on the left) is introduced spatial points are shifted in time. When the spatial points are integrated (shown on the right) the integrated pulse shows broadening.

4.3 Compensation
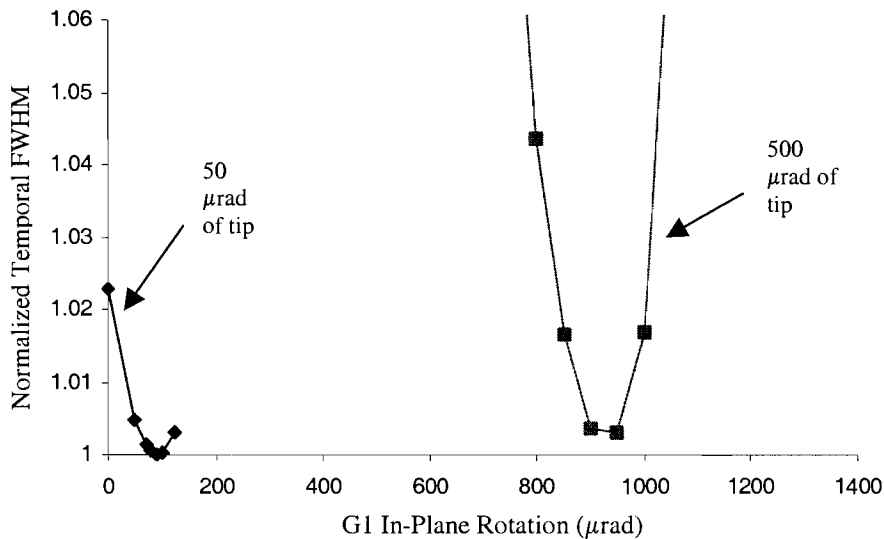
Figure 4.3.1 Compensation of 50 μrad and 500 μrad tip- Grating Tip can be compensated using in-plane rotations. Each curve represents a different amount of tip. Notice that the 50 μrad curve leaves the transform limit shown as 1.

Since the broadening of a pulse is caused by the shift in time of spatial locations

in-plane rotation can be used to compensate tip errors. This works only for small errors,

however, since large angular errors introduce a certain degree of distance mismatch.

Figure 4.3.1 shows the compensation of a small tip compared to a larger tip. Figure 4.3.2

shows an even larger tip.
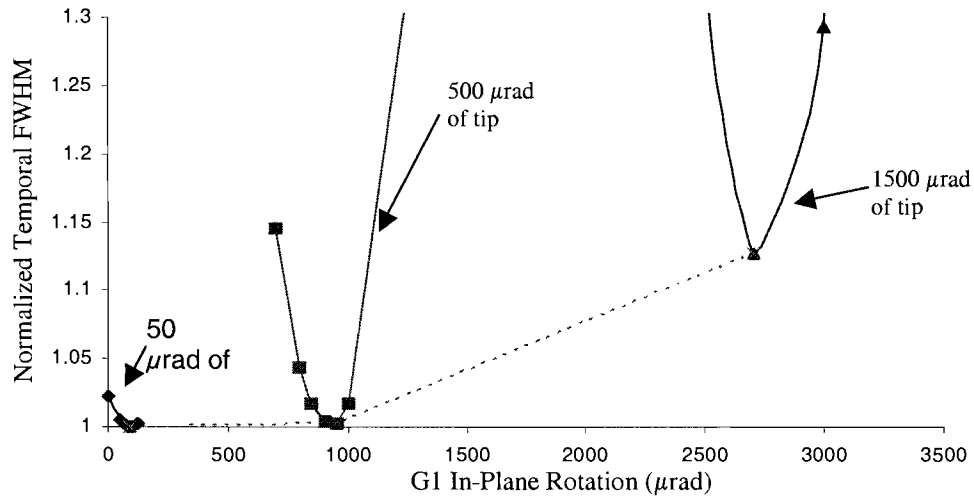
Figure 4.3.2 Compensation of 50 μrad, 500 μrad, and 1500 μrad tip- The larger the amount of tip the harder it is to compensate. Compared to a 50 μrad tip and 500 μrad tip a 1500 μrad is not broadened. The curve for the 1500 μrad tip floats above the transform limit of 1.

4.4 Angular Dispersion

A perfect compressor alignment will output spatial rays that are parallel to each

other. As error is introduced to the system, however, residual angular dispersion causes

the rays to not be parallel. Angular dispersion can be found by taking the change in angle

between wavelengths and dividing that by change in wavelength. When the wavelengths

are integrated into the far field, smearing occurs.

16

4.5 Encircled Energy

Careful inspection of the encircled energy diagrams for a circle of radius 10 μm

reveals an unexplained initial rise in encircled energy. A comparison of angular errors

encircled energy vs. radius curve shows a rippling affect. This can be attributed to the

modulations that occur in the far field, since the input pulse is not a Gaussian.

Introduction of an angular error smoothes the encircled energy diagram. Figure

4.5.1 shows a comparison of 100 μrad tilt of the first grating and a perfect grating

alignment encircled energy diagram.
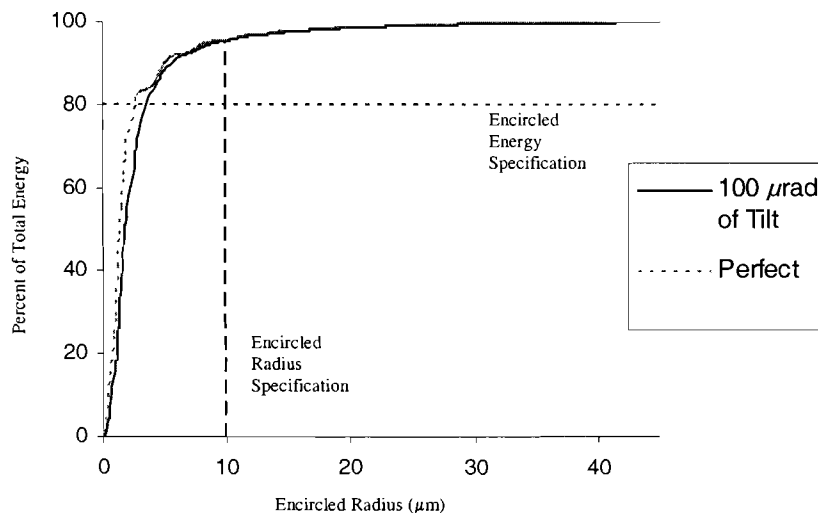
Figure 4.5.1 Comparison of Encircled Energy Diagrams- A comparison of the
encircled energy diagrams for a perfect alignment and a tilted g1 of 100 μrad, shows
how the curve smoothes as error is introduced.

The smoothing of the curve causes the diagram for errors to dip below the perfect

grating alignment. This, however, is limited to very small increments as a circle of radius

9.0 μm or 11.0 μm encircles less energy for errors (see Figure 4.5.2). Eventually,

17

however, the smoothing of the curve for larger errors causes the encircled energy to fall

below   the

perfect   case.
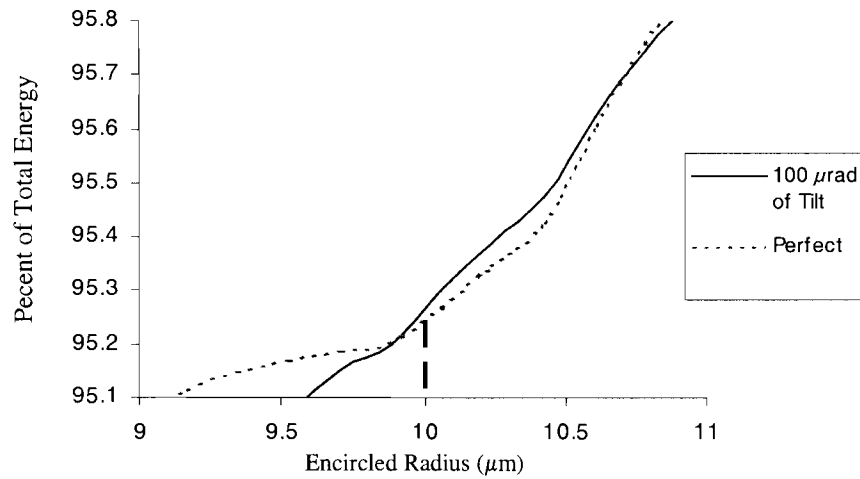
Figure 4.5.2 Comparison of Encircled Energy Diagrams- A closer look at the specified radius shows that the rippling effect causes the rise in encircled energy.

V. Conclusion

Misalignments in the grating compressor system cause broadening of the laser pulse. A 1 ps pulse width can be achieved by displacing the gratings 6 mm, or tilting the grating 75 μrad, or tipping the grating 250 μrad, or rotating the grating 450 μrad. Spatially smearing occurs. However, the requirement of 80% of the total energy to be contained within a circle of a radius of 1 μm is met for all errors that correspond to the 1 ps tolerance limit.

VI. Acknowledgement

I would like to thank Dr. Stephen Craxton for the opportunity to work at the University of Rochester Laboratory for Laser Energetics, as well as my advisor Mark Guardalben, and George Dahl and Joshua Keegan for their work on the program MANTARAY.

VI. References

[1] D. Strickland and G. Mourou, "Compression of Amplified Chirped Optical Pulses," Opt. Commun. 56, 219 (1985).

[2] E.B. Treacy, "Optical Pulse Compression With Diffraction Gratings," IEE J. of Quantum Electronics, vol. QE-5, pp 454-458, September 1969.

[3] K.Osvay, A. P. Kovács, Z. Heiner, G. Kurdi. J. Klebniczki, and M. Csatári, "Angular Dispersion and Temporal Change of Femtosecond Pulses From Misaligned Pulse Compressors," IEEE J. of Quantum Electronics, vol. 10, pp 213-220, September 2004.

VI. Acknowledgement

I would like to thank Dr. Stephen Craxton for the opportunity to work at the University of Rochester Laboratory for Laser Energetics, as well as my advisor Mark Guardalben, and George Dahl and Joshua Keegan for their work on the program MANTARAY.

VI. References

[1] D. Strickland and G. Mourou, "Compression of Amplified Chirped Optical Pulses," Opt. Commun. 56, 219 (1985).

[2] E.B. Treacy, "Optical Pulse Compression With Diffraction Gratings," IEE J. of Quantum Electronics, vol. QE-5, pp 454-458, September 1969.

[3] K.Osvay, A. P. Kovács, Z. Heiner, G. Kurdi. J. Klebniczki, and M. Csatári, "Angular Dispersion and Temporal Change of Femtosecond Pulses From Misaligned Pulse Compressors," IEEE J. of Quantum Electronics, vol. 10, pp 213-220, September 2004.

Hexapod Motion Through Remote Computer Activation

Joseph Dudek

Hexapod Motion Through Remote Computer Activation

Joseph Dudek
Laboratory for Laser Energetics
University of Rochester

August 2, 2004

Abstract

This paper describes the creation of software for a motorized platform known as a 'hexapod'. This mechanism will be used to move a parabolic mirror in all 6 degrees of freedom (3 translational, 3 rotational) to focus an ultra-fast laser beam for experiments. The mathematics behind multiple coordinate systems, matrix mathematics, and vector calculations were used to develop algorithms for the movement of the hexapod. As a part of my implementation, I used both the C programming language and the Java™ programming language created by Sun Microsystems.

Outline

Figures

1 Introduction

In order to adequately maneuver a platform using six degrees of freedom, a hexapod platform is an attractive option. This small, portable machinery consists of two circular plates and six longitudinally expandable and contractible arms. By properly calculating the necessary lengths of each of the six arms, any rotation or translation of the upper platform (within accepted limits) may be accomplished. The ultimate goal of this algorithmic project is to manipulate a hexapod platform using a driver interface and a computer program.

1.1 Hexapod Platform
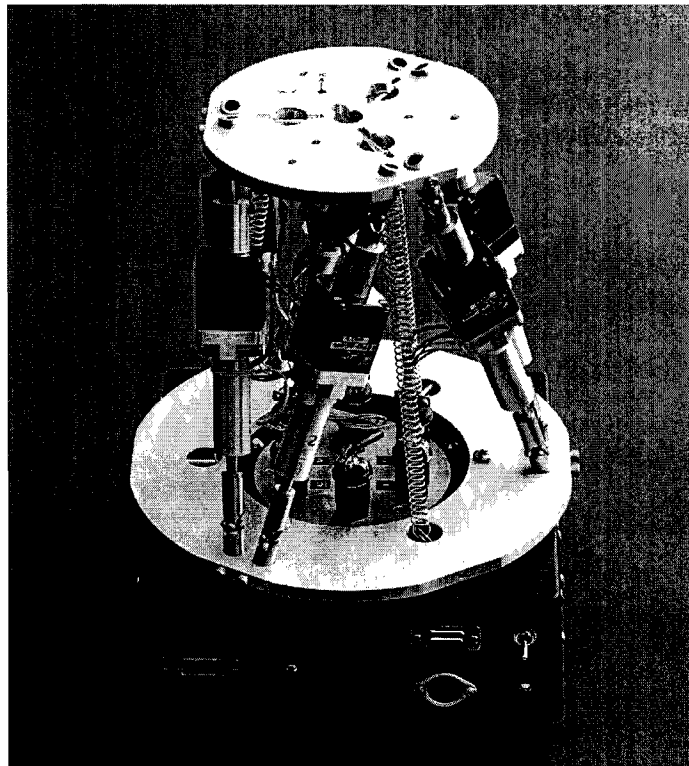
Figure 1.1
The Hexapod Platform

The hexapod itself (as seen in Fig. 1.1) is a platform structure comprised of two circular discs connected by six motorized actuators. The six actuators on the hexapod form consecutive triangles around the outside of the structure contacting each plate in three locations. As three points successfully define a plane, this method maintains stability with the geometric triangle and also needs only linear actuator motion to achieve motion in all 6 degrees of freedom of the upper disc.
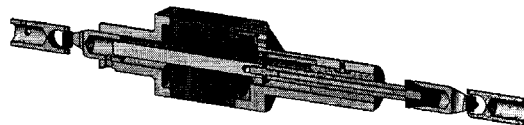
Figure 1.2
The Actuator

The motorized actuators are what provide the hexapod with extreme accuracy and flexibility. The hexapod's six actuators act as both support for the upper platform and a means for movement. Motion is achieved through the use of universal joints located at either end of the actuator. These joints allow for freedom of movement to extremely wide angles. Since the hexapod's functionality depends heavily on its flexibility, these joints are vital to the mechanism. Each actuator also contains a stepper motor that had one step equal to 3.580 μm and is activated via a control module located at the bottom of the hexapod.(Figure 1.1) The stepper motor mobilizes a shaft that leads out to one of the universal joints on the actuator.(Figure 1.2)

1.2 Hexapod Driver Unit and Protocol

Provided for this project was a custom driver unit created by Jean DePatie. This driver utilized a serial port to receive commands for the hexapod's actuators. This function utilized a rudimentary string function where the first two characters defined the actuator, the next character defined the course of action, and the final accepted character or series of characters represented a value for the function.

Function	Definition	Execution
H	Set Home Position	Creates a zero position some distance above the home switch (steps)
V	Set Velocity	Sets the velocity of the stepper motors (steps/second)
P	Move to Position...	Moves the stepper motors to a numerical position (steps)
S	Report Status	Returns a string with the current position of the motor requested (steps)

2 Mathematics

The mathematics used for this project achieved a relatively complex solution by combining more basic equations and functions. Given the goal of accomplishing six degrees of freedom and the known constraint of longitudinal motion, the most effective method of computation seemed to be using two coordinate systems. With one system at the base and another atop the plate, vectors and locations could be simply translated between the two, thus separating the rotation and translation aspect from the calculation of new arm lengths.

2.1 Managing Coordinate Systems
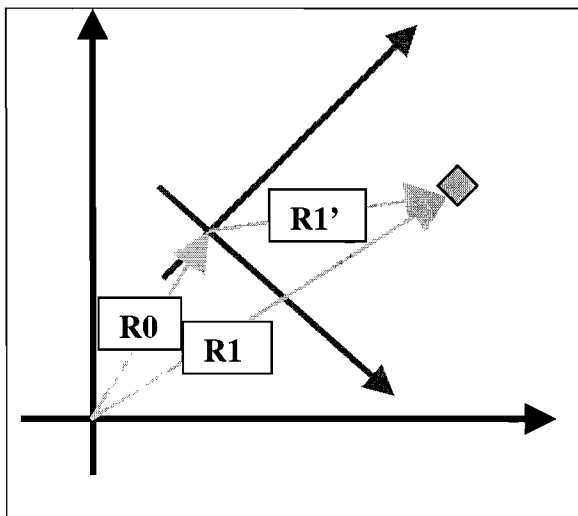
Figure 2.1
Vector Addition
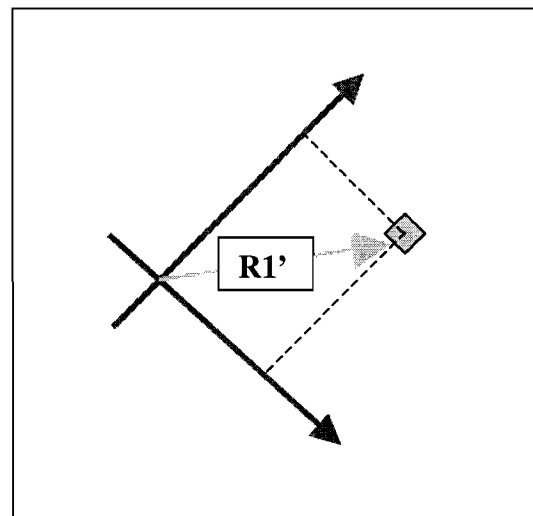
Figure 2.2
Projections Establishing Coordinates

In the case of this particular project, vectors were used as a means of translating coordinates between different coordinate systems. The hexapod must be considered to have two different sets of coordinate systems that must each be accounted for at all times. The lower, stationary platform (base) must keep track of the locations of all the parts of the hexapod as it is the only stationary point of reference. Also, the upper, mobile platform (plate) must retain its own coordinate system. Instead of constantly updating both sets of information, vector math is utilized to translate base information into the plate coordinate system, the movement is executed in the plate system, and the new coordinates are translated back into the base system. This way only the base coordinates must be retained from one movement to the next.

Vector mathematics tells us that the three vectors in Figure 2.1 are related by the equation R1-R0=R1'. This means that if a vector to the origin of the plate coordinate system(vector R0) and a vector to the point of interest were known(vector R1), the vector to the point of interest in the plate system would be a simple calculation away(vector R1'). Additionally, the magnitudes of the projections of the translated vector R1' onto the axis vectors of the plate system will create coordinates of the vector in the global system. While the demonstration above handles only two dimensional examples, this concept translates to three dimensions quite easily.
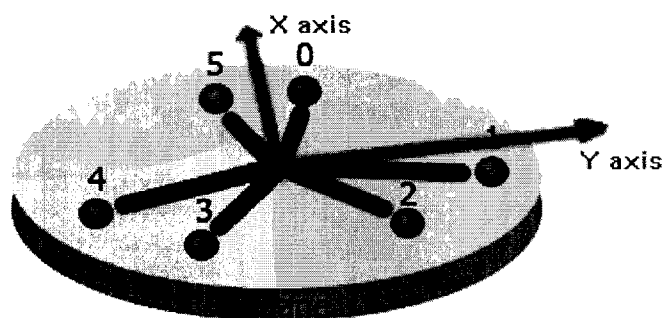
Figure 2.3
Hexapod Coordinate System Unit Vectors

Establishing the axes for translation was relatively straightforward. First, a set of axes was established at the center of the six upper universal joints. As seen in Figure 2.3, if the vectors from the center of the plane to Joint 0 and Joint 5 are added together, an x-axis is created. Additionally, if the vector to Joint 4 is subtracted from the vector to Joint 1, a y-axis is created. The cross-product of the x- and y-axes creates an orthogonal vector which becomes the z-axis. The z-axis is then elevated to compensate for the distance between the universal joints and the plate itself.

2.2 Utilizing Coordinate Translations

With coordinate system translations proven as an executable function, the ideas mentioned above can be put to use. All of the universal joints on the hexapod were tracked in the global coordinate system, here the base, and this data was stored. Whenever a user requests a rotation of the upper plate, the upper joints would be translated into the plate's perspective, thus allowing a rotation using basic rotation matrices. With the new joint locations calculated, they would be translated back into the global system and the new leg lengths would be calculated. At that point, it was just a matter of executing the movements on the hexapod.

3 Computer Programming

The primary goal of this project was not to verify a method of mobilizing the hexapod, but rather to create a fully functional computer program. Because of this, the architecture of this program must be discussed. This section will cover the programming language, target operating system, program design, and implementation.

3.1 The C Programming Language

The C Programming Language was developed in the early 1970's by Ken Thompson and Dennis Ritchie for their UNIX operating system. C has since spread to many other operating systems and builds and has become one of the most popular languages in the world. C is best known for its efficiency, one of the major reasons it was chosen for this project. C also runs several files as though they were one long program file, making long code seem simple as it is condensed into one executable file.

3.2 Code Design and Implementation

Figure 3.1
Overview of Hexapod Computer Model

In order to fulfill the requirements for the programming portion of the project, several programs were designed to work in tandem, each performing a unique function and passing its results to the next program in line. The four components used in this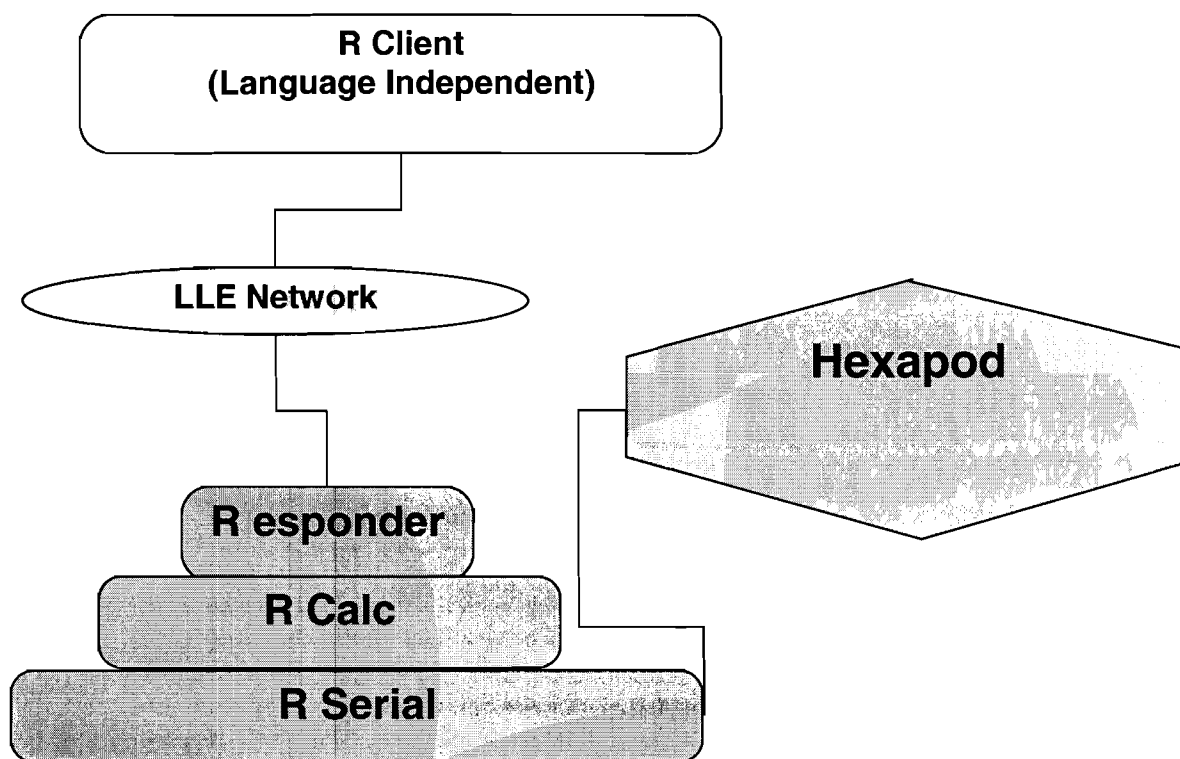 particular design are RClient, a remote access program, Responder, a receiver protocol, RCalc, the calculator and translator, and RSerial, the utility that sends messages through the serial port to the driver unit. Each of these programs are connected through different types of sockets established upon execution and must be initialized from the bottom up.

3.2.1   RSerial

This program was designed specifically for communication over a serial port. It first converts leg lengths given by RCalc into 'steps'. Steps are 3.850 micrometer lengths which the stepper motor recognizes as a unit of measurement. Once the distances have been converted, this program creates messages that the driver unit can understand. With that step complete, the strings are then transmitted across the serial port and a confirmation message is received following the message. The goal for the program series is to be able to interpret the messages received from the driver hardware and react accordingly, but that function has not yet been added to the software.

3.2.2   RCalc

The first segment of code that was created was the basic functionality required to use vector mathematics, rotational matrices, and other utility functions. Fortunately, the coding for these segments became rudimentary, as the coding was simply copying pre-defined equations into usable methods. Each matrix equation designed to interact with a vector or another matrix was designed only to handle vectors with three data segments and 3x3 matrices. While this restricts the reusability of the code, it was necessary to improve efficiency in this project.

The protocol for establishing several coordinate systems and translating between them was then established. Using sample universal joint coordinates, an intermediate coordinate system is set up during translation. That coordinate system exists as an average of the locations of all of the upper universal joints establishing the angle necessary to compensate for any previous platform adjustment. The axes are then created according to a preset system of equations (see Section 2.2). By increasing the position of the origin a constant number of millimeters up the z-axis, the coordinate system has now been transformed into the system at the center of the plate. The correct translation or rotation is then executed and the coordinate system is then translated back to the global position.

In accomplishing the above changes in coordinate systems, the methodology used is not to identify the coordinate system totally, but rather to edit the vectors to the universal joints so that they represent vectors from a different perspective. For example, the translation from the center of the upper universal joints to the center of the plate is, in reality, a subtraction from the z values of each of the vectors. In addition, translating back to the global position is merely adding a vector from the global origin to the plate origin to each of the universal joints' positions and using the stored axis vectors for the plate system to rotate back to vertical.

With the translation complete, taking a simple measurement of each of the arms, subtracting the length of a collapsed arm, and dividing by the distance in one motor step (3.580 µm) will establish a position number for that arm. This position is then forwarded to the serial port through a program entitled RSerial.

3.2.3   Responder

Responder was simply an intermediate between RClient and RCalc. It had to establish two different types of sockets, one to the network to receive messages from RClient and one to RCalc to transmit messages. No processing occurred in this module, but the information received was translated into a message that was then just passed down through the line. This program is run from a small LINUX computer situated near the hexapod platform. This LINUX computer has an Ethernet port allowing remote access from anywhere on the LLE network.

3.2.4   RClient

One of the most important facets of the coding for this project was remote access. The computer running this platform does not have input functionality besides a couple of Ethernet ports and three serial ports. Using a keyboard or mouse, therefore, is impossible. The computer will also exist inside the laser bay meaning that anything that can keep personnel away from the unit will be helpful. The code, therefore, is designed to execute upon a command from an outside program. RClient acts as a user client and allows a user to give the platform commands from any distance away so long as the user has access to the local network. This program does nothing more than forward commands over the network to Responder.

4 Conclusion

Manipulation of a six-legged platform requires both vector and matrix mathematics working through a computer interface. This interface has been created as a part of my project at the LLE and is ready for implementation in the Omega EP laser system.

In order to use the program to its fullest functionality, a much more accurate method of measuring the locations of the universal joints on the mechanism with respect to the center of the base must be found. Without this measurement, any calculations made by the program will be based on estimated numbers creating a significant amount of error. In addition, a more user-friendly client interface must be created to allow use from the control room by average personnel. Lastly, the positions of the arms must be logged to external files allowing the program to cope with a loss of power or a fatal error.

5 Acknowledgements

Appendix A: Vector and Matrix Operations

Function	Definition
$\vec{\mu} + \vec{v} = \langle (x_\mu + x_v), (y_\mu + y_v), (z_\mu + z_v) \rangle$	Sum of **u** and **v**
$\vec{\mu} \cdot \vec{v} = (x_\mu \cdot x_v) + (y_\mu \cdot y_v) + (z_\mu \cdot z_v)$	Dot Product of **u** and **v**
$\lvert \vec{\mu} \rvert = \sqrt{[(x_\mu)^2 + (y_\mu)^2 + (z_\mu)^2]}$	Magnitude of **u**
$k \cdot \vec{\mu} = \langle k \cdot x_\mu, k \cdot y_\mu, k \cdot z_\mu \rangle$	Scaling **u** k times
$proj_v\, \vec{\mu} = \dfrac{(\vec{\mu} \cdot \vec{v})}{\lvert \vec{v} \rvert^2}\, \vec{v}$	Projection of **u** onto **v**
$A \times B = \det \begin{bmatrix} \hat{i} & \hat{j} & \hat{k} \\ A_x & A_y & A_z \\ B_x & B_y & B_z \end{bmatrix}$	Cross-Product of **A** and **B**

Experimental Investigation of Far Fields on OMEGA

Laurie Graham

Experimental Investigation of Far Fields on Omega

Laurie T. Graham
Bloomfield High School
Summer High School Student Program 2004
Laboratory for Laser Energetics, University of Rochester
LLE Advisor: Sean P. Regan

Abstract

On OMEGA distributed phase plates (DPP's) are placed before the focusing lens
and produce far-field spots with highly reproducible spatial intensity envelopes and
speckle distributions. A variety of DPP's are available on OMEGA to achieve the desired
on-target laser irradiation conditions. Far field intensity distributions of a single beam on
OMEGA were measured with the ultraviolet equivalent target plane diagnostic (UVETP).
The measured profiles were fitted with a super-Gaussian function: $I(r)=I_o exp[-(r/\delta)^n]$,
where $I(r)$ is intensity, I_o is peak intensity, r is the radius, δ is the 1/e half width, and n is
the super-Gaussian order. Image analysis software was developed to fit the azimuthally
averaged measured profiles and the 2-D profiles. A survey of the far fields that can be
achieved on OMEGA will be presented. The effects of 2-D smoothing by spectral
dispersion (2-D SSD) and polarization smoothing on the far field envelope intensity will
also be reported.

Introduction

In direct-drive inertial confinement fusion, nonuniformities in target irradiation
seed the Rayleigh-Taylor hydrodynamic instability, which degrades target performance.
A combination of beam smoothing techniques is therefore implemented on OMEGA in
order to reduce these nonuniformities. These techniques include 2-D smoothing by

1

spectral dispersion (2-D SSD), polarization smoothing (PS), and distributed phase plates (DPP's) [1, 2]. This report focuses mainly on the measured single beam far field intensity profiles produced with a DPP and a constant intensity laser pulse, such as the 1 ns square laser pulse shown in Fig. 1a. Far field images captured with the ultraviolet equivalent target plane diagnostic were characterized. With one exception all of the measurements were taken with 1-THz, 2-D SSD and PS. The measured profiles were fitted with a super-Gaussian function: $I(r)=I_o\exp[-(r/\delta)^n]$, where $I(r)$ is intensity, I_o is peak intensity, r is the radius, δ is the 1/e half width, and n is the super-Gaussian order. Image analysis software was developed to fit the azimuthally averaged measured profiles and the 2-D profiles. A survey of the far fields that can be achieved on OMEGA is presented.

The following sections discuss (1) the DPP's used on OMEGA to control the far field intensity distribution, (2) the ultraviolet equivalent target plane (UVETP) diagnostic that was used to measure the far field intensity distributions, (3) the fitting procedures used to characterize the envelope of the far field intensity distributions with a super-Gaussian function, and (4) the effects of 2-D SSD and PS on the far field intensity envelope.

DPP's on OMEGA

On OMEGA DPP's are placed in the near field before the OMEGA focusing lens. DPP's are used to control the intensity distribution in the far field. Fig. 1b shows the arrangement of the DPP and the OMEGA focusing lens used to produce the far field. The OMEGA lens has a clear aperture of 30 cm and a 180 cm focal length. A wide variety of DPP's are available for use in target physics experiments on OMEGA. The

single beam intensity is adjusted by changing the size of the far field laser spot. Profiles

can range from a very high intensity, tight focus spot, used in laser plasma interaction

experiments, to a broad spot with a comparatively low, but relatively constant intensity,

used for planar hydrodynamic experiments. Far field intensity profiles used on 60-beam

direct-drive implosions fall in between these two extremes. Examples of a tight focus far

field and a far field with a large area of constant intensity are displayed with the same

spatial scale in Fig. 1c and Fig. 1d, respectively. Fig. 2 shows the range of profiles that

can be obtained on OMEGA with a DPP. The calculated super-Gaussian 'n' range for

profiles under these conditions is from 2 to 5, with 'δ' ranging from 80 μm to 450 μm.

The highest single beam intensity available on OMEGA with a DPP assuming a 500 J, 1

ns square pulse is ~ 2×10^{15} Watts/cm². Direct drive inertial confinement fusion requires

minimal beam-to-beam variations of the far field intensity profiles. Fig. 2b shows the

measured azimuthally averaged far field intensity profiles for 9 different SG4 DPP's.

Nearly identical far fields are produced on OMEGA with SG4 DPP's for 60-beam direct-

drive implosions, providing nearly uniform irradiation of a spherical target.

Elliptical DPP's can produce round far field spots for non-normal incidence beams

on planar targets. The UVETP diagnostic can only measure a far field spot at normal

incidence, so the far field images measured with an elliptical DPP installed are elliptical

in shape. However on target, at non-normal incidence, the spot is round. Image analysis

software has been developed to project the beam as it is on-target. Fig. 3a shows the

image measured with the UVETP diagnostic, while Fig. 3b shows the projected image for

a 48˚ angle of incidence.

UVETP Diagnostic

Fig. 4 shows a schematic of the UVETP diagnostic used to capture the far field images. As the beam travels toward the target a full-aperture optical wedge sends 4% of the laser light through an OMEGA lens. A DPP is placed in the near field, thus duplicating the on-target conditions. The beam is then brought to focus in a vacuum vessel, down collimated, and brought to focus before passing through a final lens and a series of filters producing a magnified image on the CCD camera. The CCD camera is a 1024 x 1024 array of pixels. Each pixel has an area of 24μm x 24μm.

Super-Gaussian Fitting

The azimuthal average of the measured intensity profile is modeled with a super-Gaussian function. The azimuthal average is calculated by dividing the beam into concentric rings that are centered on the beam. Starting in the center of a measured far field image and moving outward in concentric rings, the average intensity of each of these rings is calculated. The super-Gaussian function is: $I(r)=I_o \exp[-(r/\delta)^n]$ where I_o is peak intensity, r is radius, δ is the $1/e$ half width, and n is super-Gaussian order. Software that has been developed performs a least squares fit to generate a model super-Gaussian curve. Fig. 5a shows an example of an azimuthal average fit for a SG3 DPP with 1THz SSD and PS. The model is fitted to the azimuthal average down to 10% of the peak intensity in Fig. 5a. The program allows the user to select this percentage (10%, 5%, or 1%). The model accurately fits the profile down to approximately 5% of the peak intensity at which point the two curves begin to diverge. Similarly a 2-D fit can also be performed to model the far field with a super-Gaussian function. Fig. 5b shows

4

contour intensity rings of the far field and the model, representing from the inside to the outside, 90%, 50%, 10%, 5%, and 1% of peak intensity. Once again the model is fitted to the far field down to 10% of peak intensity, with little variation between the rings until you get out to the 5% and 1% rings. Below the 10% of peak intensity the super-Gaussian model does not fit the intensity envelope very well.

2-D SSD and PS

2-D smoothing by spectral dispersion (SSD) and polarization smoothing (PS) are implemented to reduce laser-beam nonuniformities. 2-D SSD reduces nonuniformities as a function of time while PS produces an instantaneous result. Fig. 6 shows the azimuthal average profile for SG4 DPP(249) without any smoothing and the profile with 1THz, 2-D SSD and PS. Without any smoothing, the n(1-D) value is 5.6, the n(2-D) is 5.08, δ(1-D) is 344μm, δ(2-D) is 345μm. With 1THz, 2-D SSD and PS, the n(1-D) value is 4.40, n(2-D) is 4.12, δ(1-D) is 353μm, δ(2-D) is 352μm. 2-D SSD and PS broaden the laser spot. Broadening the laser spot has the effect of decreasing n and increasing δ.

Conclusion

Far field intensity distributions measured on OMEGA with DPP's were characterized. DPP's used on OMEGA produce highly reproducible spatial intensity envelopes and speckle distribution. The ultraviolet equivalent target plane diagnostic (UVETP) was used to capture far field images of a single beam on OMEGA. A variety of DPP's are available for experimental use on OMEGA. Image analysis software was developed to fit measured profiles with a super-Gaussian function, $I(r)=I_o\exp[-(r/\delta)^n]$.

5

The single beam intensity profiles measured in this investigation had n range from 2 to 5 and δ range from 80μm to 450μm. The highest single beam intensity produced on OMEGA with a DPP assuming a 500 J, 1 ns square laser pulse was ~2 x 10^{15} Watts/cm^2. The beam smoothing techniques of 2-D smoothing by spectral dispersion and polarization smoothing have the effect of broadening the laser spot in the far field.

REFERENCES

[1] S.P. Regan et al., "Experimental Investigation of Smoothing by Spectral Dispersion", J. Opt. Soc. Am. B **17**, 1483–1489 (2000).

[2] S.P. Regan et al., "Performance of 1-THz-Bandwidth, 2-D Smoothing by Spectral Dispersion and Polarization Smoothing of High-Power, Solid-State Laser Beams", accepted for publication in J. Opt. Soc. Am. B (2004).

(a)

1 ns square pulse

(b)

DPP   OMEGA Focusing Lens

~30cm

X
Z
Y

Near Field

Far Field

180 cm

(c)

: 1THz SSD, PS, 100 micron DPP sn086,

1mm

(d)

: 1THz SSD, PS, DPP SG8, sn117, Z=0

1mm
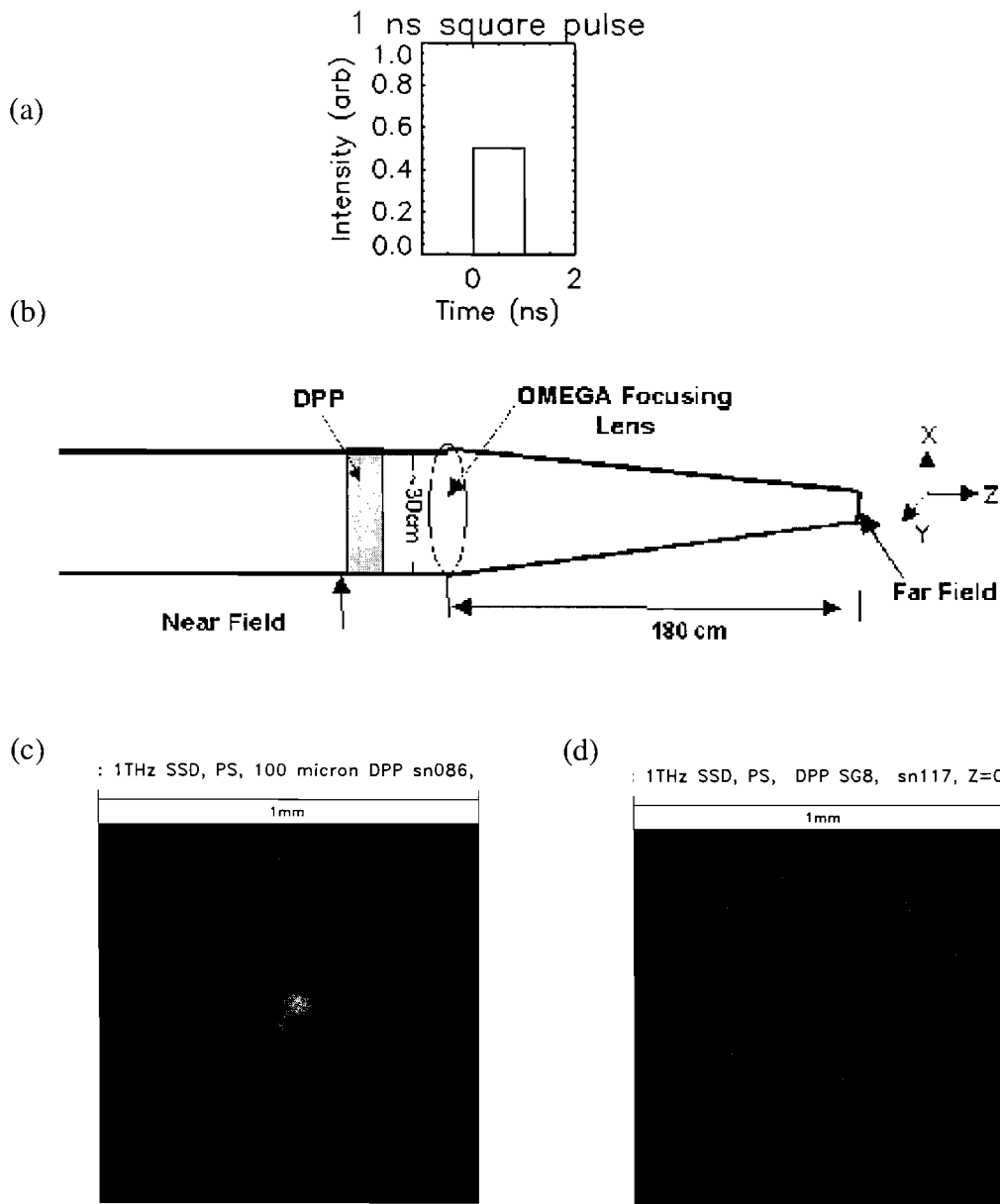
Fig. 1. (a) An intensity versus time graph for a 1 ns square laser pulse. (b) The arrangement of the DPP and the OMEGA focusing lens used to produce the far field intensity distribution. (c) Measured far field images produced with a tight focus DPP in (c) and with an SG8 DPP in (d). Changing the spot size of the far field varies the intensity on target.

7

(a)
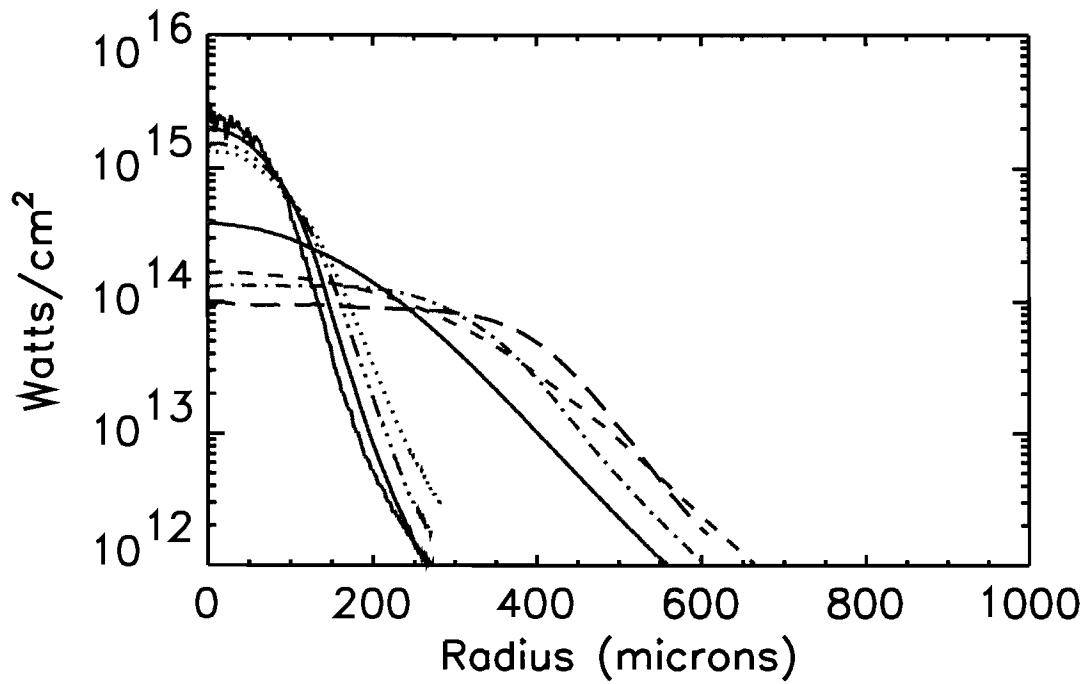
(b)
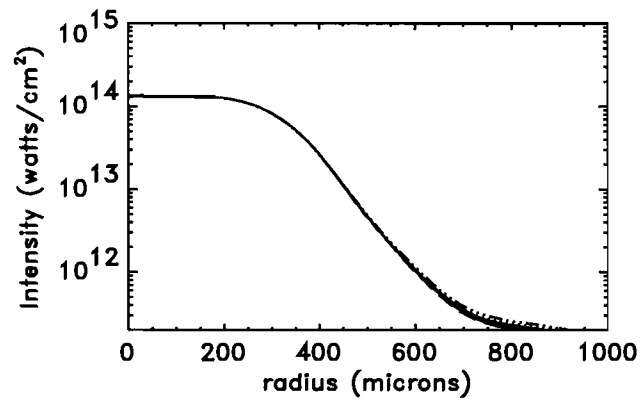
Fig. 2. The azimuthally averaged single beam intensity profiles measured on OMEGA

with the variety of available DPP's. Intensity calculations assume irradiation with a 500

J, 1 ns square laser pulse. (b) The measured azimuthal averages for 9 nearly identical

SG4 DPP's.

8

(a)
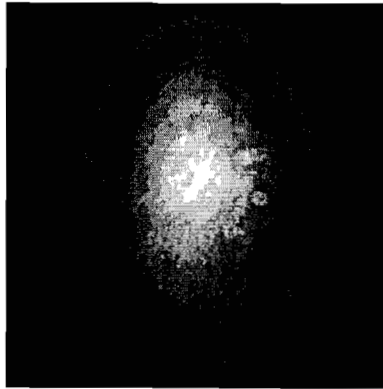
(b)
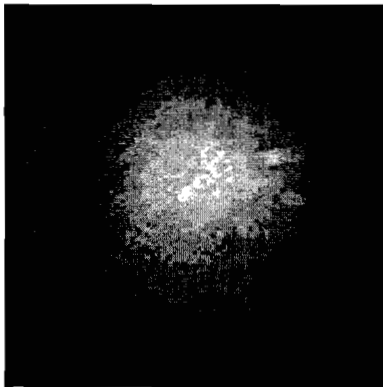
Fig. 3. (a) The measured far field spot produced with an elliptical DPP and measured at normal incidence. (b) The projected far field spot on target with a 48 degree angle of incidence.
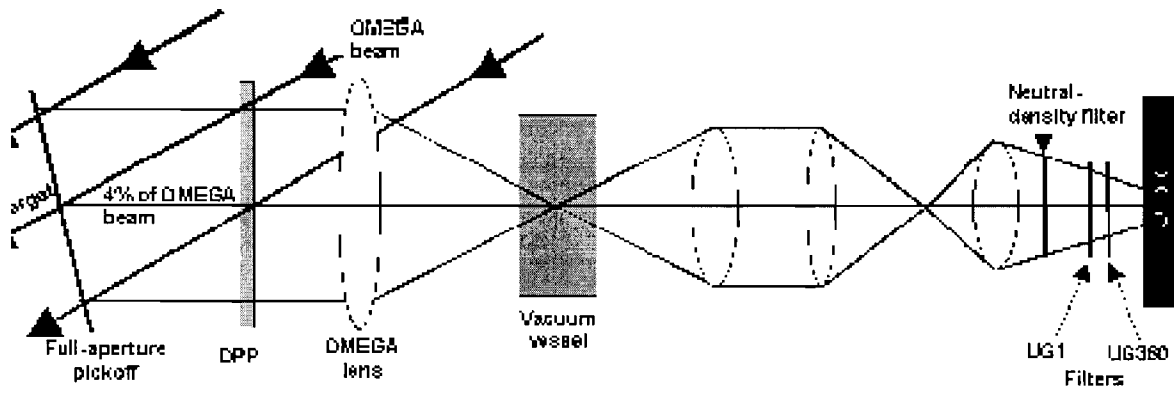
Fig. 4. A schematic of the OMEGA ultraviolet equivalent target plane (UVETP)

diagnostic. An uncoated wedge positioned in one of the 60 OMEGA beams directs 4%

of the laser light to a DPP and an OMEGA lens. A magnified far field image is recorded

on a CCD camera.

(a)

(b)
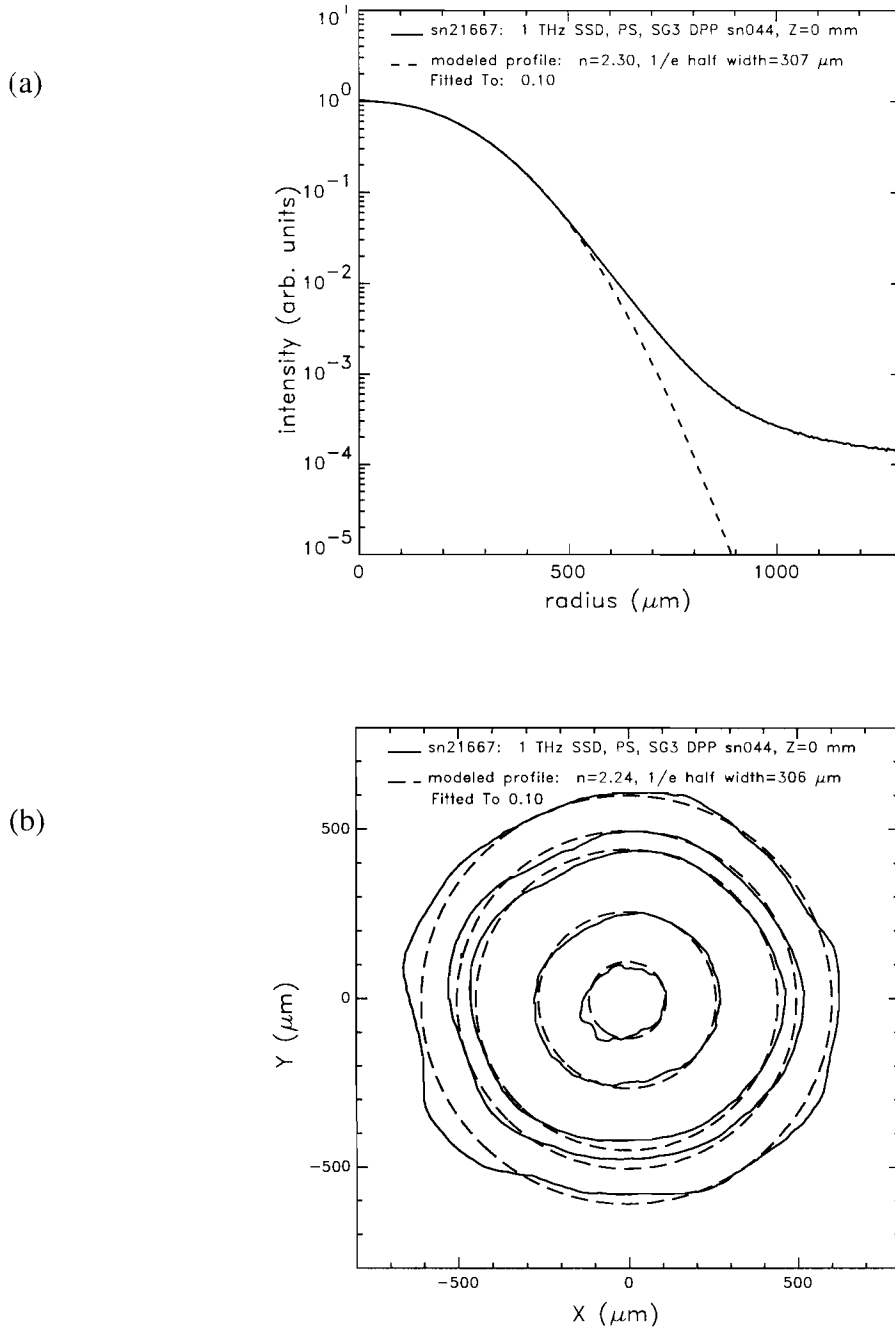
Fig. 5. (a) An example of a 1-D fit for sn21667, a SG3 DPP(044), with 1THz SSD and

PS. The calculated n value is 2.30, δ is 307μm. (b) An example of a 2-D fit also for

sn21667. The fitted n value is 2.24 and δ is 306μm.

11
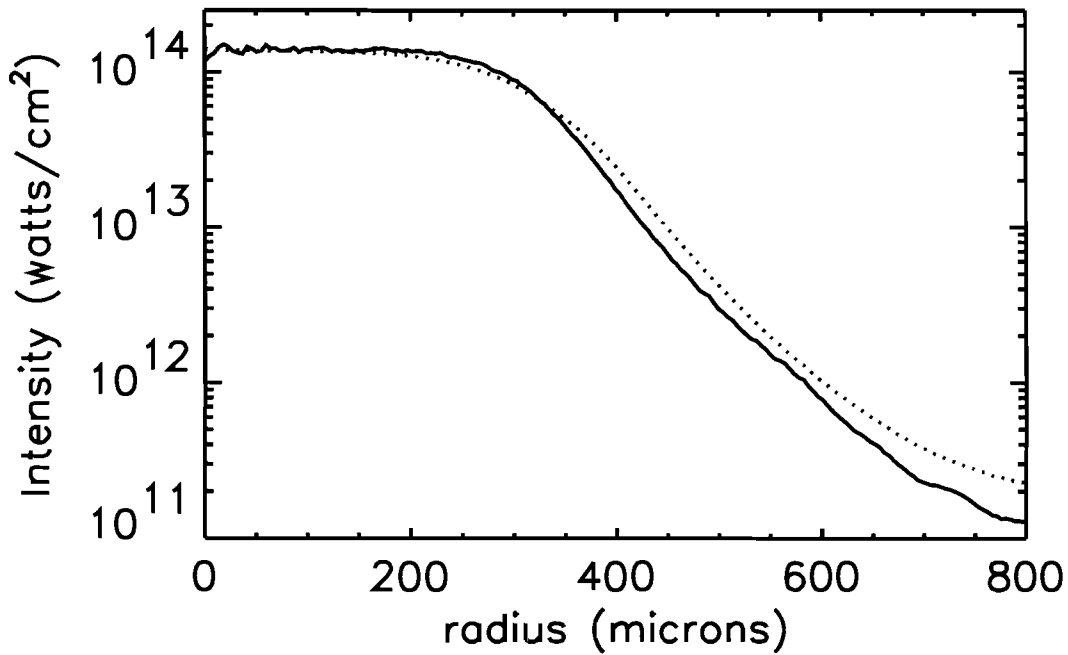
Fig. 6. The measured azimuthally averaged intensity profiles for SG4 DPP(249) on two

different shots. The dark solid line is a shot without any smoothing, the n(1-D) value is

5.6, the n(2-D) is 5.08, δ(1-D) is 344μm, δ(2-D) is 345μm. The light dashed shows a shot

with 1THz SSD and PS(in), the n(1-D) value is 4.40, n(2-D) is 4.12, δ(1-D) is 353μm,

δ(2-D) is 352μm.

Mechanical Properties of Spider Silk at Cryogenic Temperatures

Jivan Kurinec

Mechanical Properties of Spider Silk at Cryogenic Temperatures

By

Jivan Kurinec
Rush-Henrietta Senior High School
Henrietta, New York

Supervised by

Mr. Mark Bonino
Dr. David R. Harding

Table of Contents

Mechanical Properties of Spider Silk at Cryogenic Temperatures

Jivan Kurinec
Rush-Henrietta High School
Laboratory for Laser Energetics
University of Rochester, Rochester, New York

ABSTRACT

The work presented in this study was carried out as part of the High School Research Program at the Laboratory for Laser Energetics (LLE), University of Rochester during the summer of 2004. In this study, mechanical properties of dragline spider silk fiber were measured at temperatures of 293K and 158K for target mount applications in Inertial Confinement Fusion (ICF). This interest in dragline spider silk is due to its impressive mechanical properties that combine both a high tensile strength and a high elasticity. A Thermal Mechanical Analyzer system was used to apply force with high precision ($\sim$ 0.1 mN) and measure extremely small displacements ($\sim$0.1 μm). Important mechanical properties - Young's Modulus (stiffness), ultimate tensile strength (UTS) and ultimate tensile strain were determined. The results show that there is little variance in the ultimate tensile strength (UTS) and ultimate strain from room temperature to 158K, whereas the stiffness of the silk increased by a factor of two. These observations demonstrate that the spider silk maintains its desirable elastic properties at cryogenic temperatures for ICF target mount application.

I. INTRODUCTION

1.1 Laboratory for Laser Energetics (LLE)

The Laboratory for Laser Energetics (LLE) at University of Rochester was established in 1970 to investigate the interaction of high power lasers with matter. LLE is a national

---

resource for conducting implosion experiments in support of the National Inertial Confinement Fusion (ICF) program [1]. Available at the LLE for National Laser User Facility (NLUF) researchers is the OMEGA laser, a 30-kJ UV 60-beam laser system (at 35 nm) suitable for direct-drive ICF implosions.

1.2 The OMEGA System

OMEGA (see Fig.1) stands 10 meters tall and is approximately 100 meters in length [2]. This system delivers pulses of laser energy to targets in order to measure the resulting nuclear and fluid dynamic events. OMEGA's 60 laser beams focus up to 40,000 joules of energy onto a target that measures less than 1 millimeter in diameter in approximately one billionth of a second [2]. At LLE scientists continue to research what will one day become a vast source of power using the ocean's abounding storehouse of potential energy.

(a)   (b)
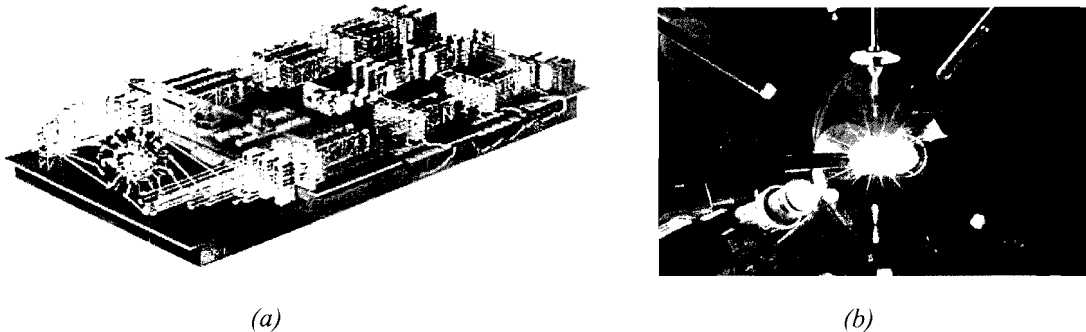
Figure 1: (a) 3-D Schematic view of the OMEGA system at LLE; (b) Illustration of the target system

1.3 The Fusion Reaction

Fusion is the joining together of small, light nuclei to form a larger, more massive nucleus. Since the incredibly powerful nuclear force is involved (as opposed to the electromagnetic force involved in chemical reactions) huge amounts of energy are released.

The final products in a fusion reaction weigh 0.7% less than the initial ingredients, thus 0.7% mc^2 is converted into energy: *One gram of fuel yields 175,000 kW-hours of energy* [3].

Fusion is the source of energy that powers the stars. In the center of a star, temperatures are so high and densities are so great that hydrogen atoms fuse together and release energy. Technologies such as laser-driven inertial confinement fusion attempt to recreate and harness the same reaction on earth. The technology would provide a clean, virtually limitless source of energy [4]. The fuel for fusion is provided by two isotopes of hydrogen: deuterium and tritium. Deuterium is widely available from seawater and is easily extracted. Tritium, on the other hand, is radioactive, with a half-life of 12.3 years; therefore tritium does not last long enough to be acquired in significant amounts naturally. Tritium is produced from lithium using the reaction:

$$^{6}\text{Li} + \text{n} \rightarrow {}^{4}\text{He} + \text{T}$$

The lithium absorbs the neutron and generates a tritium while releasing a bit more energy in the process. The D-T fusion reaction (see Fig. 2) is given as

$$\text{D} + \text{T} = {}^{4}\text{He} + \text{n}$$
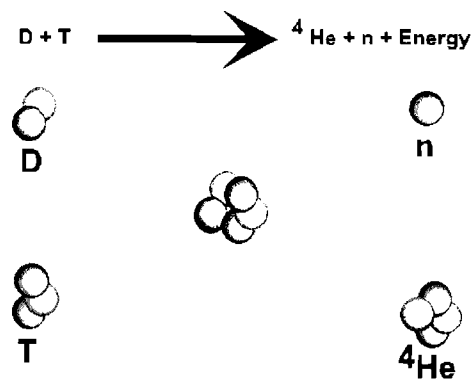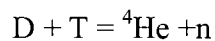
Figure 2:   Illustration of the D-T fusion reaction.

The goal of fusion is to ignite the fuel so that atoms keep combining, releasing large amounts of energy -- many times more energy than the laser or source expended to start the reaction. A combination of high temperatures and densities is required to force positively charged nuclei together, but the resulting high pressure will tend to blow fusion plasma (hot ionized gas) apart. There are three ways of confinement – gravitational (occurring at astronomical scales); magnetic (employing very high magnetic fields) and inertial (using fuel inertia). The last is known as Inertial Confinement Fusion (ICF).

1.4 Inertial Confinement Fusion (ICF)

In the ICF method, a spherical capsule filled with fuel (deuterium and tritium) is bombarded with energy, compressing and heating a small region in the center of the fuel to allow the electrostatic repulsion of the nuclei to be overcome. The fusion reactions from this central "hot spot" deposit enough energy in the rest of the fuel that fusion occurs there too– this process is referred to as *ignition*. During the very short period of ignition (a fraction of a nanosecond) the fuel is pushed inward, so its own inertia acts to impede its disassembly; hence the term *inertial confinement fusion* [5,6].

To reach sufficient density to approach ignition conditions with reasonable laser power requires cryogenic targets with uniform fuel layer thickness and density, and a smooth inner surface finish. The major challenge for ICF target designers is to ignite a small mass of fusion fuel with a minimal amount of energy from a laser or accelerator, while maximizing the target gain--the ratio of driver energy input to fusion energy output.

It is critical that the target's mount be of a material of low atomic mass – so that the implosion is minimally affected. Not only should the mount be able to support the target, but

also it should be able to absorb target vibrations. The elastic properties of spider silk are advantageous for supporting the ICF target.

1.5 Spider Silk

Silk is generally regarded as the proteinacious filament secreted from glands present in some, but not all, invertebrates of the genera Arthropoda [7-9]. Silk production is a characteristic of all spiders and is also known among various mites, mantids, moths and beetles. Of all the silks investigated thus far, it appears that silk from the orb-weaving spiders possesses some of the most exceptional mechanical properties. The fibres of spider dragline silk possess a high tensile strength that is comparable to Kevlar and a high elasticity comparable to rubber.

The structure of spider silk can be pictured as a composite consisting of an amorphous low molecular weight matrix filled with nano-crystalline particles [10-11]. The mechanical properties of spider silk are determined by the genetic regulation of fibroin proteins and chemical and physical processing during spinning. Spider silk is completely biodegradable.

1.6 Application of Spider Silk in Inertial Confinement Fusion (ICF)

The mounting of a laser fusion target for ICF requires material of low atomic number to prevent X-ray emission that results from high-Z materials. In addition to a low mass, the material must possess favorable mechanical properties at cryogenic temperatures. The elastic properties of spider silk are highly suitable as the target mount. Silk mounts remain flexible and return to rest in a fraction of a second after a sharp impulse [12].

Targets at LLE are suspended by four strands of spider silk. Spider silk is an extremely strong and relatively flexible material by weight-basis. Its properties are similar to those of

Kevlar and steel – with a fiber diameter of ~1.7μm. Figure 3 shows a photograph of four spider silk strands holding a target.

(a) *(b)*
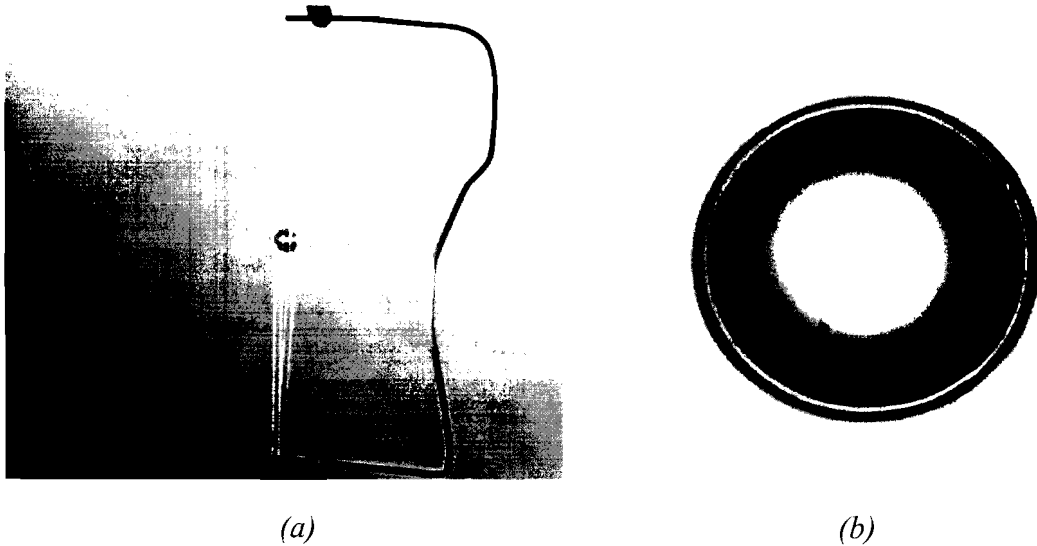
Figure 3: (a) Actual mount of 1mm diameter ICF target using four spider silk strands; (b) A D2 – gas filled target at cryogenic temperature (~18K)

1.7 Mechanical Properties

This section provides a brief description of various important mechanical properties of materials discussed in this study [13].

Stress

The engineering stress on a material is defined as the **force per unit area** as the material is stretched (Figure 4). The cross-sectional area will change if the material deforms as it is stretched, so the area used in the calculation is the original undeformed cross-sectional area A_0.

$$\sigma = \frac{Force}{A_0} \qquad (1-1)$$

The units of stress are the same as those of pressure. The standard international unit for stress (pressure) is N/m^2 and is known as Pascal, (Pa). In the polymer literature, stress often is expressed in terms of psi (pounds per square inch). (1 MPa = 145 psi)
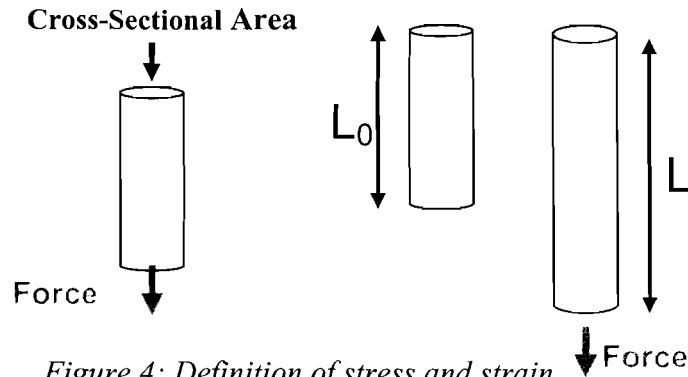
Figure 4: Definition of stress and strain

Strain

The strain is a measure of the change in length of the sample. The strain commonly is expressed as fractional change in length, $\Delta L/L_0$. Strain is a unitless number that characterizes the ductility of a material.

$$\varepsilon = \frac{L - L_0}{L_0} = \frac{\Delta L}{L_0} \qquad (1-2)$$

Stress-Strain Curves

A tensile **stress-strain curve** is a plot of stress on the y-axis vs. strain on the x-axis. In the plot shown in Figure 5, strain is expressed as elongation. Stress-strain curves are measured with an instrument designed for tensile testing. It can be observed that as the strain (length) of the material increases, a larger amount of stress (force) is required. As the elongation is increased, the sample eventually breaks.
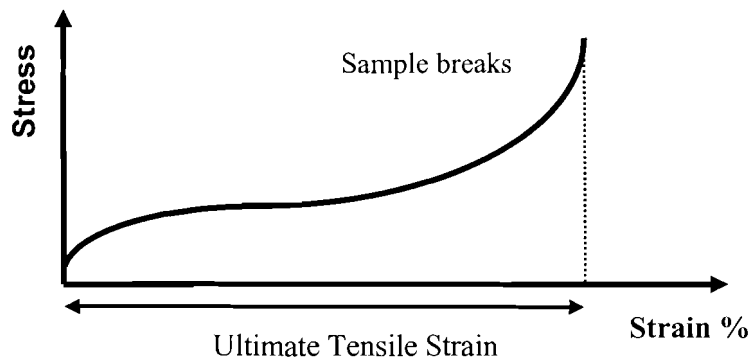
Figure 5: *A typical stress-strain characteristics of a material. The area under the curve is the toughness and the strain at the break point is defined as the ultimate tensile strain (UTS)*

Young's Modulus

The amount of force (F) applied is proportional to the amount of displacement (x) on an object, as defined in Hooke's law (with k being the spring constant).

$$F = -kx \qquad\qquad (1-3)$$

Young's modulus (E) is derived from Hooke's Law, and is defined as the ratio of stress to strain in this linear region. It also is called the modulus of elasticity or the tensile modulus. Should a sample be loaded and unloaded in this region, it will return to its original length and cross sectional area.

$$E = \frac{\sigma}{\varepsilon} \qquad\qquad (1-4)$$

Stress-strain curves often are not straight-line plots, indicating that the modulus is changing with the amount of strain. In this case the initial slope usually is used as the modulus, as is illustrated in Figure 6. Rigid materials, such as metals, have a high Young's modulus. In general, fibers have high Young's modulus values, elastomers have low values, and plastics lie somewhere in between, as seen in Table I. The point at which the slope

deviates from linearity is known as the yield point [9]. At this point, the material is strained beyond its elastic region and will not return to its original state if unloaded.
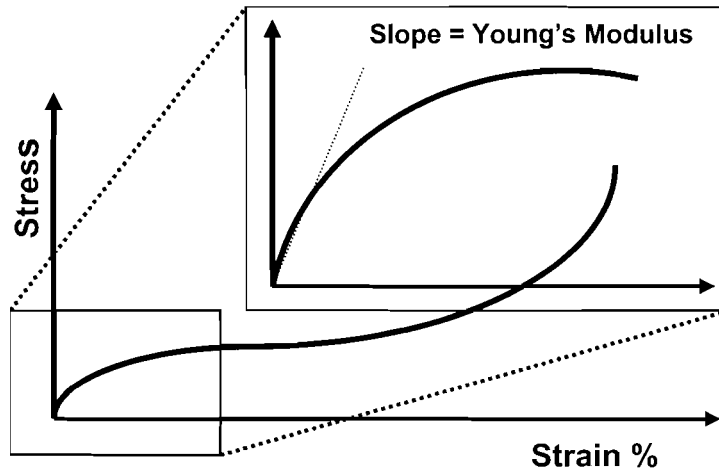
Figure 6: Young's modulus is the slope of a stress-strain curve in the linear regime

Tensile Strength

The tensile strength is the stress needed to break a sample. It is expressed in Pascals or psi (pounds per square inch). The tensile strength is an important property for materials that are going to be stretched. For instance, fibers must have strong tensile strength [9]. The maximum load defines the ultimate tensile strength (UTS) as

$$\sigma_{UTS} = \frac{P_{MAX}}{A_0} \qquad (1-5)$$

where P_{MAX} is the maximum load and A_0 is the original cross-sectional area.

Energy to Break: Toughness

The energy it takes to rupture a sample is defined as the amount of energy required to break the sample per unit mass. It is given by the area under the load-displacement curve.

1.8 Mechanical Properties of Spider Silk

Table I lists important mechanical properties of spider silk in comparison to some other known materials [7]. Spider silk's mechanical properties are largely dependent on a high degree of molecular orientation, which has previously been demonstrated in both the crystalline and the amorphous domains of dragline silk. A spider's internal liquid crystalline spinning induces the high orientation of protein molecules [16-17].

Table I: Mechanical properties of spider silk in comparison to other materials [Ref 7]

Material	Young's Modulus (GPa)	Tensile Strength (GPa)	Energy to Break (J/Kg)
Spider Silk	2.2*	1.2*	1×10^5
KEVLAR	100	4.0	3×10^4
Cellulose Fibers	30.0	0.8	9×10^3
High Tensile steel	200	3.0	1×10^3
Bone	20.0	0.2	3×10^3
* Values obtained in Bonino thesis [9]			
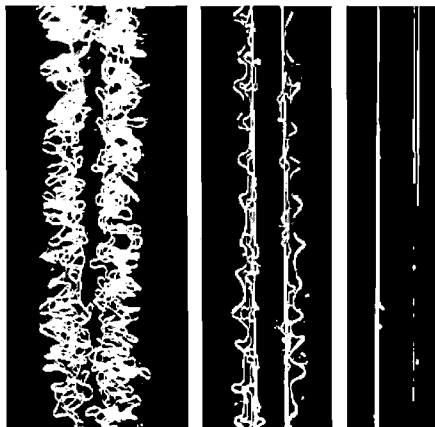
Figure 7: Spider silk shown as normal size, stretched 5 times and 20 times its original length [Reprinted from Ref. 18].

On a micro level, as the silk is loaded, the protein chains move along each other and become stretched out due to the load's force and the silk's elasticity (as depicted in Figure 7). This is the extraordinary property that makes silk very interesting scientifically.

II. OBJECTIVE

Measurement of Young's Modulus and Tensile Strength of spider silk was carried out at room temperature and at 100C, by Bonino [9]. The objective of the present study was to make these measurements at cryogenic temperatures. For this purpose, a high-precision thermal mechanical analyzer (TMA) needed to be set up and calibrated for measurements at room temperature and at 158K. Though the actual target temperature is held at nearly 20K, it was appropriate to test the physical properties at 158K based on the fact that physical properties do not change appreciably below the glass transition temperature, which is ~193K, for spider silk [19]. These quantitative results will assist the Lab in ICF modeling and further investigation.

III. EXPERIMENTAL

3.1 Silk sample

For the study presented here, a common brown spider, *Statoda Triangulosa* (Walckenaer) was chosen to produce silk. [9]. Its dragline silk was used for the experiments. Draglines are used to connect the spider to the web, as safety lines in case a spider should fall, and as the non-sticky spokes of the web. Dragline silk is the strongest kind of silk because it must support the weight of the spider. Silk samples were tested within two to eight days after being harvested. The diameter of the silk strand was determined using a LEO scanning electron microscope.

3.2 Sample Mounting

The spider silk was harvested in a class-500 cleanroom where the spiders were kept. To obtain the silk, the spider was dropped so it would generate its dragline fiber. A nonagon shaped spool with UV glue on each prong collected the strand – yielding nine separate

sections. Under a stereo microscope (50x) the silk was carefully glued to the TMA's upper chuck. A silicon carbide fiber with a diameter of 70 μm was glued onto the opposite end of the silk sample. Using the calibrated divisions of the microscope lens, the length of the sample was measured (between the glue points). Subsequently the sample was cut from the spool and the chuck was reattached to the TMA. The SiC fiber, which served as a plumb bob, was then glued to the bottom chuck (allowing for slack in-between), as shown in Figure 8(a). For tests at cryogenic temperatures, the TMA chamber was filled with liquid nitrogen vapor. Before cooling, the sample was purged with inert helium gas to prevent condensation. Tests were started once the system reached an equilibrium temperature.

3.3 Sample Testing

The PerkinElmer TMA utilized in this study is equipped with PYRIS™ software that runs the TMA and allows data capture and analysis. Figure 8 (b) shows a photograph of the test system and Figure 8 (c) is a close-up photograph showing the sample chamber.   A uniaxial force pulled on the sample at the rate of 0.1mN/minute. As the force was applied, the system measured the displacement relative to the grip's initial position. To determine when the sample begins loading, the point where the slope abruptly changes is designated as the load point. Eventually a sharp increase in slope arises (the slope becomes nonexistent), which indicates that the silk has ruptured.

The stress-strain values were calculated using displacement and force values from the load point onward. The coordinates (force, displacement) at which the sample loaded were taken as the zero force and zero displacement. Strain was calculated and recorded. Ultimate tensile stress values were determined using the diameter obtained from the SEM micrographs.

Important mechanical properties have been extracted using the American Society for Testing and Materials (ASTM) standards. The ASTM standard D3822 defines the yield strength and yield strain at a point from where the initial slope of the stress-strain characteristics begins to deviate from linearity.

(a)

(b)   (c)
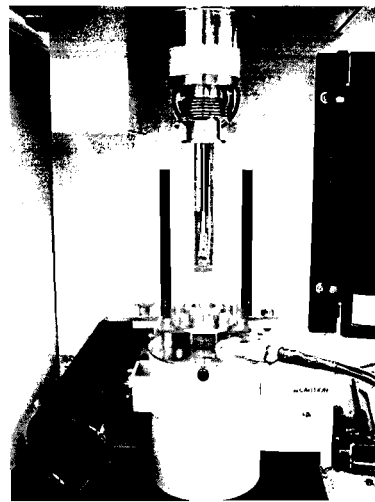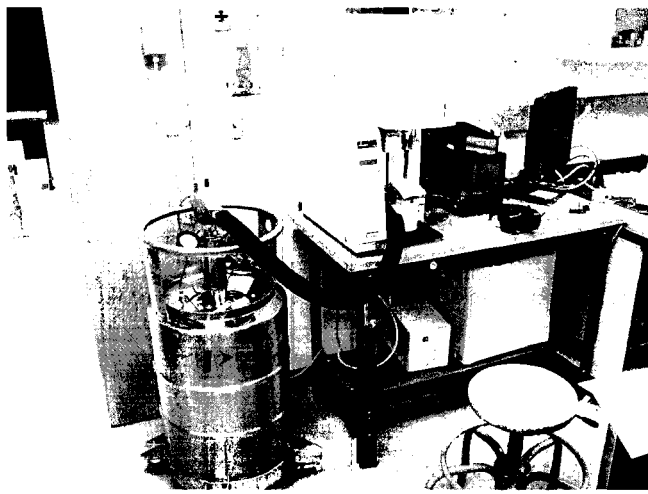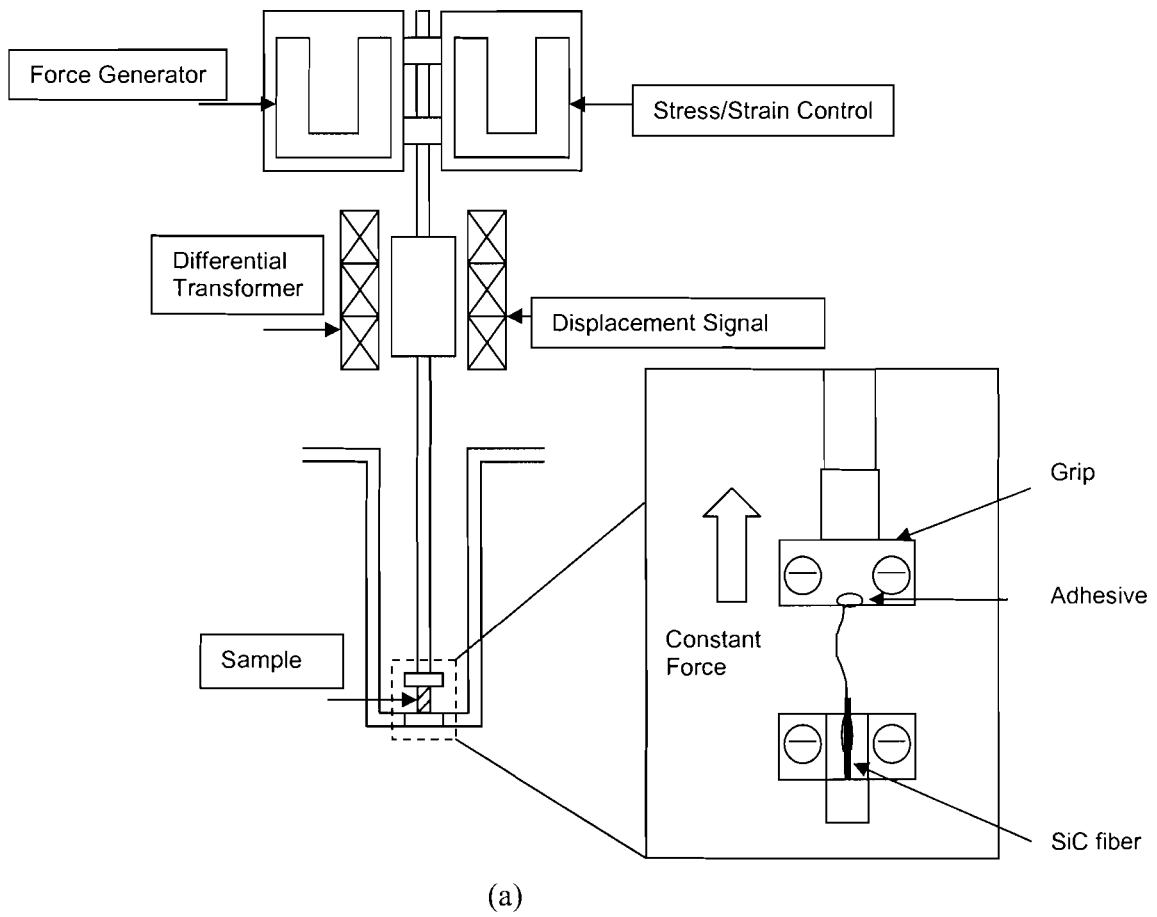
Figure 8: (a) Schematic of the thermal mechanical analyzer system; (b) and (c) actual photographs of the system showing liquid nitrogen cryostat and sample chamber.

IV. RESULTS AND DISCUSSION

4.1 Silk Diameter

Figure 9 shows an SEM micrograph of a typical silk strand tested in this study. Surprisingly, each batch of silk from the tested spider was actually a dual-stranded fiber. The average combined diameter of the five batches of silk was 1.84 μm.
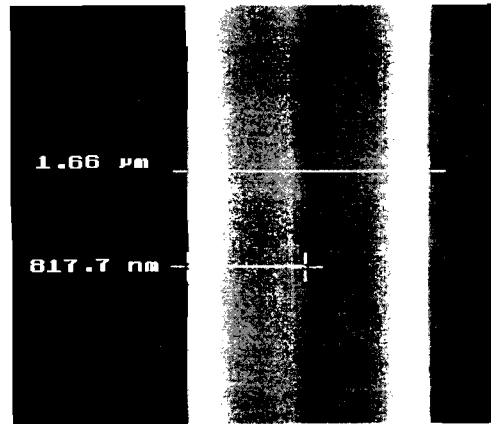
Figure 9: SEM micrograph of a typical silk strand tested in this study.

4.2 Stress-Strain Characteristics

Figure 10 shows a typical comparison between the force-strain values at different temperatures (room temperature and cryogenic).
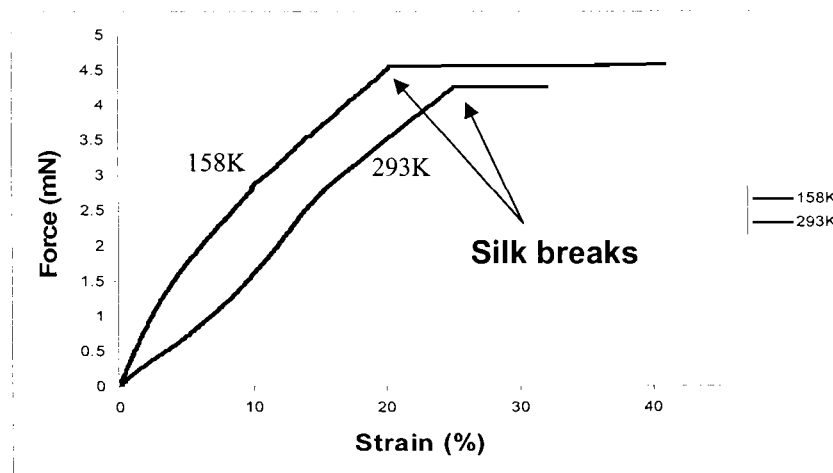
Figure 10: Force-strain characteristics of spider silk at 298K and 158K.

These values were determined from nine room temperature tests and nine cryogenic tests. The modulus values were extracted from such graphs for each run, by carefully measuring and calculating each initial slope. Figure 11 shows the statistical distribution of the modulus values.

Modulus Comparison
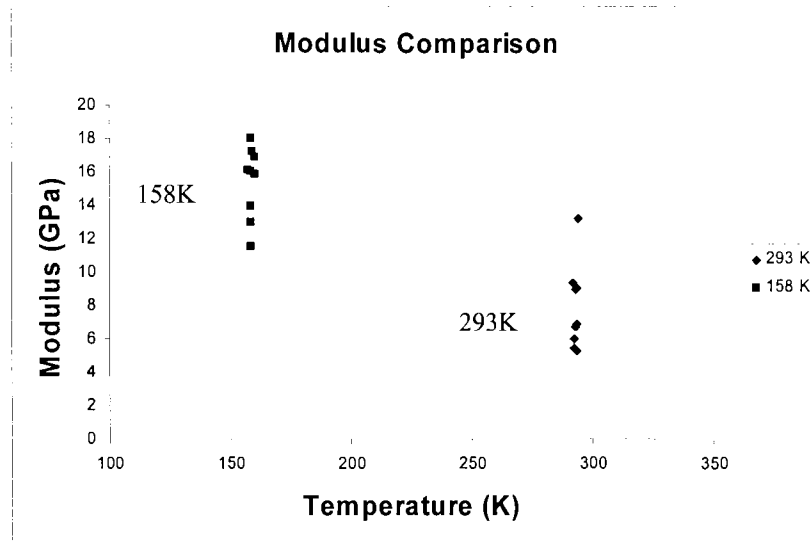
Figure 11: Modulus values obtained for different sample runs

Table II shows the final values for Young's modulus, ultimate tensile strength, and ultimate strain. It can be observed that the average UTS and ultimate strain were minimally affected, whereas the average modulus increased by a factor of two.

Table II. Measured Mechanical Properties		
Temperature	293K	158K
Average Modulus	7.9 GPa ± 1.9 GPa	15 GPa ± 1.6 GPa
UTS	1.7 GPa ± 0.40 GPa	2.1 GPa ± 0.01 GPa
Ultimate Strain	27 % ± 8.00%	23% ± 1.9%

V. CONCLUSIONS

The objectives of this experiment were met successfully. The goal of setting up and using the TMA was accomplished. Silk properties calculated at room temperature were in agreement with previous experiments. The effect of cryogenic temperatures was noted, producing little change in ultimate stress and ultimate strain, while doubling the stiffness of the silk (modulus). This change may be attributed to the composite structure of the silk. The crystalline components of the material may have become stiffer at lower temperatures due to a decrease in lattice energy. On the other hand, the change in the amorphous phase is minimal. In addition, the study reflects the resilience of spider silk over a wide range of temperature, which can be extended to various other applications of biomaterials. This data supports the continued use of spider silk as the premier mount for targets for ICF at LLE.

ACKNOWLEDGEMENS

The author would like to acknowledge Mr. Mark Bonino and Dr. David Harding of LLE for their guidance, advice, and mentoring. Special appreciation is due to Mr. Brian McIntyre of the UR Institute of Optics for SEM analysis. The author wishes to thank the entire LLE Microfabrication staff for their help and support. Lastly, the author is extremely thankful to Dr. Stephen Craxton for organizing the LLE High School Research Program.

REFERENCES

[1] http://www.lle.rochester.edu/.

[2] http://www.lle.rochester.edu/02_visitors/02_aboutomega.html.

[3] F. Peterson, Department of Nuclear Engineering, University of California, Berkeley and the UCB Thermal Hydraulics Research Group, 1998; http://www.nuc.berkeley.edu/thyd/icf/DT_fusion.html.

[4] J.G. Delene, "Updated Comparison of Economics of Fusion Reactors," *Fusion Technology*, Vol. 19, pp. 807 (1991).

[5] W.J. Hogan, Editor, *Energy from Inertial Fusion*, International Atomic Energy Agency, Vienna, Austria (1995) (457 pages).

[6] John Lindl, *Physics of Plasmas*, **2**, 3933, (1995).

[7] J. M. Gosline, M.E. DeMont and M.W. Denny, *"The Structure and Properties of Spider Silk"*, Endevour, New Series, Vol. 10, No.1, (1986).

[8] F. Vollrath, "Spider Webs and Silks", Scientific American. March 1992, pp. 70-76.

[9] M. Bonino, *"Material Properties of Spider Silk"*, M.S. Thesis, University of Rochester, Rochester NY, 2003.

[10] E. Oroudjev et al., "Segmented nanofibres of spider dragline silk: atomic force microscopy and single-molecule force spectroscopy", PNAS Early Edition, www.pnas.org/cgi/doi/10.1073/pnas.082526499.

[11] http://www.zoology.ubc.ca/labs/biomaterials/ab-paul.html.

[12] B.A. Brinker et al., "Inertial Fusion Target Mounting Methods: New Fabrication Procedures Reduce the Mounting Support Perturbation", J. Vacuum Science and Technology, A 1(2), April-June (1983), pp. 941-944.

[13] http://faculty.uscs.edu/llever/Polymer%20Resources/Mechanical.htm; National Science Foundation's Division of Undergraduate Education through grants DUE #9950809 and DUE #9950.

[14] Carraher, C. E., Jr *Polymer Chemistry: An Introduction*, 4th Ed., Marcel Dekker, NY: 1996. p. 120.

[15] "Mechanical Properties of Polymers", : http://www.psrc.edu/macrog//mech.htm [2000, May 21].

[16] F. Vollrath, Strength and structure of spider's silks, *Review in Molecular Biotechnology*. 2000, Vol. 74, 67-83.

[17] R. F. Foelix, Spider web, *Biology of spiders*. New York: Oxford University Press: Georg Thieme Verlag, 1996.

[18] E. Kullmann, H. Stern, Leben am seidenen Faden, Die rätselvolle welt der spinnen, 1975, Verlagsgruppe Bertelsmann Verlag, Munchen, Germany, ISBN 90 222 0239 9.

[19] Cunniff PM, Fossey SA, Auerbach MA, Song JW, Kaplan DL, Adams WW, Eby RK, Mahoney D, Vezie DL. Polym Adv Technol 1994;5:401.

Operational Specifications for the Two-State Motor Controller

Jonathan Kyle

**Operational Specifications
For the Two-State Motor Controller
Jonathan Kyle**
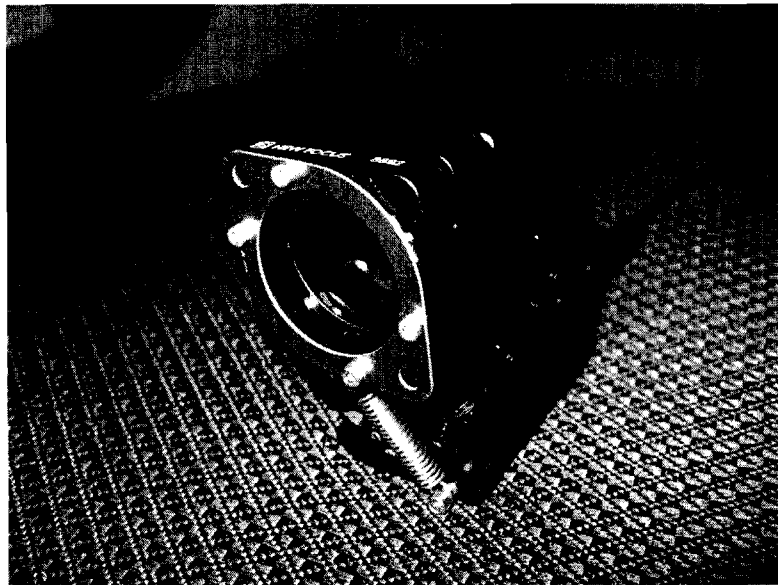
University of Rochester
Laboratory for Laser Energetics

1.0 Goals of the Control System

Currently, on the OMEGA laser system, optical lenses as well as mirrors are flipped in and out the path of the laser beam by means of pneumatic devices. These apparatuses rely on an external supply of air as well as power. This hindrance makes the pneumatic devices cumbersome and quite large, not the ideal attributes when working in confined spaces. A more elegant solution to this problem would be to use electric motors that are smaller, cheaper, and more useful. Other advantages are as follows:

- low power (no external power)

- power comes directly from the Two State Control Module (TSCM)

- smaller size

- lower cost

- can be implemented in a vacuum

- more reliable

- added status features (jam, unplugged)

With these advantageous reasons, it was determined that using electric motors for "flip-ins" was the better method as opposed to pneumatic devices. This project accomplished developing a two-state motor controller to operate an electric motor as a "flip-in" by using "off-the-shelf" motorized "flip-in" motors from New Focus. It was also able to determine 5 state functions: 1) Is the motor plugged in? 2) Is the motor jammed? 3) Is the motor in the "in" position? 4) Is the motor in the "out" position? 5) "Run-away" detection.

2.0 Overview of the hardware design

For the electric motor to communicate with the TSCM, a black box was constructed

which acted as an adaptor. As seen in fig. 1, the black box contains a micro controller, a

motor driver, and a current sensor. The micro controller sends signals to the motor driver

to control which direction the motor will turn. The current sensor monitors the current

and sends signals back to the controller for analysis. When the current spikes after a

certain period of time, it indicates that the motor has reached its desired position. If the

current spikes too soon, the micro controller assumes that it is a jam. If the current

doesn't spike initially, that's interpreted as no motor being plugged in. Finally, if the

current never spikes but remains steady, that is a "run-away" scenario, which is the

unlikely event of the optical assembly coming loose of the motor shaft.

Fig 1. **Block Diagram of the Two-Step Motor Controller**

.... = black box

3

Fig 2. Current Graph

Fig 2. Current Graph

(Graph with "Current" on the vertical axis and "Time" on the horizontal axis. Labels shown: Turn-on, Jam, Stall, Run Current, Run-away)

Fig 3. Actual Current from Motor

Fig 3. Actual Current from Motor

Illustration 7One direction followed by
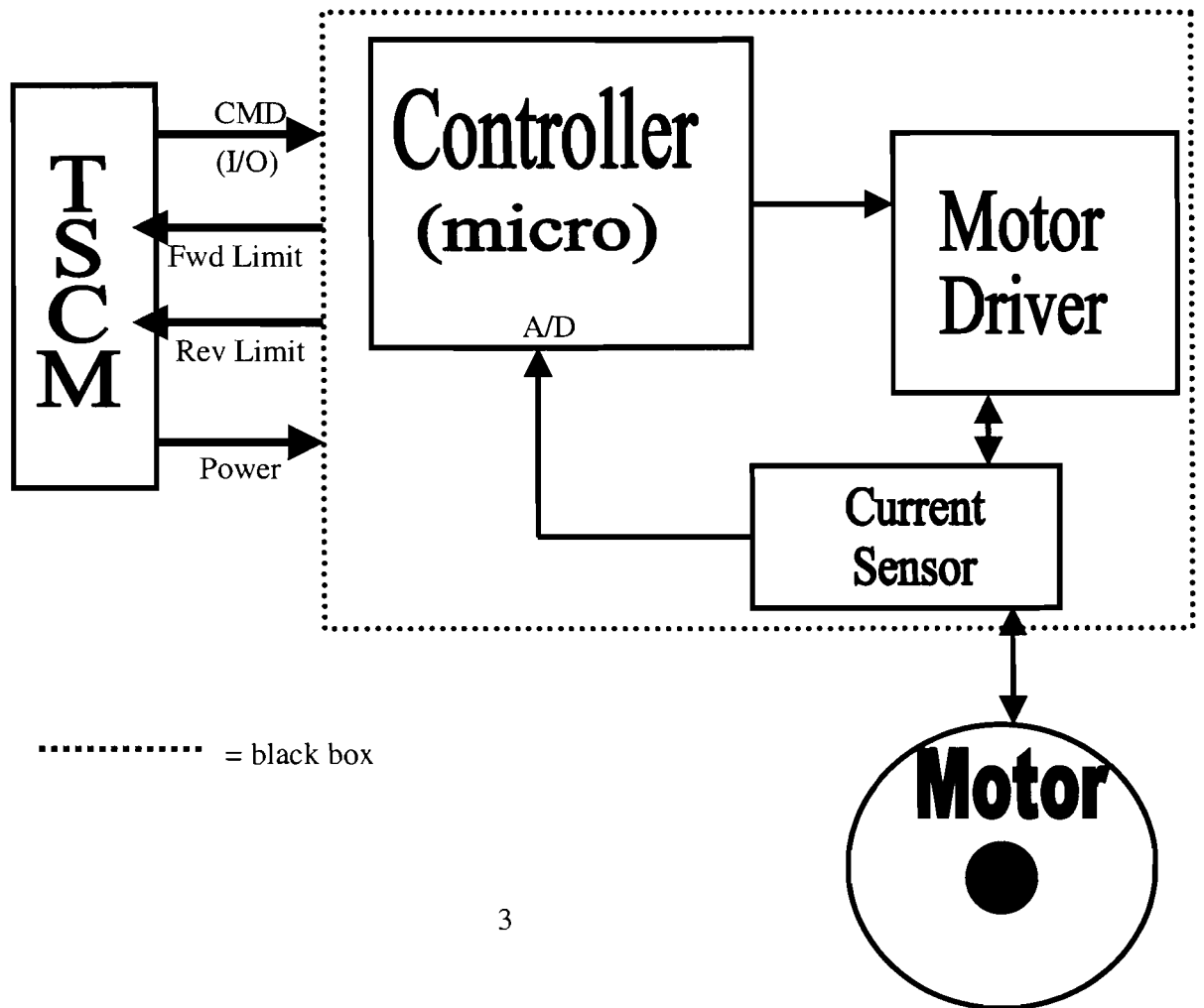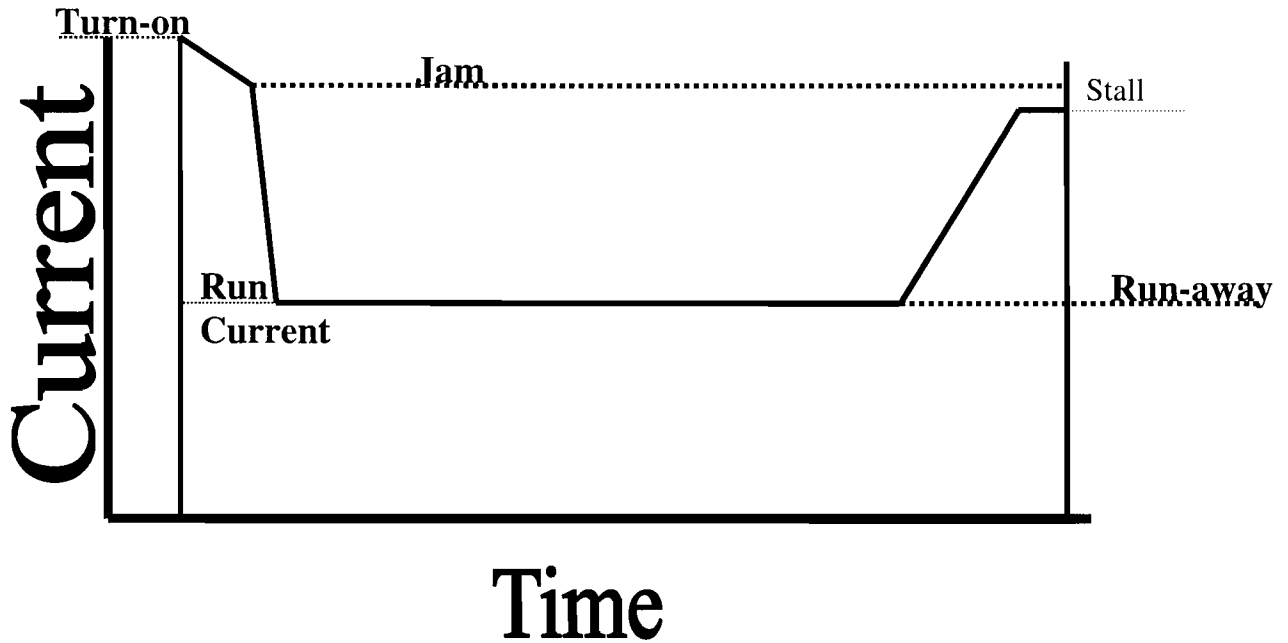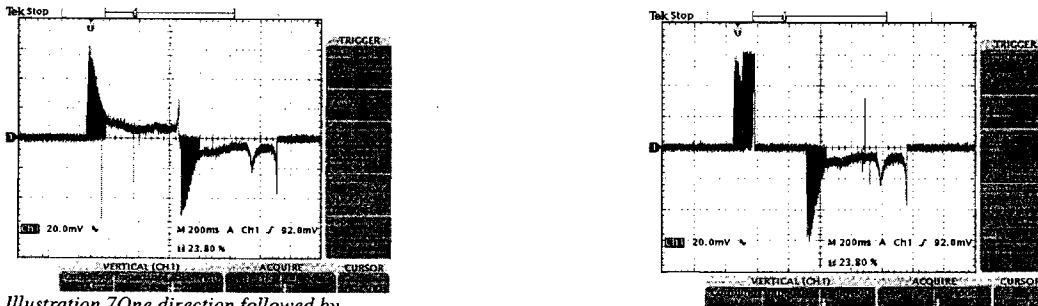
As can be seen from Figures 2 and 3, there is an initial spike in the current when the motor is first turned on. This indicates the amount of work needed to get the motor started. Once its momentum builds up, the current goes down for a certain period of time until the motor assembly hits the other side. At this moment, the motor has stalled and the current spikes again, although not as much as it did when it was first turned on. By constantly monitoring these signals, the software is able to determine what state the motor is in and react accordingly.

2.1 Microchip (PIC16F684)

The 14-Pin FLASH-Based 8-Bit CMOS Microcontroller was the best candidate for this design. It was powerful (200 nanosecond instruction execution) yet easy to program. The microcontroller contains Microchip's PIC MCU architecture in a 14-pin package and features an analog to digital converter and 128 bytes of EEPROM data memory.

Features

- 128 bytes of EEPROM data memory

- Programmable pull-up resistors

- MPLab ICD-2 programming support or debugging support with optional adapter

- 8 oscillator selections including 4 MHz RC oscillator with programmable calibration and Power-On Reset

- 8 Bit A/D

- Low cost

2.2 Motor Controller

By using two half bridges from International Rectifier, an "H" bridge was constructed. The IRF7507 HEXFET Power MOSFET is an extremely efficient and reliable device. The new Micro8 package provided the smallest footprint available in a Small-Outline Integrated Circuit, making it excellent for saving space. By utilizing advanced processing techniques, the fifth generation HEXFETs achieve a low on-resistance per silicon area.

<u>Features</u>

- Generation V Technology

- Ultra Low On-Resistance

- Dual N and P Channel MOSFET

- Very Small SOIC Package

- Low Profile (<1.1 mm)

- Available in Tape & Reel

- Fast Switching

- Low cost

3.0 Overview of the Software Design

As depicted in the flowchart in Fig. 4, the command signal from the TSCM can begin as either a 1 or a 0. If it is a 1 or high signal, the motor will move in a clockwise direction. If it's a 0 or low signal, the motor will move in a counterclockwise direction.

Counterclockwise

After the motor moves in a counterclockwise direction, the current sensor has to determine if the current is greater than the start current, which is the least amount of current needed to start the motor. This will determine if the motor is indeed connected. If it isn't, the current will not be greater than the start current and both limit switches will be set to 0 indicating that no motor was detected. If everything is normal, the current then has to be less than 70% after 1/2 of a second indicating that the motor is free from any obstructions. If the current spikes above that, that's indicative of a motor jam and both limit switches will be set to 1. Then, proceeding as normal, the current should spike

6

above 75% after 1 second, meaning the motor has reached its desired position. In this case the motor turns off and the forward limit switch is set to 0 and the reverse limit switch to 1, indicating that the motor moved in a counterclockwise direction. Finally, all the outputs of the jam scenario, as well as the no-motor-detected scenario, would feed into the interrogative asking if the command signal is still 0. If it is, the system simply loops on itself but if it's not, the system is routed back up to the beginning to go through the whole process again.

Clockwise

Moving the motor clockwise is basically the same procedure except that the command signal has to be high or 1. Also, when the motor has reached its end, the forward limit is set to 1 while the reverse limit is set to 0. Finally, the last question is asking whether the command signal is 1 and if it is, it loops on itself and if it isn't, it starts back at the beginning.

4.0 Conclusion

The two state motor controller performed its job well. It allowed the Two State Control Module to communicate with the two state motor and move the motor clockwise as well as counterclockwise. Also, the limit switches performed well and ran back signals to a bi-color LED so we could monitor its status. We were able to send signals from the TSCM to the two state motor controller. Once the motor reached a certain position, it successfully sent the correct signals back to the TSCM. In order for this to be implemented into OMEGA EP, more tests need to be conducted to ensure that every scenario works perfectly. Figures 4 through 7 are the software flowcharts and the schematic of the two state motor controller.

Fig. 4

Two State Motor Controller Software Flowchart

Start

Command Signal High=1?

No

Yes

Counterclockwise Motor Movement

Clockwise Motor Movement

Is command signal=0?

Yes

No

Is command signal=1?

Yes

No

Fig. 5

Counterclockwise Motor Movement

Start

Command Signal High=1?

No

Move motor ccw

Is current > start I?

No

Turn off motor

Set both limits= 0

Yes

Is current <70% after ½ second?

No

Turn off motor

Set both limits =1

Yes

Is current > 75% after 1 second?

No

Turn off motor

Yes

Turn off motor

Set for limit=0 and rev limit=1

Is command signal=0?

Yes

No

Fig 6.

As Fig. 5 but for clockwise motions

Fig. 7
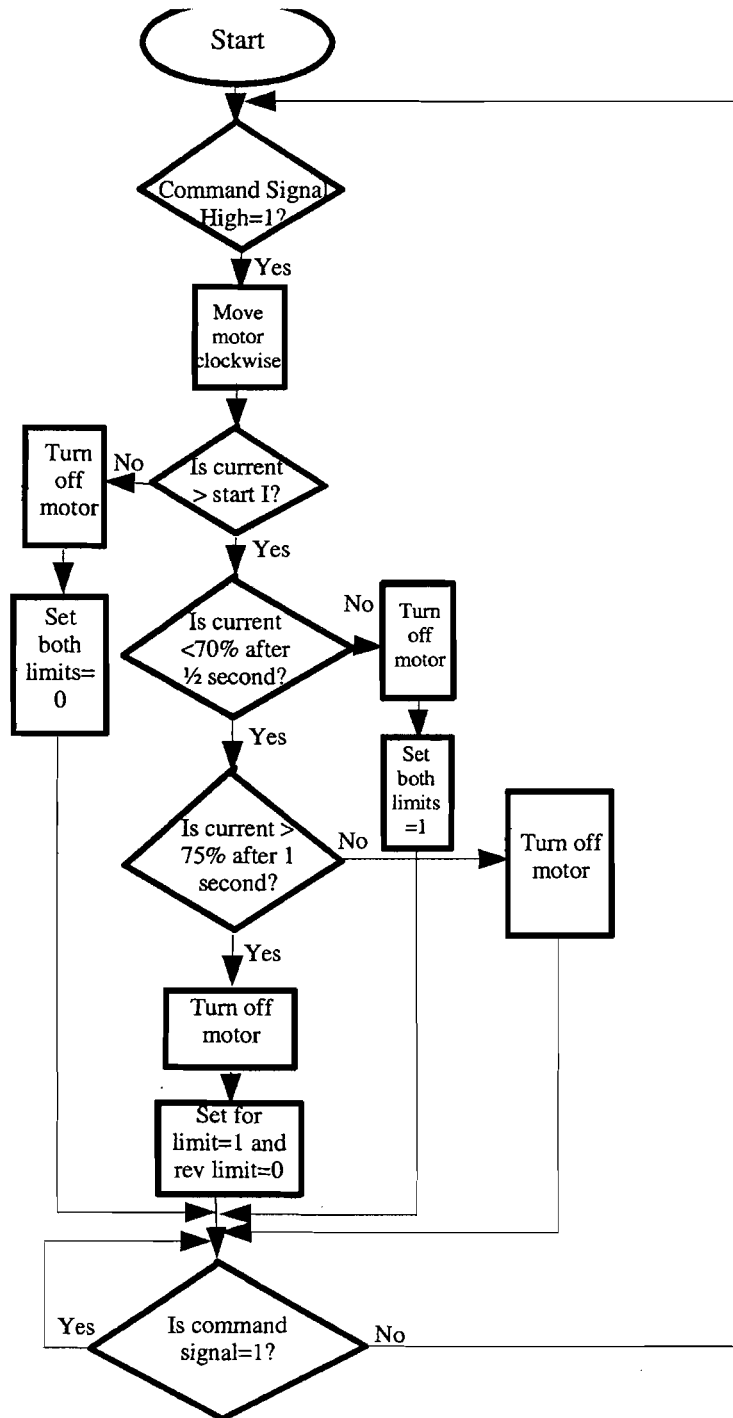
Optimal Pinhole Loading via Beam Apodization

Ted Lambropoulos

Optimal Pinhole Loading Via Beam Apodization

Ted Lambropoulos

Pittsford-Mendon High School

Pittsford, NY 14534

Advisor: Dr. John Marozas

Laboratory for Laser Energetics

University of Rochester

ABSTRACT

An important consideration in the OMEGA EP laser design is the spatial shape of the beam at the beginning of the laser path. A sharp edge maximizes beam energy but also maximizes pinhole loading due to diffraction as the beam propagates. Several different beam shapes were investigated for OMEGA EP in order to minimize pinhole loading. Beam shapes from the super Gaussian family and hyperbolic tangent family were investigated. These beam designs were composed of two distinct sections, an upper portion and a lower portion, with the steepness of the curve differing between the two. Each of these beam designs was sent through an optimization function in MATLAB that optimized either the rise rate or super Gaussian order, depending on the family of the curve, and the joining point of the two portions. The function attempted to minimize the integral outside the pinhole. It was discovered that the left-handed skew from the hyperbolic tangent family performed the best.

1.   BACKGROUND

1.1   Inertial Confinement Fusion (ICF)

At the University of Rochester Laboratory for Laser Energetics Inertial Confinement Fusion [1] is studied. ICF holds the promise of providing cheap, clean energy for many years to come. This process is achieved by firing 60 high power laser beams at a spherical target. This target is a plastic shell containing a frozen layer of deuterium and tritium that is about 0.1 mm thick. The 60 laser beams fire upon this pellet and deliver high amounts of energy to the target. Upon the laser beams coming into contact with the pellet, a dense plasma layer is created around the fuel. As this plasma heats up it expands outward, eventually releasing itself from the pellet.

As Newton's Third Law states, every action has an equal and opposite reaction. The outward expansion of the plasma layer results in an inward force being applied to the 0.1 mm thick fuel shell. Ideally, the implosion condenses the fuel shell to a radius approximately 30 times smaller than what it was prior to implosion, resulting in a very high fuel density. At this point, the fuel shell is under the conditions that allow for the fusion of deuterium and tritium to occur; the shell has extremely high temperature and extremely high pressure, all in a minute volume. Upon the fusion of the isotopes, neutrons escape at a high velocity. The expectation of the ICF program is to be able to produce more energy from this fusion reaction than is input through the firing of the laser beams.

1.2   OMEGA EP Laser System

The OMEGA EP laser system at the University of Rochester's Laboratory for Laser Energetics is capable of using two laser beams simultaneously to deposit 2.6 kJ of energy in a

target less than one millimeter in diameter in approximately one picosecond. The OMEGA EP

laser system will be used to supplement the 60-beam OMEGA system discussed in section 1.1.

The combination of the two systems will result in the world's only facility capable of fully

integrated fast-ignition experiments. This project dealt with optimizing the pinhole loading via

beam apodization in the spatial filters of the OMEGA EP laser system.

1.3   Fourier Optics

Central to the theory behind the computational work I have performed is the concept of

Fourier Optics. Fourier Optics assumes that, when dealing with a laser beam, the beam parts can

be broken up into a near field and a far field. The near field is characterized by the laser beam's

profile before it has passed through a spatial filter. The far field is the result of the near field after

it has propagated, i.e. undergone a Fourier Transform.

Essentially a Fourier Transformation (FT) decomposes a function into a series of

oscillatory functions such as sines and cosines. The equation for a Fourier Transform of a

function f(t) is [2]

$$f(t) = \frac{1}{2\pi} \int_{-\infty}^{\infty} \tilde{F}(\omega)\, e^{j\omega t}\, d\omega, \qquad \tilde{F}(\omega) = \int_{-\infty}^{\infty} f(t)\, e^{-j\omega t}\, dt$$

(1)

where — denotes frequency (units of rad/s), t is time (units of s), and F(w) is the Fourier

amplitude (a complex quantity).

Some of the applications of Fourier optics are indicated schematically in Fig.1 [3].
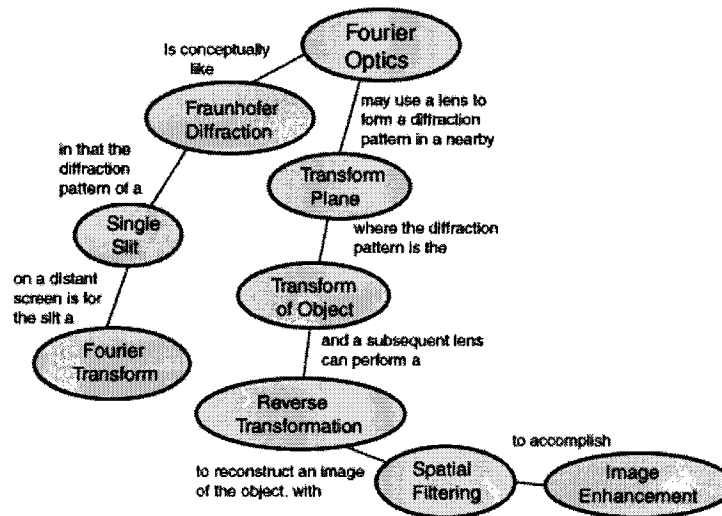
Fig. 1 – *Applications of Fourier Optics*

1.4.   Problems in Laser System

As a beam propagates it picks up phase noise, which essentially acts like a lens inside the actual laser beam. Some causes of phase noise include imperfect optics, thermal effects, and self-focusing. The phase noise eventually widens the near field intensity profile. This is detrimental to the beam's proper functioning on target implosion. This phase noise leads to laser beam self-focusing and eventual laser damage, degraded image quality, and a degraded far field spot shape. All this occurs as a result of amplitude modulation, which develops as a result of the widened near field intensity profile caused by the phase noise.

In order to eliminate the beam phase noise the beam is passed through a spatial filter (see Fig. 2) [4]. The spatial filter removes the higher spatial frequencies from the beam in the far field, for it is these higher spatial frequencies that possess the greatest tendency to create phase noise. Yet excessive removal of the high spatial frequencies is detrimental to the beam as well. The greater the amount of energy outside the pinhole edge when the beam passes through the aperture, the more will be the ringing in the reconstructed near field.
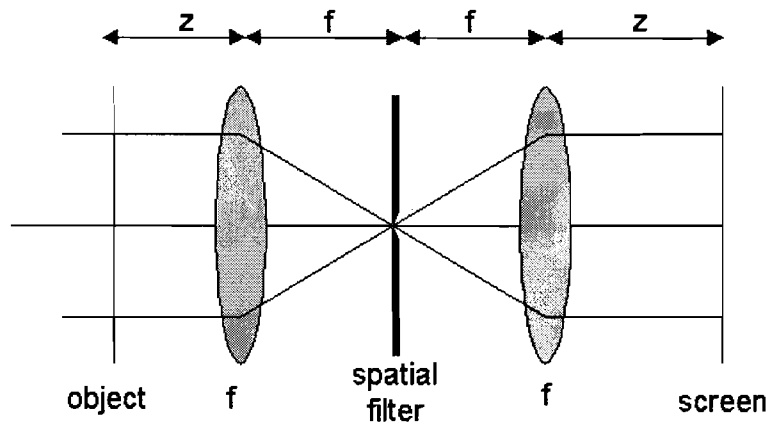
Fig. 2 – *Principle of a spatial filter: A beam is focused through a pinhole and recollimated, allowing higher spatial frequencies (or equivalently rays not propagating parallel in the incident beam) to be removed from the beam.*

Since the exact shape of the old beam's near field intensity profile can not be re-created due to the removal of the high frequencies, ringing takes place (Fig. 3). Such ringing occurs when the reconstructed near-field profile, after being recreated following passing through the pinhole with some of its original frequencies having been removed, differs from the original beam profile. Too much ringing will lead to more phase noise and then more amplitude modulation, and the cycle will continue until the laser destroys itself.
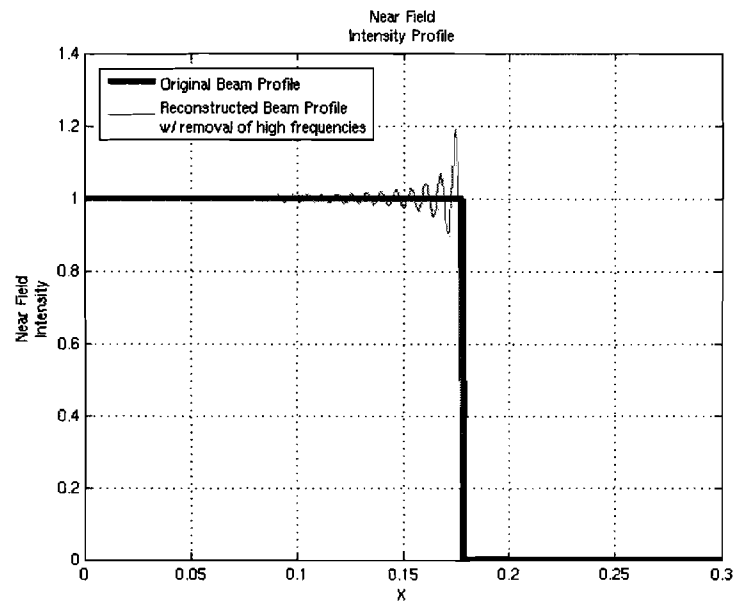
Fig. 3 – *Removing too much of the high frequency spectrum results in the reconstructed near field differing from the original near field.*

1.5 Project Goal

There are two contradictory requirements in constructing the near field beam shape. On one hand, the near-field area must be maximized so that the largest possible power can be delivered to the far field by the laser beam. On the other hand, the far field spot shape needs to be as small as possible so that pinhole loading can be minimized.

Pinhole loading occurs when excess beam energy, the side-lobes in the far field, strike the pinhole edge and, as a result, cause ringing in the reconstructed near field. In order to correct this problem, the beam must be apodized (i.e., passed through an optic that smoothens the edge of the beam profile). Unfortunately, the side lobes are a direct consequence of the diffraction of the laser beam. As we increase the near-field area, in order to get the most energy, we steepen the edge of the beam profile, the side-lobes become bigger and more pinhole loading is induced. My research task was to develop an equation for the beam shape that resulted in the most efficient balance between these two contradictory requirements.

2.   METHODOLOGY AND CALCULATIONS

2.1.   General Beam Shapes

Dickey and Holswade [5] have presented the theory and techniques of laser beam shaping. Approaches include geometric constraints via masks or optimization-based beam shaping algorithms. In the OMEGA EP system, the spatial shape of the beam is determined via a mask. We have adopted an optimization technique to design and shape the near-field intensity so as to obtain the optimal far-field distribution.

We investigated several different beam shapes for the OMEGA EP laser system. Each beam shape examined consisted of a flattop central portion, and a tailored "shoulder" connecting the central portion with the dark region outside the shoulder. The transition "shoulder" itself consists of two distinct sections, an upper section and a lower section, with the steepness of the curve differing between the two. We designed beam shapes using the super-Gaussian [6] and hyperbolic tangent families of curves. In order to have something to compare our new beam shapes to, a reference beam shape was created. This shape was defined as a beam with a square shaped near field intensity profile.

We used the symbolic and computational program MATLAB [7] to simulate the near field beam profiles, and to compute the far field diffraction pattern using Fourier optics. We optimized the rise-rate or super Gaussian order, depending on the family of the curve used, as well as the spatial location of the joining point of the upper and lower section. The optimization criterion we selected was the minimization of the integrated spectral power of the beam outside the pinhole.

2.2.   Calculating Beam Shapes

The first beam shapes we investigated were those of a super Gaussian profile, see equation (2).

$$y = e^{-\left(\frac{x}{x_o}\right)^{sg}}$$
(2)

Of the super Gaussian branch of beam shapes, three were focused on, a symmetrical beam shape, a left handed skew, and a right handed skew. The symmetric beam shape has its tailored edge comprised of super Gaussian orders that are equal (Fig. 4). In the left hand skew the upper portion of the beam edge is of a higher order than is the lower section (Fig. 5). For the right hand skew, it is just the opposite; the lower portion is of a higher order than the upper portion (Fig. 6).

Symmetric
Intensity profile for 1% anchor
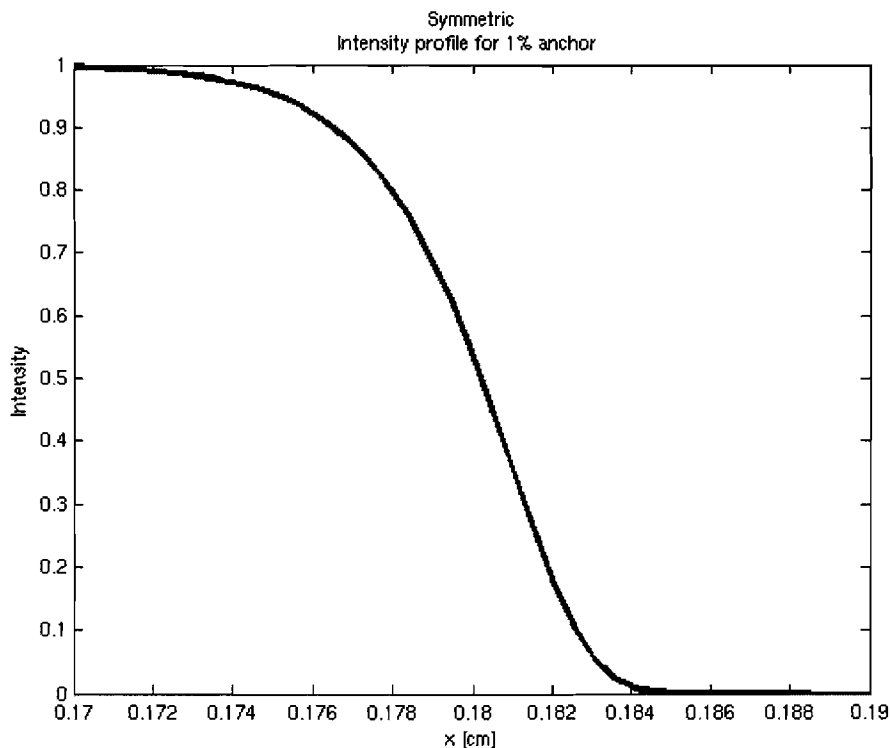
Fig. 4 – *In the symmetric beam edge, both the upper portion and lower portion have the same super*

Gaussian order.
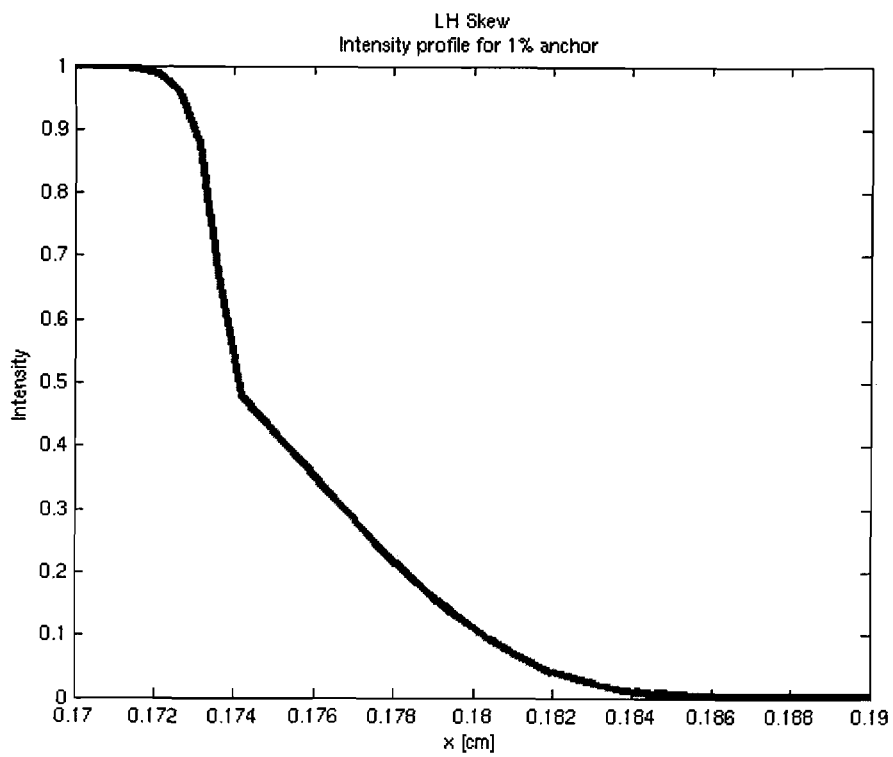
Fig. 5 – In the left handed skew, the upper portion has a higher super Gaussian order than the lower
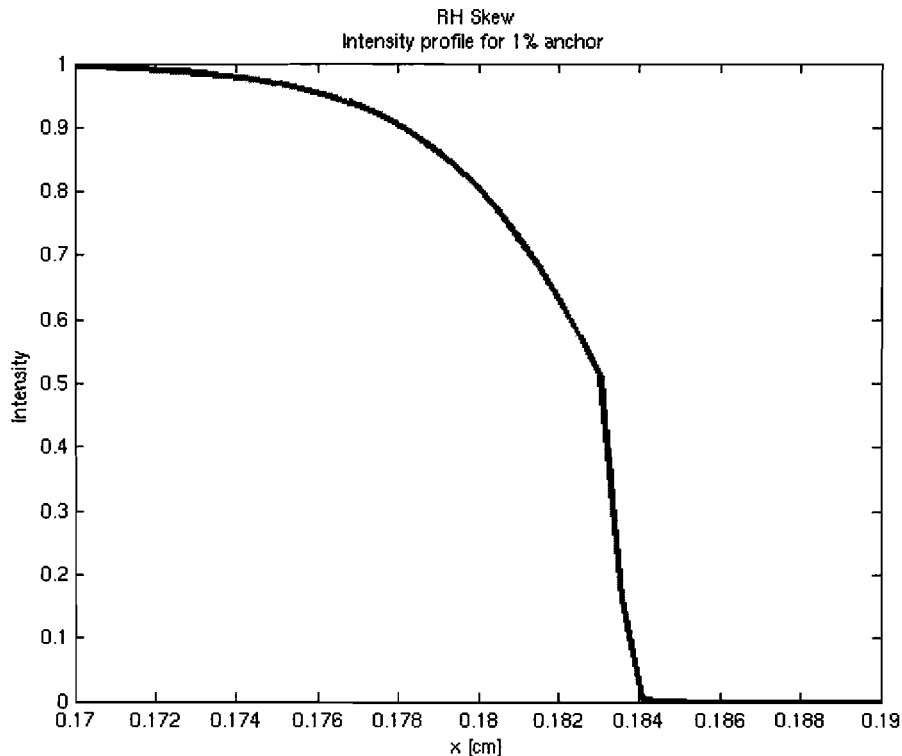
portion.

Fig. 6 – *In the right handed skew, the lower portion has a higher super Gaussian order than the lower*

portion.

In addition, there were two important criteria that our tailored beam shapes had to meet. The first

criterion was that the beam edge had to rise from the 1% intensity level to the 99% intensity level

in 1.2 cm. The second was that the beam's intensity full width half maximum needed to be 35.6

cm.

We first began by manually calculating what the super Gaussian orders should be in each

of the beam edges. Three distinct "anchor" points were used throughout the calculation. An

anchor point is the point on the beam edge at which all of our calculations would originate. The

calculations were made assuming a 1% intensity level anchor point, Xo as an anchor point, and a

99% intensity level anchor point. We proceeded to calculate what the super Gaussian orders

would be with respect to each anchor point; the expectations were that each time each super

Gaussian level would turn out the same regardless of which anchor point we used.

Upon receiving slightly different results with each anchor point, we constructed a

MATLAB script that would optimize the area outside the pinhole edge, the rise rates, and the

anchor points. In addition to investigating the super Gaussian family, we also tested the family of

hyperbolic tangents, see equation (3).

$$f(x) = \tanh(\beta x) = \frac{e^{\beta x} - e^{-\beta x}}{e^{\beta x} + e^{-\beta x}}$$

(3)

The hyperbolic tangents operated in the same manner as did the super Gaussians: there were 2

pieces to the edge with the rise rate differing between the two and the MATLAB program sought

to find the optimum rise rates that would minimize pinhole loading.

3.   RESULTS

Our main conclusion was that the left-handed skew shape from the hyperbolic tangent

family performed the best (Fig. 7). The spectral power outside the pinhole decreases by more

than ten thousand times as compared to the uniformly shaped square beam.
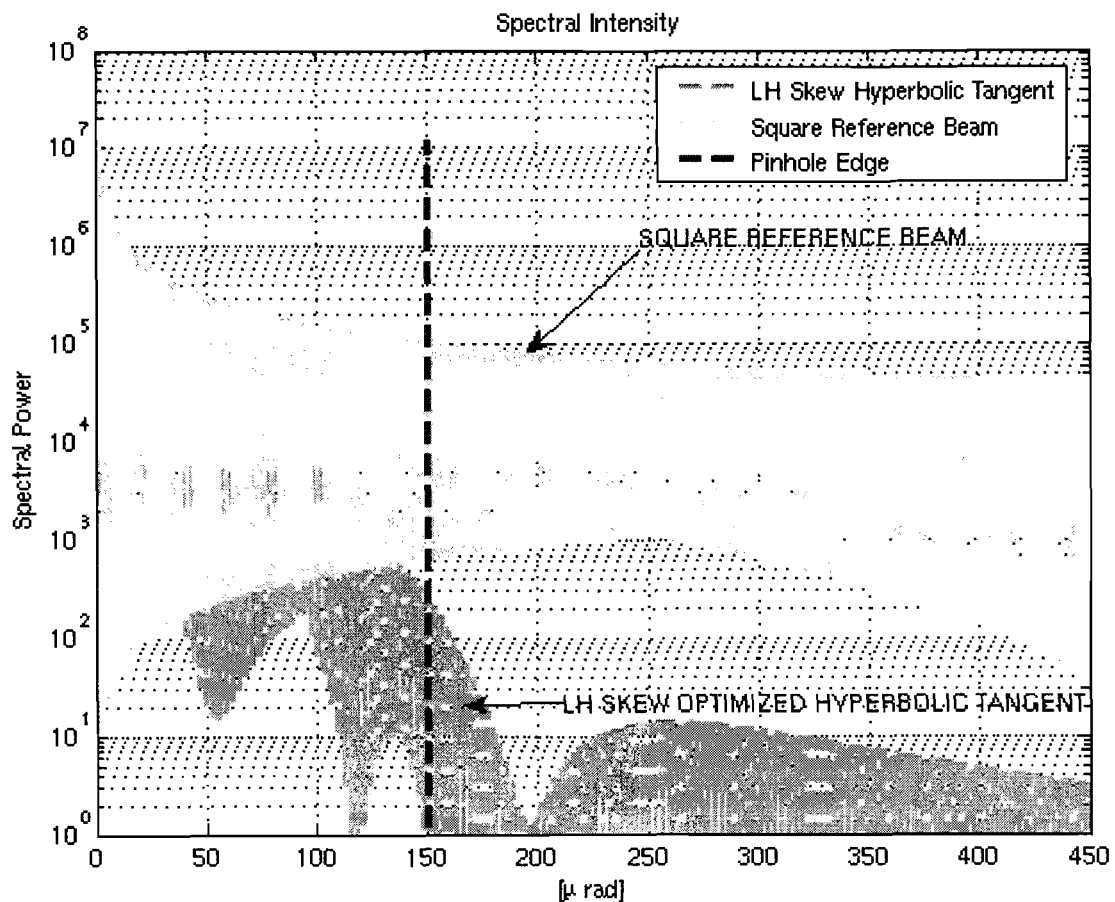
Fig. 7 – *The optimized hyperbolic tangent edge performed remarkably better than did the square

reference beam. While producing very little spectral power outside the pinhole edge, the optimized beam

edge nearly matched the square reference beam's spectral power inside the pinhole edges.*

The optimized profile eliminates nearly all "ringing" outside the pinhole by reducing phase

noise (Fig. 8, Fig. 9), and concurrently allows the beam to be as powerful as possible in the near

field.
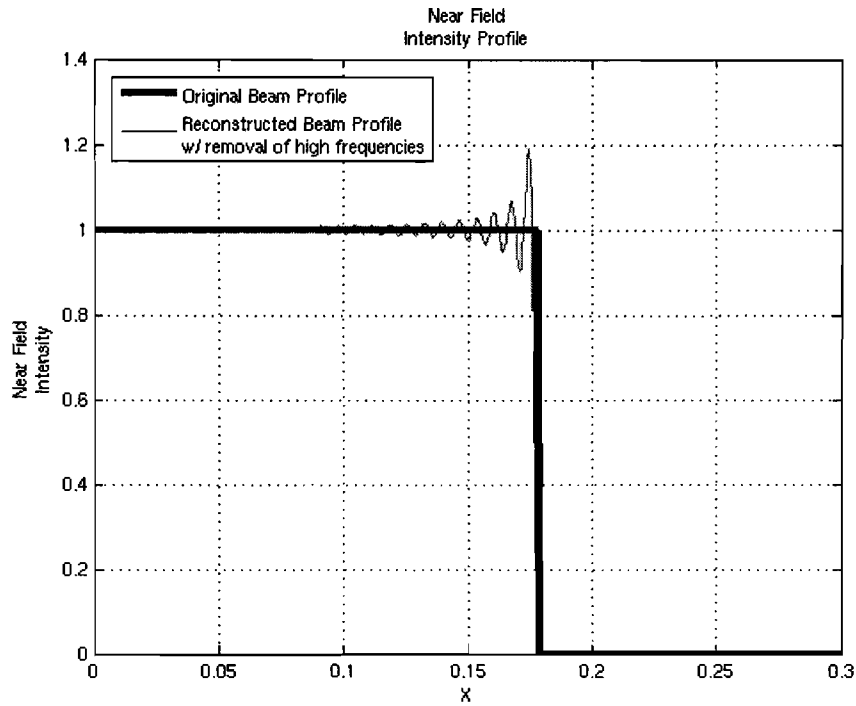
Fig. 8 – *Before optimization: The square reference beam's reconstructed near field profile shows very*

evident signs of ringing.
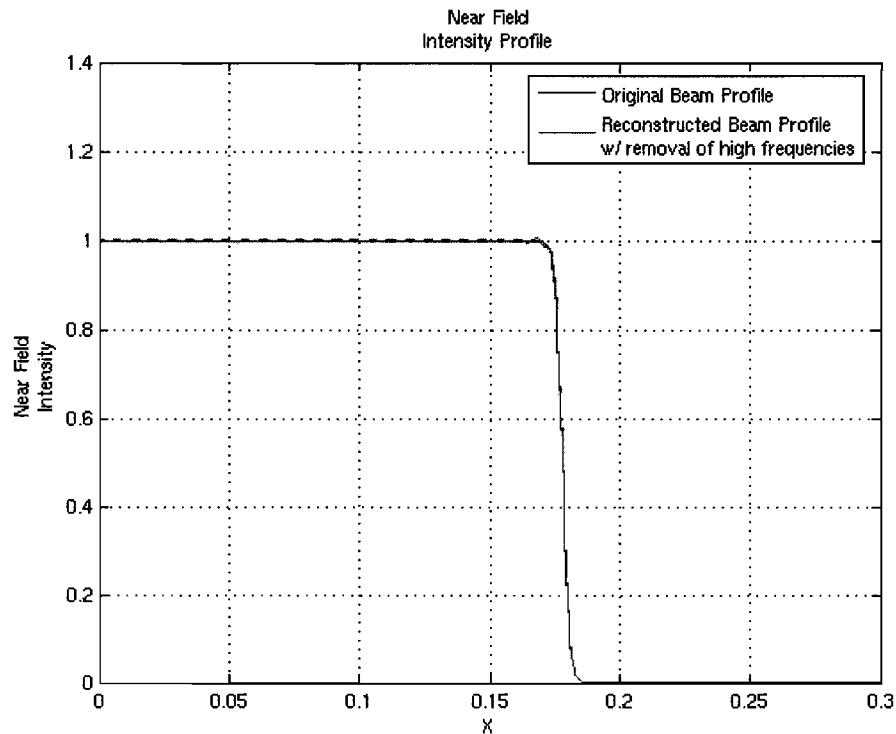
Fig. 9 – *After optimization: The reconstructed beam profile of the optimized beam is practically the same as before passing through the pinhole. The design goal has been met.*

This laser shaping technique may be applied to biomedical optics, laser surgery involving small blood vessels, and laser micropatterning of silicon or polymer materials used in displays or light emitting diodes.

ACKNOWLEDGMENTS

REFERENCES

1. R. S. Craxton, R. L. McCrory, J. M. Soures, "Progress in Laser Fusion," *Scientific American*, vol. 255, p. 5, Aug. 1986.

2. J. W. Goodman, *Introduction to Fourier Optics*, McGraw-Hill, New York, 1965.

3. Nave, R. "Fourier Optics." Diffraction. 5 Mar. 2005 <http://hyperphysics.phy-astr.gsu.edu/hbase/optmod/fouroptcon.html#c1>.

4. "Fourier Optics." 5 Mar. 2005 <http://tnweb.tn.utwente.nl/inlopt/lpmcad/examples.htm>.

5. F. M. Dicky and S. C. Holswade, *Laser Beam Shaping: Theory and Techniques*, Marcel Dekker, New YYork (2000).

6. J. A. Hoffnagle and C. M. Jefferson, Beam Shaping With a Plano-aspheric Lens Pair, Optical Engineering 42, 3090-3099 (2003).

7. E. B. Magrab, S. Azarm, B. Balachandran, J. Duncan, K. Herold, G. Walsh, *An Engineer's Guide to MATLAB*, Prentice Hall, Upper Saddle River (2000).

Spatial Distribution of the Reflected Laser Light at the Experimental Chamber Wall

Yekaterina Merkulova

Spatial Distribution of the Reflected Laser Light at the Experimental Chamber Wall

Yekaterina Merkulova
Advisor: Dr. Jacques Delettrez

Laboratory For Laser Energetics
University of Rochester

Summer High School Research Program

A computer program was created to calculate the distribution of the reflected laser light along the target chamber wall. This is needed to assess the accuracy with which the total reflected light can be estimated from the energy measurement in single detectors covering a small area of the wall. The program generates a grid for the target chamber wall and the angular distribution of the reflected light relative to the axis of a beam. This distribution is transposed from the frame of the rays to the frame of the chamber wall. A search is then performed to map the intensity distribution from the 60 OMEGA beams on the target chamber wall grid. Preliminary results show that there exists a level of non-uniformity of about ±5%.

Introduction

The energy absorbed by targets irradiated by the 60 OMEGA beams is obtained by measuring the reflected energy with calorimeters. However the techniques used in these experiments sample small areas on the chamber wall and assume that the light is reflected uniformly on the chamber wall. Since discrepancies have been discovered between these experiments and simulations, it is necessary to test that assumption. A computer program was written to calculate and map the intensity distribution of the reflected laser light. Input data came from simulations that were carried out with the one-dimensional, hydrodynamic code, LILAC.

Background

The computer program was written based on ray tracing. This method is simpler than direct modeling of the interaction of the laser with the target, and is used to determine the absorption of the laser light by the target. Ray tracing is done by dividing each beam into concentric, circular rays. For this simulation, 200 rays per beam were used. Each ray is followed from the beam, into the target (where it is absorbed and refracted), and out onto the target chamber wall.

To understand what happens to the ray on its path from the beam to the chamber wall, it is necessary to understand what goes on within the target during an

1

implosion. As the target implodes, a gradually increasing region of plasma forms outside the target called the corona. The electron density within the corona increases as the center of the target is approached. Eventually a density is reached that is so high that no light can penetrate beyond this point within the corona. This place is called the critical surface.

Rays enter the target from the beam at various angles of incidence with respect to the radial direction that determine how far into the corona each ray travels (Figure 1). As the ray enters the corona, its energy starts being absorbed. More of the laser light gets absorbed in areas with higher electron density. Rays that enter the target on the beam axis travel to the critical surface, and therefore travel further into the corona than any other rays. These rays are refracted straight back with most of their energy absorbed. Rays entering the target at angles that are close to the beam axis travel through the corona but never reach the critical surface and are refracted through the corona until they exit at an acute angle with the beam axis. Rays that enter the target further from the beam axis travel through the low-density part of the corona and are not absorbed much; they exit the target at an obtuse angle.

The reflected energy (not absorbed) of the rays from a single beam is distributed in concentric circles around the target chamber wall from the beam entrance to the opposite side. Rays that originate in the outer part of the beam emerge from the target at about 150°-160° to the incoming beam direction (0° corresponds to the rays that are reflected straight back) and yield the most reflected laser light because of their low absorption. Rays at about 165°-180° are produced only early in the pulse when the beam diameter is slightly larger than the initial target diameter and the corona has not yet expanded to a diameter larger than that of the beam. Although the rays that hit the target on axis are the most intense, they produce a very small amount of reflected laser light, because they are highly absorbed. When the corona is formed, none of the rays can pass to the other side of the target; this produces a shadow on the opposite side on the target chamber wall. This is illustrated in Fig. 1.

Figure 1: Ray trajectory and distribution of the light on the chamber wall for a single beam.

The intensity distribution from a single beam was calculated. Since all beams produce the same amount of light energy and are refracted similarly in the target, the intensity distribution from one beam can be used to map the distribution from all 60 beams on the chamber wall by transforming the reflected light distribution of a single beam to the position of all the beams on the wall. Intensity contributions from all beams were added to obtain a map of the total intensity distribution of the reflected laser light on the target chamber wall.

Program

A computer program was written in Fortran to calculate and map the intensity distribution of the reflected laser light.

The target chamber is set in the XYZ plane. The rays are generated in the UVW frame, which is the frame of a given beam. The radius of the chamber wall was arbitrarily set to 1 unit. Each kth ray from the UVW frame is reflected as a circle onto the chamber wall, with the angle of reflection β_K. The intensity of the reflected rays was calculated. For this simulation 200 rays for each beam were used. The boundary angle B_K of the concentric rays was calculated as the half way angle between the angles of rays β_K and β_{K+1}.

The circles that appear on the chamber wall from the reflected rays are divided into a θ-Φ grid on the target chamber wall with a resolution of one degree. Phi (Φ) represents the azimuthal angle within the XY plane and theta (θ) the declination angle within the ZX plane. This grid is used to map each ray into the XYZ frame. This is done by first finding the positions of each grid point of each ray in the UVW frame, transforming them into the XYZ plane using the direction cosines of the beam, and finally computing their angular position in the XYZ plane.

Spherical coordinates and rotation matrices are used to determine the position of each ray. First, direction cosines for the transformation using the position angles of the beams are determined from a table of the positions of the beams (θ', Φ') provided by the OMEGA operations group. Two rotations are required for the transformation: about the Z-axis (azimuthal) and about the Y-axis (declination):

$$\begin{pmatrix} \text{Direction} \\ \text{Cosines} \end{pmatrix} = \begin{pmatrix} \cos(\Phi') & \sin(\Phi') & 0 \\ -\sin(\Phi') & \cos(\Phi') & 0 \\ 0 & 0 & 1 \end{pmatrix} \bullet \begin{pmatrix} \cos(\theta') & 0 & \sin(\theta') \\ 0 & 1 & 0 \\ -\sin(\theta') & 0 & \cos(\theta') \end{pmatrix}$$

Rotation around: z-axis   y-axis

The equations below use the calculated direction cosines to transform the ray positions from the UVW frame to the XYZ frame.

$$\begin{pmatrix} U \\ V \\ W \end{pmatrix} = \begin{pmatrix} \rho \sin(\theta)\cos(\Phi) \\ \rho \sin(\theta)\sin(\Phi) \\ \rho \cos(\theta) \end{pmatrix} \qquad \begin{pmatrix} X \\ Y \\ Z \end{pmatrix} = \begin{pmatrix} \text{Direction} \\ \text{Cosines} \end{pmatrix} \bullet \begin{pmatrix} U \\ V \\ W \end{pmatrix}$$

The following equations were used to calculate Phi and Theta in the XYZ frame:

$$\theta_2 = \text{acos}(Z/\rho) \qquad\qquad \Phi_2 = \text{atan}(Y/X) ,$$

where $\rho^2 = X^2 + Y^2 + Z^2$.

The program takes into account that more than one angle may have the same cosine and tangent values and includes an algorithm that ensures that the correct Phi and Theta values are calculated.

The intensity and the area on the chamber wall where the ray's intensity would be distributed were determined using the following equations:

$$B_K = (\beta_K + \beta_{K+1})/2$$

$$A_K = 2\pi\rho^2(\cos(B_K) - \cos(B_{K-1}))$$

$$I_K = E_K / A_K$$

where A_K is the area of the concentric ring formed by the reflected ray K, I_K, the intensity of the ray at the tank wall, ρ, the radius of the tank wall (set to unity), B_K, the angle of the boundary between rays and E_K, the energy of the reflected ray, obtained from LILAC.

The intensity distribution for each beam was calculated at a given time during the implosion. Fig. 2 shows intensity as a function of the angle of reflection of the rays within a single beam. The steep drop in intensity from 165° to 180° is due to the shadow of the target. At this time the diameter of the corona is larger than that of the beam. Rays that are reflected from the target at angles below 90° are the inner rays of the beam and have a low intensity because they travel the longest distances through the highest densities in the corona and are highly absorbed. Rays at about 150°-165° are the outer rays of the beam that travel through the low density of the corona and thus are not highly absorbed; also there is a higher density of reflected rays at those angles than at lower angles.

4
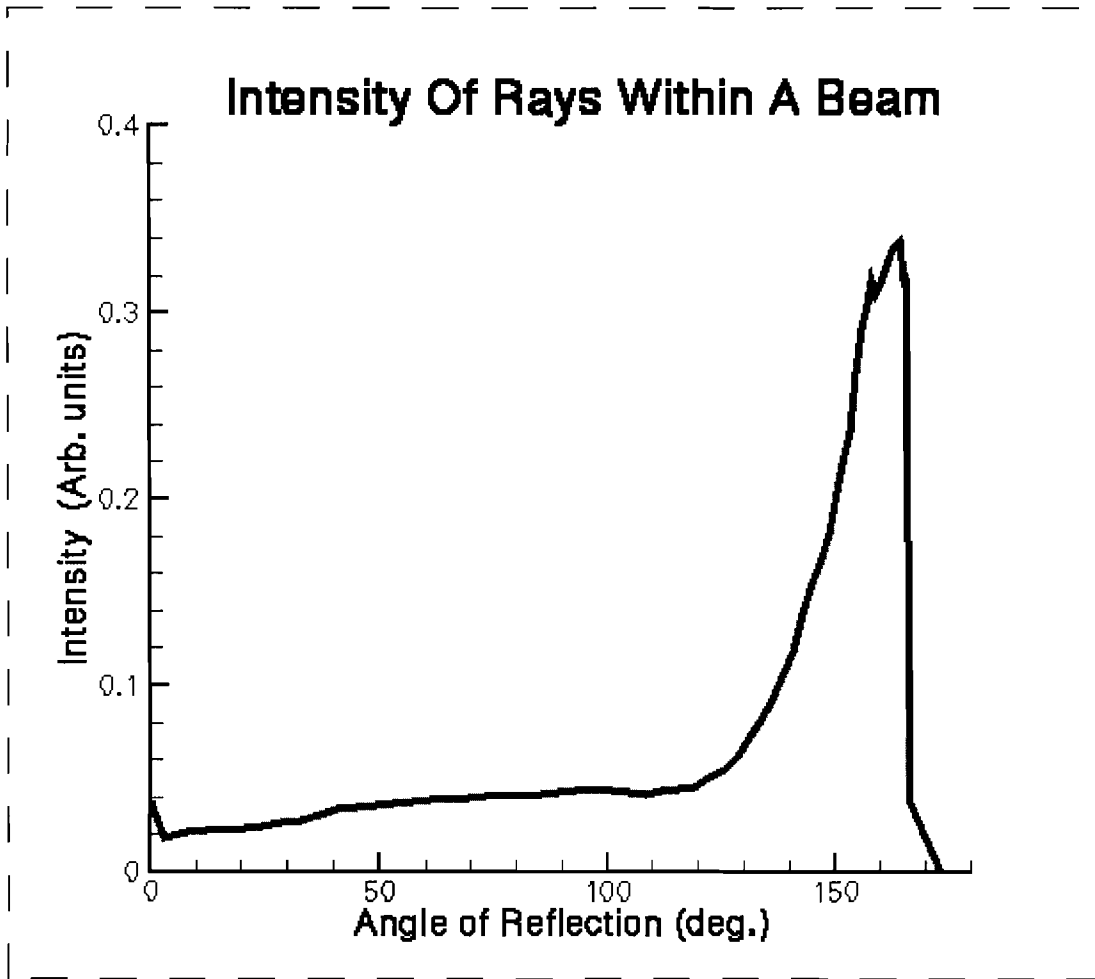
Figure 2: Intensity of the reflected rays from a single beam on the chamber wall.

The total intensity distribution of the reflected laser light along the target chamber wall is obtained by summing the intensity distributions of all 60 beams. Figure 3 is the map of the total intensity distribution of the reflected laser light integrated over the 1-ns pulse of the simulation.

5
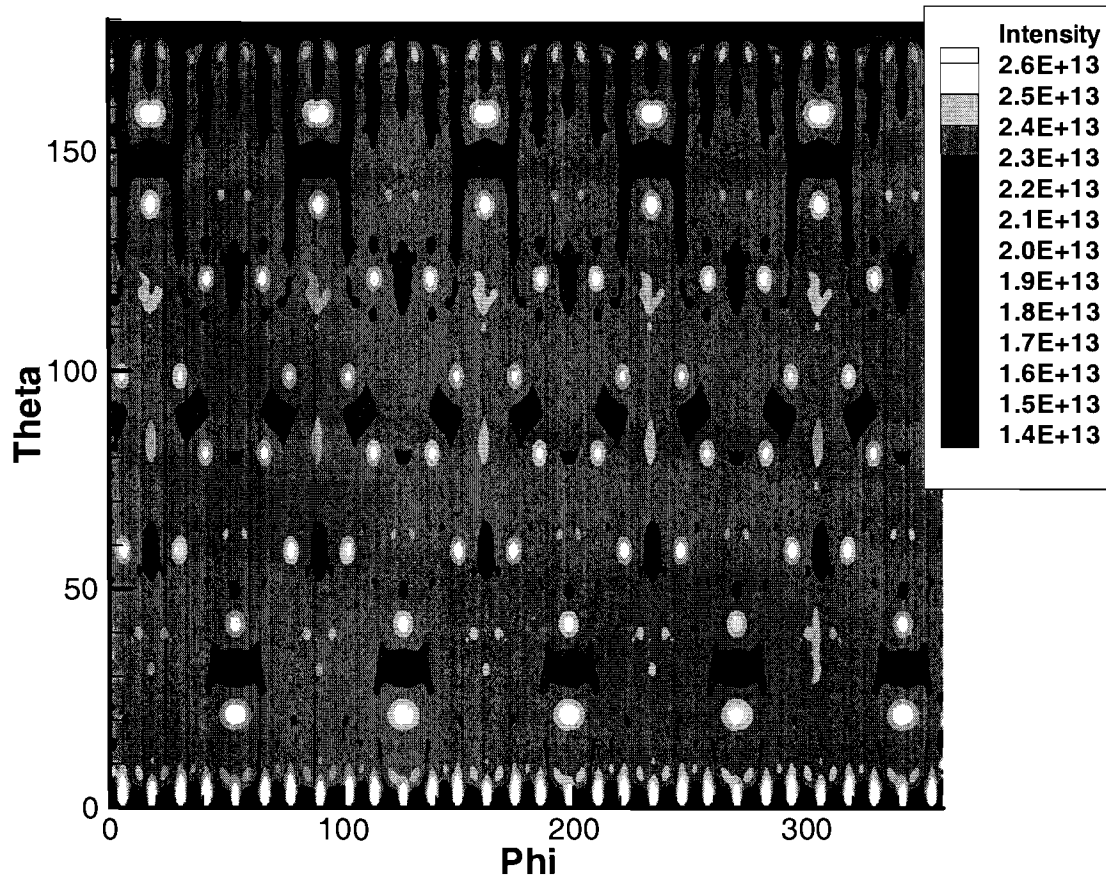
Figure 3: Mapping the 60 beams on the tank wall results in large-scale intensity non-uniformities of about ±5%.

The light areas on the graph represent regions of the tank wall with the highest intensity of the reflected laser light and the dark areas represent regions with the least intensity. The small bright regions result from the rays missing the target early, before the formation of a corona, and collected in the opposite beam lens. The noise at the top and the bottom of the map is due to the use of the simplest mapping methods to generate this graph. From the main part of the graph we can conclude that there is about ±5% peak-to-peak non-uniformity in the reflected light distribution.

Acknowledgements

6

Numerically Calculated Spherical Rayleigh–Taylor Growth Rates

Arun Thakar

Numerically calculated spherical Rayleigh-Taylor growth rates

Arun Thakar
Advised by Reuben Epstein

Summer High School Research Program 2004
Laboratory for Laser Energetics
University of Rochester

Abstract

In inertial confinement fusion, laser beams irradiate a spherical CH shell filled with deuterium-tritium gas, causing it to implode. The deceleration at the end of the implosion creates a Rayleigh-Taylor (RT) instability at the interface between the DT gas and the solid CH shell where small perturbations grow and quench the fusion reaction. Anderson and Betti have proposed reducing RT growth rates by altering the DT composition, thereby smoothing the density profile. Their estimated growth rates however, are inaccurate. A computer program for calculating RT growth rates was adapted to spherical geometry. Growth rates from this program and realistic density profiles confirm that the proposed technique is effective.

I. Introduction

In inertial confinement fusion (ICF), laser beams irradiate a small spherical capsule, causing it to implode. The compression of the capsule during the implosion creates conditions for fusion, a reaction where deuterium (D) and tritium (T), two isotopes of hydrogen, collide and fuse, forming a larger Helium-4 atom as well as a neutron, thereby converting mass into kinetic energy. The spherical capsule, or "target", consists of a thin plastic CH shell filled with DT. The targets used at the OMEGA laser, located at the Laboratory for Laser Energetics (LLE) of the University of Rochester, are approximately 1mm in diameter. The OMEGA laser is a 60-beam, 30-kJ, 351-nm wavelength laser used for direct-drive ICF[1]. The heat created by the compression of implosion on OMEGA—which can produce ion temperatures of 2 to 3 keV—

1

sustains the reaction.

In the first stage of ICF, called the acceleration phase, the initial heat of the absorbed laser pulse causes the CH shell to evaporate, or ablate. The pressure created by the ablation mimics rocket exhaust, forcing the target to implode. During the acceleration phase, there are three density regions: the hot ablating CH shell, the solid CH shell, and the cold DT core. After the laser pulse is complete, the target continues to converge as it enters the second phase called the coasting stage. In the third and final stage, the deceleration phase, the target reaches its maximum density and compression; fusion reactions occur in the core. Following the point of peak compression, the target bounces outwards, bringing an end to the process.

A major problem associated with ICF is the Rayleigh-Taylor instability.[2] When a fluid of lower density accelerates a fluid of higher density, the interface is said to be Rayleigh-Taylor unstable. The force applied to the system causes the initial imperfections, or perturbations, of an unstable interface to grow as an exponential function of time.

As seen in Fig.1, instability occurs within the plasma target at one of two interfaces. There is an outer location at the ablation surface—between the ablating CH shell and solid CH shell—and an inner location, at the fuel-shell interface—between the DT fuel and CH shell. The two instabilities do not occur simultaneously. Instability occurs at the exterior interface as the ablating CH shell drives the implosion during the acceleration phase and at the interior interface as the target compresses during the deceleration phase. Although both sites are important, this project focuses on the interior fuel-shell interface.
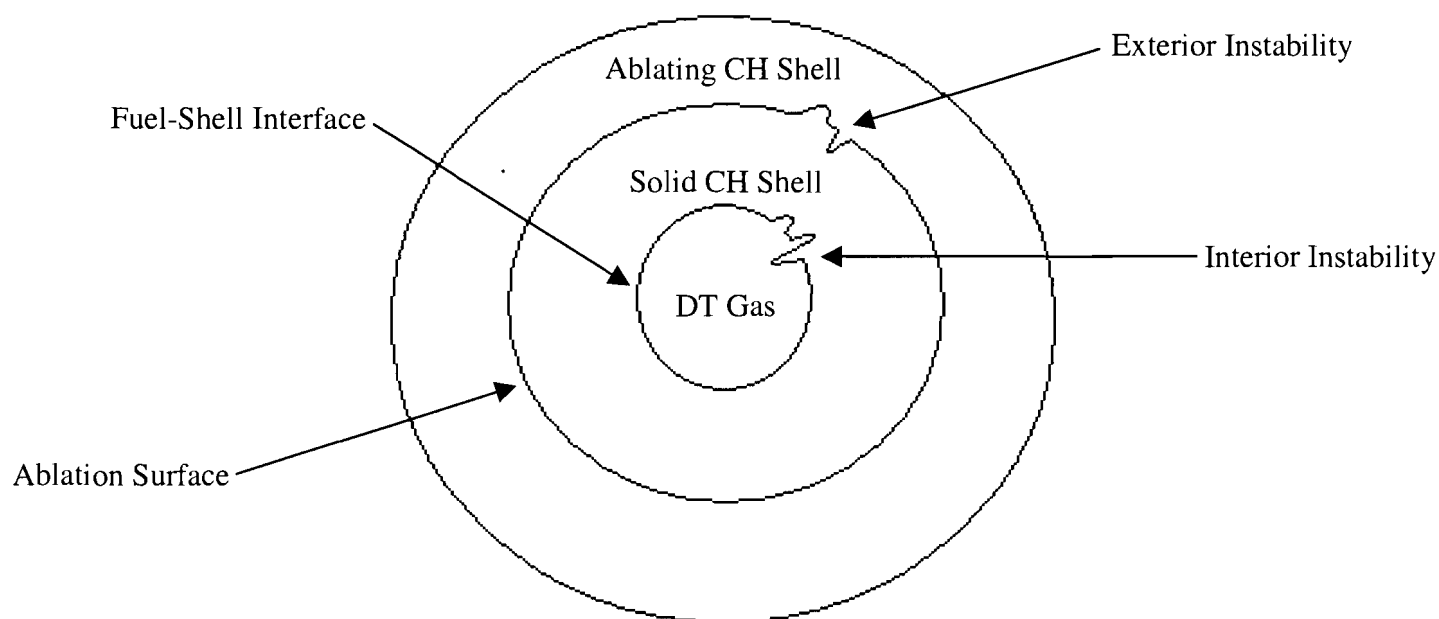
Figure 1: A cross-section of an imploding target. The RT instability occurs at the interfaces between different layers of contrasting density.

The sharp changes in density at the interfaces and the acceleration of the shell are what primarily determine the growth rate of the perturbations. The Rayleigh-Taylor instability is detrimental to the fusion reaction, because when the cooler shell dips into the hotter core, the shell quenches the process by drawing heat away from the fusion reactions. To reduce the growth rate of the instability, LLE scientists Kenneth Anderson and Ricardo Betti propose smoothing the density jump at the fuel-shell interface by altering the molecular composition of DT gas[3], making it heavier, so there is a more gradual increase in density between the fuel core and the shell. The method they use to estimate the change in growth rate, however, does not take into account the realistically varying density profiles. A numerical method can provide a more reliable value for the growth rate than a simple estimate because it takes into account the whole density profile. Thus, the objectives of this project are to: (a) calculate Rayleigh-Taylor growth

rates in spherical geometry by using a numerical method that considers the details of the shell's

density profile, and (b) apply this method to Anderson and Betti's density profiles to verify that

their technique is effective.

II. Finding a Rayleigh-Taylor Equation

The Rayleigh-Taylor instability is accurately modeled by a partial differential

equation which expresses the instability in terms of the velocity of the perturbation, the growth

rate of the perturbation, the acceleration of the system, and the density profile. S. Chandrasekhar

presents such an equation[4] for a perturbation of an incompressible fluid that takes the form of a

sinusoidal ripple along a perturbed planar surface. In the derivation of this equation v_i, $(i=x,y,z)$

represents the components of the velocity perturbation, ρ represents the unperturbed density, $\delta\rho$

is the density perturbation, δp is the pressure perturbation, and g is the acceleration. λ_i denotes a

unit vector in the z direction, the direction of the acceleration of magnitude g. We then know the

following three equations:

$$\rho \frac{\partial v_i}{\partial t} = -\frac{\partial}{\partial x_i}\delta p - g\delta\rho\lambda_i, \tag{1}$$

$$\frac{\partial v_i}{\partial x_i} = 0, \tag{2}$$

and

$$\frac{\partial}{\partial t}\delta\rho + v_i \frac{\partial\rho}{\partial x_i} = 0. \tag{3}$$

Eq.1 is Newton's second law, $F=ma$, Eq.2 tells us that the fluid does not diverge, meaning that it

does not spread. Finally, Eq.3 tells us that as we follow a fluid that does not diverge, its density

does not change. Eq.3 come from the conservation of mass. The next step is to rewrite Eq.1 in the x, y and z directions (*u, v and w*) separately:

$$\rho \frac{\partial u}{\partial t} = \frac{-\partial}{\partial x} \delta p,$$ (4)

$$\rho \frac{\partial v}{\partial t} = \frac{-\partial}{\partial y} \delta p,$$ (5)

and

$$\rho \frac{\partial w}{\partial t} = \frac{-\partial}{\partial z} \delta p - g \delta p.$$ (6)

Eq.2 states that the sum of the velocity gradients in the x, y and z directions must equal 0. This is mathematically expressed as:

$$\frac{\partial u}{\partial x} + \frac{\partial v}{\partial y} + \frac{\partial w}{\partial z} = 0.$$ (7)

Stipulating that the unperturbed density profile is a function of z only, we have:

$$\frac{\partial \rho}{\partial x} = \frac{\partial \rho}{\partial y} = 0,$$ (8)

and Eq.3 can be rewritten as:

$$\frac{\partial}{\partial t} \delta \rho = -w \frac{d\rho}{dz}.$$ (9)

Chandrasekhar assumes that the temporal and spatial dependence of the perturbation velocity and density are modeled by exponentials. This technique is called "separation of variables." One advantage of this technique is that it is relatively easy to integrate and differentiate exponentials. The equations are:

$$\delta \rho(\vec{x}, \vec{t}) = \delta \rho(z) e^{i(k_x x + k_y y)} e^{nt},$$ (10)

and

$$\delta \vec{v}(\vec{x}, \vec{t}) = \delta \vec{v}(z) e^{i(k_x x + k_y y)} e^{\gamma t}. \qquad (11)$$

The wave number, k, is defined as $2\pi/\lambda$ where λ is the wavelength and γ is defined as the

dimensioned growth rate (in units of inverse time). If we take the derivatives with respect to t, x,

y and z we can make some simplifications:

$$\frac{\partial}{\partial t} = \gamma, \frac{\partial}{\partial x} = -ik_x, \frac{\partial}{\partial y} = -ik_y, \text{ and } \frac{d}{dz} = D. \qquad (12)$$

We can also say that:

$$u = \delta v_x, \ v = \delta v_y, \text{ and } w = \delta v_z. \qquad (13)$$

This changes Eq.4-7, and Eq.9 respectively into:

$$\rho \gamma u = -ik_x \delta p, \qquad (14)$$

$$\rho \gamma v = -ik_y \delta p, \qquad (15)$$

$$D \delta p = -\rho \gamma w - g \delta \rho, \qquad (16)$$

$$ik_x u + ik_y v = -Dw, \qquad (17)$$

and

$$\gamma \delta p = -w D \rho. \qquad (18)$$

Next, Chandrasekhar multiplies Eq.14 and 15 by ik_x and ik_y respectively and adds the products

together, yielding:

$$(k_x^2 + k_y^2)\delta p = \rho \gamma (ik_x u + ik_y v). \qquad (19)$$

Substituting Eq.17 and 18 into Eq.19 produces:

$$k^2 \delta p = -\gamma \rho D w, \qquad (20)$$

where k^2 is defined as:

$$k^2 = k_x^2 + k_y^2. \qquad (21)$$

In order to eliminate the pressure perturbation we will need one more equation, obtained by

substituting Eq.18 into Eq.16:

$$D\delta p = -n\rho w + \frac{g}{\gamma}wD\rho \ .$$

(22)

Chandrasekhar eliminates δp using Eq.20 and Eq.22, producing a differential

equation for the perturbation velocity in planar geometry:

$$\frac{d}{dz}\left[\rho\frac{dw}{dz}\right] - \rho k^2 w + \frac{k^2 g}{\gamma^2}\left[\frac{d\rho}{dz}\right]w = 0 \ .$$

(23)

This equation assumes no surface tension and no viscosity. In the equation, γ^2/kg is a

dimensionless squared growth rate of the perturbations, where γ is the dimensioned growth rate.

Dimensionless quantities are used because they allow the simplification of complex

mathematical expressions in computer code. Also, seeking the dimensionless quantities of a

problem reveals the characteristic scales, such as time, $(kg)^{-1/2}$, and distance, k^{-1}.

To find an analytic solution to Eq.23, we need a sample case. For a simple step

density jump, where ρ_2 is greater than ρ_1, the dimensionless squared growth rate is equal to the

Atwood number

$$\frac{\gamma^2}{kg} = A$$

(24)

defined as:

$$A = \frac{(\rho_2 - \rho_1)}{(\rho_2 + \rho_1)} \ .$$

(25)

Anderson and Betti used the Atwood number to gauge the effectiveness of their proposed

smoothing technique. The formula assumes that there is a discontinuity in the density profile and

that the rest of the density along the profile is constant. However, the density profiles that

Anderson and Betti consider are continuously variable, not simple in shape. Therefore the

Atwood number's use in the situation is likely to be a poor approximation of the true

dimensionless squared growth rate.

To investigate how one finds an analytic solution to the differential equation, I

solved Eq.22 for a square-wave density profile. The square wave creates a second interface from

which instability can arise, as well as a third density region, ρ_3. However, for simplicity, we

assume that ρ_3 is equal to ρ_1.

Figure 2 illustrates the square-wave problem. The function which peaks on the left

is the perturbation velocity, and the square wave is the density profile. The z labels will be used

later to explain the analytic solution for the equation.
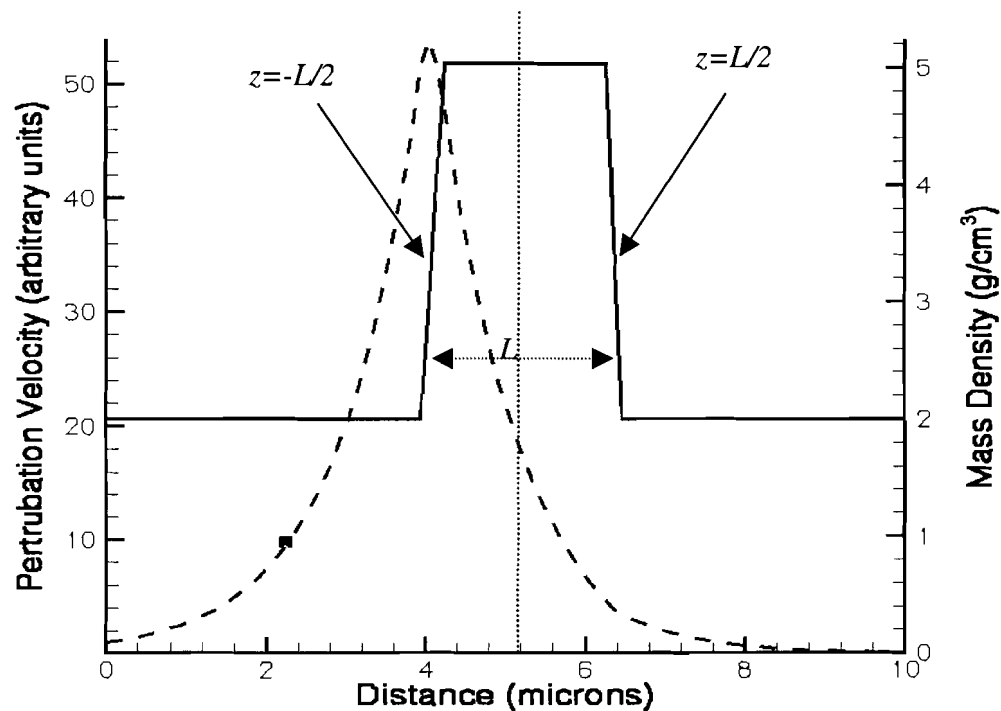
Figure 2: The solid line represents the density profile of the shell, and the dashed line represents the perturbation velocity. The perturbation velocity peaks at the first interface.

The type of differential equation we are solving is called an eigenvalue equation.

The set of solutions to eigenvalue equations is a set of eigenfunctions each with a corresponding eigenvalue. In this case, $w(z)$, the velocity perturbation is the eigenfunction, and γ^2/kg, the dimensionless squared growth rate, is the eigenvalue. To solve the differential equation and obtain the eigenfunction, one must integrate it and apply matching and boundary conditions, which depend on the chosen case.

How we expect the function to act as it goes to negative and positive infinity are the boundary conditions. We know the solution to the differential equation over the different constant regions of the density profile. Logically, the perturbation speed cannot be growing infinitely large when we are very far from the interface. The boundary conditions state that the velocity perturbation must approach zero as we travel away from the density jump. Assuming that

$$\frac{\partial \rho}{\partial z} = 0 , \tag{26}$$

within the constant density regions. The solution to the differential equation for the first region, ρ_1, is:

$$w_1 = Ae^{kz} , \tag{27}$$

for the second region, ρ_2 is:

$$w_2 = Be^{kz} + Ce^{-kz} , \tag{28}$$

and for region, ρ_3, is:

$$w_3 = De^{-kz} . \tag{29}$$

The matching conditions are found at the interfaces where two perturbation velocity equations come into contact. Because the velocities of Eqs.27 and 28 are continuous at the first peak in Figure 2, we know that Eqs.27 and 28 give equal values for the perturbation at $z = -L/2$.

9

Using this information we get:

$$A = B + Ce^{kL}.\tag{30}$$

The other matching condition is at the second density discontinuity at $z=L/2$ where Eqs.28 and

29 are continuous. The equation we get from this is:

$$D = Be^{kL} + C.\tag{31}$$

An expression for the dimensionless growth rate can be found much the same way

as in the single-jump case. We integrate Eq.23 over the first density discontinuity, getting:

$$\rho_2 \frac{dw_2}{dz} - \rho_1 \frac{dw_1}{dz} + \frac{gk^2}{\gamma^2}(\rho_2 - \rho_1)w_1 = 0.\tag{32}$$

Doing the same over the second density discontinuity yields:

$$\rho_3 \frac{dw_3}{dz} - \rho_2 \frac{dw_2}{dz} + \frac{gk^2}{\gamma^2}(\rho_3 - \rho_2)w_2 = 0.\tag{33}$$

After allowing $\rho_1 = \rho_3$, we have enough information to solve for the dimensionless growth rate,

expressed as:

$$\frac{\gamma^4}{k^2 g^2} = \frac{(e^{2kL} - 1)(\rho_2 - \rho_1)^2}{e^{2kL} \cdot (\rho_2 + \rho_1)^2 - (\rho_2 - \rho_1)^2}.\tag{34}$$

$\gamma^4/k^2 g^2$ is the square of the squared growth rate quantity, which is what we are trying to find, the

heavy fluid mass density is ρ_2 and the light fluid mass density is ρ_1, g is the acceleration of the

implosion, and L is the thickness of the shell. Because the product $k\,L$ is dimensionless, we are

expressing the thickness of the shell in units of the wavelength. This makes kL more significant

than just L. I verified the analytic solution using Jue Liao's program[5], which calculates the

dimensionless growth rate of the perturbation velocities in the planar geometry when given a

shell length, L, and a density profile.

If we evaluate Eq.34 for the limit of kL approaching infinity, the dimensionless

squared growth rate, γ^2/kg, becomes the Atwood number, the rate given by Eq. 24 for a single interface. In this limit where a large number of wavelengths separate the two interfaces, the perturbations act independently as they do at single-step interfaces. They are isolated and do not influence each other.

III. A Rayleigh-Taylor equation in spherical geometry

The next step was to write a program that calculates Rayleigh-Taylor growth rates in spherical geometry. To do this I needed a differential equation for the velocity perturbation in spherical geometry. Dr. Epstein assisted me by deriving the equation[6], which is:

$$\frac{l(l+1)}{x^2}\left[1-\frac{g}{\gamma_0^2 \cdot R_0}\frac{1}{\rho}\frac{d\rho}{dx}\right]\cdot y - \frac{1}{\rho}\frac{\partial}{\partial x}\left[\rho\frac{\partial y}{\partial x}\right]=0. \tag{35}$$

There are striking similarities between this spherical equation and the planar Eq.23, with the wave number k replaced by l/R_0. l is called the modal index and R_0 is the radius of the target at the instant where the shell is momentarily static, or at the "bounce." The change in k makes the new dimensionless squared growth rate $\gamma_0^2 R_0/g$ found inverted in the formula. The perturbation function is expressed as y, which is defined as $y=wr^2$ where w is the perturbation velocity and r is the radial coordinate. The shell radius is made dimensionless by letting $x=r/R_0$. Finally, the $(l+1)$ term arises due to properties of spherical harmonics. Harmonic functions such as those we use to model the perturbations behave differently in spherical geometry than sine and cosine do in planar geometry in subtle but important ways.

Another significant difference between Eq.35 and 23 is that the boundary conditions in the spherical case are now expressed as a power law and no longer exponential functions. The solution to Eq.35, assuming constant density, is for a radius, r near $r=0$:

$$y = x^{l+1} \tag{36}$$

and for a radius, r far greater than R_0,

$$y = x^{-l} .$$ (37)

We see that Eqs.36 and 37 satisfy the boundary conditions requiring that the inner and outer velocity perturbations be equal to zero. This is similar to the boundary conditions in planar geometry, except that the inner boundary condition now applies at $r=0$ rather than at $z=-\infty$.

IV. Adapting an existing program to function in the spherical geometry

Next, I adapted Jue Liao's program to function in spherical geometry. To do this, equations in the program used to solve Eq.23 were reworked to solve Eq.35. In spherical geometry, the user must enter R_0 and l instead of kL. Also, the program allows the user to enter an arbitrary density profile, by importing it through a data file. This is a significant improvement over the old program where the user entered simple density profiles by hand.

The numerical method used by the program to determine the growth rate is called the "shooting method". The shooting method works as follows: The user enters an initial guess for the growth rate (eigenvalue) into the program, and the perturbation velocity is calculated for the whole density profile by integrating Eq.35 from $r=0$ to the end of the density profile. We are shooting for a perturbation velocity of zero as r approaches infinity. If the boundary condition is not satisfied, the guess of the growth rate is adjusted based whether or not the perturbation velocity was overestimated or underestimated at the right boundary, and the perturbation velocity is recalculated for the entire density profile. The iteration process continues until the program converges on the growth rate which allows the perturbation velocity to satisfy the boundary conditions. When the perturbation velocity satisfies the boundary condition, the dimensionless squared growth rate is the eigenvalue, and the perturbation velocity is the eigenfunction.

In order to input the equation into the computer, one must split the second-order differential equation into two first-order differential equations. The equation becomes easier to work with once some substitutions are made:

$$\Gamma = \frac{\gamma_0^2 R_0}{g} \text{ and } A = \frac{1}{\rho}\frac{d\rho}{dx}.$$ (38)

The dimensionless squared growth rate will now be referred to as Γ. Entering these substitutions into Eq.35 yields:

$$\frac{l(l+1)}{x^2}\left[1-\frac{A}{\Gamma}\right]y - \frac{1}{\rho}\frac{\partial}{\partial x}\left[\rho\frac{\partial y}{\partial x}\right] = 0.$$ (39)

Next, we can carry out the indicated differentiation on the second term, making the equation:

$$\frac{l(l+1)}{x^2}\left[1-\frac{A}{\Gamma}\right]y - \frac{1}{\rho}\frac{\partial\rho}{\partial x}\frac{\partial y}{\partial x} - \frac{\partial^2 y}{\partial x^2} = 0.$$ (40)

This creates another A term making the equation:

$$\frac{l(l+1)}{x^2}\left[1-\frac{A}{\Gamma}\right]y - A\frac{\partial y}{\partial x} - \frac{\partial^2 y}{\partial x^2} = 0.$$ (41)

One more substitution will greatly simplify the equation before the final split:

$$B = \frac{l(l+1)}{x^2}\left[1-\frac{A}{\Gamma}\right].$$ (42)

Now the equations can be split by defining:

$$v = \frac{\partial y}{\partial x} \text{ and therefore } \frac{\partial^2 y}{\partial x^2} = \frac{\partial v}{\partial x}.$$ (43)

This results in two first-order differential equations:

$$\frac{\partial y}{\partial x} = v \text{ and } \frac{\partial v}{\partial x} = By - Av.$$ (44)

To convert these equations into a form suitable for entry in a programming

13

language, FORTRAN in my case, I needed to write these as simple step equations. Numerical

methods utilize step equations, which calculate values for y and v at each iteration. In the

program J denotes which spatial point the program has calculated last. As the program creates

the whole integration grid, J increases until it reaches its final value (specified by the user). The

step equations are centered half-way between each integration point:

$$\frac{y_{J+1} - y_J}{x_{J+1} - x_J} = \frac{v_{J+1} - v_J}{2} \qquad (45)$$

and

$$\frac{v_{J+1} - v_J}{x_{J+1} - x_J} = B\left(\frac{y_{J+1} + y_J}{2}\right) - A\left(\frac{v_{J+1} + v_J}{2}\right). \qquad (46)$$

Making the substitution

$$H = \frac{x_{J+1} - x_J}{2} \qquad (47)$$

into Eqs. (45) and (46) and solving the two equations simultaneously, we obtain the step

equations used in the FORTRAN program:

$$y_{J+1} = \frac{\left(H^2 B + HA + 1\right)y_J + 2Hv_J}{\left(-H^2 B + HA + 1\right)} \qquad (48)$$

and

$$v_{J+1} = \frac{2HBy_J + \left(H^2 B - HA + 1\right)v_J}{\left(-H^2 B + HA + 1\right)}. \qquad (49)$$

V. Application of the program to proposed density profiles

The next step was to apply the working program to realistically important density

profiles. Kenneth Anderson and Ricardo Betti simulated density profiles where the fuel-shell

density jump is smoothed out in order to reduce the growth rate of the instability. They did this

by altering the composition of deuterium-tritium gas proportions of the fuel in hydrodynamic

simulations of OMEGA implosions. As stated earlier, the Atwood number is not an accurate

estimate because it is defined for a single interface separating fluids of constant density, which is

not a good description of the density profile of the shell of an ICF implosion near peak

compression. The numerical program can find a growth rate in spherical geometry for the

proposed density profile.

Figure 3 below shows a graph of the perturbation velocities calculated by the

program, as well as three corresponding density profiles that Anderson and Betti used. The

density profiles are functions that peak on the right, and the perturbation velocities are the

functions that peak on the left. Each line corresponds to a different composition of DT gas. The

solid line is the altered DT_8 gas that creates a smoothed density profile. The ratio of tritium

molecules to deuterium molecules is eight to one. Since more of the heavy molecule is used, the

mass density increases, accounting for the smoothing effect. The dashed line represents the

density obtained using standard DT gas as the fill gas, and the dotted line is obtained using DD

gas. The program gives us values for the dimensionless growth rates which we can convert back

to dimensional units. We assume there are 100 points of spatial integration, and the l mode

index value is 5; making the wavelength $\lambda=56.5$ µm for $R_0=45$µm. 100 points of integration

insures that the shape of the eigenfunction will be resolved without creating unnecessary steps,

while still accurately describing the eigenfunction's form. The value for $R_0=45$µm is chosen

because it is the radius at which the fuel-shell interface is located at peak compression. The

dimensionless squared growth rate (Γ) produced by the program for DT_8 is 0.65. The

dimensionless squared growth rates for standard DT and DD are $\Gamma = 0.75$ and 0.81, respectively. Anderson and Betti's estimates using the Atwood number are as follows: $\Gamma = 0.0$ for DT_8, 0.26-0.33 for standard DT and 0.43-0.47 for DD gas. It is clear that the numerical solution has provided a better estimate of the instability's growth rate and makes an important correction.

We also have enough evidence to state that even for low l mode values, smoothing the density ramp by altering the composition of the DT gas reduces the growth rate of the Rayleigh-Taylor instability. It is important to note that an infinite number of possible eigenfunctions for smaller values of Γ exist; we are primarily interested, however, in the function with the highest eigenvalue. For instance, the program produces an eigenfunction with a lower growth rate. This function dips far below the x-axis before returning up to meet the right boundary condition.

The perturbation velocity in Fig.3 is expressed in terms of "arbitrary units" because changing the normalization of the eigenfunctions by a constant factor does not affect the growth rates. One can multiply any of the eigenfunctions by constants and the calculated growth rates will remain the same.
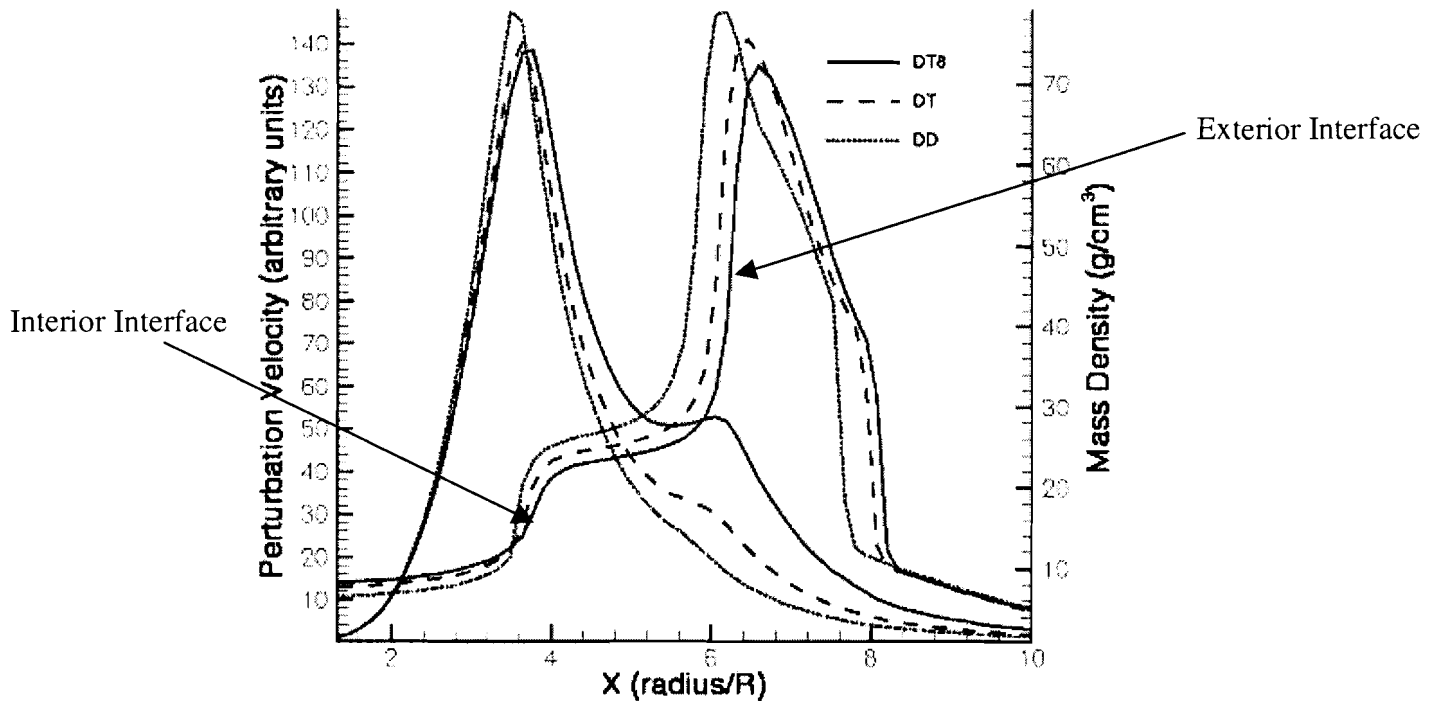
Figure 3: The three representative density profiles peak on the right, while the perturbation velocity profiles peak on the left. The smoothed DT8 density profile produces the lowest peak of the three meaning that the perturbation velocity and the instability is the lowest of the three.

VI. Conclusions

The spherical Rayleigh-Taylor program is a useful tool that can be used to see the impact of altering the density profile on the growth rate of the Rayleigh-Taylor instability. In addition to this primary purpose, the program also provides the perturbation velocity across the whole density profile. The results show us a variety of interesting features of the perturbation velocities: First, the velocity perturbation is significantly larger at the fuel-shell interface than the ablation surface. This is interesting because the second density jump, the one located at the ablation surface, is far greater than the one at the fuel-shell interface. Intuitively, one would expect the more conspicuous features of the density profile to have a greater effect on the perturbation velocity; however, this is not so. This verifies that the instability is greatest at the fuel-shell interface at peak compression. As we move to higher l values, the second peak will

become better defined. This is because the wavelength of the velocity perturbations at high l values is very small; accordingly the interaction between the perturbations is less. Another interesting result is that the smooth DT_8 profile has a significantly larger second velocity perturbation peak, relative to the DT and DD gases.

A problem with the program is that the step equations are "stiff", which makes it difficult for the program to function with high l mode values. The step equations used in the program are very sensitive at high l values, meaning that results vary greatly with minor changes in input. If the program is given a guess that is slightly too high or too low it will not give the eigenfunction with the highest eigenvalue, the one we seek. In the future, it would be beneficial to apply the program to high l mode values. This can give us even more information about the perturbation velocity and the growth rate. At this stage of development, however, the program still serves as a valuable tool because it more accurately calculates RT growth rates for arbitrary density profiles in spherical geometry than previous approximate methods.

VII. Acknowledgements

VIII. References

1. "A Unique Natural Resource." <u>Laboratory for Laser Energetics.</u> 1 November 2004.

<http://www.lle.rochester.edu/02_visitors/02_aboutomega.html >.

2. G. Taylor, Proc. R. Soc. London Ser. A **201**, 192 (1950).

3. K. Anderson and R. Betti, private communication.

4. S. Chandrasekhar. *Hydrodynamic and Hydromagnetic Stability.* International Series of

Monographs on Physics (Dover Publications, Inc., New York, 1961), Chap. X, p. 428.

5. Jue Liao. "Rayleigh-Taylor growth rate for arbitrary density profiles calculated with a

variational method." <u>Laboratory for Laser Energetics Summer High School Project Report.</u> 2002.

6. R. Epstein, private communication.

Computer Modeling of Polymer Cholesteric Liquid Crystal Flake Reorientation

Glen Wagner

Computer Modeling of Polymer Cholesteric Liquid Crystal Flake Reorientation

Glen Wagner

Fairport High School

Advisors: Tanya Z. Kosc and Kenneth L. Marshall

Abstract

A polymer cholesteric liquid crystal (PCLC) flake suspended in a host fluid of differing dielectric constant will reorient due to the difference between the dielectric constants of the flake and the fluid host. A basic equation of motion for flake reorientation has been developed, but it is necessary to investigate the details of the electrical torque acting on the flake. The electrical torque is driven by Maxwell-Wagner polarization, and computer modeling using COMSOL's software, FEMLAB, allows this phenomenon to be investigated. Modeling results have confirmed the experimental phenomenon of flake reorientation based on the examination of the electric field, the electric potential distribution, and the surface charge density.

Background

As their name suggests, liquid crystals have properties of both crystals and liquids. In crystals the molecules have fixed positions, arranged geometrically. In liquids, orientation and position are random and disorganized. In liquid crystals, the molecules are partially organized. In nematic liquid crystals, for instance, all the molecules point the same way, but aren't arranged in a neat box pattern, or any other pattern, for that matter. In cholesteric liquid crystals, the molecules orient in a helical fashion (Fig 1) [1]. This helical pattern of orientation gives cholesteric liquid crystals some of their unique properties, such as selective reflection of circularly polarized light[2]. Polymer liquid crystals are polymers that include liquid crystal molecules either as part of the backbone or side chains of the polymer.

Polymer cholesteric liquid crystal (PCLC) flakes are formed by applying a thin PCLC film to a silicon wafer. Liquid nitrogen is then applied to cause a

Figure 1: Molecular arrangement of cholesteric liquid crystals. (from Ref. 1)

1

sudden temperature change. Differential thermal expansion of the PCLC film and silicon wafer causes the PCLC film to fracture into flakes[3]. This generally leads to irregularly shaped flakes. However, it is possible to etch out patterns through soft lithography, to allow flakes of a desired shape to be formed[2].

The orientation of polymer cholesteric liquid crystal (PCLC) flakes in a slightly conducting host fluid can be controlled by electric fields. An AC field causes the flakes to rotate about their longest axis, so that their second longest axis aligns parallel to the electric field. When the field is turned off, the flakes gradually return to an orientation such that both the longest and the second longest axes are parallel to the substrates[2].

Due to this property, PCLC flakes show great promise in the display field. Normal liquid crystal displays (LCDs) operate by sandwiching a nematic liquid crystal fluid between two crossed polarizing filters. The orientation of the liquid crystal molecules controls the polarization of light, either permitting or preventing the light from passing through both polarizing filters[4]. The orientation of the liquid crystal molecules can be controlled by the application of an electric field. Using polarizers places a strict limit on the amount of light that can be reflected back or transmitted, no better than 50% of the incident light[3]. PCLC flake based displays could offer greater reflection, and thus brightness. PCLC flakes also offer the ability to use circularly polarized light, which is useful in some applications. The other major advantage of PCLC flakes lies in microencapsulation. Microencapsulation involves enclosing small droplets of flake-containing host fluid inside a sheet of rubber-like material. Advantages include the ability to make flexible displays, increased ease of creating pixilated devices as compared to non-microencapsulated designs, and the possibility of making bi-stable displays, displays that only need power to change the image they show, not to maintain the image[3].

The driving mechanism behind the flake reorientation is Maxwell-Wagner polarization, a build up of surface charge at the interface between two different dielectrics[2]. Opposite charges are built up on the top and bottom of the flake, as shown in Fig. 2. The applied electric field will exert a torque upon the flake in Fig.2 if and only if the flake has some slight tilt bias with respect to the substrates. Both PCLC flakes and the host fluid are dielectric materials. Each molecule of a dielectric has a slightly asymmetric charge distribution. Normally, the molecules are oriented randomly, so no charge develops. However, in an electric field, the molecules reorient so that the positive side of the molecule points in the direction of the electric field. There is no net change in charge, as no charges leave the flake. However, at each end of the dielectric object, a surface charge is generated where the charged ends of the molecules line up[5]. The charge is opposite at opposite ends of the flake, generating a dipole moment.

2

Figure 2: Charge distribution around flake due to Maxwell-Wagner interfacial polarization. The red rectangles represent the electrodes, while the arrow indicates the electric field direction. The flake will only reorient if it is not perfectly parallel to the substrates (i.e, if there is a tilt bias in the flake long axis)
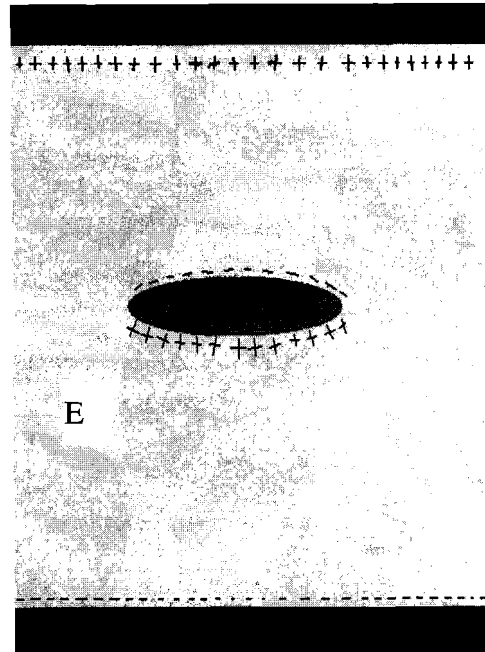
The dipole moment can be acted upon by the electric field surrounding the flake, generating a torque which causes the flake to rotate. The direction of the torque can be visualized by placing the base of the electric field vector at the tip of the dipole moment vector.

Equations that predict how long it will take for the flake to align with its second longest axis parallel to the electric field have been derived from first principles using an ellipsoidal shape flake, instead of the more rectangular cross-section of most flakes, for simplicity's sake[3]. There are two problems: it is not well understood what the equations mean in the physical sense (i.e. what was actually happening to cause the rotation), and the equations are incomplete, as their predictions don't match perfectly with the experimental results. The object of this project was to model the electric fields and potentials in and around the flake to try to come to a better understanding of the physical process involved, and hopefully, determine what is missing from the derived equations.

Parameters used to describe configuration of the cell

PCLC flakes are generally suspended in a host fluid between two glass plates coated with indium-tin oxide (ITO). Almost all modeling conducted in the course of this project used $5*10^{-5}$ S/m (Siemens/meter) and 69 as the conductivity and dielectric permittivity of the host fluid, respectively. $1*10^{-12}$ S/m and 2.89 were used as the conductivity and relative permittivity of the flake. These values were used for all FEMLAB model-derived figures in this report. All figures also use a cell gap, or

3

distance between the glass substrates, of 50 μm. The flakes are modeled as ellipses, with a major axis of 40 μm , representing the second longest axis of the flake, and a model minor axis of 6 μm, representing the flake's shortest axis. In all models except ion transport models, a voltage of 10 V was applied to the bottom plate, this representing the peak voltage in AC models. In ion transport models, the applied peak voltage was only 0.03 V. The upper plate was grounded in all modeling.

FEMLAB modeling

In order to explore flake reorientation, FEMLAB was used to generate computer models of the flake/host fluid capacitor-like system under AC and DC fields. FEMLAB is a multi-physics simulation program made by COMSOL. It is based on partial differential equations (PDE), which can either be written by the user, or selected from a series of provided application modes. The provided application modes consist of a set of PDEs designed to model certain circumstances, such as static electric fields. All that is then required is to define the geometry of the objects to be modeled and insert proper values for the variables representing the properties of the materials, such as conductivity. For this investigation, only the built-in application modes were used. FEMLAB is called a multi-physics simulation because of its ability to couple multiple application modes together by linking variables. It is possible to use the output variables of one model to define the input variables of a second, and even to use the output of the second model to define the input of the first model. This feature allows even rather complex systems to be modeled without having to directly define custom PDEs. The version of FEMLAB used for this report (v3.0.0.228), can't model rotating flakes. All the geometric domains of the model, which are used to define the shape and position of the flake, must be static.

Initially, a series of models of flake systems in a DC field were generated, with the flake at varying angles with respect to the horizontal. The flakes were modeled as ellipsoidal, despite actually being more rectangular, because the theoretical work of Ref. 3 treated them as ellipsoids. These early models showed that the electric potential dropped much more rapidly across the flake than across the host fluid (in this case, propylene carbonate). This led to interesting electric field distributions in which the electric fields outside the flake follow the contour of the flake's external surface fairly closely. The most interesting result was the direction of the electric field inside the flake itself. For a wide range of angles, the internal electric field of the flake was nearly perpendicular to the second longest axis of the flake, and this field direction was maintained when the flake was rotated 45 degrees with respect to the electrode plates. When the flake was rotated 30 degrees from the plane of the electrodes, the internal

4

electric field in the flake is at an angle that is roughly 75 degrees to the normal of the flake's second longest axis (Fig 3). Dielectric materials in an electric field align themselves so as to set up an electric field opposing the applied field. The molecules of the dielectric rotate, or the electric distribution changes, so that the molecules align with the applied electric field. Because the molecules merely realign there is no net charge in the material or any charge in the body of the dielectric material. However, surface charges do build up at the edges of the material. In the flakes, this would generate a dipole moment parallel to the internal electric field upon which the electric field could work, causing the flakes to move. The torque applied is equal to the cross-product of the induced dipole moment vector and the electric field vector. If the dipole moment were along the second longest axis, as originally believed, the torque exerted by the modeled electric field would force the flake towards a vertical orientation. However, the modeled internal electric field of the flake would lead to a dipole moment fairly perpendicular to the second longest axis, which would cause a restoring torque on the flake, forcing it back towards the horizontal. This predicted rotation is in the opposite direction of the observed rotation, presenting a major problem.

Next, the flake system was modeled in an AC field, using the Quasi-statics, small in-plane current application mode of FEMLAB's Electromagnetics module. This application mode uses a time harmonic solver, which assumes that the model undergoes periodic, rather than transient changes.

After FEMLAB solves the model, it is possible to change the field's phase during post processing. Solutions to this sort of model were very similar to that of the DC models (Fig 4). Two things are of interest, however. The AC models confirmed that the dipole moment would switch directions with the field, although not necessarily without some lag. Therefore, the flake would always rotate in the same direction, regardless of the actual direction of the applied electric field. This behavior reflects the quadratic dependence upon the electric field seen in the theoretical equations, which implies that rotation is independent of the sign of the applied electric field.

Although FEMLAB is not currently capable of modeling rotating flakes, it is possible to get around this limitation in certain cases in which the solution at a given angle could be solved independently of the solution at an earlier angle. Because the electric field changes so much faster than the flake rotates, it was assumed that a series of static flake models at different angles would be a suitable approximation of a rotating flake. MATLAB was used to generate the series of models needed, generating a static model of a flake at the angle it would achieve at a certain point in time. In each model, the magnitude of the applied electric field was determined by what the phase of the AC field would be at the point in time the model represents. An equation was derived from

5

the previously done theoretical work to predict how much the flake would rotate in a set period of time. This new position was used to create a FEMLAB model. The plot of this model was then saved as a unique, separate image file, and then this cycle was repeated. The program automatically ended once the flake reached a preset angle. A separate program was then written to cycle through the generated images, displaying each in turn, to function as an animation.

It is believed that the motion of ions within the host fluid and the flake plays an important role in explaining flake rotation, including, possibly, the reason that the theoretical calculations were off by a significant factor in calculating the rotation time. Therefore modeling of ion movement was undertaken. For this, a multiphysics model had to be created by coupling the Electrokinetics application mode of the Chemical Engineering module to the Electrostatics generalized application mode of the Electromagnetics module. The Quasi-statics, small in-plane currents application mode wasn't used, because a time dependent, rather than time harmonic model was needed. Initial attempts at coupling these two application modes via voltage were unsuccessful, apparently because the values used for the applied potential were excessively high. Before this problem was resolved, a series of models were then made using only the Electrokinetics application mode, which allowed for different diffusion properties between the flake and host fluid, but could only apply a uniform electric field.

After the problems coupling the Electrokinetics and the Electrostatics generalized application modes were resolved, models were created that could simulate ion movement in the electric fields set up by the flake-capacitor system. Two nearly identical species of ions were used in most models, the first with a charge of one positive elementary charge, the other with one negative elementary charge. Later, the concentration of ions was linked to the space charge density in the electrostatics model. However, to retain comprehensible modeling, the space charge density so calculated had to be multiplied by 1×10^{-6}, so it probably was inaccurate. One major problem was never resolved. There is very little information available on the type, mobility, and concentration of the ion species involved, so out of necessity much of the modeling relied on reasonable guesses and various idealizations to get a model in which it was easy to see what was happening. From these it was easy to see the charge build up on each plate. As would be expected, a positive charge built up on the negative plate, and vice versa. At every polarity switch of the applied electric field, the collected ions would be forced off the plate in a layer. Where not obstructed, this layer of ions would soon disperse and neutralize. Ions built up on both sides of the flake. On the side of the flake nearest to the negative electrode, a negative charge would build up, and vice versa (Fig 5). As time progressed, these ion concentrations would move towards the center of the flake

6

All the modeling that has been done so far has indicated that the flake would not align with its second longest axis parallel to the electric field, but rather rotate so that the second longest axis is parallel to the substrates. There is one possible answer, however. The equation for the dipole moment of one axis is [2]

$$p_i = \frac{4\pi}{3} a_i a_j a_k \left[\frac{\varepsilon_h \left(\varepsilon_p - \varepsilon_h \right)}{\left[\varepsilon_h + A_i \left(\varepsilon_p - \varepsilon_h \right) \right]} \right] E_{oi}$$

p_i = induced dipole moment along flake axis i
a_i = length of flake axis i
ε_h = relative dielectric constant of host fluid
ε_p = relative dielectric constant of PCLC flake
E_{oi} = electric field applied along flake axis i

When ε_p is less than ε_h, which is the case in the examined system, the dipole term is negative. This would mean that the dipole moment is actually *anti-parallel* to the electric field, rather than parallel to the electric field, as had been previously assumed.
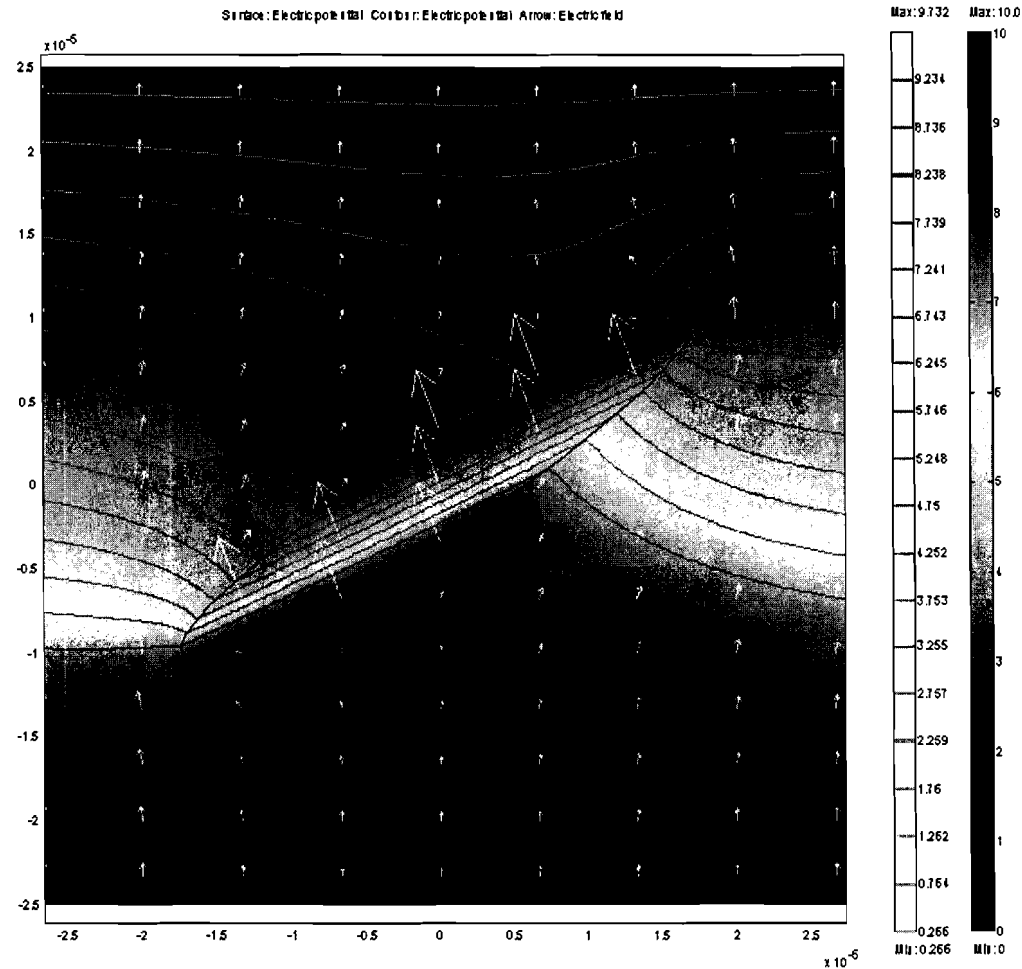

| Figure 3: A flake in a DC field, rotated with its long axis approximately at a 30 degree angle from the substrates. | Surface: Electric potential Contour: Electric potential Arrows: Electric field |

Now, taking the cross product of the induced dipole moment and the exterior electric field would result in a torque forcing the flake towards a vertical orientation with its second longest axis parallel to the applied electric field.

This argument also makes sense physically. In the previous discussion of the dipole moment, the host fluid's contribution to the surface charge at the host fluid-flake interface was neglected. The host fluid has a higher dielectric constant than the flake does, which means that the dielectric particles of the host fluid align more closely to the applied electric field than those of the flakes. The host fluid would therefore generate a stronger surface charge in a given applied electric field than the flake would. Because
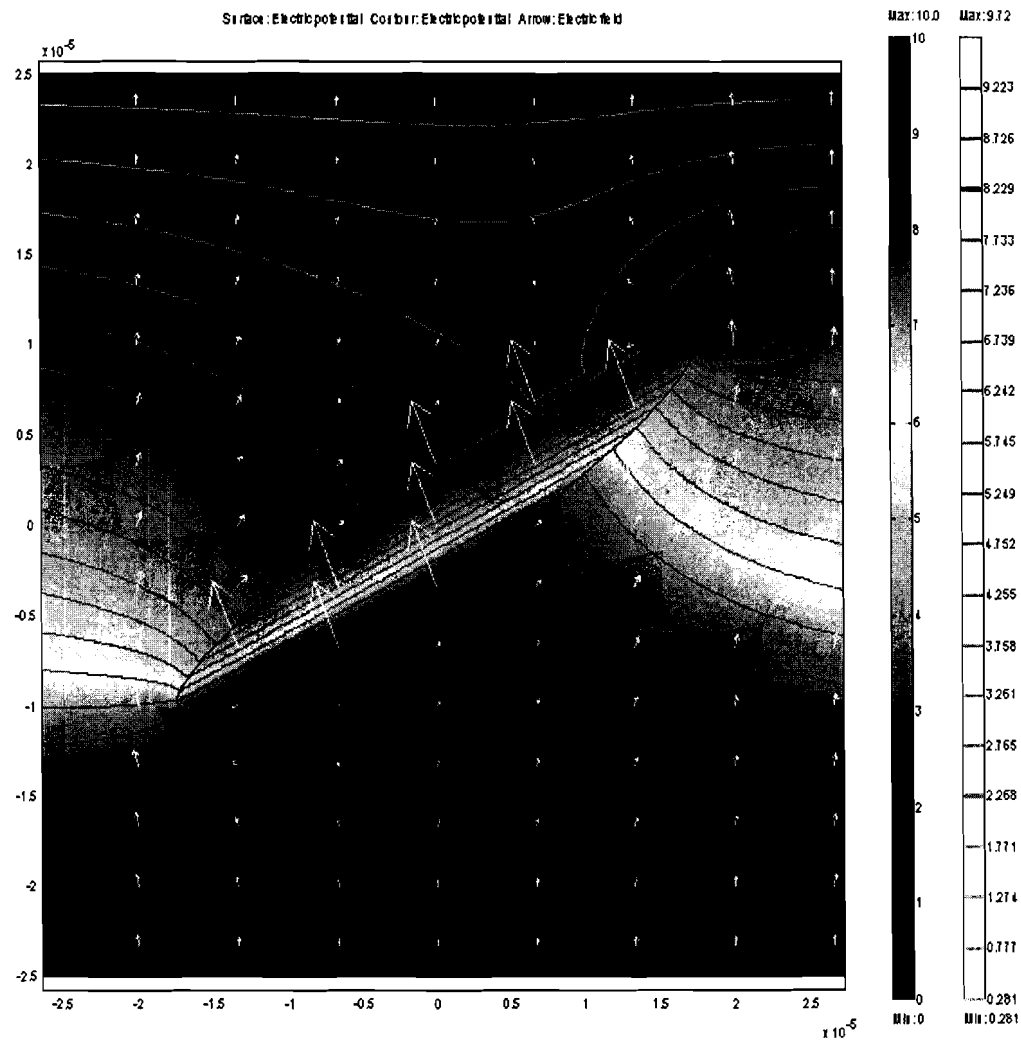

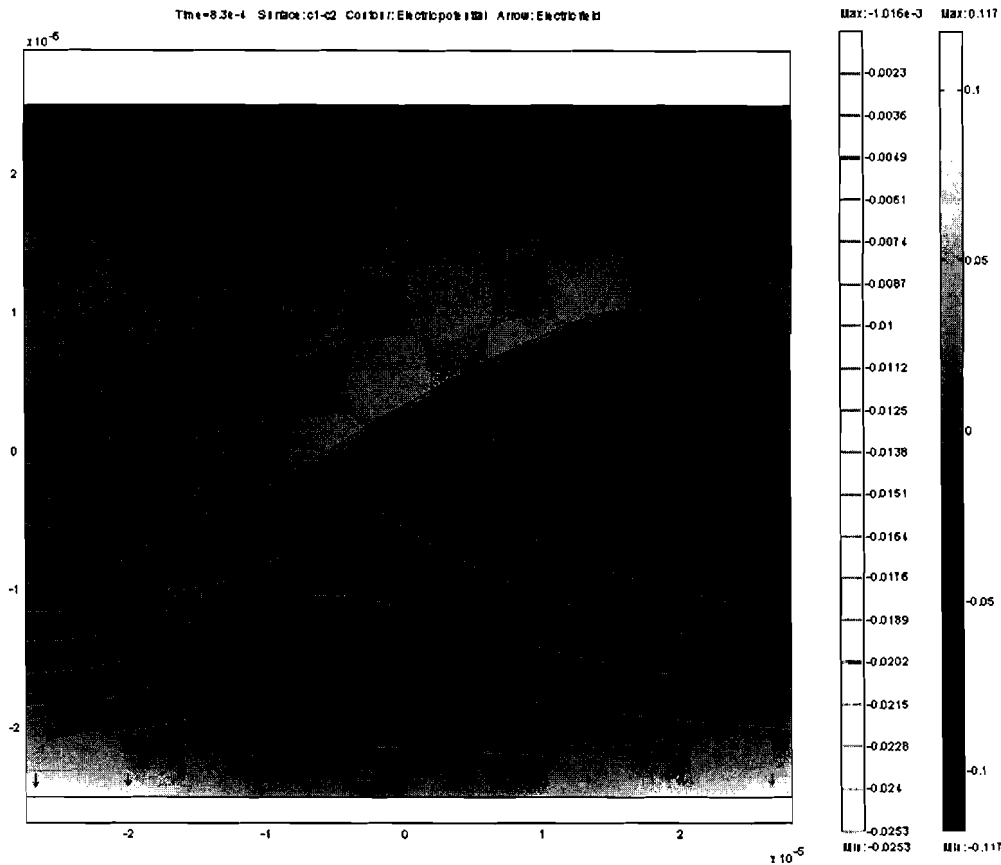| Figure 4: A flake in an AC field of 50 hertz. The flake is rotated 30 degrees above the horizontal, and the field is at 0 degrees in phase.	Surface: Electric potential Contour: Electric potential Arrows: Electric field

Figure 5: The surface plot is the difference between the concentration of the positive and negative ion species. The mobility of both ion species in the host fluid is set as 1×10^{-10} (m/s)/(N/mol), while the diffusivity constant is 1×10^{-10} *2476 kg/(m^2*s). The bottom electrode in the Figure is negatively charged.

Surface: c1-c2
Contour: Electric potential
Arrows: Electric field

of the geometry of the situation, the surface charges created by the host fluid and the flake would be of opposite polarity, so if the surface charge generated by the host fluid, instead of the flake, dominate, than the induced dipole moment would be anti-parallel to the electric field.

Confirming this in FEMLAB is difficult. FEMLAB does have a variable for surface charge, but unfortunately, this is for the free charge, not the bound surface charge. However, FEMLAB allows a custom equation to be input that will govern the boundary plot. The equation below can be used to generate a surface charge plot.[6]

$$\rho_s = \varepsilon_0 \left(\frac{\varepsilon_p - \varepsilon_h}{\varepsilon_p} \right) E_{norm}$$

ρ_s = surface charge density

ε_0 = dielectric constant

E_{norm} = component of electric field perpendicular to the surface

In the FEMLAB model, the electric field term of the above equation is the dot product of the simulated electric field and the unit vector perpendicular to the flake at a given point. This yields the magnitude of the electric field perpendicular to the flake surface.

So far, this has only been properly done on spherical objects and horizontal ellipsoidal flakes (Fig 6), but the surface charge distribution calculated indicates a dipole moment anti-parallel to the electric field. The torque can be found by taking the cross-product of the external (to the flake) electric field, and the dipole moment, when it is
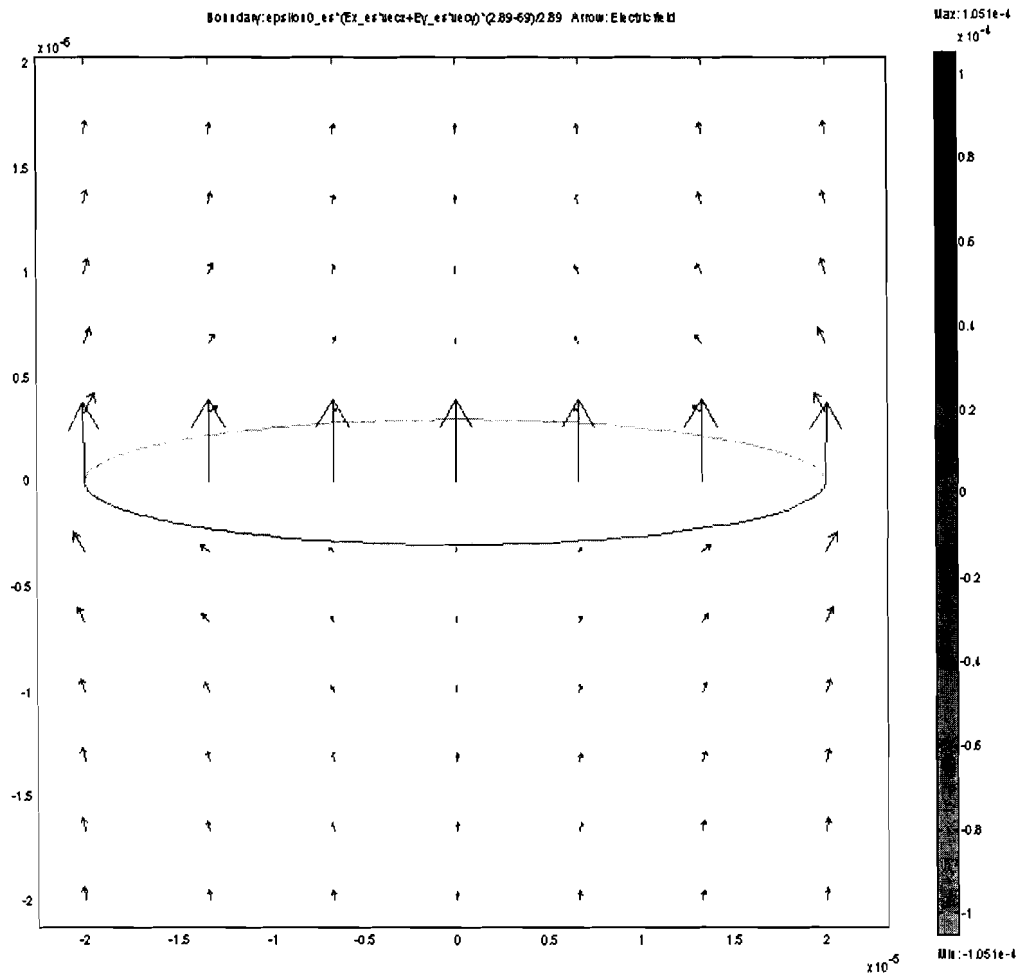

Figure 6: The surface charge distribution indicates that the induced dipole moment is anti-parallel to the internal electric field of the flake.

Arrows: Electric field
Boundary: Surface charge density

taken to be antiparallel to the internal electric field of the flake. The predicted torque would then force the flake towards the vertical, with the second longest axis orienting parallel to the applied electric field. This agrees with experimental observation, as well as the predictions of theory

Summary

PCLC flakes, when subjected to an electric field while in a host fluid of greater dielectric constant, develop an induced dipole moment antiparallel to the internal electric field of the flake. This has been indicated by theory, empirical reasoning, and FEMLAB modeling, and agrees well with experimental results. Further work on fully integrating surface charge into the FEMLAB models, expanding the modeling of ion mobility, using FEMLAB to calculate torques, and modeling true rotating geometries when FEMLAB becomes capable of doing so is still needed.

Appendix 1
FEMLAB modeling

2D AC Capacitor With Flake

The following are instructions for building a capacitor inside of which is a flake of polymer liquid crystal in FEMLAB energized by an AC source. The capacitor is assumed to consist of a pair of plates, a dielectric, and the flake. The capacitor is assumed to be rectangular in shape, and only a cross section will be modeled. The plates and the dielectric of the capacitor are assumed to have the same width and to be assembled in sandwich fashion, i.e. with nothing wrapping around the end of the dielectric. Furthermore, the plates are idealized, in that they are assumed to have no eddy currents or unevenness in potential.

To load FEMLAB, log onto a server from the terminal, maple if it isn't busy, otherwise lime might be the best choice, using xrlogin servername. From there, type femlab to start the program. FEMLAB will launch the model navigator, which has four tabs along the top, New, Model Library, User Models, and Settings. Clicking on the Model Library tab displays a listing of folders containing FEMLAB's demos. The User Models tab displays all the FEMLAB files in the folder which is set as the library root. It is not possible to go up folders in this view. Any files you wish to access have to be either in this folder or in folders within the library root. However, it is quite easy to change the library root by pressing the library root button when the User Models tab is active. To start a new model, click on the New tab.

When the New tab is selected, FEMLAB displays a file tree showing all of its application modes, grouped by applications. Immediately above the file tree is a drop-down menu to select geometry type, 1D, 2D, 3D, 1D axis symmetric, and 2D axis symmetric. 2D is the default, and is what should be used for this application. In the file tree, double click on the Electromagnetics module folder. If you were modeling a DC capacitor, you would want to use the Electrostatics mode, if the conductivity can be ignored, or the Electrostatics, generalized, if conductivity is to be included, inside the Statics folder. However, to model an AC capacitor, select the Quasi-Statics folder, then the Small In-Plane Currents application mode. Then click on the OK button, or you could just double click on the Small In-Plane Currents icon in the file tree.

This launches FEMLAB's Graphical User Interface (GUI). The large white area in the bottom right corner is the geometry modeling area. Before starting to model, open the Options>Visualization/Selection Options menu and turning off face highlighting, or if you're working in 3D, both face rendering and face highlighting. This greatly increases the program's speed, although it can occasionally make selecting certain geometries difficult.   Select Options>Axis/Grid Settings. This is where the size of the axes and the spacing of the grid is set. Set the axes so that they are a bit larger than the total size of the capacitor. It's probably best to set the axis so that the origin is in the center. That will make everything much easier. Next, go to Draw>Specify Object>Rectangle. This is where you can enter values to create a rectangle in the geometry space, as opposed to having to draw it. Set the dimensions equal to the dielectric of the capacitor. (FEMLAB will change the dimensions of the axis so that they will fit into the geometry space properly and without distortion.) Set its base to center, which means that the coordinates specified below will be at the rectangle's center, not its corner. Leave the coordinates at (0,0), again just for ease. Then create the flake, either using yet another rectangle or an ellipse, it doesn't really matter. Remember, if you are making an ellipse, that you are specifying the flakes semi-axis.
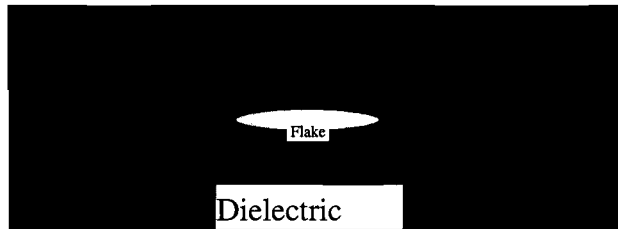
Now it is time to specify the physical characteristics of the model. Open Physics>Subdomain Settings. This sets the characteristics of the insides of the geometries. There should be two subdomains, corresponding to the dielectric, the first subdomain, and the flake, the second. Open the dielectric and the flake subdomains, and set the proper dielectric constant and conductivity. Next open Physics>Boundary Settings. This is where you set the properties of the boundaries between geometries. Notice that there is a checkbox labeled interior boundaries. This will display any boundaries that are between two geometries, as opposed to boundaries with essentially empty space. Leave this empty, as only the external boundaries need to be changed. If the flake is ellipsoidal, boundaries 1 and 4 should correspond to the sides of the dielectric. These should be set to the electric insulation boundary setting. Boundary two should be the bottom of the dielectric. Set this to the Electric potential boundary setting,

and set the voltage to the maximum voltage you want the AC field to reach. Leave boundary 3 set to ground.

Next, select Mesh>Initialize Mesh, or press the button with a single triangle on it. This displays the mesh that will be used to calculate the solution. If it looks too coarse, either select Mesh>Refine Mesh, or press the button with four gray triangles arranged as one larger triangle, and repeat until the mesh looks fine enough. Remember that the finer the mesh, the longer it will take to calculate the solution.

Finally, select Solve>Solve Problem, or press the button with the equals sign on it, and wait for FEMLAB to finish solving the problem. When it does so, you should see a surface graph (the coloring in of the surface) that plots the electric potential at any point within the geometries. To display different properties, or different or more graphs, select Postproscessing>Plot Parameters, or press the button with the amorphous colored blob and the question mark on it. Here you can select multiple different plots at once, displaying many different properties, or even the same properties. To change the view, you can open Options>Zoom and select a command from there, or there are 4 buttons on the toolbar. The + and − magnifying glasses are pretty standard. The magnifying glass with the rectangle on it allows you to select an area of the plot to view by drag-selecting it with the mouse. The magnifying glass with the four arrows is zoom extents, which zooms out until you can see all the geometries you created. Plotting the same value on the surface and contour plots works quite nicely, as the contour plot makes details of the surface plot much easier to see. Remember that you aren't limited to the default expressions to plot. You can input your own expressions in the plot expression box, to make the plot show whatever you want. You can use the various generated variables, such as Ex_qvw for the x-component of the electric field in a quasi-statics, small in-plane current model, as well as the variables x and y to make an expression position dependent. Also, under the general tab, there is a box in which you can place a logical expression to limit which elements are displayed. I generally used this to place spatial limits on the plots, although you could probably use any valid expression.

Finally, if you want to animate something that FEMLAB itself can handle, such as an AC field or moving ions, but not rotating flakes, you can use the Animate mode of postprocessing. Unfortunately, this doesn't work on Linux systems, at least not well. It works much better to create and solve the model in FEMLAB. Go to a PC that has the FEMLAB viewer installed (ask Dr. Kosc or another experienced user about this) and then use the animate selection of the FEMLAB viewer's postprocessing mode menu. Although you can't make changes to the physics of the model here, you can chose whatever plots you wish, and the animation works much better.

14

3D Capacitor Modeling

3D capacitor modeling is almost identical to 2D modeling, there is just one more dimension to specify in the model. There are, however, two important things to remember, boundary suppression and solve preconditioner.

When modeling in 3D, one major problem is that the outside geometries hide those inside. During modeling itself, just setting transparency in Options>Visualization Options to about 0.5 will work [even transparent geometries can make post-processing difficult to look at, especially if using a boundary plotting mode]. The way around this is through boundary suppression. After having set the physics of the model, go to Options>Suppression>Boundary. Then in the pop-up menu select the boundaries that lie between the camera and the flake. Then press apply, and leave. The boundaries selected will disappear, no longer impairing vision.

In 3D Quasi-Statics, Small Currents, FEMLAB defaults the solver preconditioner to Algebraic Multigrid. Unfortunately, this doesn't work. Select Solver>Solver Parameters, and the under preconditioner select SSOR. Then just solve normally.

Appendix 2
Model/Program inventory

<u>FEMLAB Models by folder</u>

In general, the dielectric constant of the dielectric is 69, and its conductivity is 5e-5. The dielectric constant of the flake is 2.89, and its conductivity is 1e-12.
<u>FEMLAB</u>

Ion transport useful #
DC models of ion transport in a uniform DC electric field. The potential is set directly proportional to the y-coordinate. The flake is modeled with a different diffusivity and mobility than the dielectric. Electrically, however, it is identical. These are not multiphysics models.

<u>Ion transport AC no multiphysics</u>
-Identical to *Ion transport useful #* except that the potential is time dependent. This is accomplished through the subdomain physics menu.

Ion movement multi_model # degrees
-These are a series of models similar to *Ion transport AC no Multiphysics*. They are all identical except for the angle at which the flake is from the horizontal.

Ion Transport, 2 species
-Similar to *Ion transport useful#* except it models the transport of 2 different types of ions with opposite charge, but identical mobilities.

Encapsulated flake 1, # degrees
-DC models of the electric properties of an encapsulated flake, using the Electrostatics, generalized application mode.

Encapsulated flake conductive wall layer, # degrees
-Similar to *encapsulated flake 1, # degrees*, but uses a different boundary condition on the capsule. Instead of the continuity boundary condition, the thin conductive layer

16

boundary mode is used instead.

Flake capacitor 1, # degrees
-DC models of a simple flake-capacitor system.

Bound...
-These are assorted electrostatics models, that use an expression for the bound surface charge to try to properly map the surface charge of a flake.

AC modeling
These are early attempts to model flake systems. The models in the Standardized Models folder are probably of more use.

split_flake_1 # degrees
-AC modeling of a rectangular flake with a conducting layer of material running through the middle of the flake.

split_flake_oval_imperfect dip
-Similar to *split_flake_1 # degrees*, but with an oval rather than rectangular flake. At each corner of the flake there is a small triangular sub-domain that was the result of a simplified modeling process. They are set to have the same properties as the dielectric and can be ignored.

Standardized Models
These are a series of models, all using the same design parameters for easy comparison. The dielectric is 100 um thick, and the flake is 20 um long and 6 um thick. The applied voltage is 10 V, applied to the bottom boundary of the dielectric field. This is an AC model, so this voltage varies from 10 V to -10 V, depending on the phase. Frequency can be controlled in the physics-scalar variables menu.

Elip Flake # degrees
-models of the electric properties of flakes in 2D. Does not include ion transport.

Rect Flake # degrees
-Similar to *Elip Flake # degrees*, but with rectangular flake.

Rotated_Capacitor_45_Degrees
-Similar to *Elip Flake # of degrees*, but with a longer flake, and with capacitor not the flake, rotated out of the horizontal. Useful for examining vector values on the surface relative to the flake instead of the capacitor.

Elip Flake sigma comparison
-2 parallel models of flake systems. The dielectrics are shorter, and have differing conductivities. The flakes are longer than standard.

3D Elip Flake 0 degrees
3D Rect Flake 0 degrees
-3D versions of these models. In order to actually see the insides, it is necessary to suppress the outside boundaries.

Ion Transport

All of these models are multiphysics combinations of the Electrostatics, generalized, and the Electrokinetics, transient analysis, application modes. As a shorthand, I use dif for diffusivity, mob for ion mobility, and c(0) for the initial concentration. All the models have equal concentrations of positive and negative ions. Sub 1 is the subdomain representing the dielectric, and sub 2 is the subdomain representing the flake. For those models including surface charge coupling, charge is the fudge factor included in the coupling.

Ion Transport 1 degrees #
-Early multiphysiscs models of ion transport in a flake-capacitor system. Only one species of ion is modeled, and the application modes are only coupled via voltage.

	Vmax = .03 V		
sub 1	dif = 1e-10*2476	mob = 1e-10	c(0) = 2
sub 2	dif = 1e-12	mob = 1e-12/2476	c(0) = 0

Ion transport 2 species # degrees space charge coupled # herz
-Ion transport with two ion species. The two species are identical except for charge. Species one has a single positive elementary charge, while species two has a single negative elementary charge. The application modes are coupled by both voltage and surface charge.

Vmax = .03   Charge = 1e-6

sub1	dif = 1e-10*2476	mob = 1e-10	c(0) = .5
sub 2	dif = 1e-12	mob = 1e-12/2476	c(0) = 0

Ion Transport 2 species # degrees higher voltage
-Similar to *Ion transport 2 species # degrees space charge coupled # herz* but with different subdomain and voltage settings

Vmax = 2.5		frq = 10	charge = 1e-6
sub1	dif = 1e		

Ion Transport/Movie Files

This subfolder of the Ion transport holds movie files generated by FEMLAB postproscesing from the Ion Transport femlab file of the same name. The one exception is *Elec_only_30_degrees.avi*, which is an animation of a static flake in an AC field.

MATLAB programs by folder

Flake

Flake_2D_angular_position#.m
   –Uses theoretical equations to drive a rotating flake model. The theory determines the angle of the flake, which is used in a FEMLAB model. At each new angle, a new FEMLAB model is generated.

Flake_Charge_plotter#.m
-Uses theoretical equations to plot charge on a flake's axis, assuming point charges at the ends of the axis. This is done for a series of different angles of the second longest axis above the horizontal. Version # 2 also plots predicted torques at the angles.
Flake_Phase_Sim1.m
-Changes the phase of applied voltage to a stationary 2D flake using the FEMLAB quasi-static model.

Ion_transport_sim_1.m
-Animates a single discrete ion within a capacitor without a flake.

rotation_time_chart_writer.m
-displays the time needed for a flake to rotate about 90 degrees for varying conductivities and dielectric constants of the dielectric part of the capacitor.

19

time_to_rotate_angle_1.m
-Displays the time needed to rotate about 0 degrees above the horizontal to various angles, as determined by a one dimensional array.

torque_check_1.m,   torque_check_2.m,   torque_sim1.m
-These programs attempt to use the FEMLAB cemtorque function to calculate the torque on the flake. These were not very successful. For the energy expression required by the cemtorque function torque_check_1 uses Weav, while torque_check_2 uses V, the electric potential. Version 2 of the torque_check program is an improvement, but it is still highly inaccurate when compared to the theoretical torques.

2D Simulation Images
This is a collection of programs used to generate a series of images, and then display them in series, to show a rotating flake. This appears to be an early folder, with many of its images removed, so programs in other folders would probably be more useful. One general rule, though, is that anything called a writer is used to generate and save a series of images derived from FEMLAB models, while anything labeled a player is meant to play back a specific series of images. This is dependent upon the name of the image, so changing image names would cause errors.

Flake_animation
This is a similar folder to 2D Simulation Images, but is later, and with a complete set of images. The different mode numbers refer to different values plotted on the surface plot by separate programs. Mode one plots electric potential, mode two plots the x-component of the total current density, and mode three plots the y-component of the total current density. *Flake_2D_mode_1_writer.m* is more or less fully commented. The rest aren't.

Flake_2D_mode_#_writer.m
-Generates a series of images using the plot parameters given by the mode number. It generates images for three different frequencies, 10 Hz, 70Hz, and 150 Hz.

Flake_2D_mode_#_frq_#_player.m
-Plays the images created by one of the writer programs for the specified plot mode and frequency.

Animation_generator.m

-This program runs the three *Flake_2D_mode_#_writer.m* programs as subroutines, to allow them all to be run as a single program overnight.

Flake animation/Alternate Style

Very similar to the programs in Flake animation, except that the conductivity is plotted on the surface plot, and electric potential is plotted on the contours.

Flake_2D_Alternate_writer.m

-Creates images of rotating flakes according to the plotting parameters above.

Flake_2D_frq_#_player.m

-plays the images at the specified frequency generated by *Flake_2D_alternate_writer.m*.

Ion Transport

These files contains models that were generated at a time when we were not completely certain how to use the Chemical Engineering module to model ion transport. These models trace a small number (no more than 24) of discrete ions. The movement is governed by an electrophoresis equation, using FEMLAB models to run this equation. The function postinterp() was used to get the value of the electric fields from the FEMLAB models for use in the MATLAB program. Given the presence of the FEMLAB chemical engineering module ion transport models, the files in this folder are not of great use.

Ion Transport Movie

Flake_ion_transport_writer.m

This is a very crude method of modeling a rotating flake with ion transport. This model works by making a series of FEMLAB ion transport models, each with a flake at a different angle, and then solving them from an initial condition with homogeneous ion distributions up to a point in time determined by the angle of the flake. It stiches these images together to generate a movie. This is probably highly inaccurate. As currently set up, it takes around 30 hours to run, and the output is very suspect.

Flake_ion_transport_writer.m

-This program runs the series of images generated by *Flake_ion_transport_writer.m*

Phase Change Images

This folder contains programs to animate a stationary flake in an AC field. This is better done using the FEMLAB viewer Animation post-processing mode.

Quasi Static flake simulator

The files in these folders animate a rotating flake using parameters and plots typical of the later style, i.e. longer flakes and potential plotted both on the surface and on the contour plots.

Flake_quasi_writer_#.m

-Generates 1 image every 11/10 of a field cycle to keep play and generation time reasonable.

Flake_quasi_reader_1.m

-Plays images generated by *Flake_quasi_writer_#.m*.

Flake_quasi_movie_gen_#.m

-More or less unsuccessful attempts to get MATLAB to generate avi files.

References

1) "Introduction to Liquid Crystals"
http://www.barrettresearch.ca/teaching/liquid_crystal/LC01.htm (20 June 2004).

2) T. Kosc, K. Marshall, S. Jacobs, and J. Lambropoulos. "Polymer Cholesteric Liquid Crystal Flakes in an AC Electric Field," to be submitted to *J. Appl. Phys.*

3) T. Z. Kosc, "Motion of Polymer Cholesteric Liquid Crystal Flakes in an Electric Field." Ph.D. thesis, University of Rochester, 2003.

4) Tyson, Jeff. "How LCDs work" http://electronics.howstuffworks.com/lcd10.htm (30 January, 2005).

5) D. Halliday, and R. Resnick, *Physics, part II* (New York: John Wiley & Sons, Inc. 1960) 752.

6) M. A. Plonus, *Applied Electromagnetics* (New York: McGraw-Hill, 1978)

Modeling of X-Ray Emission in Spherical Implosions on OMEGA

Tina Wang

Modeling of X-Ray Emission in Spherical Implosions on OMEGA

Tina Wang

Webster Schroeder High School

Rochester, N.Y.

Advisor: Vladimir A. Smalyuk

Research Scientist

Laboratory for Laser Energetics

University of Rochester

Rochester, N.Y.

INTRODUCTION

Our society at present is dependent on fossil fuels. The object of our dependence, however, is a finite resource and the source of both pollution and regional conflict. As a result of the dwindling fossil fuel supply, alternate sources of energy will be needed in the future. While solar, wind, and hydroelectric power are all viable options, each has its own disadvantages. Another possibility, nuclear fission, is considered a dangerous one due to the radioactive nature of the materials used and created in the involved reactions.

There is a cleaner and more ideal way to make energy: nuclear fusion. Fusion does not use a dangerously radioactive fuel source-- instead, the reaction relies on a commonly found element, hydrogen. Unlike the fission reaction, which splits a heavy, radioactive atom, fusion combines two smaller atoms into a larger one; both processes follow the concept of converting mass into energy. As the materials involved in fusion are much less dangerous and practically inexhaustible as a resource, the advent of a reactor capable of maintaining the reaction to produce power for human needs is highly desirable.

The Laboratory for Laser Energetics (LLE) at the University of Rochester, with its 60 -beam OMEGA laser system, is a leading institution in direct-drive inertial confinement fusion (ICF). Laser-induced ICF at LLE involves the irradiation of a target capsule about 1 mm in diameter, usually containing the hydrogen isotopes deuterium and tritium. The laser beams cause the target to heat up to extreme temperatures. The outer shell of the target explodes outward, causing the inner portion of the target to implode, dramatically compressing the target and increasing its density so fusion can occur.

OMEGA currently uses D_2 as fuel for its target pellets because D_2 targets are easier to produce than DT targets and are more useful for

diagnosing the target's conditions near peak compression. Primary fusion reactions with D_2 can occur in two ways. Deuterium can react with deuterium to produce a Helium isotope with ~~three~~ one neutron~~s~~ and a free neutron: D + D → ^{3}He (0.82 MeV) + n (2.45 MeV). Deuterium can also react with deuterium to produce a tritium atom and a proton: D + D → T (1.01 MeV) + p (3.02 MeV). Each of these reactions has an equal probability of occurring, and each primary reaction results in products that can also undergo fusion: D + T (0 to 1.01 MeV) → ^{4}He + n (11.9 to 17.2 MeV). The ability for both primary and secondary reactions to occur with maximum yield depends on the temperature and density of the imploded target.

If the target is not irradiated uniformly, it can be subject to irregularities due to Raleigh-Taylor instability and will not implode uniformly. These irregularities cause the plastic shell and fuel to mix and prevent the target from reaching high enough temperature and density for the above reactions to continue at maximum efficiency. The perturbations that result cause the fusion reaction to lose its dynamic. They therefore stand as another obstacle to the attainment of ignition. The deviations caused by Raleigh-Taylor instability can be seen through images mapping the intensity of x-rays emitted by the target during the experiments. Therefore, it is important to consider images of x-ray emission while trying to diagnose what conditions the target was subject to during irradiation and implosion and how these conditions deviated from those in an "ideal" experiment. The project described in this report involved using computer programs written in the PV-Wave language to calculate and visualize x-ray intensity using both experimental and theoretical data, then attempted to find density and charge profiles that would generate x-ray intensity images similar to ones captured experimentally.
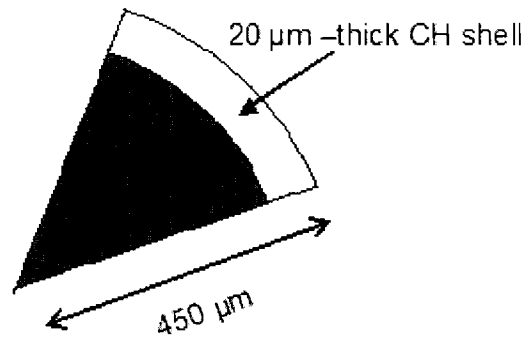
METHODS

Experimental Configuration

Figure 1. Diagram of deuterium-filled plastic pellet.

The experiment was carried out with a target sphere with an initial radius of approximately 450 μm. This target consisted of a plastic CH shell, about 20 μm thick, filled with 15 atm deuterium gas (fig. 1). The target was driven by 60, 351 nm laser beams by the OMEGA system, inputting energy of a total of ~23 kJ in a 1-ns, square-shaped pulse.
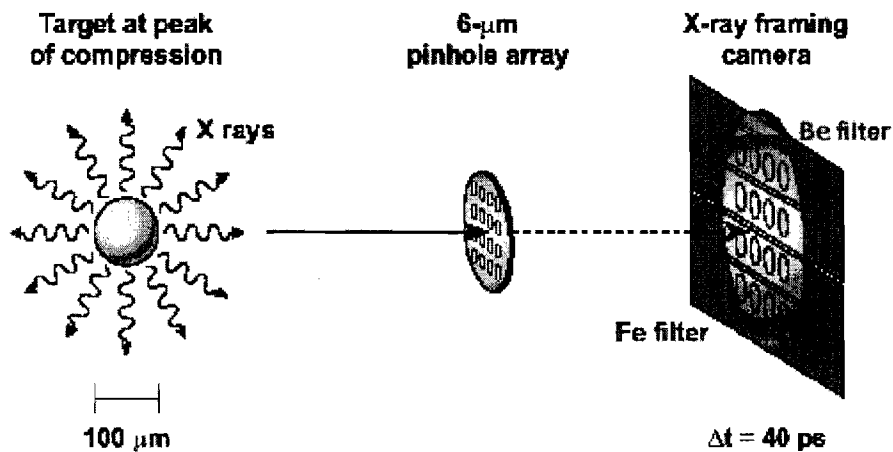
Data Collection

Figure 2. Capturing images of x-ray intensity.

Images mapping x-ray intensity were captured by an x-ray framing camera (fig. 2). X-rays were emitted by the target during peak compression;

these x-rays first encountered a 6 μm pinhole array, then a 200 μm Be filter and a 50 μm Fe filter. Only photons of a certain energy could pass through these filters and proceed. These selected photons then met a microchannel plate (MCP), followed by a phosphor plate. The X-ray photons struck the pores of the MCP, ejecting electrons via the photoelectric effect, which were multiplied in number as they struck the sides of the pores, ejecting even more electrons from the material of the pores. The electrons then hit the phosphor plate, ionizing it and producing an image representing the x-ray intensity of the target at a given time as the target nears peak compression. The camera was designed to capture a series of progressive images at ~40ps time intervals by running a voltage pulse along the MCP.

ANALYTICAL TECHNIQUES USED

Simulation Under Ideal Conditions

$$\frac{dI_v}{ds} = \frac{\varepsilon}{4\pi} - kI_v$$

$$\varepsilon = 3.031024 \times 10^{-15} z^2 d^2 e^{\frac{-energy}{T}}$$

The free-free absorption and emission radiation transport equation solves for x-ray intensity, I_v (in au) in relation to distance (s, in microns) from the center of the target. The Emissivity is ε, k is the absorption coefficient, and z is the charge of the target, d the target's density (cm^{-3}), and T its temperature (eV). Energy is measured in units of eV. Theoretical data simulating the temperature, density, and charge of the target had it reached peak compression under ideal conditions were provided. The data profiles' information was placed into a two-dimensional, 400 by 400 array, each point in the array representing a value for temperature, density, charge, and ionic temperature, since solving for x-ray intensity by integration required data to be in two dimensions. Taken as a whole, these arrays represented images of

the above properties' respective values with respect to distance from the center of the target, in microns (fig. 3).
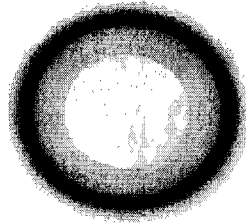

Figure 3. Array of ideal data modeling electron temperature.

The program integrated each of these data arrays (of electron temperature, density, and charge) down their columns (defined as each one-pixel vertical line down the array) to solve the equation for x-ray intensity, producing a one-dimensional array of values that essentially represented x-ray intensity as a function of radius (distance in microns from the center of the image).

Another program took the above lineout of intensity and produced a two-dimensional representation of the x-ray intensity image (similar to the profiles that had been used to generate the x-ray lineout) by setting the value at a certain index in the one-dimensional array at every point in a two-dimensional array that distance away from the center of the image. This was possible because the data was ideal and the produced image had radial symmetry. Each of these intensity images was 400 pixels in width, simulating a circular area modeling the center of the target. These circular models' diameters varied, becoming very small as the target reach peak compression. The images were then run through a series of calculations that simulated the effects that the numerous filters would have on x-ray intensity. These included a 200 μm Be filter, a 50 μm Fe filter, and a resolution filter that was applied through the Fast Fourier Transform (FFT) function on PV-Wave. The Be and Fe filter simulations acted as their experimental equivalents would have, allowing only photons of a certain energy to pass

through them, while the resolution filter moderated the sharp peaks in the original intensity lineout to reduce noise by spreading the intensity at each pixel in the original image over an area with the shape given by the graph (fig. 4).
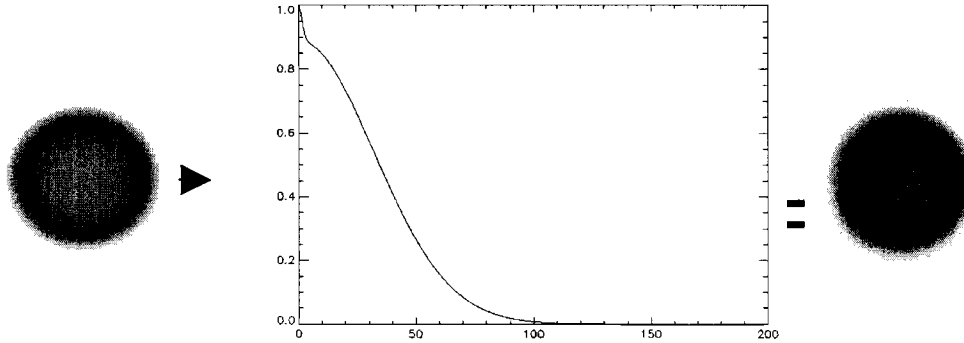

Figure 4. Modulation Transfer Function.

Simulating Modulations

Density and charge profiles were generated in a trial-and-error attempt to produce lineouts of intensity similar to those of the experiments. Different density and charge profiles were characterized by relative areal-density nonuniformity. Instead of the perfectly symmetrical data that had been used to generate ideal x-ray images, irregularities were now imposed upon the density and charge profiles in order to create a less-symmetric and more realistic representation of the imploding plastic pellet. Profiles with modulations were created by polar functions generating irregular, non-symmetric graphs about the origin. By altering the amplitude or constant term of the polar function, the areal-density nonuniformity could be modified and the profile could be made to have more or less wave-like modulations. These profiles were then run through the program for calculating x-ray intensity and used to create lineouts to compare with experimental ones.

RESULTS/DISCUSSIONS

7

Comparison of Experimental Images with Ideal Images

The intensity images produced with ideal profiles of density, charge, and temperature agreed fairly well with the experimental data (fig. 5). However, the experimental images showed intensity near the center of the image and the generated, ideal intensity images displayed a bright-ring characteristic, indicating that the intensity peaked around the circumference of the circular image. The only explanation for this deviance was that the experimental target had imploded nonuniformly, resulting in modulations that produced the center peak of x-ray intensity.
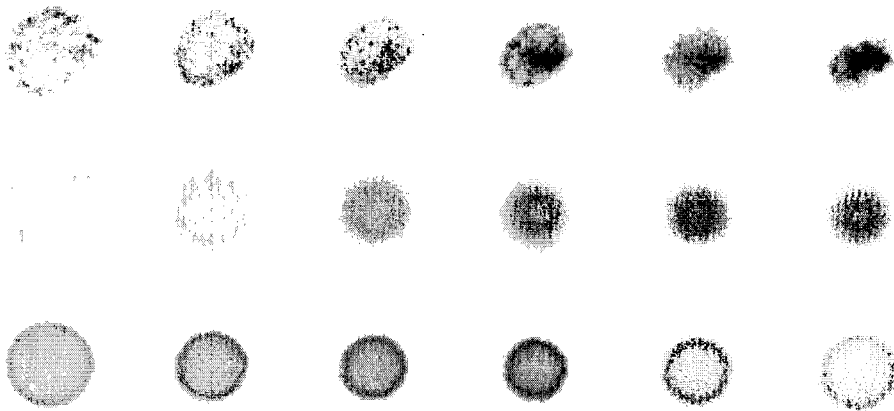
Figure 5. Comparison of experimental images (top row) with images from LILAC (middle row) and nonuniformly generated images (third row).

Profiles were simulated using polar graphs of trigonometric functions, in the form of $r(\theta)=\sin(a_1\theta + c_1) + \cos(a_2\theta + c_2) + ...$, where $a_1, a_2, c_1, c_2,$ and so on are constants. It was found that, if the simulated profile had too large of an areal-density nonuniformity, it would generate a lineout with too many wavelengths (fig. 6).

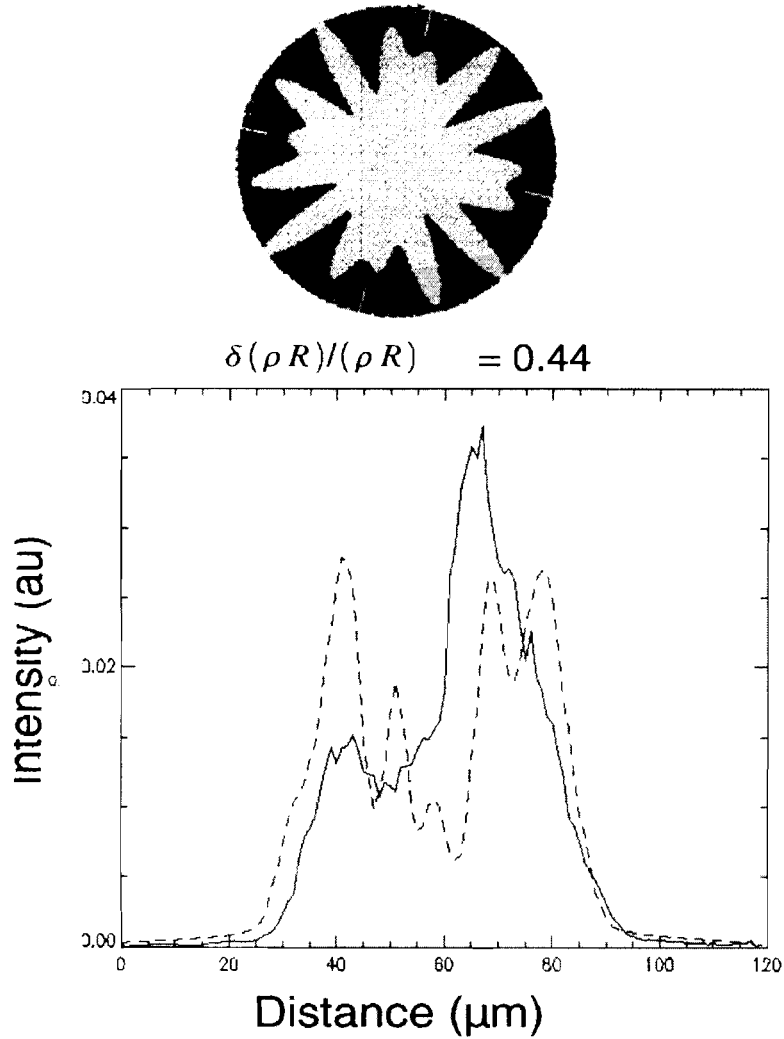$\delta(\rho R)/(\rho R) \quad = 0.44$

Figure 6. Comparison of generated (dotted line) and experimental lineout (solid line).

Conversely, if the profile had little or no areal-density nonuniformity, it would generate a lineout with too few wavelengths. It was found that profiles with about 18% areal-density nonuniformity produced x-ray intensity lineouts that resembled the experimental data the closest (fig. 7)
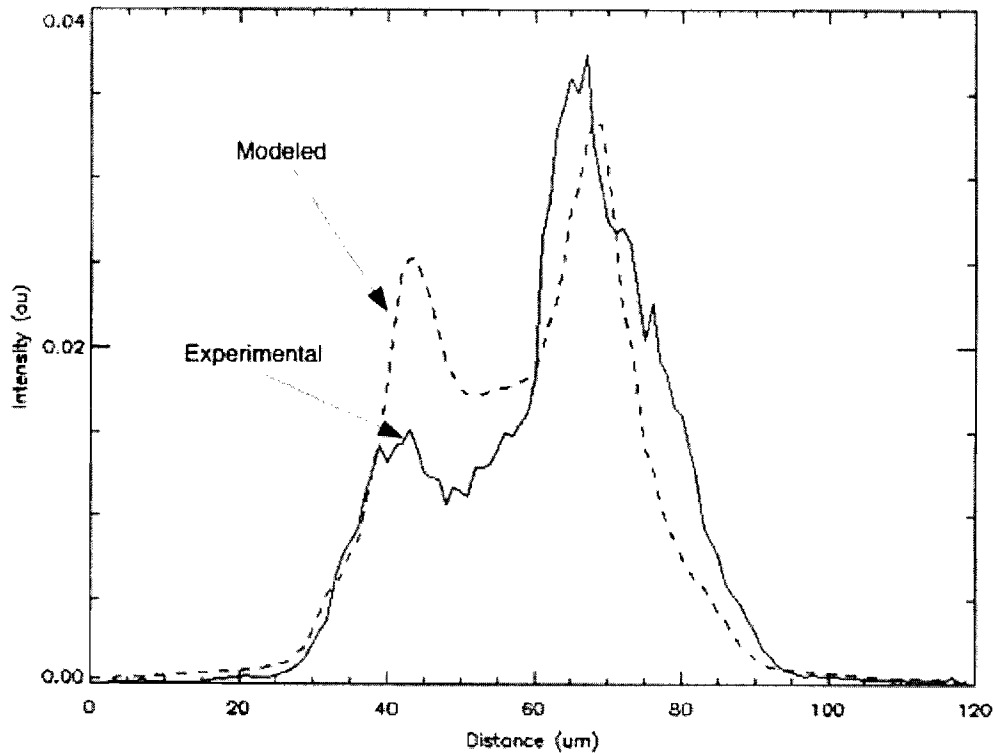
Figure 7. Best comparison of generated (dotted line) and experimental lineout
(solid line).

CONCLUSIONS

Using simulated profiles of imploding targets, x-ray intensity lineouts
of such targets were generated and compared with experimental data to
determine the experimental conditions of the reaction. X-ray lineouts of
targets that had undergone idealized implosion were also produced; the
experimental lineouts were then compared with the theoretical and found to
be in good agreement, but they were not entirely similar. It was decided that
the dissimilarities were a result of modulations present in the experimental
profiles. Thus, modulations were imposed on simulated profiles to better
mimic experimental lineouts (in the future, a method different from the trial-
and-error approach used for modeling described in this report might be more
desirable). It was found that increasing the areal-density nonuniformity of a

profile increased the number of wavelengths present on the generated x-ray lineout. After determining that too large of an areal-density nonuniformity produced an x-ray lineout with too many wavelengths and little or no areal-density nonuniformity generated too symmetrical and ideal of a lineout, it was found that lineouts generated by profiles with 18% areal-density nonuniformity agreed with the best experimental lineouts.

ACKNOWLEDGEMENTS

Photopatterning of Liquid Crystal Alignment Cells

Ariel White

Photopatterning of Liquid Crystal Alignment Cells

Ariel White
Eastridge High School

Advisor: Kenneth L. Marshall

University of Rochester
Laboratory for Laser Energetics
Summer High School Research Program 2004

1. Abstract

Recently, "photobuffing" has emerged as a clean and efficient means of aligning liquid crystals on a polymer surface without contacting it. This process may also be used in combination with a photoresist mask to create cells with patterned directional alignment. Photopatterning has been used to create cells with multiple, separate alignment domains. When made with indium-tin oxide (ITO)-coated substrates and exposed to a voltage, the conductive coating can induce a change in the alignment of the liquid crystal material, making the cells electrically switchable. This feature could have useful applications in both passive and electrically addressable multi-domain liquid crystal devices, including tunable liquid crystal gratings and passive distributed polarization rotators.

2. Introduction

For many years, the accepted process for aligning liquid crystals was the mechanical buffing, or "rubbing" technique. In this process, a coated substrate is contacted by a cloth-covered buffing wheel, which is believed to scratch the coating and cause alignment[1], or to pull on the polymer molecules, creating a "preferential alignment" along the direction of rubbing[2]. However, this procedure has had the

drawbacks of leaving the substrate with many particles and static charges on it.

Rubbing has also limited the creation of multi-domain devices for optics or photonics, as it was difficult to achieve distinct boundaries without disclinations at the edges.

The process of "photobuffing" has recently emerged as a cleaner alternative to the rubbing method of aligning liquid crystals[3]. It also makes possible the use of a mask and polarized UV light source to perform "photopatterning" on substrates coated with an LPP (linearly photopolymerizeable polymer). The polymer, exposed to UV light, then forms chains, along which the liquid crystal molecules align themselves[4,5]. When multiple patterned substrates are combined to produce cells, various optical effects may be achieved[6].

3. Experimental Data[7-10]

ITO-coated substrates were obtained pre-cut to size, while uncoated glass substrates were cut from glass microscope slides. All substrates were cleaned in an ultrasonic bath, then scrubbed with Texwipe® Miraclewipes™ and deionized water. They were then dried with a nitrogen air gun and left for 90 minutes on a hotplate at 110° C. After cooling, they were placed on a spin coater and flooded with the LPP coating solution (Rolic R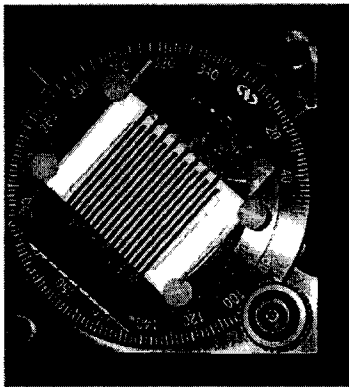OP-203/2CP.) After 30 seconds, they were spun at 3000 rpm for 60 seconds and then baked on a hotplate for 10 minutes at 130° C. A Newport rotating stage measuring 8.5 cm square calibrated in 1-degree increments was modified to hold a chrome photo-mask with 1-mm wide stripes against a glass or ITO substrate coated with the LPP material (Fig. 1). Spacers ranging from 3 to 12 μm were placed on the

Figure 1 :Rotating stage used to expose substrates.

2

corners of the substrate to create a gap between the substrate and the mask. To hold the stage in place and avoid exposing the coating to other light during the exposure process, the stage was placed inside a box 110 cm x 90 cm x 125 cm at a distance of 2.5 cm from the end of the light source setup. A 100-watt xenon light source was used to expose the samples. It was placed behind a polarizer made of 14 fused quartz microscope slides arranged at Brewster's angle. All cleaning, coating, and cell assembly took place in a class 1000 clean room.
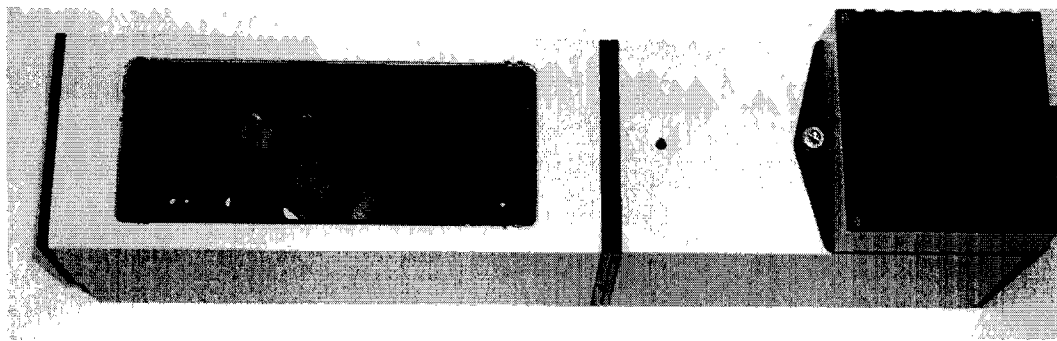

Figure 2: Setup with light source at right and view of brewster's angle polarizer at left.

One set of cells was produced by exposing the first substrate, with no mask, for 8 minutes at 0° rotation. The second substrate was exposed at 0° rotation for 4 minutes with the striped mask over it, then the mask was removed and the substrate was rotated 45° for another 4 minutes of exposure. Cells were made with both thin glass and ITO substrates. Glass cells were assembled by hand, while ITO cells were assembled with a cell assembly mount. In both cases, the two substrates were assembled into cells with the initial direction of 0° rotational exposure of each substrate set 180° away from that of the other. The cells were assembled with 22.1 μm UV epoxy, and cured with a 100W mercury vapor lamp for 90 seconds. The cells were then filled with the nematic liquid crystal E7 by Merck.
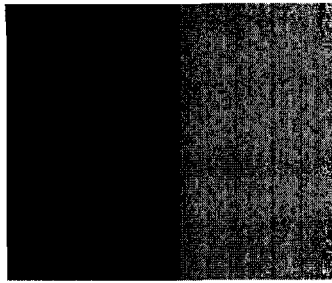
3

Figure 3: boundary between two adjacent alignment domains, viewed at 100x magnification.

These cells are composed of 1-mm wide alignment domains in the shape of alternating stripes. They show good contrast and alignment, and are comparable in quality to mechanically buffed cells on a macroscopic scale. The boundaries between domains are quite clear (fig. 3). These devices are also switchable when a voltage of 0-15 volts is applied across them, and demonstrate clear and gradual transition between alignment stages.
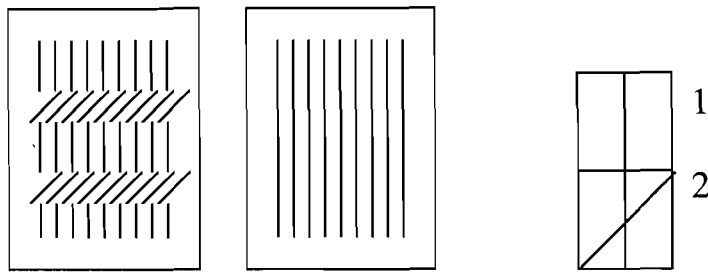

Figure 4: A diagram representing, at left, the patterned and uniformly exposed substrates used to produce a 2-domain cell, and at right, a representation of the alignment created in the two repeating domains of this cell; in domain 1, uniform untwisted alignment, and in 2, 45- degree twist.

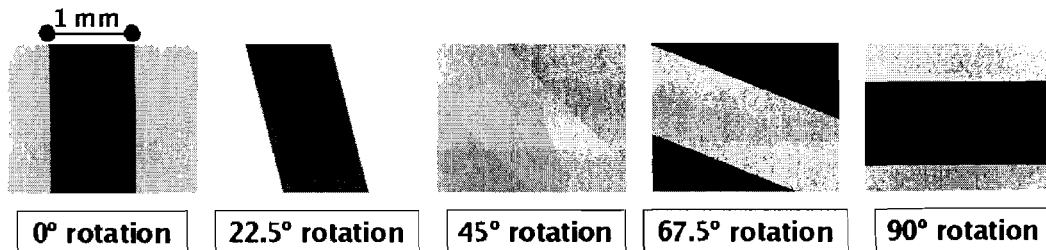| 0° rotation | 22.5° rotation | 45° rotation | 67.5° rotation | 90° rotation |

Figure 5: 2-domain cell rotated under crossed polarizers to show contrast.

Cells with four repeating alignment domains were also created. Two patterned substrates were created with 1-mm stripes of alignment at a 45° orientation to one another. The cell was then assembled with the stripes at right angles to one another at

4

a thickness of 22.1 μm. These cells were first filled with E7, and displayed some evidence of what was thought to be reverse twist along the boundaries between domains, in which certain regions of "twisted nematic" areas of the cell twist the opposite direction from the rest of the cell. A mixture of E7 and .002% CB15, a reverse twist agent, was then used to fill another cell, and did not entirely correct the situation. It is still not clear what causes these regions of disclination, or flaws in the alignment of the cell. However, decreasing the thickness of the cell somewhat while still including some reverse twist agent when filling the cell may prevent these regions of reverse twist.

The alignment domains in these cells alternate between having 45° and 90° twist between the substrates, as illustrated in figure 6. Although they demonstrate disclinations along some boundaries when voltage is applied across the cell, within the individual alignment domains the contrast is good and the switching action is uniform. The cells display some surface flaws as well as the boundary disclinations. However, the previous process of buffing (using the rubbing technique on a coated substrate) through a mask that only allowed the buffing wheel to contact certain areas of the coating while moving in one direction, then moving the mask and buffing in another direction, tended to create regions of alignment separated by unaligned regions, as well as leaving the static charges and particles discussed in the introduction. The devices produced by photopatterning (figure 7) do not have the gaps between domains that were present in comparable devices produced by mechanical buffing[11].
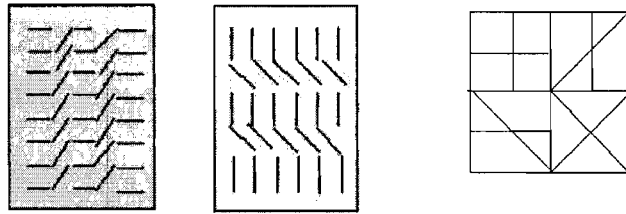
Figure 6:At left, diagrams of alignment directions on the two substrates of a 4-domain cell. At right is a diagram of the twist created in the pattern of four repeating alignment domains when the cell is assembled with the two substrates shown at left: clockwise from top left, 90°, 45°, 90°, and 45° of twist are visible.
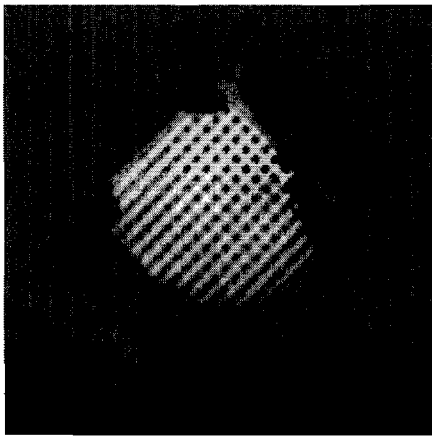

Figure 7: A cell produced with a pattern of four repeating alignment domains

Both sets of cells demonstrate the possibilities of photopatterning, but more investigation must be done into the causes of surface flaws and boundary disclinations in twisted cells, particularly if they are to be used in electrically-addressable devices. Thinner cells should be made to investigate whether this will eliminate regions of reverse twist. Photo-masks with smaller patterns must also be used if useful devices, such as tunable gratings, are to be produced with this process. Larger devices should be attempted, and devices should be produced in a cleaner environment to prevent coating flaws. However, the process of photopatterning is clearly a useful one for producing multidomain liquid crystal devices intended to alter the polarization of light in a controlled manner.

6

References:

[1] J. M. Geary, J. W. Goodby, A. R. Kmetz, and J. S. Patel. *J. Appl. Phys.*, **62**, 4100 (1987).

[2] J. Stohr, M.G. Samant, A. Cossy-Favre, J. Diaz, Y. Momoi, S. Odahara, T. Nagata. *Macromolecules,* **31**, 1942 (1998).

[3] M. Schadt, K. Schmitt, V. Kozinkov, and V. Chigrinov. *Jpn. J. Appl. Phys.,* **32**, 2155 (1992).

[4] M. Schadt, H. Seiberle, A. Schuster, and S. M. Kelly. *Jpn. J. Appl. Phys.,* **34**, L764 (1995).

[5] J. Chen, D. L. Johnson, P. J. Bos, X. Wang, and J. L. West. *Phys. Rev. E.,* **54**, 1599 (1996).

[6] H. G. Galabova, D. W. Allender, and J. Chen. *Phys. Rev. E.,* **55**, 1627 (1997).

[7] P. J. Collings, J. S. Patel. 1996. *Handbook of Liquid Crystal Research* Oxford: Oxford University Press.

[8] C.Y. Tran, *Photochemically Induced Alignment of Liquid Crystals on a Polymer Surface.* LLE High School Summer Symposium, July-August 2003.

[9] C.Y. Tran (private communication).

[10] B.P. Kolodzie (private communication).

[11] LLE 1999 Annual Report (front cover, picture of prototype DPR produced for OMEGA laser).